UNIVERSITY OF WARSAW
FACULTY OF PHYSICS

DOCTORAL THESIS

Joint precision limits and measurement compatibility in realistic quantum photonics sensing

Jayanth Jayakumar

Supervisor: Prof. UW, dr. hab. Magdalena Stobińska

November 8, 2025

Abstract

The sensitivity of a probe to a parameter characterizing a system can be described within the single-parameter estimation framework. In the simplest treatment, the parameter is estimated under ideal conditions, neglecting imperfections from system–environment interactions. More advanced analyses consider estimation in the presence of known environmental noise. Although Heisenberg-limited sensitivity is lost, suitably engineered probes can still offer quantum enhancements. When the noise itself is unknown, the estimation problem becomes more complex, requiring a multiparameter approach.

Fundamental precision bounds for multiparameter estimation are well established, but their practical attainability remains elusive due to the challenge of constructing measurements with good multiparameter sensitivity. For a given probe, the incompatibility of optimal observables associated with different parameters poses an additional roadblock to achieving simultaneous optimal estimation. In practice, assessing the compatibility of separable measurements is essential, since very often collective strategies that are impractical are required to saturate the bound capturing fundamental incompatibility.

To this end, we consider the joint estimation of phase and phase diffusion, introducing quantifiers for information extraction and availability. We find that double homodyne measurement on states generated by the interference of N photons injected into one beamsplitter port yields the highest sensitivity. With respect to measurement compatibility, we study the joint estimation of phase and photon loss, and of phase and phase diffusion. Using the same multiphoton states, we compare double homodyne detection and photon counting against multiparameter precision benchmarks for collective and separable measurements. Among the cases considered, photon counting generally offers better performance for joint phase and loss estimation, while double homodyne still performs reasonably in some regimes for both estimation problems.

Streszczenie

Czułość sondy na parametr charakteryzujący układ można opisać w ramach estymacji jednoparametrowej. W najprostszym ujęciu parametr ten jest szacowany w warunkach idealnych, z pominięciem niedoskonałości wynikających z oddziaływań między układem a środowiskiem. Bardziej zaawansowane analizy uwzględniają estymację w obecności znanego szumu środowiskowego. Choć w takich przypadkach traci się czułość ograniczoną przez granicę Heisenberga (ang. Heisenbeg-limited sensitivity), odpowiednio zaprojektowane sondy wciąż mogą zapewnić kwantową poprawę dokładności. Gdy jednak sam szum jest nieznany, problem estymacji staje się bardziej złożony i wymaga podejścia wieloparametrowego.

Fundamentalne granice precyzji dla estymacji wieloparametrowej są dobrze znane, lecz ich praktyczne osiągnięcie jest trudne ze względu na problem skonstruowania pomiarów o dobrej czułości wieloparametrowej. Dla danej sondy niezgodność (ang. incompatibility) optymalnych obserwabli dla różnych parametrów stanowi dodatkową przeszkodę w osiągnięciu optymalnej estymacji dla wszystkich parametrów jednocześnie. W praktyce kluczowe znaczenie ma ocena zgodności pomiarów separowalnych, ponieważ często tylko strategie kolektywne, które są niepraktyczne, pozwalają osiągnąć granicę wyznaczoną przez fundamentalną niezgodność.

W związku z tym rozważamy wspólną estymację fazy i dyfuzji fazy, wprowadzając miary ilości informacji możliwej do wydobycia i dostępnej w układzie. Pokazujemy, że pomiar podwójnie homodynowy (ang. double homodyne measurement) dla stanów powstałych w wyniku interferencji N fotonów wprowadzonych do jednego portu z rozdzielaczem wiązki (ang. beamsplitter) zapewnia najwyższą czułość.

Jeśli chodzi o zgodność pomiarów, badamy wspólną estymację fazy i strat fotonów oraz fazy i dyfuzji fazy. Używając tych samych stanów wielofotonowych porównujemy detekcję homodynową i zliczanie fotonów w testach porównawczych (ang. benchmark) wieloparametrowej precyzji dla pomiarów kolektywnych i separowalnych. Spośród analizowanych przypadków zliczanie fotonów zapewnia zazwyczaj lepsze wyniki w jednoczesnej estymacji fazy i strat, natomiast pomiar homodynowy wciąż daje zadowalające rezultaty w niektórych przypadkach obu problemów estymacyjnych.

To my mom...

Acknowledgements

Firstly, I would like to thank my supervisor, Prof. Magdalena Stobińska, for her guidance and timely financial support throughout my PhD. I am also grateful to her for connecting me with renowned researchers in my field, enabling valuable collaborations.

Particularly, I acknowledge funding from the National Science Centre "Sonata Bis" Project No. 2019/34/E/ST2/00273 620 and the Foundation for Polish Science "First Team" Project No. POIR.04.04.00-00-220E/16-00 (originally No. 622 FIRST TEAM/2016-2/17).

I would also like to thank Marco Barbieri for his mentorship, support, and long collaboration. It has been a great pleasure working with him on both of my papers.

I thank Rafał Demkowicz-Dobrzański who taught me the foundations of quantum estimation theory and metrology, kick starting my interest in the field, Lorcan Conlon and Francesco Albarelli for fruitful discussions that further refined the understanding of my work.

I am also grateful to Adam Buraczewski for his extensive support, both in programming and in administrative matters over the years.

A special mention goes to my friends and colleagues: Michał Siemaszko, for translating the abstract into Polish; and Monika Mycroft, Srikanth Korutla, Sachin Gadakh, Morteza Moradi, Valerii Kachin, Moein Naseri, and Maryam Afsary, for the nice moments I shared with them, making my PhD journey enjoyable both in and outside of work.

Last but not least, I cannot thank my parents and my wife Sahana enough for their unwavering emotional support.

List of Publications

J. Jayakumar, M. E. Mycroft, M. Barbieri, and M. Stobińska, *"Quantum-enhanced joint estimation of phase and phase diffusion"*, New J. Phys. **26**, 073016 (2024)

J. Jayakumar, M. Barbieri, and M. Stobińska, *"Measurement compatibility in multiparameter quantum interferometry"*, Phys. Rev. A **112**, 042604 (2025)

List of Figures

Abbreviations

POVM **P**ositive **O**perator-**V**alued **M**easure

MZI **M**ach-**Z**ehnder **I**nterferometer

BS **B**eam **S**plitter

SNS **S**hort **N**oise **S**caling

HS **H**eisenberg **S**caling

HB **H**olland-**B**urnett state

SPDC **S**pontaneous **P**arametric **D**own **C**onversion

BHD **B**alanced **H**omodyne **D**etection

LO **L**ocal **O**scillator

MLE **M**aximum **L**ikelihood **E**stimator

OBE **O**ptimal **B**ayesian **E**stimator

MSE **M**ean **S**quare **E**rror

CRB **C**ramér-**R**ao **B**ound

FI **F**isher **I**nformation

FIM **F**isher **I**nformation **M**atrix

QCRB **Q**uantum **C**ramér-**R**ao **B**ound

QFI **Q**uantum **F**isher **I**nformation

QFIM **Q**uantum **F**isher **I**nformation **M**atrix

SLD **S**ymmetric **L**ogarithmic **D**erivative

RLD **R**ight **L**ogarithmic **D**erivative

HCRB **H**olevo-**C**ramér-**R**ao **B**ound

NHCRB **N**agaoka-**H**ayashi-**C**ramér-**R**ao **B**ound

MIB **M**ost **I**nformative Bound

JS **J**ordan-**S**chwinger map

gHB **g**eneralized **H**olland-**B**urnett state

SQB **S**ingle **Q**ubit **B**ound

CQE **C**ollective **Q**uantum **E**nhancement

Contents

Introduction and Problem Statement

With the birth of *quantum mechanics* at the start of the 20th century, the *quantization* of the electromagnetic field [1] led to the development of *quantum optics*. As a consequence, sensors built on the *quantum photonics* platform emerged, utilizing the *quantum* features of light such as *squeezing* [2, 3] and *entanglement* [4, 5]. These offered improved sensitivities compared to conventional sensors, and as a result, quantum sensing holds great promise for advancing classical sensing technologies by leveraging quantum states as probe components [6, 7, 8]. These quantum probes are not limited to light-based systems [9, 10], but also include matter-based systems such as nanoparticles [11, 12] and Bose-Einstein condensates [13, 14], as well as hybrid systems involving the interaction of light and matter through optomechanics [15, 16].

One of the most remarkable achievements of quantum sensing to date is the detection of gravitational waves from the merger of two black holes 1.4 billion light years away from Earth, detected by the LIGO gravitational wave detector in 2015 [17]. Subsequently, this accomplishment was awarded with the Nobel prize in physics in 2017.

In this thesis, we use the term *quantum sensing* in a general operational sense to refer to the entire sensing process, from probe preparation to inference, and the term *sensor* to denote the sensing scheme that encompasses all components involved at each stage. In contrast, *quantum metrology* investigates the precise extent of quantum enhancement in parameter-estimation precision, as well as the search for optimal quantum states and measurement strategies that attain the fundamental precision limits set by quantum mechanics. Accordingly, we use this term specifically in the context of our search for quantum-enhanced sensors. Quantum metrology is intrinsically tied to the estimation theory from statistics which provides its underlying mathematical framework. Casella and Berger's *Statistical Inference* [18] defines an estimate as "the realized value of an estimator (that is, a number) that is obtained when a sample is actually taken". Thus, it should be clear that, in practice, the estimate is an inference made about the underlying probability distribution through sampling. Hence, in practice, an estimation process involves an *estimator* which is a function of the chosen sample and outputs an estimate; merely on a classical level, sampling the system multiple times improves the accuracy of estimation.

In quantum physics, the state of a physical system is reflective of the probability distribution of values of quantum observables through the *Born rule*. Hence, the observables such as position, momentum, energy are directly measured with a generalized measurement or *positive operator-valued measure* (POVM) [19]. At the same time, there exist latent or unknown parameters characterizing the properties of a physical system such as temperature of a gas, tensile strength of a rod, concentration of a solution etc. Such parameters can only be *indirectly* inferred by measuring a suitable observable on the quantum state of the system, thereby paving the way for quantum estimation theory [20, 21]. This can then be tied back to quantum metrology, which dictates the resourcefulness of quantum probe states to quantum-enhance the accuracy of estimation.

Therefore, a *single* parameter leaves its signature on the measurement data of an observable

and in practice, the sampling of the corresponding probability distribution leads to the estimation of the parameter with the estimator. However, in reality, there are always *multiple* parameters to be estimated in a system, which then introduces the *trade-offs* [22, 23] of estimation precision between the parameters. This is fundamentally linked to the *compatibility* [24] of observables that correspond to the optimal information extraction of each parameter.

Furthermore, the efficiency of *practical* sensors are bound to be depreciated by environmental noise and imperfections in the fabrication of the sensor itself, for example, in the presence of photon losses [25, 26] and dephasing [27]. These noise effects characterized by the so-called *nuisance parameters* [28, 29] are like a black-box during the sensing process. Thus, an efficient estimation process necessitates a combined estimation of the parameter such as an optical phase [30, 31], magnetic field [32, 33] along with the nuisance parameters.

To this end, we investigate two research problems exploring the aspects of joint estimation limits and measurement compatibility in noisy optical interferometry.

Our first problem deals with the quantum-enhanced joint estimation of phase and phase diffusion in a metrological scheme involving the Mach-Zehnder interferometer (MZI). A comprehensive assessment of the performance of any general metrological scheme should include quantifiers based on (i) the *information extraction* of the measurement and (ii) the *information content* of the probe states. This two-fold assessment of the quality of the scheme is unique to our methodology which was not considered in the previous investigations of the same problem to the best of our knowledge. We investigate the joint-precision limits for an important class of two-mode multiphoton states of fixed photon number in each mode. These states are generated by varying the partition of the photons injected into the ports of a beamsplitter, allowing for the interplay of both mode and particle entanglement that are necessary for quantum enhancement. We make use of an informational trade-off relation holding for qubits formulated by Vidrighin et al. [34] and gauge the performance of our separable measurement with higher order multiphoton states.

The investigation of our second problem begins with the following related question: How far-off are we from the performance of collective measurements and optimal information extraction if we consider practical separable measurements? Naturally, this translates to the investigation of *compatibility* of a separable measurement i.e., the *additional* estimation trade-offs between the two parameters resulting from our choice of measurement. Once again, we operate in the setting of realistic quantum interferometry and estimate two parameters at once: (i) phase and photon loss, and (ii) phase and phase diffusion (phase noise). Using the same class of definite photon number multiphoton states, we explore the performance of practical separable measurements such as homodyne detection and photon counting with respect to multiparameter precision benchmarks for correlated and uncorrelated measurement strategies. Our figure of merit for this assessment incorporates the two key factors limiting the performance of a chosen separable measurement: (i) compatibility of the optimal separable measurement and (ii) the fundamental compatibility i.e., the *intrinsic* trade-off estimation trade-offs between the two parameters.

The thesis is structured as follows: Chapter 1 summarizes the state-of-the-art in quantum sensing within the quantum photonics domain. Chapter 2 introduces the mathematical tools necessary to quantify and understand the advanced multiparameter bounds employed in our research. Chapter 3 investigates the performance of a metrological protocol constituting an important class of multiphoton probe states and double homodyne measurement for the joint estimation of phase and phase diffusion. Considering the same protocol, Chapter 4 explores measurement and fundamental compatibility through examples of joint estimation of phase and loss, as well as phase and phase diffusion. Chapter 5 presents the numerical methods and showcases the program used to perform computations related to Chapter 4. Chapter 6 concludes the thesis with conclusions and outlook.

Chapter 1

Towards realistic sensing with quantum photonics

This chapter addresses the key aspects that connect theoretical concepts with experimental implementations in the pursuit of realizable quantum sensing schemes. The efficiency of such schemes depends both on their robustness to noise and on the proper realization of their constituent elements. Accordingly, we first present the state of the art in (i) noisy phase estimation techniques and (ii) the experimental implementation of essential components of a quantum sensor, spanning state engineering, detection, and inference. We then discuss recent developments in multiparameter metrology, with a focus on the joint estimation of phase and accompanying nuisance parameters. While describing these facets, we briefly juxtapose the formalisms of quantum interferometry, multiphoton state generation, homodyne detection, likelihood, and Bayesian inference. In this way, the chapter places our work in the context of recent advances and illustrates the relevance of the theoretical results presented in chapters 3 and 4 for practical quantum sensing.

The organization of the chapter is as follows. We begin with a brief motivation for utilizing photonic degrees of freedom to encode quantum information. This naturally leads to information encoding in the modes of an optical interferometer and its implications for phase estimation. We then provide the formalism necessary to understand the constituent operations involved. Subsequently, we present an overview of phase estimation in both lossless and noisy optical interferometry, focusing on the most important and recent advances in the noisy case. Next, we introduce the experimental implementation of a quantum sensor in terms of probe state preparation, detection, and inference, along with the relevant formalism. Finally, we conclude by discussing experimental and theoretical advancements in multiparameter phase sensing, complementing the succeeding theoretical framework of quantum estimation presented in Chapter 2.

1.1 Photonic degrees of freedom

Some of the commonly used photonic degrees of freedom to encode quantum information include polarization [35, 36], spin angular momentum [37], orbital angular momentum [38, 39], time-bin [40, 41, 42], and time-frequency [43, 44, 45], and others to encode continuous variable states [46, 47, 48]. In particular, the horizontal and vertical polarizations of light were used to encode states of two dimensional quantum states and the interaction of polarized light with matter such as a non-linear medium allowed for the manipulation and preparation of these states. A particularly relevant encoding for quantum metrology is path encoding [6, 35, 49], in which information is carried by

the spatial modes of photons i.e., the well-defined paths they traverse, typically facilitated by waveguides. This lies at the heart of quantum interferometry where photonic states described in terms of spatial modes are manipulated by linear optical elements such as beamsplitters and phase shifters.

1.2 Quantum interferometry

The advantage of encoding information in the spatial modes of an interferometer has profound applications in optical quantum metrology. Therefore, in this section, we motivate the interferometric platform using the basic single-photon model. This is essential for understanding the interferometric framework used in our research.

The wave aspect of a photon becomes apparent in an interferometer through the introduction of "path uncertainty" for the photons before detection. Fig. 1.1 depicts a Mach-Zehnder interferometer (MZI) with a second 50:50 beamsplitter that mixes paths ABD and ACD, so we do not know whether the detected photons traversed ABD or ACD, but only with a probability of 1/2. If L_a and L_b denote the lengths of paths AC and AB respectively, and ΔL_a and ΔL_b denote the small changes in the respective path lengths, the associated phase shifts are given by $\phi_a = k\Delta L_a$ and $\phi_b = k\Delta L_b$, where a and b denote the spatial modes corresponding to the paths or "arms" of the interferometer. We note that interference occurs only if the path difference between the arms $\Delta L = |L'_a - L'_b| \leq \Delta L_{\text{coh}}$, where $L'_a = L_a + \Delta L_a$, $L'_b = L_a + \Delta L_b$, and $\Delta L_{\text{coh}} = c/\Delta\omega$ is known as the *coherence length* related to the bandwidth of the incoming wave $\Delta\omega$. This criterion is essential to maintain the untraceability of the paths taken by the detected photons on which interference effects are predicated upon. Therefore, the output state of the MZI is a result of the interference of these paths taken by the photons carrying the information about the phase difference or what we will call as simply the relative phase $\phi = \phi_b - \phi_a$ which naturally affects the amount of interference.

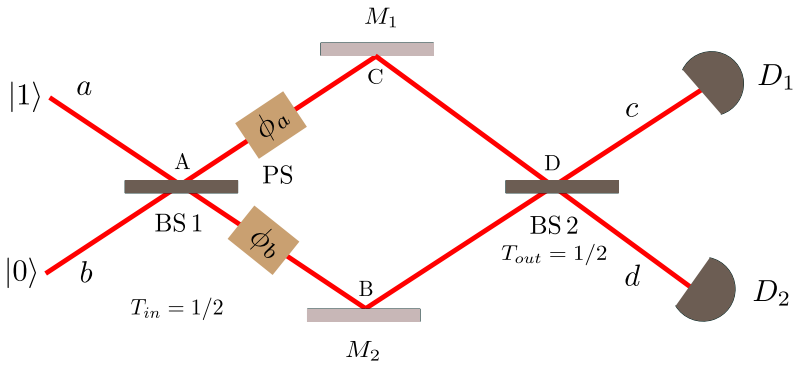

FIGURE 1.1: Scheme of the MZI setup demonstrated here for a single photon interference.

In practice, the presence of an object in one of the arms of the MZI changes the path length of that arm and consequently, the phase, which in turn affects the photon interference. Hence, the MZI and other interferometers, such as the Michelson, Fabry-Perot, and Sagnac ring interferometers [1], all of which fundamentally use the relationship between phase difference and photon interference, find significant applications in astronomy, astrophysics, and general relativity. A most notable application is the detection of gravitational waves by the LIGO and Virgo interferometers where the gravity wave stretches the region of space-time it occupies. Thus, when the wave arrives at one of the interferometer arms, it changes the distance between the first beamsplitter and the mirrors

$M_{1(2)}$, thereby changing the path length AC or AB (Fig. 1.1) and introduces a path difference between the arms. As a result, the signature of such weak signals are captured in the relative phase imprinted in the input state of light known as the probe. The subsequent measurement of the output probe yields information about the unknown phase, and thus phase estimation becomes a crucial task in quantum metrology with light. This will be the main focus starting from Section 1.3 onward.

1.2.1 Formalism

For our purposes, we focus on the MZI and provide a brief summary of its formalism constituting the sequence of operations starting from the beamsplitter operation. The beamsplitter consists of two pathways for the photon to enter and splits the photon in a given path into transmitted and reflected components (Fig. 1.2). Hence, the two input ($\hat{a}$, $\hat{b}$) and the output ($\hat{a}'$, $\hat{b}'$) spatial modes are related as

$$\hat{a}' = r\hat{a} + t\hat{b} \tag{1.1a}$$

$$\hat{b}' = t\hat{a} + r\hat{b} \tag{1.1b}$$

with $|r|^2 + |t|^2 = 1$ and $r^*t + rt^* = 0$, such that the commutation relations[1] between all the mode operators are satisfied. If the transmitted and the reflected beams differ by a phase $\pm\pi/2$, then $t = |t|$, $r = \pm i|r|$. Letting $|t|^2 = T = \frac{1}{2}$, the transmittivity of a 50:50 beamsplitter, the input modes are transformed to the output modes in the Heisenberg picture as

$$\begin{bmatrix} \hat{a}' \\ \hat{b}' \end{bmatrix} = \begin{bmatrix} \frac{1}{\sqrt{2}} & \pm\frac{i}{\sqrt{2}} \\ \pm\frac{i}{\sqrt{2}} & \frac{1}{\sqrt{2}} \end{bmatrix} \begin{bmatrix} \hat{a} \\ \hat{b} \end{bmatrix} \tag{1.2}$$

Alternatively, the transformation in Eq. 1.2 is given by[2]

$$\begin{bmatrix} \hat{a}' \\ \hat{b}' \end{bmatrix} = \mathcal{U}_{\mathrm{BS}}^{\dagger} \begin{bmatrix} \hat{a} \\ \hat{b} \end{bmatrix} \mathcal{U}_{\mathrm{BS}}, \tag{1.3}$$

where $\mathcal{U}_{\mathrm{BS}} = \exp\left[\pm i\frac{\pi}{4}(\hat{a}^{\dagger}\hat{b} + \hat{a}\hat{b}^{\dagger})\right]$

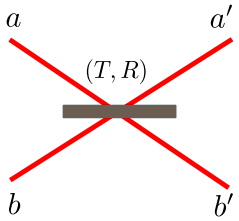

FIGURE 1.2: A beamsplitter with transmittivity T and reflectivity R has two input ports and two output ports, labeled by the modes (a, b) and (c, d), respectively.

Similarly, the phase shift (PS) results in the following mode transformation

[1] If $\hat{a} \to \hat{a}_1$, $\hat{b} \to \hat{a}_2$, then: $[\hat{a}_i, \hat{a}_j^{\dagger}] = \delta_{i,j}$, $[\hat{a}_i, \hat{a}_j] = [\hat{a}_i^{\dagger}, \hat{a}_j^{\dagger}] = 0$; $i, j = 1, 2$.

[2] The equivalence between Eq. 1.2 and Eq. 1.3 can be shown using the Baker-Campbell-Hausdorff (BCH) formula in a straightforward manner.

$$\begin{bmatrix} e^{i\phi_a} & 0 \\ 0 & e^{i\phi_b} \end{bmatrix} = e^{i(\phi_a+\phi_b)/2} \begin{bmatrix} e^{-i(\phi_b-\phi_a)/2} & 0 \\ 0 & e^{i(\phi_b-\phi_a)/2} \end{bmatrix}. \tag{1.4}$$

The factor $e^{i(\phi_a+\phi_b)/2}$ becomes an irrelevant factor for the computation of the probability distribution. Assuming that the transmitted and the reflected beams differ by phases $-\pi/2$ and $\pi/2$ at the first (BS 1) and the second (BS 2) beasmplitters respectively, the MZI transforms the input modes ($\hat{a}$, $\hat{b}$) to the output modes ($\hat{c}$, $\hat{d}$) as follows

$$\begin{bmatrix} \hat{c} \\ \hat{d} \end{bmatrix} = \underbrace{\frac{1}{\sqrt{2}} \begin{bmatrix} 1 & i \\ i & 1 \end{bmatrix}}_{\text{BS 2}} \underbrace{\begin{bmatrix} e^{i\phi_a} & 0 \\ 0 & e^{i\phi_b} \end{bmatrix}}_{\text{phase shift}} \underbrace{\frac{1}{\sqrt{2}} \begin{bmatrix} 1 & -i \\ -i & 1 \end{bmatrix}}_{\text{BS 1}} \begin{bmatrix} \hat{a} \\ \hat{b} \end{bmatrix} \tag{1.5}$$

More compactly, one can write

$$\begin{bmatrix} \hat{c} \\ \hat{d} \end{bmatrix} = e^{i\phi'/2} \begin{bmatrix} \cos\frac{\phi}{2} & -\sin\frac{\phi}{2} \\ \sin\frac{\phi}{2} & \cos\frac{\phi}{2} \end{bmatrix} \begin{bmatrix} \hat{a} \\ \hat{b} \end{bmatrix}, \tag{1.6}$$

where $\phi' = \phi_a + \phi_b$ and $\phi = \phi_b - \phi_a$.
Inversely,

$$\begin{bmatrix} \hat{a} \\ \hat{b} \end{bmatrix} = e^{-i\phi'/2} \begin{bmatrix} \cos\frac{\phi}{2} & \sin\frac{\phi}{2} \\ -\sin\frac{\phi}{2} & \cos\frac{\phi}{2} \end{bmatrix} \begin{bmatrix} \hat{c} \\ \hat{d} \end{bmatrix}, \tag{1.7}$$

1.3 Phase sensing

In this section, we describe how information about an unknown phase can be extracted using resourceful probe states. Since we employ multiphoton probe states in our research, we briefly examine how the choice of such states enables enhanced sensitivities in phase estimation. We focus our attention on the achievable phase sensitivities in ideal and lossy interferometry.

The measurement of photons in the two output arms of the MZI carries information about ϕ. Hence, loosely one can expect that as more photons traverse through the arm undergoing phase shift, more phase information can be obtained. More precisely, it is the photon number uncertainty of the input state that influences phase uncertainty. Thus, in a classical sense, the larger the photon number uncertainty, the smaller is the phase uncertainty [27]. The addition of non-classical effects such as entanglement between particles, modes and quadrature squeezing further increases the photon number uncertainty leading to a much reduced phase uncertainty (Section 2.2 of Chapter 2).

1.3.1 Lossless phase sensing

In a MZI with photon-counting detectors, the measured observable is the photon number difference, $\hat{O} = \hat{c}^\dagger\hat{c} - \hat{d}^\dagger\hat{d}$, and the corresponding phase uncertainty is given by the error propagation formula (EPF):

$$\Delta\phi = \frac{\Delta\hat{O}}{\left|\frac{d\langle\hat{O}\rangle}{d\phi}\right|}, \quad \Delta\hat{O} = \sqrt{\langle\hat{O}^2\rangle - \langle\hat{O}\rangle^2}. \tag{1.8}$$

Using the Jordan-Schwinger mapping to angular momentum operators $\hat{J}_{x,y,z}$, $\hat{O}$ can be replaced by $\hat{J}_z$, allowing simpler computation of $\Delta\phi$ for Fock state inputs. Thanks to this mapping, it can be shown that the use of the input state $|N,0\rangle_{a,b}$ leads to the *Shot-noise scaling* (SNS)[3] [9]

$$\Delta\phi = \frac{1}{\sqrt{N}}. \tag{1.9}$$

Other non-classical states: More general Gaussian states with squeezing in both modes can yield improved precision scaling $\frac{1}{\langle N\rangle}$ [3, 50]. The N00N state $\frac{1}{\sqrt{2}}(|N,0\rangle + |0,N\rangle)$ (see Section. 1.4.3 for more details) achieves the *Heisenberg scaling* (HS)

$$\Delta\phi = \frac{1}{N}. \tag{1.10}$$

In the frequentist approach (see Section 2.2 of Chapter 2), the N00N state is optimal, as its phase evolution is N times faster than a coherent state: $\frac{1}{\sqrt{2}}(|N,0\rangle + |0,N\rangle) \xrightarrow{\text{PS}} \frac{1}{\sqrt{2}}(e^{iN\phi_a}|N,0\rangle + |0,N\rangle)$, amplifying phase shifts and increasing fringe density and sensitivity [51, 52, 53].

Definite photon number states $|k,N-k\rangle_{a,b}$, can surpass the SNS. In particular, the twin-Fock or *Holland-Burnett (HB) state* $|\psi_{in}\rangle = |N/2,N/2\rangle$ gives $\Delta\phi = \frac{1}{N(N/2+1)}$ [54, 55]. After the first beamsplitter, $\mathcal{U}^{(1)}_{\text{BS}}|k,N-k\rangle$ forms the main probe states studied in Chapters 3 and 4. These scalings are general and not restricted to the MZI.

1.3.2 Realistic phase sensing

With respect to our research problem, we are particularly interested in the investigation of phase sensitivities in a realistic interferometer. Therefore, we describe here the two types of noise (Fig. 1.3) relevant to our setup. These represent some of the most detrimental and common forms of noise affecting phase sensitivity, and we therefore review recent and significant investigations in the literature concerning the achievable precision limits in this scenario.

Photon loss: In a MZI, the loss of the photons to the environmental modes is an inevitable type of noise which affects the phase estimation. This is typically modeled using fictitious beamsplitters of transmissivity η, with the photons being reflected into the environment modes.

Phase diffusion: Another type of noise is the fluctuation of path lengths along the arms of the MZI leading to random changes in the phase. These types of noise are discussed in detail in Chapters 3 and 4, together with their motivation and the mathematical formalism.

1.3.2.1 Investigations towards quantum-enhancement

Despite the presence of these noise effects, it is still possible to realize quantum enhancement of phase estimation and operate above the SNS. Extensive experimental and theoretical efforts have been devoted to this direction, as we will outline in the following.

The optimal states in the presence of photon losses in both MZI arms have been found analytically in [56]. Such states of low photon number have been engineered and demonstrated to yield quantum-enhanced sensitivity [57]. In contrast, the performance of N00N states that achieve the HS significantly deteriorates under photon losses [58, 59, 60]. Classical multi-pass strategies have been known to mimic the behavior of N00N states considering the susceptibility of the latter to noise [61, 62]. However, in [63], it has been shown that such a strategy performs worse than a

[3] Note that the use of coherent state and vacuum: $|\psi_{in}\rangle = |\alpha,0\rangle_{a,b}$ results in the scaling $\frac{1}{\sqrt{2\langle N\rangle}\sin\phi}$.

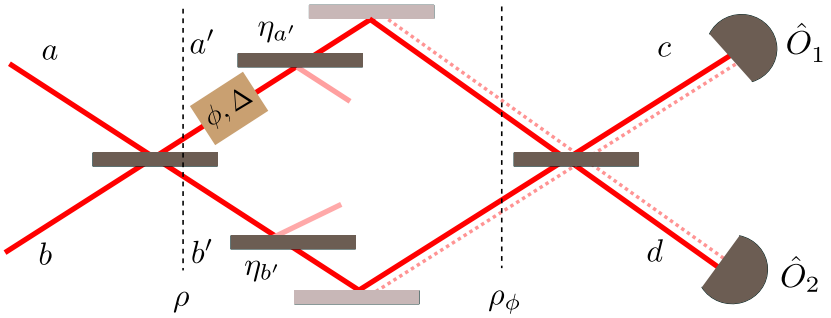

FIGURE 1.3: The MZI scheme with three types of noises included: (i) photon loss modeled using beam-splitters of transmission coefficients η_a and η_b and (ii) phase diffusion modeled as the spread Δ of a Gaussian probability distribution.

quantum multi-pass strategy involving the optimal states of [56] signifying the precedence of the experiment in [57]. In the MZI, the addition of an optical component known as the parametric amplifier [64, 65] after the phase shift but before the losses hit the probe has been used to combat the effects of losses [66]. Such a technique works by broadcasting the phase information encoded on a single photon state into a state with large number of photons. Other investigations concerning the photon losses include [67, 68, 69, 70].

Theoretical and experimental investigations involving phase diffusive noise demonstrated the use of a near-optimal homodyne measurement scheme involving Gaussian states even in the presence of large diffusion [30, 31, 71]. An analysis of phase estimation in the presence of diffusion considering qubits in polarization degrees of freedom was carried out in [72].

Lastly, we highlight works addressing phase estimation in the presence of various noise sources. In the presence of a general noise channel, and in particular, the depolarizing and the amplitude damping channels, entanglement-assisted precision enhancement have been experimentally demonstrated in [73]. Theoretical techniques to restore the HS under noisy scenarios in particular under dephasing have been demonstrated in [74]. The effect of another type of noise in the form of random phase generators on phase estimation using two-level probe has been investigated in [75].

We emphasize that the phase estimation precision achieved via the aforementioned efforts are only strategies or schemes to get closer to the ultimate precision limits in noisy quantum metrology. Therefore, as mentioned for the noiseless case, we will revisit the phase-estimation precision limits with optimal strategies using the tools described in Section 2.2 of Chapter 2.

1.3.2.2 The importance of noise-robust states

Although, the N00N states are renowned for attaining the HS, they are highly susceptible to photon losses. In the context of optical remote sensing [76, 77], light has to propagate over long distances through the Earth's atmosphere to collect ground data for mapping, and undergoes attenuation due to scattering and absorption. In this case, unfortunately, N00N states are not the ideal candidates. The sensitivity of the N00N state rapidly falls even below the SNS and even performs worse than coherent states under losses. On the other hand, the structure of the optimal states in the presence of losses derived in [56] differ significantly from that of N00N states which also supports their high susceptibility.

Therefore, in general, one must turn to definite photon-number states, squeezed states, or more general Gaussian states when searching for probes that remain robust under losses, as encountered in tasks such as long-distance optical remote sensing. This constitutes one of the main objectives

explored in Chapters 3 and 4, where we investigate the potential of definite photon-number states in the broader multiparameter setting.

1.4 Towards experimental implementations

Having provided an overview of phase estimation in both noiseless and noisy scenarios, this section is dedicated to techniques relevant for the successful realization of practical quantum sensing schemes. These include: (a) the engineering of probe states, (b) the measurements used for information extraction, and (c) inference methods. Here, we incorporate the latest state-of-the-art developments in these areas alongside the corresponding formalism.

1.4.1 Generation of resourceful probe states

We focus on the generation of multiphoton states, beginning with the simpler single-photon states. Subsequently, a two-mode multiphoton state with N photons in total is interfered on a 50:50 beam splitter, producing a class of definite photon-number states with useful metrological properties. These states are non-Gaussian and with respect to our need to produce noise-robust states are suitable for noisy phase estimation tasks [55]. A process that lies at the heart of the preparation of these states is the *spontaneous parametric down conversion* (SPDC) [78, 79] which finds applications not only in quantum metrology [80] but also in quantum cryptography [81, 82], quantum teleportation [83] and quantum computation [84, 85]. Hence, we will provide rather a detailed description of the SPDC formalism and its experimental implementation for the generation of multiphoton states in the next section. For completeness, we also discuss the generation of N00N states notwithstanding their lack of noise-robustness.

1.4.2 Generation of definite photon number states

1.4.2.1 The process

SPDC is a *non-degenerate* parametric process that, classically, arises from the interaction of a strong incident field with the atomic dipoles of a crystal possessing second-order nonlinearity. As a result, in addition to the usual linear polarization term, the induced polarization includes a non-linear term: $P^{(2)} = \chi^{(2)}E^2$, where $\chi^{(2)}$ is the second-order electric susceptibility and E is the electric field component of the incident field. However, for a complete description of this interaction, one needs to invoke quantum mechanics. Thanks to field quantization, a photon of high energy referred to as the *pump* photon in a mode p of the incident field probabilistically splits into *signal* and *idler* photons of lower energies in modes s and i respectively as depicted in Fig. 1.4. This conversion follows the energy and momentum conservation relation leading to $\hbar\omega_p = \hbar\omega_s + \hbar\omega_i$ and $\vec{k}_p = \vec{k}_s + \vec{k}_i$ (phase-matching condition), where ω_l and $\vec{k}_l$ denote the frequency and the wave vectors of the photons in the mode l. SPDC can only be described quantum mechanically due to the spontaneous creation of signal and idler photons from initial vacuum states.

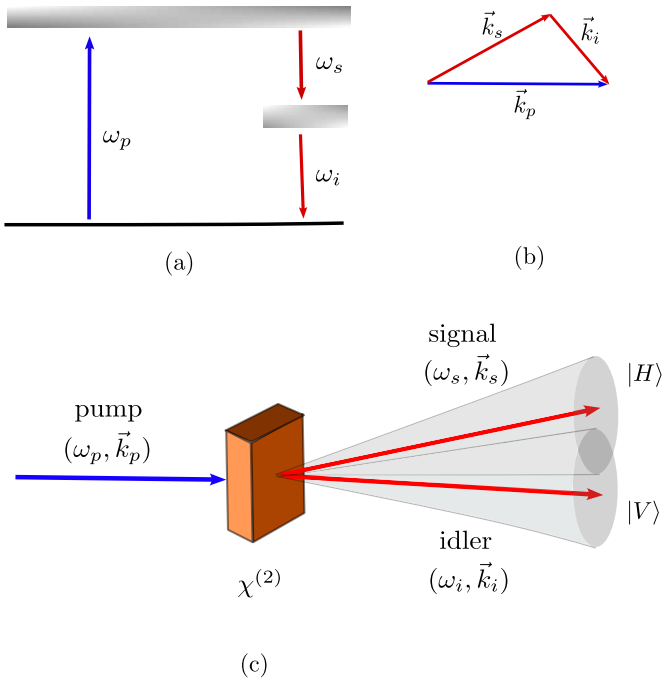

FIGURE 1.4: (a) An illustration of energy conservation relation. (b) A vectorial representation of the phase matching condition. (c) Schematic of a Type-II SPDC process using a nonlinear crystal. The signal and idler photons emerge as cones corresponding to the possible directions of their wave vectors, in accordance with the phase-matching condition. The overlapping region of the cones represents indistinguishable photon pairs, which are necessary to produce an output state entangled in the two polarization modes.

1.4.2.2 Relation to two-mode squeezing

Since the pump field is strong, one can treat it classically leading to the approximation $\hat{a}_p \approx \alpha$. Thus, under this approximation, setting $\hbar = 1$, the interaction part of the actual Hamiltonian[4] characterizing the SPDC process is given by [87]

$$\tilde{H}_{int}(t) = i\chi^{(2)}(\alpha^* \hat{a}_s \hat{a}_i - \alpha \hat{a}_s^\dagger \hat{a}_i^\dagger), \tag{1.11}$$

In the interaction picture,

$$H_{int}(t) = i\chi^{(2)}(\gamma^* \hat{a}_s \hat{a}_i e^{-i(-\omega_p+\omega_s+\omega_i)t} - \gamma \hat{a}_s^\dagger \hat{a}_i^\dagger e^{i(-\omega_p+\omega_s+\omega_i)t}), \tag{1.12}$$

If one can control the pump to match the energy conservation relation $-\omega_p + \omega_s + \omega_i = 0$, Eq. 1.12 can be simplified into

$$H_{int} = i(\beta^* \hat{a}_s \hat{a}_i - \beta \hat{a}_s^\dagger \hat{a}_i^\dagger), \tag{1.13}$$

where $\beta = \chi^{(2)}\gamma$.

[4]The Hamiltonian consists of contributions from two processes: (i) sum-frequency generation (SFG) [86] and SPDC as follows: $\tilde{H}_{int}(t) = i\chi^{(2)}(\underbrace{\hat{a}_p^\dagger \hat{a}_s \hat{a}_i}_{\text{SFG}} - \underbrace{\hat{a}_p \hat{a}_s^\dagger \hat{a}_i^\dagger}_{\text{SPDC}})$. SFG is the reverse process of SPDC wherein the two photons of frequency ω_1 and ω_2 combine to produce a photon of frequency ω_3 such that $\omega_3 = \omega_1 + \omega_2$. Unlike SPDC, SFG has both classical and quantum descriptions.

The time evolution operator corresponding to 1.13 takes the exact form of the two-mode squeezing operator $S^{(2)}(\xi)$ as follows

$$\mathcal{U}_{\text{SPDC}} = e^{-iH_{int}t} = e^{(\beta^* t\hat{a}_s\hat{a}_i - \beta t\hat{a}_s^\dagger\hat{a}_i^\dagger)} = e^{(\xi^*\hat{a}_s\hat{a}_i - \xi\hat{a}_s^\dagger\hat{a}_i^\dagger)} = S^{(2)}(\xi), \tag{1.14}$$

where $\xi = \beta t = re^{i\theta}$. We emphasize that this formalism of SPDC is restricted to single modes of the pump, signal, and idler fields and a general description would involve summing over all modes.

1.4.2.3 Single photon states

Considering only the real squeezing parameter at $\theta = 0$, it should be clear by noticing $r = |\gamma|\chi^{(2)}t$, the amount of squeezing is proportional to the pump strength $|\gamma|$. Therefore, by operating the pump in the low squeezing limit i.e., $r << 1$, we have $\mathcal{U}_{\text{SPDC}} \approx 1 + r\hat{a}_s\hat{a}_p - r\hat{a}_s^\dagger\hat{a}_p^\dagger$ and its action on the input state $|\alpha, 0, 0\rangle$ is given as

$$|\psi^{\text{SPDC}\,(l)}\rangle \approx \mathcal{U}_{\text{SPDC}}\,|\alpha,0,0\rangle \approx |\alpha,0,0\rangle - r\,|\alpha,1,1\rangle \tag{1.15}$$

$$= c_0\,|\alpha,0,0\rangle + c_1\,|\alpha,1,1\rangle\,. \tag{1.16}$$

where c_0 and c_1 are probability amplitudes introduced after normalization. The first, second, and the third modes correspond to the pump, signal, and idler modes respectively.

As for any two-mode squeezed vacuum (TMSV) state, the state $|\psi^{\text{SPDC}\,(l)}\rangle$ is entangled in the signal and idler modes, and a measurement of the idler photon collapses the state in the signal mode to a single photon state by process known as *heralding*. Therefore, SPDC combined with heralding can be treated as a single-photon source. Thus, in the low squeezing regime, one can generate single photon states via heralding (see Fig. 1.5(c) for an experimental scheme).

1.4.2.4 Multiphoton states

For the generation of higher order photon number states, the squeezing strength needs to be increased by increasing the pump power. The full SPDC output state in the relevant signal and idler modes is a TMSV state which reads

$$|\psi^{\text{TMSV}}\rangle = \frac{1}{\cosh r}\sum_{n=0}^{\infty}(-\tanh r)^n\,|n,n\rangle \tag{1.17}$$

Similar to the heralding of single photon states, the detection of n photons using a photon number resolving detector in the idler mode collapses the state in the signal mode to a multiphoton state $|n\rangle$ as illustrated in Fig. 1.5(a). We note that, in the general multimode case, the heralded photon state is not necessarily pure, as the state may differ across modes. Suitable state-engineering techniques are required to align the modes and produce heralded pure multiphoton states within a single common mode.

1.4.2.5 Experimental requirements

The phase matching condition is an important requirement for the successful implementation of SPDC and unfortunately, not all materials satisfy it with the exception of birefringent crystals. Unlike ordinary crystals, these special materials can have multiple refractive indices along different symmetry axes and are classified into uniaxial or biaxial crystals when they possess two or three

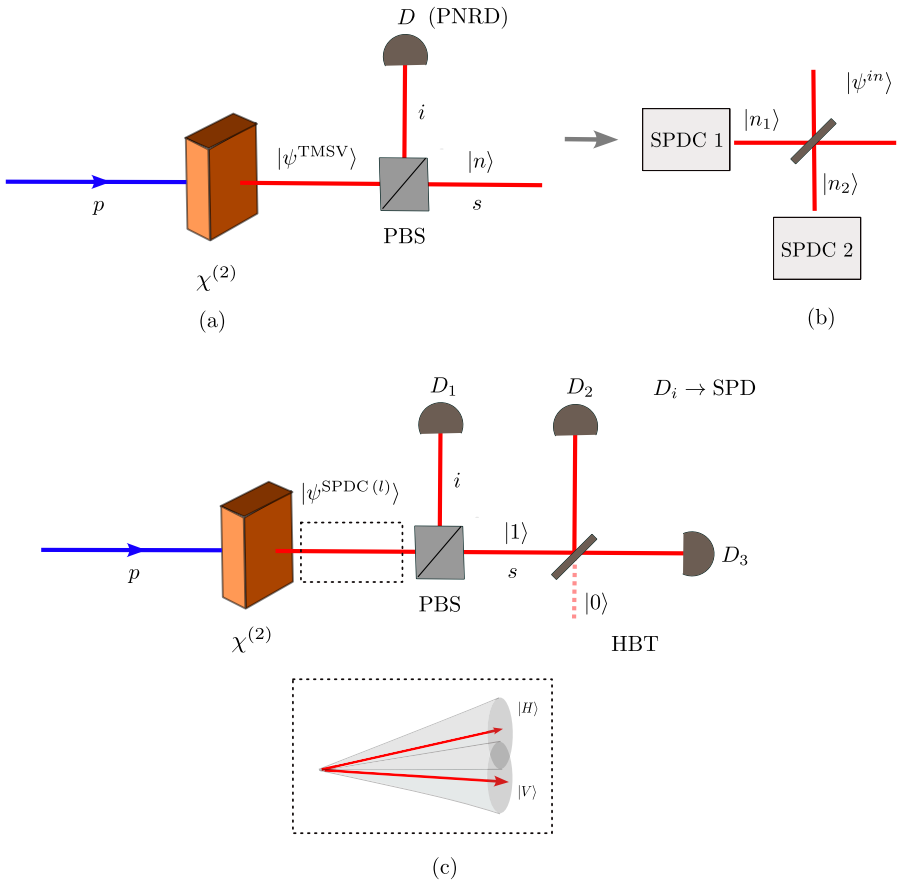

FIGURE 1.5: (a) Generation of a multiphoton state in the high squeezing SPDC regime (type-II). The output state in this case $|\psi^{\text{TMSV}}\rangle$ is passed through a polarization beamsplitter (PBS) which spatially separates the orthogonally polarized photons. Following this, the idler mode is detected using a photon-number-resolving detector (PNRD) to herald the signal mode in a multiphoton state $|n\rangle$. (b) The prepared multiphoton states are incident on a 50:50 beamsplitter to produce multiphoton states that are useful in quantum metrology. (c) Generation of a single photon state in the low squeezing SPDC regime. This time, the idler mode is detected using a single photon detector to prepare a single photon state.

distinct refractive indices, respectively, for a given wavelength of the incident beam. In these crystals, one can have a type-I SPDC process, where the signal and idler modes have the same polarization orthogonal to the pump mode or a type-II SPDC process, where the signal and the idler modes have orthogonal polarization. The heralding of multiphoton states from the TMSV states described above makes use of a type-II SPDC process. Additionally, one must not forget the importance of the the energy conservation relation which must be satisfied to implement the SPDC operation (Eq. 1.13).

1.4.2.6 Potential drawbacks

As we can see from Eq. 1.15, the SPDC in the low squeezing regime is a probabilistic process with the success of producing a pair of photons being significantly low with $|c_0|^2 >> |c_1|^2$ and most of the times, we end up with the vacuum state. Thus, one has to be increase the pump power to detect more photon pairs which is not always experimentally feasible. To overcome this, one can deploy post-selection techniques using coincidence counters and increase the probability of detecting two

photons at each spatially separated detectors with a time delay τ (Fig. 1.5). This keeps the desirable $|1,1\rangle$ states in the signal and the idler modes and discards the vacuum states without increasing the pump power.

1.4.3 Generation of N00N states

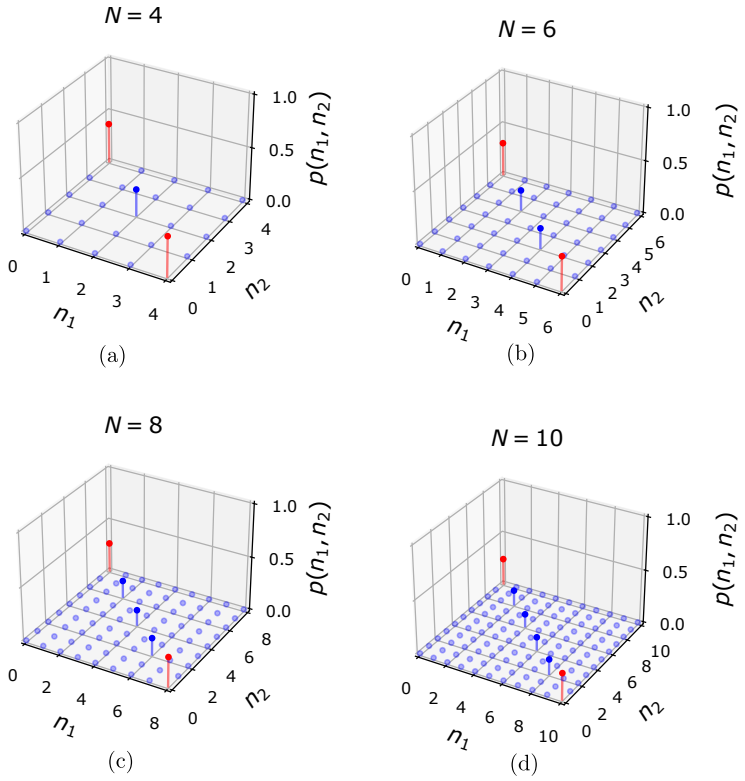

FIGURE 1.6: Three-dimensional plots of the photon number probability distribution corresponding to the output states of a generalized HOM interference with $N = 4, 6, 8, 10$. For a particular value of N, the end states, i.e., $\{|0, N\rangle, |N, 0\rangle\}$, appear with the highest probability, indicated using the taller red projections (compared with the shorter blue ones).

The experimental realization of the generation of N00N states involves the input state $|\alpha, \xi\rangle_{a,b}$ in a MZI (Fig. 1.7) and measured with photon-number-resolving detectors (PNRDs) up to $N = 2, 3$ in polarization degrees of freedom [88]. In particular, the preparation of single-mode squeezed vaccum state $|\alpha, \xi\rangle_{a,b}$ involves the use of *degenerate* SPDC, where the split photons from the pump have the same frequency in the signal mode i.e., $\omega_p = 2\omega$ [87]. Similar methods to generate N00N states were demonstrated using photon counting [89, 90, 91] and homodyne [92] measurements. These strategies achieve the HS $\frac{1}{\langle N \rangle}$. The first beamsplitter operation on $|1,1\rangle_{a,b}$ gives $|1,1\rangle_{a,b} \xrightarrow{\text{BS1}} \frac{-i}{\sqrt{2}}(|2,0\rangle_{a',b'} + |0,2\rangle_{a',b'})$, known as the Hong-Ou-Mandel (HOM) effect [93], where two photons always exit in pairs and the state $|1,1\rangle_{a',b'}$ interferes destructively. As a "generalized" HOM effect, for N photons, the input state $|N/2, N/2\rangle_{a,b}$ results in the state

$$|N/2, N/2\rangle \xrightarrow{\text{BS1}} \sum_{n=0}^{N} c_n |n, N-n\rangle = c_0 |0, N\rangle + c_1 |1, N-1\rangle + \cdots + c_{N-1} |N-1, 1\rangle + c_N |N, 0\rangle , \tag{1.18}$$

which still possess a sensitivity close to the HS, and, remarkably, the states at the end: $\{|0, N\rangle , |N, 0\rangle\}$ occur with the highest probability [51, 94] which we demonstrate in Fig. 1.6.

The special case at $N = 2$, the HOM effect, provides a deterministic method to obtain the N00N state $\frac{-i}{\sqrt{2}}(|2, 0\rangle + |0, 2\rangle)$. Crucially, this requires the interfering photons to be indistinguishable in all modes except the spatial ones, enabling destructive interference of the $|1, 1\rangle$ state and resulting in the HOM dip in coincidence counts—a signature of indistinguishable photons [95, 96]. Such deterministic ways to create N00N states do not exist for $N > 2$ [97].

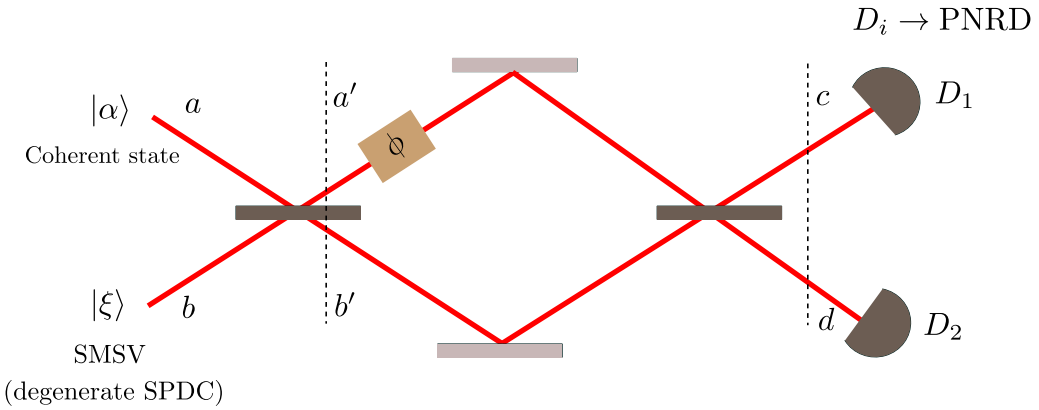

FIGURE 1.7: A schematic for the generation of N00N states through the interference of a coherent state $|\alpha\rangle$ and a single-mode squeezed vacuum state $|\xi\rangle$ in a MZI setup with photon-number-resolving detectors.

1.4.4 Detection methods

As much as the resourcefulness provided by careful engineering of probe states, detection methods are equally important to realize an efficient quantum sensing scheme. Interestingly, there exist two contrasting approaches to detection methods in quantum optics namely the intensity and the field measurement and the results of these converge in appropriate limits. Intensity measurement is essentially the measurement of photons at the output of experiments involving the MZI, the Hanbury Brown-Twiss (HBT) interferometer, and the HOM effect to investigate different aspects of quantum light such as interference, autocorrelation, and indistinguishably of photons as seen earlier. Therefore, such a detection technique is a *discrete-variable measurement* where photons are measured individually. On the other hand, field measurement involves the determination of the amplitude and the phase of a single mode of a quantized field encapsulated by the measurement of a generalized quadrature operator. These measurements are particularly useful for the detection of single mode Gaussian states which are characterized by the mean and variance associated to their Wigner functions that involves the field quadratures. As a result, field measurements essentially measure the field quadratures and are referred to as *continuous-variable measurement*. Therefore, these two classes of measurements probe the complementary particle (intensity) and wave (field) aspects of light. With this in mind, in the following sections we will show that field measurements are effectively implemented through intensity measurements, making the latter more fundamental.

1.4.4.1 Photon counting

In general, photon counting detectors are used to detect photons by means of a "click" or "no click". These detectors use electric signals that are proportional to the amount of incoming photons with a certain amount of quantum efficiency η which quantifies the fraction of incoming photons that are actually detected while the rest are lost to the environment as we have seen in the case of photon losses in phase estimation. The presence of dark counts from external sources could be avoided by means of gating the detectors so that the detector remains on moments before the arrival of relevant photons. However, other involved cases such as parity detection [91] which requires the detection of exactly odd or even number of photons or the heralding of multiphoton states (Fig. 1.5) requires the detection of n photons from a SPDC cannot be performed by generic photon counters. For these reasons, a PNRD that resolves the exact number of photons is necessary. If we label a given output mode as a', then the measured observable in that mode is the photon number $\hat{n} = \hat{a}'^{\dagger}\hat{a}'$. On the other hand, single-photon detectors (SPDs) are useful in experiments involving the measurement of the second-order quantum coherence function, $g^{(2)}(\tau)$, for instance (Fig. 1.5). The resulting probability for the measurement of n photons from the input state is given by $p_n = \mathrm{Tr}(\rho_{in} \left|n\right\rangle \left\langle n\right|)$.

Performance metrics: The performance of an detector is characterized by the following attributes: (i) quantum efficiency, (ii) timing jitter, which is the random fluctuations in the response time of the detector, and (iii) dead time, which is amount of time for which the detector is inactive after a detection event. Other performance metrics [98] include dark count rate, which is the number of times the detector produces an output in the absence of photons; spectral range, which is the range of detectable wavelengths; photon-resolving capability; ability to operate in non-cryogenic conditions; and integrability, which refers to the availability of the device in a ready-to-use or plug-and-play form without the need for customization of individual components.

Photon number detectors: Some of the common photon number detectors are the avalanche photodiodes (APD) [99, 100], photomultipliers [101], multiplex detectors [102], and superconducting detectors such as the transition edge sensors (TES) [103] and superconducting nanowire single-photon detectors (SNSPD) [104]. APDs are a type of SPD that work based on the conventional photoelectric effect where a single photon generates an electron-hole pair which further triggers more pairs leading a large output current. However, the APD cannot resolve the number of photons since the current due to a single photon event and multiple photons are practically indistinguishable. This issue can be circumvented by the use of multiplex detectors, which split the incoming photons in a mode into photons in individual output modes, each detected via an APD, thereby enabling photon-number resolution. The TES use detection based on the rise in temperature of superconducting materials and the number of photons detected is proportional to the temperature making them also photon number resolving. Additionally, they must be operated at cryogenic temperatures and exhibit large dead time and timing jitters due to thermal fluctuations which are overcome by the use of SNSPD and relatively cheaper APDs at the cost of losing the photon number resolution. Table 1.1 provides a comparison of various detectors operated under controlled conditions (in the absence of external noise) with respect to some of the performance metrics described above.

1.4.4.2 Homodyne detection

To precisely understand electric field quadratures, we consider a single mode a of the quantized electric field component of light confined to a one dimensional cavity along z axis given by $\hat{E}_x(z,t) = E_0 \sin kz(\hat{a}_0 e^{-i\omega t} + \hat{a}_0^{\dagger} e^{i\omega t})$. In terms of the quadrature operators $\hat{X} = \frac{1}{2}(\hat{a}_0 + \hat{a}_0^{\dagger})$, $\hat{P} = \frac{1}{2i}(\hat{a}_0 - \hat{a}_0^{\dagger})$, we have: $\hat{E}_x(z,t) = 2E_0 \sin kz(\hat{X}\cos\omega t + \hat{P}\sin\omega t)$. Thus, homodyne measurements allow one

Detector	Operating temperature (K)	Integrated	Intrinsic PNR	Timing jitter (ns)	Dead time (Max. count rate (10^6/s)	Quantum efficiency (%)
APD	Moderate ($\leq$ 300) [105, 106, 107]	Yes [108]	No	Low ($\geq$ 0.0121) [109]	Low ($\leq$ 330) [109]	Moderate ($\leq$ 55) [109]
Multiplex	Moderate ($\sim$ 250) [110, 111]	Yes [112]	To some extent	Low ($\geq$ 0.05) [113]	Low ($\leq$ 1500) [114]	High ($\leq$ 90) [114]
TES	Low ($\sim$ 0.1) [115, 116]	Yes [117]	Yes	High ($\geq$ 4) [118, 116]	High ($\leq$ 1) [115, 116]	High ($\leq$ 98) [116]
SNSPD	Low ($\leq$ 10) [103]	Yes [119]	No	Low ($\geq$ 0.0026) [120, 121]	Low ($\leq$ 1500) [122]	High ($\leq$ 98) [123]
BHD	High ($\leq$ 373) [124, 125]	Yes [126]	NA	NA	NA	High ($\leq$ 86) [127]

Table 1.1: Profiles of both intensity and field detectors according to their attributes. *Note:* red rows represent intensity detectors and blue row represents field detector. PNR: Photon Number Resolving and NA: not applicable used to indicate that the corresponding performance metric does not apply to field detection. The values in brackets indicate the maximum (for operating temperature, count rate, and quantum efficiency) or minimum (for timing jitter) values of the metric for each detector, as specified in the corresponding references. The dead time is represented in terms of the maximum count rate of the detector, which is inversely proportional to it, and hence a higher count rate indicates a lower dead time. All data refers to the intrinsic performance of the detectors devoid of external noise.

to reconstruct the quadratures $\hat{X}$ and $\hat{P}$ using the inverse Radon transform, and find plethora of applications in quantum key distribution [128, 129, 130], quantum state and process tomography [131, 132, 133], and quantum metrology [17, 92]. Unlike, most photon counting detectors, homodyne detectors exhibit high efficiency at non-cryogenic temperatures. However, the fabrication of a fully integrated homodyne detector did not exist until recently [126, 134, 135, 136] as its requires the assembling of bulk optical components and careful characterization of each component achieve to optimal performance.

Formalism: The signal mode a is mixed on a 50:50 beamsplitter with a strong local oscillator (LO) in mode b, described by the coherent state $|\beta e^{-i\omega t}\rangle$, where $\beta = |\beta|e^{i\varphi_l}$ specifies the amplitude and phase of the LO explicitly. The output modes a' and b' are detected using photon counting (intensity) detectors that measure the respective photocurrents which is then subtracted (Fig. 1.8). Thus, the measured observable is the photon number difference

$$\hat{O}_- = \hat{a}'^{\dagger}\hat{a}' - \hat{b}'^{\dagger}\hat{b}' \tag{1.19}$$

In particular, we consider a *balanced homodyne detector* (BHD). Hence, we make use of Eq. 1.2 for a 50:50 beamsplitter in Eq. 1.19, assuming a phase of $\pi/2$ between the transmitted and the reflected beams. After simplification, one can write in terms of the input modes as

$$\hat{O}_- = i(\hat{a}^{\dagger}\hat{b} - \hat{a}\hat{b}^{\dagger}) \tag{1.20}$$

The LO being strong allows us treat it classically, and hence we can make the approximation $\hat{b} \approx \beta e^{-i\omega t}$ resulting in

$$\hat{O}_- = |\beta|(\hat{a}^{\dagger}e^{-i\omega t}e^{i\varphi} + \hat{a}e^{i\omega t}e^{-i\varphi}), \tag{1.21}$$

where $\varphi = \varphi_l + \pi/2$. Assuming that the signal field is also driven with the same frequency ω, we make the substitution $\hat{a} \to \hat{a}_0 e^{-i\omega t}$. Hence, we have

$$\hat{O}_- = |\beta|(\hat{a}_0 e^{-i\varphi} + \hat{a}_0^\dagger e^{i\varphi}) = 2|\beta|\hat{X}(\varphi), \tag{1.22}$$

where $\hat{X}(\varphi) = \frac{1}{2}(\hat{a}_0 e^{-i\varphi} + \hat{a}_0^\dagger e^{i\varphi})$ is the generalized quadrature operator. Thus, by changing φ through the phase of the LO, one can measure different field quadratures, in particular, the field amplitude operators $\hat{X}(0) = \hat{X}$ and $\hat{X}(\pi/2) = \hat{P}$ satisfying the eigenvalue equation: $\hat{X}(\varphi)\,|X(\varphi)\rangle = X(\varphi)\,|X(\varphi)\rangle$. The associated probability distribution is $p(X(\varphi)) = \mathrm{Tr}(\rho_{in}\,|X(\varphi)\rangle\,\langle X(\varphi)|)$, where $\Pi_{X(\varphi)} = |X(\varphi)\rangle\,\langle X(\varphi)|$ is the homodyne POVM.

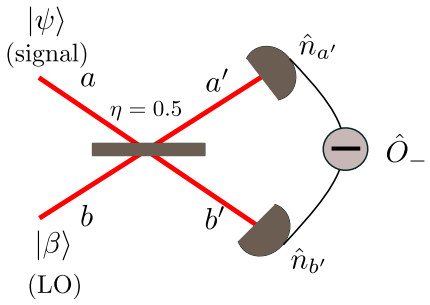

FIGURE 1.8: Scheme of a balanced homodyne detection.

1.4.5 Inference in practice

The post-processing of the measurement data to infer the parameter by means of constructing an estimator is the final step of a metrological scheme (Fig. 2.1). In this section, we will review some of the useful methods that are available in literature until now. We note that although some of these methods have been demonstrated for specific estimation problems, they can still be applied for our problem of phase estimation in the MZI.

1.4.5.1 Likelihood inference

For the estimation of a general parameter θ, if we consider the photon counting and homodyne measurements, for instance, data obtained from N independent repetitions of the experiment would result in the probability distributions

$$p_\theta(x) = \Pi_{i=1}^N p_\theta(x_i) \equiv \mathcal{L}(x|\theta), \tag{1.23}$$

where $\mathcal{L}(x|\theta)$ is called the *likelihood function*. The *maximum likelihood estimator* (MLE) is then given by

$$\tilde{\theta}^{\mathrm{MLE}}(x) = \arg\max_\theta p_\theta(x). \tag{1.24}$$

One can refer to Section 2.1.2.5 for a detailed description. For large repetitions of the experiment or on increasing the size of the data sample, it tends to the true parameter value θ. This is typically obtained by finding the value of θ that maximizes the log-likelihood function $\ln \mathcal{L}(x|\theta)$.

In [137], considering homodyne measurements, the authors considered three examples, namely, the Gaussian state estimation, where one has to estimate parameters that describe the average number of photons in a thermal, squeezed or coherent state, estimation of phase of the radiation field, estimation of quantum efficiency. The maximization of the log-likelihood function to obtain the parameter values for these examples required the use of Monte-Carlo simulations.

1.4.5.2 Bayesian inference

Another inference method is through the construction of the Bayesian estimator which is ideal under scenarios where one possess some ignorance about the value of the parameter before estimation. This is quantified by the *prior* distribution of the parameter $p(\theta)$ obtained based on past estimates. Using the Bayes theorem, one can write $p(\theta|x) = p(x|\theta)p(\theta)/p(x)$, where $p(\theta|x)$ is now referred to as the *posterior* distribution, $p_\theta(x) = p(x|\theta)$, and $p(x)$ acts as its normalization factor and is obtained as $p(x) = \int d\theta p(x|\theta)p(\theta)$. The *optimal Bayesian estimator* (OBE) is obtained as the mean of the posterior distribution given by

$$\tilde{\theta}^{\text{OBE}} = \langle\theta\rangle\big|_{p(\theta|x)} = \int d\theta p(\theta|x)\theta. \tag{1.25}$$

Unlike the MLE, the OBE provides the value of the parameter under the lack of prior knowledge. However, for a large data sample, the performance of the OBE tends to that of the MLE. For more details on Bayesian estimators see Section A1.

The Bayesian inference method described above has been employed in optical interferometry both theoretically [50] and experimentally [31]. In [138], phase estimation using a squeezed-displaced vacuum state and homodyne measurement was considered and $p(\theta|x)$ at different values of N (number of measurements) and squeezing parameter r were constructed. For all the cases considered, the means of the posterior distribution remained the same. In [31], phase estimation in the presence of large phase diffusion is considered, where data obtained from homodyne measurements obtained at an optimal value of θ_l (LO phase) for three different values of $|\beta|$ (LO strength) were analyzed. For these cases, the means of the posterior distributions obtained from the homodyne data were very close to each other with small deviations. In both works, a flat prior $p(\theta) = 1/2\pi$, showcasing maximal ignorance and Monte-Carlo techniques were used.

1.4.5.3 Real time sensing

It is clear that the determination of the posterior distribution is the main objective in Bayesian inference. Furthermore, the parameter θ is static in nature i.e., its value does not change much for a given estimation run and the prior contains information about what the values assumed by θ in the past. A more realistic scenario would involve estimating a parameter that varies rapidly in time, such as the weak magnetic field generated by the brain (magnetoencephalography) or the electrical signals of the heart (electrocardiography). Such cases require a real time sensing of parameters, where there is a need to produce the estimates of the parameter dynamically. As a result, one needs to determine the posterior quick enough and methods used in the static approach need refinement. In [139], the authors propose a numerical algorithm using which one can approximately reconstruct $p(\theta|x)$ through sampling from a library of measurement data predetermined for different values of θ. This avoids the tedious computation of $p(x|\theta)$ for every value of θ and generates estimated values matching the rate of the incoming signal. This has been applied to a system of two-level atom and an optomechanical system undergoing open system dynamics.

1.5 Realistic multiparameter phase sensing

Up until now, we have provided an overview of the most important techniques involved in probe state preparation, detection, and estimation. Multiphoton states coupled with photon counting and homodyne detectors are deployed for phase estimation and the presence of noises (Section 1.3.2)

largely impacts the performance of both the probe and the detector. Therefore, it is not only important to investigate the precision limits of phase estimation (Section 1.3.2.1) but also to estimate the noise parameter (which is typically unknown at the time of measurement) along with phase. A simple motivation is the need to realize measurements that are sensitive to noise parameters as well: this is particularly relevant for those ranges in which phase sensitivity is affected the most. This strategy is known to make the estimation more reliable [140, 141]. The latter provides a comprehensive approach to parameter estimation and has to be dealt using the tools of multiparameter estimation theory (see Chapter 2), a domain that has seen a recent surge of progress from a theoretical point of view.

1.5.1 Advances towards concurrent sensing of phase and noise

From a practical standpoint, the realization of multiparameter protocols presents significant challenges. These challenges form the main focus of this thesis and will be addressed in detail in Chapters 3 and 4. In the following, to place our research in the contemporary context, we provide a brief review of the current state of the art and the most relevant literature in multiparameter noisy optical quantum metrology.

Theoretical and experimental investigations towards the simultaneous estimation of phase and loss include [142, 143] and simultaneous estimation of phase and phase diffusion include [34, 140, 144]. The most important difference between single and multiple parameter estimation is the fact that there exist scenarios where one cannot extract information optimally from all parameters at once. This is a fundamental characteristic of the estimation problem which is tied to the existence of incompatible observables used to estimate the parameters. As a result, if one were to deploy the measurements described in Section 1.4.4 individually on each identical copy of the probe state, the presence of incompatibility would hinder the attainability of optimal joint precision. This can be overcome to certain extent by the use of collective measurements as demonstrated in [34, 140].

Chapter 2

Multiparameter estimation theory and compatibility

In the previous chapter, we have introduced several techniques and recent technological progress from the stand point of practical implementation of quantum sensing schemes. In this chapter, we adopt a fully theoretical approach and introduce the mathematical formalism of multiparameter quantum estimation theory. This exposition is necessary for our analysis of joint estimation limits and the associated compatibility problem in practical optical interferometry. These tools are introduced in a pedagogical manner by describing the foundational aspects of the sophisticated multiparameter bounds employed in Chapters 3 and 4.

The chapter is organized as follows. We begin with the building blocks of classical multiparameter estimation from the single parameter perspective. This is followed by its quantum counterpart and a tighter bound for correlated measurements which captures fundamental incompatibility. Subsequently, we introduce the bound for uncorrelated measurements and examine its attainability. We conclude with a discussion of the notion of metrological compatibility, which forms the central theme of Chapter 4.

2.1 The multiparameter estimation toolbox

In this section, we will review the necessary tools pertaining to the fundamental bounds in multiparameter estimation theory arising from the optimization of the *Mean Square Error* (MSE) with respect to all possible estimators and measurements. In particular, we mention how the consideration of multiple parameters in our estimation leads to tighter bounds that yield information about the deviation from the simultaneous optimal estimation of the parameters.

2.1.1 Prelude

We start the multiparameter estimation formalism by considering a system in which p parameters are to be estimated represented as a vector: $\vec{\theta} = (\theta_1, \ldots, \theta_p)^\top \in \Theta \subset \mathbb{R}^p$, where Θ is the parameter space. A general quantum state $|\psi\rangle \in \mathcal{H} \equiv \mathbb{C}^d$ lives in a Hilbert space $\mathcal{H}$ of d dimensions. We explicitly mention the notations Θ and $\mathcal{H}$ here to serve our future purposes of describing certain entities of the fundamental bounds in reference to the parameter space and the Hilbert space of states separately. As a result, we reserve Tr(.) when traces act on objects in $\mathcal{H}$ and tr(.) for traces acting on objects in Θ. Although, we begin with a pure state $|\psi\rangle$ as the input, it is convenient to

consider the density operator formalism to account for the formation of mixed states at the output of a given metrological scheme. Letting $\mathcal{L}(\mathcal{H}) \equiv \mathbb{C}^{d\times d}$ to denote the space of all linear operators on $\mathcal{H}$, and in particular $\mathcal{L}_h(\mathcal{H}) \subset \mathcal{L}(\mathcal{H})$ to denote the set of all Hermitian operators, we have $\rho \in \mathcal{L}_h(\mathcal{H})$.

A typical quantum metrological scheme (Fig. 2.1) starts with an *input* "probe" state. The *encoding* of unknown parameters occurs during the evolution of the state through a quantum channel $\Lambda_{\vec{\theta}}$ which is not necessarily unitary. The *measurement* of a suitable quantum observable O is carried on the output state $\rho_{\vec{\theta}}$ to obtain the probability distribution $p_{\vec{\theta}}(x_i) = \mathrm{Tr}(\rho_{\vec{\theta}}\Pi_{x_i})$, where Π_{x_i} is the POVM characterizing the measurement of O, and x_i denote the random variable corresponding to the outcomes of the i-th measurement. By performing N independent measurements on N copies of $\rho_{\vec{\theta}}$, we sample the underlying joint probability distribution $p_{\vec{\theta}}(x) = \Pi_{i=1}^{N} p_{\vec{\theta}}(x_i)$, where $x \equiv (x_1, \ldots, x_N)$ is the collection of N random variables. The scheme ends with the further *post-processing* of the distribution $p_{\vec{\theta}}(x)$ to estimate the value of the parameters through an estimator vector $\vec{\tilde{\theta}} = (\tilde{\theta}_1, \ldots, \tilde{\theta}_p)^\top \subset \mathbb{R}^p$. Since the estimator depends on the sampled distribution and the number of times it is sampled, it is explicitly denoted as $\vec{\tilde{\theta}}_N(x)$. However, henceforth, for the sake of readability, we will drop the explicit dependence and simply write $\tilde{\theta}_i$.

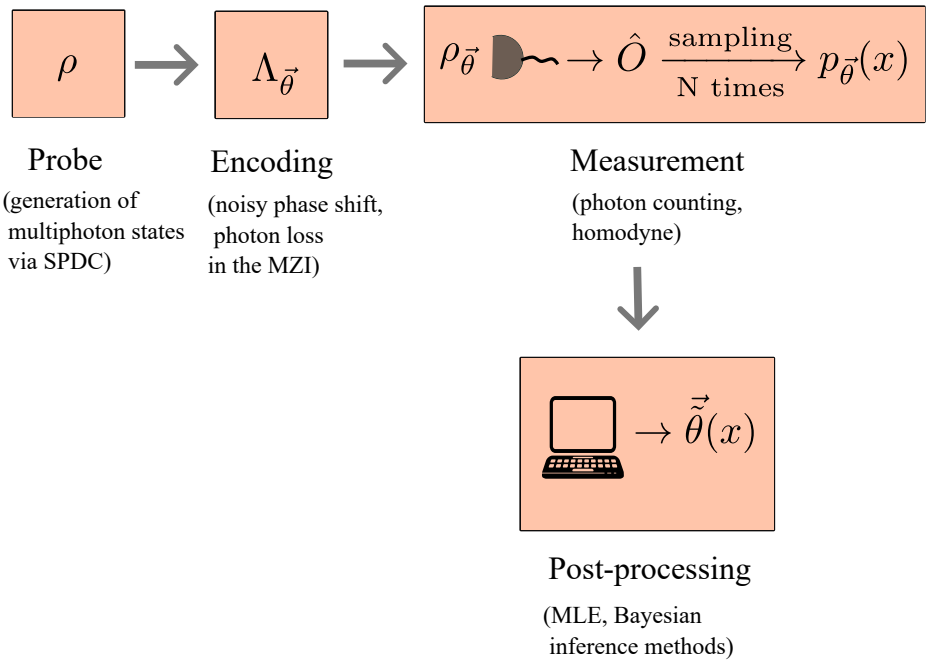

FIGURE 2.1: A general multiparameter scheme.

2.1.2 The Cramér-Rao bound

2.1.2.1 Mean square error and unbiased estimators

For the moment, we confine our attention to single-parameter estimation in order to provide a clear explanation of key concepts, before generalizing them to the multiparameter case. The performance of the estimator can be quantified by the MSE for a given parameter θ as

$$\mathrm{MSE}(\tilde{\theta}, \theta) = \int dx p_\theta(x)(\tilde{\theta} - \theta)^2 \tag{2.1}$$

The variance of the estimator is given by

$$\mathrm{Var}(\tilde{\theta}) = \int dx p_\theta(x)(\tilde{\theta} - \langle\tilde{\theta}\rangle)^2 = \langle\tilde{\theta}^2\rangle - \langle\tilde{\theta}\rangle^2, \tag{2.2}$$

where $\langle\tilde{\theta}\rangle = \int dx p_\theta(x)\tilde{\theta}(x)$ is the mean of the estimator. If an estimator attains the true value in the asymptotic limit i.e., $\lim_{N\to\infty}\tilde{\theta} = \theta$, then it is termed as *consistent*, which can be viewed as the convergence of the probability distribution of the estimator to a delta function at θ. In particular, $\lim_{N\to\infty}\langle\tilde{\theta}\rangle = \theta$ and $\lim_{N\to\infty}\mathrm{Var}(\tilde{\theta}) = 0$.

The MSE of the estimator is related to its variance as
$\mathrm{MSE}(\tilde{\theta}) = \mathrm{Var}(\tilde{\theta}) + \underbrace{(\langle\tilde{\theta}\rangle - \theta)^2}_{\mathrm{B}(\tilde{\theta})^2}$, where $\mathrm{B}(\tilde{\theta})$ is the *bias* of the estimator.

We restrict ourselves to *unbiased estimators* which have the property of *zero* bias i.e., $\mathrm{B}(\tilde{\theta}) = \langle\tilde{\theta}\rangle - \theta = 0$ implying

$$\langle\tilde{\theta}\rangle = \int dx p_\theta(x)\tilde{\theta}(x) = \theta \tag{2.3}$$

so that on average they yield the true value θ under which Eqs. 2.1 and 2.2 coincide. Thus, the fundamental figure of merit in estimation theory is the MSE which must be optimized over all possible estimators to achieve the best possible precision provided the measurement and the probe states are fixed.

2.1.2.2 Locality assumption

We consider that the true value of θ is *fixed* but lies in the interval $\mathcal{I} = [a_1, \ldots, a_n]$. Hence, the *optimal estimator* must be optimal for all values in $\mathcal{I}$. However, one can clearly see from the way Eq. 2.1 is defined, the MSE can be optimized only for a particular value of θ from $\mathcal{I}$ i.e., after we *know* that value, which contradicts the whole point of estimation. Thus, we remedy this situation by further restricting ourselves to a *local* estimation approach, where we assume that we know a value θ' in the neighborhood of the true value. From the point of view of Bayesian inference, this can be interpreted as the knowledge gained about the value of θ through updating it based on outcomes from past estimation processes. In other words, local estimation is formulated within the *frequentist* framework.

Within this framework, we can reasonably approximate our unbiased estimators up to the first order around θ'. Hence, the mean of the estimator reads

$$\langle\tilde{\theta}\rangle \approx \langle\tilde{\theta}\rangle|_{\theta=\theta'} + \left.\frac{d\langle\tilde{\theta}\rangle}{d\theta}\right|_{\theta=\theta'}\delta\theta + \mathcal{O}(\delta\theta^2) \tag{2.4}$$

where $\delta\theta = \theta - \theta'$.

From the coefficients of the first and second terms of Eq. 2.4 and Eq. 2.3, one can infer that the *locally unbiased estimator* satisfies the following relations

$$\langle\tilde{\theta}\rangle|_{\theta=\theta'} = \theta' \tag{2.5a}$$

$$\left.\frac{d\langle\tilde{\theta}\rangle}{d\theta}\right|_{\theta=\theta'} = 1 \tag{2.5b}$$

2.1.2.3 Multiparameter Cramér-Rao bound

We revert our attention back to multiparameter estimation, and the aforementioned concepts described using the single-parameter approach, can be easily translated to the multiparameter paradigm. Firstly, considering the parameter vector $\vec{\theta}$ and the estimator vector $\vec{\tilde{\theta}}$ defined earlier, the MSE can be generalized to the MSE matrix which, for unbiased estimators, becomes the *covariance matrix* as follows

$$\mathrm{Cov}(\vec{\tilde{\theta}}) = \int dx p_{\vec{\theta}}(x)(\vec{\tilde{\theta}} - \vec{\theta})(\vec{\tilde{\theta}} - \vec{\theta})^{\top} \tag{2.6}$$

where the elements $[\mathrm{Cov}(\vec{\tilde{\theta}})]_{ij} = \int dx p_{\vec{\theta}}(x)(\tilde{\theta}_i - \theta_i)(\tilde{\theta}_j - \theta_j)$. The diagonal elements $[\mathrm{Cov}(\vec{\tilde{\theta}})]_{ii}$ are the variances for a given parameter θ_i, and the off-diagonal elements $[\mathrm{Cov}(\vec{\tilde{\theta}})]_{ij}\,; i \neq j$ quantify the correlation between the estimators $\tilde{\theta}_i$ and $\tilde{\theta}_j$. This quantity vanishes for estimation problems where the estimation of one parameter is independent of the other and does not impact the joint-estimation precision.

The covariance matrix is related to the change of the underlying probability distribution with respect to an infinitesimal change in the value of the parameter. The greater the distribution changes from the initial one, the higher will be its *sensitivity* to the changes. As a result, the quality of a locally unbiased estimator is fundamentally limited by the sensitivity of the probability distribution which is captured by the *Cramér-Rao bound* (CRB)

$$\mathrm{Cov}(\vec{\tilde{\theta}}) \geq \frac{F_C^{-1}(\vec{\theta})}{N}, \tag{2.7}$$

where

$$F_C(\vec{\theta}) = \int dx \frac{\nabla p_{\vec{\theta}}(x)[\nabla p_{\vec{\theta}}(x)]^{\top}}{p_{\vec{\theta}}(x)} \tag{2.8}$$

is the *Fisher Information Matrix* (FIM) and $\nabla p_{\vec{\theta}}(x) = (\partial p_{\vec{\theta}}/\partial\theta_1, \ldots, \partial p_{\vec{\theta}}/\partial\theta_p)^{\top}$ is the vector of derivatives of $p_{\vec{\theta}}(x)$ with respect to the parameters. The elements of the FIM read

$$F_{C\,i,j} = \int dx \frac{1}{p_{\vec{\theta}}(x)} \left(\frac{\partial p_{\vec{\theta}}(x)}{\partial \theta_i}\right)\left(\frac{\partial p_{\vec{\theta}}(x)}{\partial \theta_j}\right) \tag{2.9}$$

and the diagonal elements $F_{C\,i,i}$ quantify the sensitivity of the probability distribution for a given parameter θ_i known as the *Fisher Information* (FI).

We note that the presence of N in the denominator of the R.H.S. of Eq. 2.7 is due to the *additivity* property of FI stemming from N independent trails of the experiment with $F_{C\,i,i}(\Pi_{k=1}^{N} p_{\vec{\theta}}(x_k)) = N F_{C\,i,i}(p_{\vec{\theta}}(x_k))$.

Therefore, the variance of individual parameters read

$$\mathrm{Var}(\tilde{\theta}_i) \geq \frac{(F_C^{-1})_{ii}}{N}, \tag{2.10}$$

We note that $\mathrm{Var}(\tilde{\theta}_i) \geq (F_C^{-1})_{i,i} \geq (F_{C\,i,i})^{-1}$. The second inequality is not tight in the presence of estimator correlations i.e., when $F_{C\,i,j} \neq 0\,; i \neq j$, but the first inequality is tight. However, if there are no estimator correlations, $(F_C^{-1})_{i,i} = (F_{C\,i,i})^{-1}$, the precision of a simultaneous estimation scheme coincides with that of individual estimation [24].

The CRB can be proven using the Cauchy-Schwarz inequality in a straightforward manner with two important conditions: (i) the local unbiasedness condition (Eq. 2.5b) and (ii) the regularity[1] of the probability distribution [145]. The latter condition implies $\int dx \partial p_{\vec{\theta}}(x)/\partial\theta_i = 0$.

2.1.2.4 Average cost

We denote the set of real and complex matrices on Θ as $\mathcal{S}^{\mathbb{R}}(\Theta) \subset \mathbb{R}^{p\times p}$ and $\mathcal{S}^{\mathbb{C}}(\Theta) \subset \mathbb{C}^{p\times p}$ respectively. Introducing a positive-definite *cost matrix* $W \in \mathcal{S}^{\mathbb{R}}(\Theta)$, which quantifies the extent of penalization for the error in each parameter, we obtain a scalar bound

$$\overline{\mathcal{C}}(\vec{\tilde{\theta}}, \vec{\theta}) = \mathrm{tr}(W\mathrm{Cov}(\vec{\tilde{\theta}})) \geq \frac{1}{N}\mathrm{tr}(WF_C^{-1}(\vec{\theta})) = C_C(\Pi_{i=1}^N p_{\vec{\theta}}(x_i)), \tag{2.11}$$

where $\overline{C}$ is referred to as the *average cost*[2]. $\overline{C}$ may be understood as an average of the *cost function* from the equivalent expression: $\overline{\mathcal{C}} = \int dx p_{\vec{\theta}}(x)\mathcal{C}(\vec{\tilde{\theta}}, \vec{\theta})$, where $\mathcal{C}(\vec{\tilde{\theta}}, \vec{\theta}) = (\vec{\tilde{\theta}} - \vec{\theta})^\top W(\vec{\tilde{\theta}} - \vec{\theta})$ is a *quadratic* cost function appropriate in the Frequentist approach, where we typically consider only small deviations of the estimator $\vec{\tilde{\theta}}$ from the true values $\vec{\theta}$.

2.1.2.5 Saturability of the CRB

In general, any estimator saturating the CRB is known as an *efficient* estimator and a *sufficient statistic* satisfying the condition [20]

$$\frac{\partial \ln p_{\vec{\theta}}(x)}{\partial\theta_i} = NF_{C\,i,i}(\theta_i)(\tilde{\theta}_i - \theta_i) \tag{2.12}$$

Since this estimator is optimal regardless of the value of θ_i, it is a *global* estimator. In particular, the local estimator saturating the CRB at the value θ_i' in the vicinity of θ_i can be trivially obtained from Eq. 2.12 as

$$\tilde{\theta}_i = \theta_i' + \frac{1}{NF_{C\,i,i}(\theta_i')}\frac{\partial \ln p_{\vec{\theta}}(x)}{\partial\theta_i}\bigg|_{\theta_i=\theta_i'} \tag{2.13}$$

Finite N saturability

In the finite N regime, the efficient (global) estimators are known only for the *exponential family* of probability distributions such as the Gaussian, Poisson, and Gamma distributions to name a few [145]. However, for highly non-Gaussian distributions and at finite N, the Ziv-Zakai bound [146] is demonstrated to be tighter and closely attains the CRB in the asymptotic limit.

Asymptotic saturability

The sufficient statistic condition holds only for a particular class of estimators and it breaks down in the asymptotic limit. Fortunately, in such a case, we have the MLE [147], guaranteed to attain the CRB asymptotically. The MLE is defined as

$$\tilde{\theta}_i^{\mathrm{MLE}} = \arg\max_{\theta_i} p_{\theta_i}(x), \tag{2.14}$$

[1] We note that for probability distributions that are not regular, there is no lower bound on the uncertainty of the estimator. We direct the interested reader to [145] for the derivation of the CRB.

[2] We note that the definition of the cost function $\mathcal{C}(\vec{\tilde{\theta}}, \vec{\theta})$ uses the deviation of the estimator $\vec{\tilde{\theta}}$ from the parameter $\vec{\theta}$ and hence, the average cost $\overline{C}$ has an additional dependence on $\vec{\theta}$. More generally, for biased estimators, one should have $\overline{\mathcal{C}}(\vec{\tilde{\theta}}, \vec{\theta}) = \mathrm{tr}(W\mathcal{M}(\vec{\tilde{\theta}}, \vec{\theta}))$, where $\mathcal{M}(\vec{\tilde{\theta}}, \vec{\theta}))$ is the MSE matrix

Hence given the outcomes x, it is a function that outputs the parameter value at which the observed data is most likely to occur. The likelihood function is given by the probability distribution $\mathcal{L}(x|\theta_i) \equiv p_{\theta_i}(x)$. Equivalently, by defining the *Log-likelihood estimator*: $\arg\max_{\theta_i} \ln p_{\theta_i}(x)$, and from the saturability condition (Eq. 2.12), one can see that the maximum value obtained through

$$\frac{\partial \ln p_{\theta_i}(x)}{\partial \theta_i} = 0 \tag{2.15}$$

occurs when $\theta_i = \tilde{\theta}_i$. Hence, the MLE is a global estimator. Furthermore, the second derivative

$$\frac{\partial^2 \ln p_{\theta_i}(x)}{\partial \theta_i^2} = -N F_{C\,i,i}(\theta_i) \quad ; F_{C\,i,i} > 0 \tag{2.16}$$

shows that the solution from Eq. 2.15 is indeed a maximum. For finite N, the MLE is generally a biased estimator. However, due to the more fundamental consistency property we defined earlier, the MLE becomes asymptotically unbiased, i.e., $\lim_{N\to\infty} \langle \vec{\tilde{\theta}}_N^{\mathrm{MLE}} \rangle = \vec{\theta}$. Thanks to the existence of the MLE that the difficulties to saturate CRB at finite N may be overcome it can always be asymptotically saturated.

It is easier to compute the log-likelihood estimator for well-behaved distributions like the Gaussian distribution. However, in practice, one encounters multiple unknown parameters $\vec{\theta}$ stemming from sophisticated physical models such as noisy optical interferometry with non-Gaussian states. For such models, the difficulty is two-fold: (i) obtaining a closed-form solution of the associated probability distribution and (ii) optimization of the log-likelihood function i.e., $\ln(\mathcal{L}(x|\theta_i))$ over different parameters to find the maxima. In particular, for the latter, one resorts to Monte-Carlo optimization methods such as approximate Monte-Carlo maximum likelihood approach [148, 149].

2.1.3 The quantum Cramér-Rao bound

2.1.3.1 Quantum generalization

The quantum version of the CRB, stems from the consideration of $p_{\vec{\theta}}(x)$ as not just classical probability distributions, but originating from the quantum properties of a quantum state $\rho_{\vec{\theta}}^{\otimes N}$ acted upon by the POVM Π_x as

$$p_{\vec{\theta}}(x) = \mathrm{Tr}(\rho_{\vec{\theta}}^{\otimes N} \Pi_x) \tag{2.17}$$

where $\Pi_x = \bigotimes_{i=1}^{N} \Pi_{x_i}$ is the collective POVM characterizing the measurement M of an observable O.

For the estimation of a single parameter θ_i, we can plug Eq. 2.17 into the FI to obtain

$$F_{C\,i,i} = \int dx \frac{1}{\mathrm{Tr}(\rho_{\vec{\theta}}^{\otimes N} \Pi_x)} \mathrm{Tr}\left(\frac{\partial \rho_{\vec{\theta}}^{\otimes N}}{\partial \theta_i} \Pi_x \right)^2 \tag{2.18}$$

At this point, we introduce the self-adjoint operator known as the *Symmetric Logarithmic Derivative* (SLD), $L_{\theta_i}(\vec{\theta}) \in \mathcal{L}_h(\mathcal{H})$ which are the solutions of the Lyapunov matrix equation:

$$\frac{\partial \rho_{\vec{\theta}}^{\otimes N}}{\partial \theta_i} = \frac{\rho_{\vec{\theta}}^{\otimes N} L_{\theta_i}(\vec{\theta}) + L_{\theta_i}(\vec{\theta}) \rho_{\vec{\theta}}^{\otimes N}}{2} \tag{2.19}$$

In the following, we drop the explicit dependence of the L_{θ_i} on $\vec{\theta}$.
Using Eq. 2.19, we can write Eq. 2.18 as

$$F_{C\,i,i} = \int dx \frac{1}{\mathrm{Tr}(\rho_{\vec{\theta}}^{\otimes N}\Pi_x)} \mathrm{Tr}\left(\left[\frac{\rho_{\vec{\theta}}^{\otimes N}L_{\theta_i} + L_{\theta_i}\rho_{\vec{\theta}}^{\otimes N}}{2}\right]\Pi_x\right)^2 \tag{2.20}$$

$$= \int dx \frac{1}{\mathrm{Tr}(\rho_{\vec{\theta}}^{\otimes N}\Pi_x)} \mathrm{Tr}\left(\frac{\rho_{\vec{\theta}}^{\otimes N}L_{\theta_i}\Pi_x + L_{\theta_i}\rho_{\vec{\theta}}^{\otimes N}\Pi_x}{2}\right)^2 \tag{2.21a}$$

$$= \int dx \frac{[\mathrm{Tr}(\rho_{\vec{\theta}}^{\otimes N}L_{\theta_i}\Pi_x) + \mathrm{Tr}(L_{\theta_i}\rho_{\vec{\theta}}^{\otimes N}\Pi_x)]^2}{4\,\mathrm{Tr}(\rho_{\vec{\theta}}^{\otimes N}\Pi_x)} \tag{2.21b}$$

Using the fact the cyclic property of trace and since $\rho_{\vec{\theta}}^{\otimes N}$, Π_x, and L_{θ_i} are Hermitian operators,

$$= \int dx \frac{[\mathrm{Tr}(L_{\theta_i}\Pi_x\rho_{\vec{\theta}}^{\otimes N}) + \mathrm{Tr}(\rho_{\vec{\theta}}^{\otimes N}\Pi_x L_{\theta_i})]^2}{4\,\mathrm{Tr}(\rho_{\vec{\theta}}^{\otimes N}\Pi_x)} \tag{2.22a}$$

$$= \int dx \frac{[\mathrm{Tr}([\rho_{\vec{\theta}}^{\otimes N}\Pi_x L_{\theta_i}]^\dagger) + \mathrm{Tr}(\rho_{\vec{\theta}}^{\otimes N}\Pi_x L_{\theta_i})]^2}{4\,\mathrm{Tr}(\rho_{\vec{\theta}}^{\otimes N}\Pi_x)} \tag{2.22b}$$

$$= \int dx \frac{\mathrm{Re}[\mathrm{Tr}(\rho_{\vec{\theta}}^{\otimes N}\Pi_x L_{\theta_i})]^2}{\mathrm{Tr}(\rho_{\vec{\theta}}^{\otimes N}\Pi_x)} \leq \int dx \frac{|\mathrm{Tr}(\rho_{\vec{\theta}}^{\otimes N}\Pi_x L_{\theta_i})|^2}{\mathrm{Tr}(\rho_{\vec{\theta}}^{\otimes N}\Pi_x)} \tag{2.22c}$$

In Eq. 2.22c, we made use of the fact $\mathrm{Re}(z)^2 \leq |z|^2$, where z is a complex number.
Noting that,

$$|\mathrm{Tr}(\rho_{\vec{\theta}}^{\otimes N}\Pi_x L_{\theta_i})|^2 = |\,\mathrm{Tr}\,(\sqrt{\rho_{\vec{\theta}}^{\otimes N}}\sqrt{\Pi_x}\sqrt{\Pi_x}L_{\theta_i}\sqrt{\rho_{\vec{\theta}}^{\otimes N}})|^2 \tag{2.23}$$

we make use of the Cauchy-Schwarz inequality for a Hilbert-Schmidt inner product of matrices: $\mathrm{Tr}(AB^\dagger) \leq \mathrm{Tr}(A^\dagger A)\,\mathrm{Tr}(B^\dagger B)$ to obtain

$$\begin{aligned} &|\,\mathrm{Tr}\,(\underbrace{\sqrt{\rho_{\vec{\theta}}^{\otimes N}}\sqrt{\Pi_x}}_{A}\underbrace{\sqrt{\Pi_x}L_{\theta_i}\sqrt{\rho_{\vec{\theta}}^{\otimes N}}}_{B^\dagger})|^2 \\ &\leq \underbrace{\mathrm{Tr}\,(\underbrace{\sqrt{\Pi_x}\sqrt{\rho_{\vec{\theta}}^{\otimes N}}}_{A^\dagger}\underbrace{\sqrt{\rho_{\vec{\theta}}^{\otimes N}}\sqrt{\Pi_x}}_{A})\,\mathrm{Tr}\,(\underbrace{\sqrt{\Pi_x}L_{\theta_i}\sqrt{\rho_{\vec{\theta}}^{\otimes N}}}_{B^\dagger}\underbrace{\sqrt{\rho_{\vec{\theta}}^{\otimes N}}L_{\theta_i}\sqrt{\Pi_x}}_{B})}_{\mathrm{Tr}(\rho_{\vec{\theta}}^{\otimes N}\Pi_x)\;\mathrm{Tr}(L_{\theta_i}\rho_{\vec{\theta}}^{\otimes N}L_{\theta_i}\Pi_x)} \end{aligned} \tag{2.24}$$

Making use of the inequality Eq. 2.24 in Eq.2.22c, we have the following upper bound for the FI.

$$F_{C\,i,i} \leq \int dx\,\mathrm{Tr}(L_{\theta_i}\rho_{\vec{\theta}}^{\otimes N}L_{\theta_i}\Pi_x) = \mathrm{Tr}(\rho_{\vec{\theta}}^{\otimes N}L_{\vec{\theta}_i}^2) \tag{2.25}$$

where we have made use of the property: $\int dx\Pi_x = \mathbb{1}$.
The quantity $F_{Q\,i,i} = \mathrm{Tr}(\rho_{\vec{\theta}}^{\otimes N}L_{\vec{\theta}_i}^2)$ is known as the *Quantum Fisher Information* (QFI).

The QFI may be understood as follows. It should be evident that $F_{C\,i,i}$ is as a function of the probe state, measurement, and the parameter. Hence, for a given state, there is still room to reduce the uncertainty in $\tilde{\theta}_i$ by searching for the optimal measurement M^{opt}. Conversely, this would correspond to the maximum value $\max_M F_{C\,i,i}(\rho_{\vec{\theta}}^{\otimes N}, M, \theta_i) = F_{Q\,i,i}(\rho_{\vec{\theta}}^{\otimes N}, M^{\text{opt}})$ given by the QFI.

2.1.3.2 Multiparameter quantum Cramér-Rao bound

Now in the multiparameter case, one has to take into account even the bounds on the estimator correlations. Therefore, the bound on the average cost is given by the *quantum Cramér-Rao bound* (QCRB)

$$\overline{\mathcal{C}}(\vec{\tilde{\theta}}, \vec{\theta}) \geq \frac{1}{N} \operatorname{tr}(W F_Q^{-1}(\vec{\theta})) = C_Q(\rho_{\vec{\theta}}^{\otimes N}), \tag{2.26}$$

where

$$F_Q(\vec{\theta}) = \frac{1}{2} \operatorname{Tr}(\rho_{\vec{\theta}} \{\vec{L}, \vec{L}^\top\}) \tag{2.27}$$

is the *Quantum Fisher Information Matrix* (QFIM) and $\vec{L} = (L_{\theta_1}, \cdots, L_{\theta_p})^\top$ is a vector of SLDs for each parameter. Replacing $\vec{L}^\top = \vec{\tilde{L}}$, the elements of the QFIM should be read from the definition $\{\vec{L}, \vec{\tilde{L}}\}_{i,j} = \{L_i, \tilde{L}_j\}$, where L_i and $\tilde{L}_i$ are the i-th element of $\vec{L}$ and $\vec{\tilde{L}}$ respectively.

Thus, the QFIM elements are as follows

$$F_{Q\,i,j} = \frac{1}{2} \operatorname{Tr}(\rho_{\vec{\theta}} \{L_{\theta_i}, L_{\theta_j}\} \tag{2.28}$$

with the diagonal entries $F_{Q\,i,i} = \operatorname{Tr}(\rho_{\vec{\theta}} L_{\theta_i}^2)$ as given in Eq. 2.25. Since L_{θ_i} and $\rho_{\vec{\theta}}$ are Hermitian, one can also write: $F_{Q\,i,j} = \operatorname{Re}(\operatorname{Tr}(\rho_{\vec{\theta}} L_{\theta_i} L_{\theta_j}))$.

The corresponding single parameter QCRB reads

$$\operatorname{Var}(\tilde{\theta}_i) \geq \frac{(F_Q^{-1})_{i,i}}{N}, \tag{2.29}$$

where the presence of N in Eqs. 2.26 and 2.29 is due to the additivity property: $F_Q(\rho_{\theta_i}^{\otimes N}) = N F_Q(\rho_\theta)$.

The SLDs for each parameter satisfy the vector equation

$$\nabla \rho_{\vec{\theta}} = \frac{1}{2} \{\rho_{\vec{\theta}}, \vec{L}\} \tag{2.30}$$

with each element corresponding to Eq. 2.19.

For a given parameter θ_i, the optimal measurement saturating the single-parameter QCRB is constructed from the eigenbasis of the SLD operator L_{θ_i}. In the multiparameter case, if the SLDs for each parameter commute i.e.,

$$[L_{\theta_i}, L_{\theta_j}] = 0, \tag{2.31}$$

then there exists a common eigenbasis for the construction of a single optimal measurement saturating the QCRB. However, if $[L_{\theta_i}, L_{\theta_j}] \neq 0$, then the optimal measurements for the parameters are fundamentally incompatible leading to *fundamental incompatibility*. In this case, the QCRB is not tight. This results in trade-offs for the estimation of each parameter with a given measurement.

The usefulness of consideration of scalar inequality i.e., bounds on the average cost (Eqs. 2.11 and 2.26) instead of the covariance matrix (Eq. 2.7) becomes evident in the case when there is fundamental incompatibility. To see this, if we were to consider the matrix inequality for the weighted covariance matrix $W\mathrm{Cov} \geq WF_Q^{-1}$. Different choices of W would yield different weighted covariance matrices, and due to the partial ordering of matrices, a quantitative comparison of these matrices to WF_Q^{-1} cannot be made. Thus, a scalar inequality yields total ordering, and thus a meaningful assessment of the gap between the average cost and C_Q for different Ws. However, one can still work with the matrix inequality form for the CRB, since for a given measurement, the optimal estimator yields a unique covariance matrix satisfying: $\min_{\vec{\theta}} \mathrm{Cov} = F_C^{-1}$ at least in the asymptotic limit.

The SLD as the solution of Eq. 2.19 may be written as

$$L_{\theta_i} = 2\int_0^\infty dt e^{-\rho_{\vec{\theta}}t}\left(\frac{\partial\rho_{\vec{\theta}}}{\partial\theta_i}\right)e^{-\rho_{\vec{\theta}}t} \tag{2.32}$$

Expressing $\rho_{\vec{\theta}}$ in its eigenbasis: $\rho_{\vec{\theta}} = \sum_n \lambda_n |e_n\rangle\langle e_n|$, where λ_n and $\{|e_n\rangle\}$ are the eigenvalues and the (normalized) eigenvectors respectively and using $e^{\pm\rho_{\vec{\theta}}t} = \sum_{k=0}^{\infty}\frac{(\pm t)^k\rho_{\vec{\theta}}^k}{k!}$, we get

$$= 2\int_0^\infty dt\Bigg[\sum_{k=0}^{\infty}\frac{(-t)^k}{k!}\underbrace{\sum_{n'}\lambda_{n'}^k|e_{n'}\rangle\langle e_{n'}|}_{\rho_{\vec{\theta}}^k}\left(\frac{\partial\rho_{\vec{\theta}}}{\partial\theta_i}\right)\underbrace{\sum_{n''}\lambda_{n''}^l|e_{n''}\rangle\langle e_{n''}|}_{\rho_{\vec{\theta}}^l}\sum_{l=0}^{\infty}\frac{t^l}{l!}\Bigg] \tag{2.33}$$

$$= 2\sum_{n',n''}\int_0^\infty dt\Bigg[\sum_{k=0}^{\infty}\frac{(-t\lambda_{n'})^k}{k!}|e_{n'}\rangle\langle e_{n'}|\left(\frac{\partial\rho_{\vec{\theta}}}{\partial\theta_i}\right)|e_{n''}\rangle\langle e_{n''}|\sum_{l=0}^{\infty}\frac{(t\lambda_{n''})^l}{l!}\Bigg] \tag{2.34}$$

$$= 2\sum_{n',n''}\left[\int_0^\infty dt e^{(-\lambda_{n'}+\lambda_{n''})t}\langle e_{n'}|\left(\frac{\partial\rho_{\vec{\theta}}}{\partial\theta_i}\right)|e_{n''}\rangle|e_{n'}\rangle\langle e_{n''}|\right] \tag{2.35}$$

Using $\int_0^\infty dt e^{(-\lambda_{n'}+\lambda_{n''})t} = \frac{1}{\lambda_{n'}+\lambda_{n''}}$, we obtain the SLD expressed in the eigenbasis as

$$L_{\theta_i} = \sum_{n',n''}\frac{2\langle e_{n'}|\partial_{\theta_i}\rho_{\vec{\theta}}|e_{n''}\rangle}{\lambda_{n'}+\lambda_{n''}}|e_{n'}\rangle\langle e_{n''}|, \tag{2.36}$$

where $\partial_{\theta_i}\rho_{\vec{\theta}} = \frac{\partial\rho_{\vec{\theta}}}{\partial\theta_i}$.

2.1.3.3 SLD for pure states and QFI for unitary models

If the state is pure, i.e., $\rho = |\psi_{\theta_i}\rangle\langle\psi_{\theta_i}|$, one may use the idempotent property $\rho_{\theta_i}^2 = \rho_{\theta_i}$ to write

$$\frac{\partial\rho_{\vec{\theta}}^2}{\partial\theta} = \frac{\partial\rho_{\theta_i}}{\partial\theta_i}\rho_{\theta_i} + \rho_{\theta_i}\frac{\partial\rho_{\theta_i}}{\partial\theta_i} \tag{2.37}$$

Also, since Eq. 2.37 must coincide with Eq. 2.19 (for a single copy of the state), the SLD for pure states read

$$L_{\theta_i} = 2\frac{\partial\rho_{\theta_i}}{\partial\theta_i} = 2(|\dot{\psi}_{\theta_i}\rangle\langle\psi_\theta| + |\psi_{\theta_i}\rangle\langle\dot{\psi}_{\theta_i}|) \tag{2.38}$$

where $|\dot{\psi}_{\theta_i}\rangle = \partial_{\theta_i} |\psi_{\theta_i}\rangle$. Substituting Eq. 2.38 in the QFI equation (Eq. 2.25), it is straightforward to see

$$F_{Q\,i,i} = \langle\psi_{\theta_i}| L^2_{\theta_i} |\psi_{\theta_i}\rangle = 4(\langle\dot{\psi}_{\theta_i}|\dot{\psi}_{\theta_i}\rangle - |\langle\psi_{\theta_i}|\dot{\psi}_{\theta_i}\rangle|^2) \tag{2.39}$$

If ρ_{θ_i} is generated by the action of a unitary quantum channel $\mathcal{U}_{\theta_i}\rho\mathcal{U}^\dagger_{\theta_i}$, where $\mathcal{U}_{\theta_i} = e^{-iG\theta_i}$ and G is the generator of θ_i, then Eq. 2.39 may be written as

$$F_{Q\,i,i} = 4\mathrm{Var}(G) \tag{2.40}$$

where $\mathrm{Var}(G) = \langle\psi| G^2 |\psi\rangle - \langle\psi| G |\psi\rangle^2$. Thus for unitary family of pure states, the QFI is proportional to the variance of the parameter generator with respect to the unencoded state $|\psi\rangle$ and it is independent of the parameter. Due to Eq. 2.40, for N separable copies of the state i.e., $\rho^{\otimes N}_{\theta_i}$, one can use the additivity property $F_{Q\,i,i}(\rho^{\otimes N}_{\theta_i}) = NF_{Q\,i,i}(\rho_{\theta_i})$ to write the single-parameter QCRB in a form reminiscing the familiar Heisenberg uncertainty relation as follows

$$\mathrm{Var}(\tilde{\theta}_i)\mathrm{Var}(G) \geq \frac{1}{4N} \tag{2.41}$$

2.1.4 The Holevo Cramér-Rao bound

The main issue with the QCRB is that it is not a tight bound in the presence of fundamental incompatibility. Furthermore, the QCRB represents a fundamental minimum on the average cost of estimating p parameters for a given probe state. Thus, one cannot learn about the incompatibility of the optimal measurements for each parameter from the QCRB directly. Hence, one needs to optimize the covariance matrix in a nuanced manner to infer about the attainable bound in this case. This is given by the Holevo-Cramer Rao bound (HCRB).

2.1.4.1 Formulation and proof

In the following, we present the formulation and the proof of the HCRB, which is based on [150, 151]. This exposition is necessary to understand the key components of the numerical SDP formulation presented in Chapter 5, which has been used to compute the HCRB in our research presented in Chapter 4.

Assuming a discrete outcome POVM Π_x, from the first local unbiasedness condition Eq. 2.5(a), we can write

$$\sum_x \mathrm{Tr}(\rho_{\vec{\theta}}\Pi_x)\tilde{\theta}_i = \theta_i \tag{2.42}$$

$$\sum_x \mathrm{Tr}(\rho_{\vec{\theta}}\Pi_x)\tilde{\theta}_i = \sum_x \mathrm{Tr}(\rho_{\vec{\theta}}\Pi_x)\theta_i \tag{2.43}$$

Since $\sum_x \Pi_x = \mathbb{1}$ and $\mathrm{Tr}(\rho_{\vec{\theta}}) = 1$.

After rearrangement, we get

$$\mathrm{Tr}(\rho_{\vec{\theta}}X_i) = 0 \tag{2.44}$$

where

$$X_i = \sum_x (\tilde{\theta}_i - \theta_i)\Pi_x \tag{2.45}$$

is a Hermitian matrix in terms of the estimator and the POVM with $X_i \in \mathcal{L}_h(\mathcal{H})$. Therefore, Eq. 2.44 represents the local unbiasedness condition for X_i.

Furthermore,

$$\frac{\partial}{\partial\theta_j}\operatorname{Tr}(\rho_{\vec{\theta}}X_i) = 0 \tag{2.46}$$

$$\implies \operatorname{Tr}\left(\frac{\partial}{\partial\theta_j}\left[\rho_{\vec{\theta}}\sum_m \tilde{\theta}_i\Pi_m - \sum_m \rho_{\vec{\theta}}\theta_i\Pi_m\right]\right) = 0 \tag{2.47}$$

$$\implies \operatorname{Tr}\left(\left[\frac{\partial\rho_{\vec{\theta}}}{\partial\theta_j}\sum_m \tilde{\theta}_i\Pi_m - \frac{\partial\rho_{\vec{\theta}}}{\partial\theta_j}\sum_m \theta_i\Pi_m - \sum_m \rho_{\vec{\theta}}\delta_{i,j}\Pi_m\right]\right) = 0 \tag{2.48}$$

$$\implies \operatorname{Tr}\left(\frac{\partial\rho_{\vec{\theta}}}{\partial\theta_j}\sum_m(\tilde{\theta}_i - \theta_i)\Pi_m\right) = \operatorname{Tr}(\rho_{\vec{\theta}}\delta_{i,j}\Pi_m) \tag{2.49}$$

$$\implies \operatorname{Tr}\left(\frac{\partial\rho_{\vec{\theta}}}{\partial\theta_j}X_i\right) = \delta_{i,j} \tag{2.50}$$

Using, $\sum_x \Pi_x = \mathbb{1}$ and $\operatorname{Tr}(\rho_{\vec{\theta}}) = 1$.

Therefore, Eqs. 2.44 and 2.50 represent the local unbiasedness conditions rewritten in terms of X_i.

In the multivariate version, we define the vector $\vec{X} = (X_i, \ldots, X_p)^\top$

$$\vec{X} = \sum_x(\vec{\tilde{\theta}} - \vec{\theta})\Pi_x, \tag{2.51}$$

and Eqs. 2.44 and 2.50 become

$$\operatorname{Tr}(\rho_{\vec{\theta}}\vec{X}) = 0 \tag{2.52a}$$

$$\operatorname{Tr}(\nabla\rho_{\vec{\theta}}\vec{X}^\top) = \mathbb{1} \tag{2.52b}$$

Now, we note that the covariance matrix may be rewritten in the following way

$$\operatorname{Cov}(\vec{\tilde{\theta}}) = \operatorname{Tr}\left(\rho_{\vec{\theta}}\sum_x(\vec{\tilde{\theta}} - \vec{\theta})\Pi_x(\vec{\tilde{\theta}} - \vec{\theta})^\top\right), \tag{2.53}$$

where we define a linear operator

$$\mathbb{L} = \sum_x[(\vec{\tilde{\theta}} - \vec{\theta}) \otimes \mathbb{1}](\mathbb{1} \otimes \Pi_x)[(\vec{\tilde{\theta}} - \vec{\theta}) \otimes \mathbb{1}]^\top \tag{2.54}$$

with $\mathbb{L} \in \mathcal{S}^{\mathbb{R}}(\Theta) \otimes \mathcal{L}_h(\mathcal{H})$ i.e., acting on the total space of parameters and the space of Hermitian operators, and henceforth, we use *blackboard bold* notation to denote such objects.

Hence,

$$\operatorname{Cov}(\vec{\tilde{\theta}}) = \operatorname{Tr}(\mathbb{S}_{\vec{\theta}}\mathbb{L}), \tag{2.55}$$

where $\mathbb{S}_{\vec{\theta}} = \mathbb{1} \otimes \rho_{\vec{\theta}}$

Now, we define a more general positive semidefinite linear operator [151] based on Eq. 2.54 such that

$$\mathbb{M} = \sum_x [(\vec{\tilde{\theta}} - \vec{\theta}) \otimes \mathbb{1} - \vec{X}] \Pi_x [(\vec{\tilde{\theta}} - \vec{\theta}) \otimes \mathbb{1} - \vec{X}]^\top \geq 0 \tag{2.56}$$

with $\mathbb{M} \in \mathcal{S}^{\mathbb{C}}(\Theta) \otimes \mathcal{L}_h(\mathcal{H})$. Therefore, the trace of $\mathbb{M}$ with $\mathbb{S}$ is also positive, and can be expanded into

$$\mathrm{Tr}(\mathbb{S}_{\vec{\theta}} \mathbb{M}) = \mathrm{Tr}\left(\mathbb{S}_{\vec{\theta}} \left[\sum_x (\vec{\tilde{\theta}} - \vec{\theta}) \Pi_x (\vec{\tilde{\theta}} - \vec{\theta})^\top - (\vec{\tilde{\theta}} - \vec{\theta}) \Pi_x \vec{X}^\top - \vec{X} (\vec{\tilde{\theta}} - \vec{\theta})^\top \Pi_x + \vec{X} \Pi_x \vec{X}^\top \right] \right) \geq 0 \tag{2.57}$$

$$\implies \mathrm{Tr}\left(\mathbb{S}_{\vec{\theta}} \sum_x (\vec{\tilde{\theta}} - \vec{\theta}) \Pi_x (\vec{\tilde{\theta}} - \vec{\theta})^\top \right) - \mathrm{Tr}\left(\mathbb{S}_{\vec{\theta}} \left[\sum_x (\vec{\tilde{\theta}} - \vec{\theta}) \Pi_x \vec{X}^\top - \vec{X} (\vec{\tilde{\theta}} - \vec{\theta})^\top \Pi_x + \vec{X} \Pi_x \vec{X}^\top \right] \right) \geq 0 \tag{2.58}$$

Making use of Eqs. 2.54, 2.55 and 2.51, we write

$$\implies \mathrm{Cov}(\vec{\tilde{\theta}}) - \mathrm{Tr}(\mathbb{S}_{\vec{\theta}} \left[\vec{X} \vec{X}^\top - \vec{X} \vec{X}^\top + \sum_x \vec{X} \Pi_x \vec{X}^\top \right]) \geq 0 \tag{2.59}$$

Making use of $\sum_x \Pi_x = \mathbb{1}$,

$$\implies \mathrm{Cov}(\vec{\tilde{\theta}}) - \mathrm{Tr}(\mathbb{S}_{\vec{\theta}} \vec{X} \vec{X}^\top) \geq 0 \tag{2.60}$$

Therefore, we obtain

$$\mathrm{Cov}(\vec{\tilde{\theta}}) \geq Z(\vec{X}), \tag{2.61}$$

where $Z(\vec{X}) = \mathrm{Tr}(\mathbb{S}_{\vec{\theta}} \vec{X} \vec{X}^\top) \in \mathcal{S}^{\mathbb{C}}(\Theta)$, a complex matrix and $\mathrm{Cov}(\vec{\tilde{\theta}}) \in \mathcal{S}^{\mathbb{R}}(\Theta)$, a real symmetric matrix.

In particular, for projective measurements we have $\Pi_x \Pi_{x'} = \delta_{x,x'} \Pi_x$. Therefore

$$Z(\vec{X}) = \mathrm{Tr}\left(\mathbb{S} \sum_{x,x'} (\vec{\tilde{\theta}} - \vec{\theta}) \Pi_x \Pi_{x'} (\vec{\tilde{\theta}} - \vec{\theta})^\top \right) \tag{2.62}$$

$$= \mathrm{Tr}\left(\mathbb{S} \sum_{x,x'} (\vec{\tilde{\theta}} - \vec{\theta}) \Pi_x \delta_{x,x'} (\vec{\tilde{\theta}} - \vec{\theta})^\top \right) \tag{2.63}$$

$$= \mathrm{Tr}\left(\mathbb{S} \sum_x (\vec{\tilde{\theta}} - \vec{\theta}) \Pi_x (\vec{\tilde{\theta}} - \vec{\theta})^\top \right) = \mathrm{Tr}(\mathbb{S}_{\vec{\theta}} \mathbb{L}) = \mathrm{Cov}(\vec{\tilde{\theta}}) \tag{2.64}$$

Eq. 2.61 which represents a general lower bound (for all measurements) on the covariance matrix by the complex matrix $Z(\vec{X})$, plays a key role in unraveling the contribution due to fundamental incompatibility which will present in the following

As we deal with scalar bounds, Eq. 2.61 may be written as

$$\mathrm{tr}(W \mathrm{Cov}(\vec{\tilde{\theta}})) \geq \mathrm{tr}(W Z(\vec{X})) \tag{2.65}$$

The R.H.S. of Eq. 2.65 represents a fundamental, global minimum on the average cost for a given W. This may be seen by performing the remaining minimization over $\vec{X}$, which actually yields the QCRB, C_Q i.e.,

$$\min_{\text{Cov},\vec{X}}\{\text{tr}(W\text{Cov})\,|\,\text{Tr}(\nabla\mathbb{S}_{\vec{\theta}}\vec{X}^{\top})=\mathbb{1}\}=\min_{\vec{X}}\{\text{tr}(WZ(\vec{X}))\,|\,\text{Tr}(\nabla\mathbb{S}_{\vec{\theta}}\vec{X}^{\top})=\mathbb{1}\}=C_Q(\rho_{\vec{\theta}}),\tag{2.66}$$

where $\nabla\mathbb{S}_{\vec{\theta}}=\nabla\rho_{\vec{\theta}}\otimes\mathbb{1}$ and note that for the sake of brevity of notation, we drop dependence of the covariance matrix on the estimators and parameters henceforth i.e., $\text{Cov}(\vec{\tilde{\theta}})\equiv\text{Cov}$. The proof of Eq. 2.66 is a bit involved, and hence we will not present it here. For the interested reader, the detailed proof can be found in [151]. However, we know that $Z(\vec{X})$ is a complex matrix, and taking a trace with W to obtain its scalar form causes the information contained in the imaginary part of $Z(\vec{X})$ to be lost. Therefore, although C_Q represents a fundamental minimum for the optimal information extraction about all parameters, it is not informative. An informative bound known as the *Holevo-Cramér-Rao bound* (HCRB), C_H, may be obtained by minimizing the average cost over all covariance matrices with the restriction given by Eq. 2.61 which reads

$$C_H(\rho_{\vec{\theta}})=\min_{\text{Cov},\vec{X}}\{\text{tr}(W\text{Cov})\,|\text{Cov}\geq Z(\vec{X}),\text{Tr}(\nabla\mathbb{S}_{\vec{\theta}}\vec{X}^{\top})=\mathbb{1}\}\tag{2.67}$$

In terms of $\mathbb{L}$, the HCRB takes the following equivalent form

$$C_H(\rho_{\vec{\theta}})=\min_{\mathbb{L},\vec{X}}\{\text{tr}[W\,\text{Tr}(\mathbb{S}_{\vec{\theta}}\mathbb{L})]\,|\,\text{Tr}(\mathbb{S}_{\vec{\theta}}\mathbb{L})\geq Z(\vec{X}),\text{Tr}(\nabla\mathbb{S}_{\vec{\theta}}\vec{X}^{\top})=\mathbb{1}\}\tag{2.68}$$

From Eqs. 2.66 and 2.67, one can infer that the bounds on the average cost reads

$$\overline{\mathcal{C}}\geq C_H\geq C_Q\tag{2.69}$$

For N separable identical copies of the probe state: $\rho_{\vec{\theta}}^{\otimes N}$, the HCRB reads

$$\overline{\mathcal{C}}\geq\frac{C_H(\rho_{\vec{\theta}})}{N}=C_H(\rho_{\vec{\theta}}^{\otimes N})\tag{2.70}$$

We note that, for our purposes, we will be dealing with only a single copy of the probe. Thus, we denote: $C_H(\rho_{\vec{\theta}})\equiv C_H$, and in cases where multiple copies are involved we use the explicit notation: $C_H(\rho_{\vec{\theta}}^{\otimes N})$ henceforth.

2.1.4.2 The HCRB captures fundamental incompatibility

The HCRB represents another fundamental bound in the multiparameter setting. From its construction, it is more informative than the QCRB, yielding information about the fundamental incompatibility of the problem through the imaginary of part of $Z(\vec{X})$, which we will see more explicitly below.

The minimization over Cov in Eq. 2.67 may be performed analytically which yields [152]

$$C_H=\min_{\vec{X}}\{\text{tr}(W\text{Re}(Z(\vec{X}))+||\sqrt{W}\text{Im}(Z(\vec{X}))\sqrt{W}||_1\,|\,\text{Tr}(\nabla\mathbb{S}_{\vec{\theta}}\vec{X}^{\top})=\mathbb{1}\},\tag{2.71}$$

where $||A||_1=\text{Tr}(\sqrt{AA^{\dagger}})$ is the trace norm, which represents the sum of the square roots of the eigenvalues of matrix $AA^{\dagger}$.

Alternative to Eq. 2.66, in [24], it has been shown that

$$\min_{\vec{X}}\text{tr}(W\text{Re}(Z(\vec{X})))=C_Q\tag{2.72}$$

Furthermore, the result of the full minimization in Eq. 2.71, reveals the contribution due to fundamental incompatibility originating from the imaginary part of $Z(\vec{X})$.

D-invariant models: We note that, in general, the minimization over $\vec{X}$ in Eq. 2.71 is not feasible analytically. However, for the so-called *D-invariant models*, indeed a closed-form solution, $\overline{C}_H$, for C_H exists such that $C_H \leq \overline{C}_H$. This bound reads [153, 152]

$$\overline{C}_H = C_Q + \|\sqrt{W}F_Q^{-1}IF_Q^{-1}\sqrt{W}\|_1, \tag{2.73}$$

where $I = \frac{1}{2}\operatorname{Tr}(\rho_{\vec{\theta}}\vec{L}.\vec{L}^\top)$ with $I_{i,j} = \frac{1}{2}\operatorname{Tr}(\rho_{\vec{\theta}}[L_{\theta_i}, L_{\theta_j}])$.

Through the upper bound $\overline{C}_H$, one can quantitatively capture fundamental incompatibility through the term $\|\sqrt{W}F_Q^{-1}IF_Q^{-1}\sqrt{W}\|_1$.

Additionally, it has been shown that [154, 155]

$$C_H \leq 2C_Q, \tag{2.74}$$

which implies that the fundamental incompatibility always manifests in such a way that the HCRB is at most two times the QCRB.

2.1.4.3 Saturability of the HCRB

The HCRB is a tighter bound than the QCRB, and thanks to the mapping of the HCRB to the Quantum Local Asymptotic Normality (QLAN) theory, we have identified that collective measurements on multiple identical copies of the probe attain the HCRB asymptotically [156, 157, 158, 159, 160]. Therefore, in a true multiparameter approach, not only the probes need to possess quantum features but also the measurements [24].

A necessary and sufficient condition for the equivalence of the HCRB and the QCRB reads

$$\operatorname{Tr}\left(\rho_{\vec{\theta}}[L_{\theta_i}, L_{\theta_j}]\right) = 0, \quad \forall\, \theta_i, \theta_j \in \Theta,\, i \neq j \tag{2.75}$$

This condition, known as the commutation condition indicates the presence of *weak fundamental compatibility* in the problem [24, 161, 162, 163].

Eq. 2.75 represents an important criteria for the asymptotic optimal information extraction using collective measurements even if the SLDs for the parameters do not commute i.e., $[L_{\theta_i}, L_{\theta_j}] \neq 0$.

2.1.5 The Nagaoka-Hayashi Cramér-Rao bound

Although the HCRB is tight i.e., saturable with collective measurements, the practical implementation of such measurements are very often infeasible. Hence, it is natural to ask: what is the best precision one can achieve with only separable measurements i.e., measurements acting individually on each identical copy of the probe state? In fact, some of the most practical, standard detection techniques in quantum optics such as the homodyne detection and photon counting are easier to implement as separable measurements. To this end, indeed a separable measurement[3] based bound exists which was proposed and formulated independently by Nagaoka and Hayashi known as the *Nagaoka-Hayashi Cramér-Rao bound* (NHCRB), C_N [164, 150].

[3]With respect to the saturability of the bounds, we start with the optimization of the covariance matrix over the class of measurements that act individually on identical copies of the probe state (separable measurements). The optimal measurement is then used to construct the optimal estimator such as the MLE using techniques we briefed earlier. Therefore, by construction, the NHCRB holds only for separable measurements.

We can infer that the HCRB (Eq. 2.67 and Eq. 2.68) is obtained as a result of optimizing the average cost over all covariance matrices Cov. However, through this, we gain no information about the optimal separable measurement which is contained in $\mathbb{L}$ and $\vec{X}$. To remedy this, if we optimize in particular over $\mathbb{L}$ instead of Cov, we obtain the NHCRB bound that is more informative than the HCRB which reads

$$C_N = \min_{\mathbb{L},\vec{X}} \{\mathrm{tr}(W\mathrm{Cov}) \,|\mathbb{L} \geq \vec{X}\vec{X}^\top, \mathrm{Tr}(\nabla \mathbb{S}_{\vec{\theta}} \vec{X}^\top) = \mathbb{1}\} \tag{2.76}$$

Given that we have proven the condition $\mathrm{Cov} \geq Z(\vec{X})$ from the positivity of the operator $\mathbb{M}$, it is straightforward to prove $\mathbb{L} \geq \vec{X}\vec{X}^\top$ from the same argument only this time, we do not take the trace with the state: $\mathrm{Tr}(\mathbb{S}_{\vec{\theta}}\mathbb{M})$.

Eq. 2.68 and Eq. 2.76 represent convex optimization problems, whose solutions yield C_H and C_N respectively. In general, an analytical solution to both is not feasible. Thus, we convert them into a numerically solvable semi-definite programming (SDP) problems. The SDP formulation of the HCRB will be presented in Chapter 5, while for the SDP formulation of the NHCRB, the interested reader is referred to [165].

As collective measurements are the most powerful form of measurements, they offer increased precision than any other measurement. Alternatively, the HCRB can be thought of as a relaxation of the NHCRB, in the sense that the former is optimized over all covariance matrices, while the latter is optimized specifically over the matrices $\mathbb{L}$. Thus,

$$\overline{\mathcal{C}} \geq C_N \geq C_H \tag{2.77}$$

2.1.5.1 Maximal advantage offered by collective measurements

The advantage offered by the collective measurements over separable ones may be understood from the ratio

$$r_H^N = \frac{C_N}{C_H}. \tag{2.78}$$

Therefore, the greater the value of r_H^N, the greater is the advantage. However, in [166], it has been shown that the maximal advantage offered is at most a factor of p i.e., $r_H^N \leq p$.

2.1.5.2 Saturability of the NHCRB

In Eq. 2.76, after the minimization over $\mathbb{L}$ respectively, the optimal separable measurement acting on a single copy $\rho_{\vec{\theta}}$ is deduced from the numerical solution $\vec{X}$ where the individual X_i are given by Eq. 2.45 by treating $\tilde{\theta}_i - \theta_i = \xi_i$ as coefficients such that $X_i = \sum_x \xi_i \Pi_x$. However, we caution the reader that the measurement inferred this way or by other means *do not* always saturate the NHCRB. For instance, the authors of [167] have found a case for which $C_N = C_Q$, and due to the fundamental incompatibility of the problem, the NHCRB becomes unattainable with separable measurements.

A tight bound for separable measurements: In 1997, Hayashi derived a bound tighter than the NHCRB [168]. More recently, this bound has been revisited by Hayashi et al. in [169], where the authors provide a unified framework for all the multiparameter bounds using conic programming techniques. The aforementioned bound is simply referred to as the *the tight bound* for all uncorrelated measurement strategies, and numerical estimates to it are provided along with a

study of its distance to the NHCRB. It has been demonstrated that the tight bound can be strictly tighter than the NHCRB further cautioning the reader that there exists cases where the NHCRB is unattainable.

Interestingly, the NHCRB is only *subadditive*[4]. Thus, implying that the sum of Thus, considering multiple copies $\rho_{\vec{\theta}}^{\otimes N}$, we have

$$NC_N(\rho_{\vec{\theta}}^{\otimes N}) \leq C_N \tag{2.79}$$

The proof of Eq. 2.79 is found in [170]. As a result we have $C_N \geq NC_N(\rho_{\vec{\theta}}^{\otimes N}) \geq C_H$. The last inequality is tight when[5] $\lim_{N\to\infty} NC_N(\rho_{\vec{\theta}}^{\otimes N}) = C_H$. Therefore, although we deal with only separable measurements, asymptotically, we expect the NHCRB to converge to the HCRB [170, 165].

In cases, where the NHCRB is saturated, we denote $\vec{X}_N^* \equiv (\Pi_N^*, \vec{\tilde{\theta}}_N^*)$ as the solution of C_N, where Π_N^* and $\vec{\tilde{\theta}}_N^*$ are the optimal POVM and the optimal estimator obtained from $\vec{X}_N^*$. Therefore, the optimal covariance matrix reads:
$N\mathrm{Cov}(\Pi_N^*, \vec{\tilde{\theta}}_N^*) = C_N \geq NC_N(\rho_{\vec{\theta}}^{\otimes N})$. As demonstrated in [165], for the estimation of rotations of a qubit in the presence of phase damping channel and joint-estimation of phase and loss in optical interferometry, the optimal separable measurement may be constructed from the solution $\vec{X}_N^*$. For the former example, increasing the number of qubits resulted in the reduction of the gap between the HCRB and the NHCRB, which further supports the asymptotic convergence of the NHCRB to the HCRB as stated before. As a result, from Eq. 2.78, we note that this gap is influenced by the number of parameters to estimate as well as the number of probe states (resources) [165, 166, 170].

On the other hand, for the HCRB, if we denote $\vec{X}_H^* \equiv (\Pi_H^*, \vec{\tilde{\theta}}_H^*)$ as the solution of C_H, where Π_H^* and $\vec{\tilde{\theta}}_H^*$ are the optimal POVM and the optimal estimator obtained from $\vec{X}_H^*$, the optimal covariance matrix reads[6]: $\lim_{N\to\infty} N\mathrm{Cov}(\Pi_H^*, \vec{\tilde{\theta}}_H^*) = C_H$ [171].

A necessary and sufficient condition to saturate the QCRB with separable measurements has appeared recently in the papers [167, 170] that reads

$$\mathrm{Tr}(|\rho_{\vec{\theta}}[L_{\theta_i}, L_{\theta_j}]|) = 0 \quad \forall\, \theta_i, \theta_j \in \Theta, i \neq j, \tag{2.80}$$

where $\mathrm{Tr}(|A|)$ is the sum of the absolute values of the eigenvalues of matrix A. For an estimation problem, when this condition is satisfied we have: $C_N = C_S$. We note the following: (i) Eq. 2.80 opens the door to the possibility of optimally extracting information about the parameters with separable measurements without utilizing collective measurements. (ii) In [170] it has been demonstrated that the single-copy saturability of the QCRB is a fundamental one i.e., if the QCRB can be saturated with a measurement on a single copy, then it can be saturated with any number of finite copies. These two conditions provides a solution to one of the five open problems in quantum information theory presented in [172].

[4] A subadditive function has the property $f(x+y) \leq f(x) + f(y)$

[5] This is only for cases where the NHCRB is tight, the HCRB may be attained asymptotically with separable measurements. In cases, where the NHCRB is not tight, one still needs to resort to a collective measurement which attains the HCRB asymptotically.

[6] From this, one can infer that the HCRB is also constructed for separable measurements. However, its correspondence to the QLAN theory introduces the collective measurement character in the asymptotic limit.

2.1.5.3 Most informative bound

Finally, we introduce the most informative bound (MIB), C_{MI} which is attained by the optimal POVM Π^*_{MI} and the optimal estimator $\vec{\tilde{\theta}}^*_{\mathrm{MI}}$. As the name suggests, the MIB is "most informative" out of all bounds in the sense that it yields information about the optimal POVM and the optimal estimator separately. Specifically, once Π^*_{MI} is obtained, we may use the MLE or similar optimal estimator to construct $\vec{\tilde{\theta}}^*_{\mathrm{MI}}$. This information is lost during the optimization procedure in the NHCRB as $\mathbb{L}$ and $\vec{X}$ mix information about the POVM and estimators, which then leads to a post-processing of $\vec{X}_N$ to obtain Π^*_N and $\vec{\tilde{\theta}}^*_N$ as we have seen earlier.

We summarize the informativeness of all the bounds based on the following ordering: $C_{\mathrm{MI}} \geq C_N \geq C_H \geq C_Q$ with the MIB being the most informative and C_Q being the least informative. In terms of the relaxations made during the optimization, the NHCRB is a relaxation of the MIB over single optimization variables, $\mathbb{L}$ and $\vec{X}$, which jointly encode information about the POVM and the estimators. The HCRB is a further relaxation of the NHCRB, as it involves optimization over all covariance matrices. The QCRB is an even looser relaxation of the HCRB, providing a fundamental lower bound that does not account for fundamental incompatibility.

2.2 Metrological resourcefulness of important probe states

As we now know that the QFI corresponds to the performance of the optimal measurement, in this section, we will review the phase sensing scaling obtained using optimal strategies. This is in contrast to the simple measurement strategies in Section 1.3, where we considered specific input states in the MZI.

Using, Eq. 2.29 we have

$$\sigma_\phi \geq \frac{1}{\sqrt{F_Q(\rho_\phi)}}, \tag{2.81}$$

where we have made the replacement $\mathrm{Var}(\tilde{\phi}) \to \sigma^2_\phi$ to avoid a notational clash with Δ, which is reserved for the phase diffusion parameter introduced shortly. Considering the phase evolution: $\rho_\phi = e^{-i\phi\hat{a}^\dagger\hat{a}}\rho e^{i\phi\hat{a}^\dagger\hat{a}}$, The QFI for the (pure) coherent state can be calculated using Eq. 2.40 as

$$F_Q(|\alpha e^{i\phi}\rangle) = 4\sigma^2_{\hat{a}^\dagger\hat{a}}\big|_{|\alpha\rangle} = 4|\alpha|^2 = 4\langle N\rangle. \tag{2.82}$$

Therefore, we have

$$\sigma_\phi \geq \frac{1}{2\sqrt{\langle N\rangle}}. \tag{2.83}$$

Comparing this to the MZI setup with a coherent and a vacuum state, we find an improvement in precision by a constant factor of $1/\sqrt{2}$, implying that the MZI scheme was not optimal.

For the N00N state $|\psi^{\mathrm{N00N}}\rangle = \frac{1}{\sqrt{2}}(|N,0\rangle + |0,N\rangle)$, we have

$$F_Q(|\psi^{\mathrm{N00N}}_\phi\rangle) = 4\sigma^2_{\hat{a}^\dagger\hat{a}}\big|_{|\psi^{\mathrm{N00N}}\rangle} = N^2. \tag{2.84}$$

Hence,

$$\sigma_\phi \geq \frac{1}{N}, \tag{2.85}$$

which yields the HS (Eq. 1.9).

Furthermore, we note that the N00N state is the optimal state only in the frequentist or local approach, where we assume minimal variations in the value of ϕ i.e., we possess enough prior knowledge about ϕ to narrow down its true value within a small neighbourhood in $\phi \in [0, 2\pi]$. Hence, N00N states cannot distinguish phase values that differ by $2\pi/N$ as they are designed to work optimally for a narrow range of values. In cases where there are large variations of ϕ, one needs to use the Bayesian approach with a prior distribution, typically a flat prior $p(\phi) = 1/2\pi$, to operate under maximal ignorance. The optimal state obtained in this case has a very different structure compared to the N00N state [9]. The resulting precision here is expected to be lower than the same obtained using the local approach given our lack of knowledge about ϕ. Nevertheless, from Eq. 2.84, in the local approach, we can infer that the maximum phase sensing precision is provided by the state that has maximum photon number uncertainty [27].

2.3 Compatibility in multiparameter quantum metrology

2.3.1 Metrological compatibility

The key feature that distinguishes single parameter estimation from the multiparameter one is that the observables corresponding to optimal estimation of each parameter may be fundamentally incompatible [24]. This is a manifestation of the *Heisenberg Uncertainty Principle* of quantum mechanics which can be inferred from the fundamental bounds on the uncertainty for each parameter. Fundamental incompatibility often acts as an impediment for the optimal information extraction about all parameters simultaneously [22, 173, 174]. Moreover, strong incompatibility also forces one to use more resources for estimation through the use of dedicated optimal measurements for every parameter. Given a probe state $\rho_{\vec{\theta}}$, for the estimation of p uncorrelated parameters i.e., $F_{Q\,i,j} = 0, i \neq j$, the QCRB can be operationally realized by using p separate schemes of dedicated optimal measurements for each parameter. Therefore, the aforementioned scheme utilizes p times more resources than a single scheme for the simultaneous estimation of p parameters in the presence of *fundamental compatibility*. Although, at the preparation level, one needs to consider whether a single probe state exists that is optimal for the estimation of all parameters, which is referred to as *probe compatibility* [175, 176, 177]. This aspect is crucial for *metrological compatibility* which is attained under three conditions [24]: (i) presence of uncorrelated estimators, (ii) presence of weak compatibility (Eq. 2.75) even if there is strong fundamental incompatibility (Eq. 2.31), and (iii) presence of probe compatibility. Furthermore, given a scheme that satisfies these conditions for metrological compatibility, we know that entangled probe states offer advantage over separable ones and the presence of condition (ii) necessitates the need for collective measurements i.e., entangling measurement as seen in Section 2.1.4.3. Therefore, in Fig. 2.2, we depict a "fully quantum" scheme (at the level of both probe and measurement) not only offers the maximal attainable precision of all parameters but also utilizes p times fewer resources, thus being resource-efficient.

2.3.2 Figure of merits for fundamental compatibility

The problem of fundamental compatibility due to the optimal observables for each parameter has been studied by deriving a figure of merit and its features were demonstrated with simple examples involving qubit and qutrit probe states [171]. Another related figure of merit that has appeared recently has been termed Asymptotic Incompatibility (AI) quantifying the gap between the HCRB and the QCRB [178]. Using AI, an intriguing relation has been found between the dimensions of

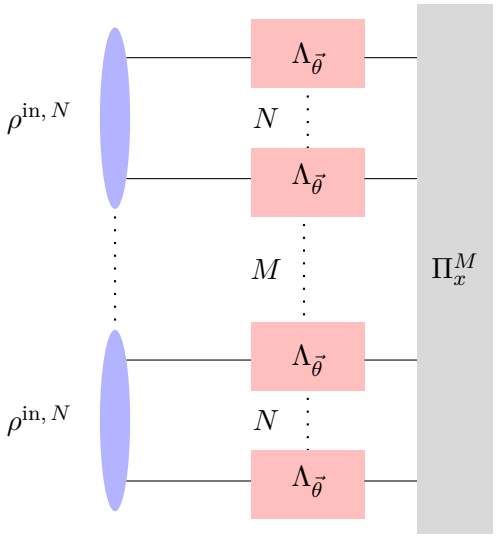

FIGURE 2.2: For a quantum channel $\Lambda_{\vec{\theta}}$, a general metrological scheme achieves optimal information extraction about all parameters by using an optimized probe state that is entangled on N copies and a collective measurement Π_x^M acting on M copies of the probe state.

the probe state, the number of parameters, and the compatibility. The properties of AI have been summed up in details in another work [179]. Yet another measure defined as the ratio of the mean Uhlmann curvature to the QFIM has been used to quantify the "quantumness" of multiparameter metrological schemes [155]. Through the Uhlmann curvature, this figure of merit remarkably allows one to view the incompatibility in the context of quantum information geometry. From the point of view of practical relevance, the tightness of the HCRB compared to the QCRB has been investigated with an example of joint-estimation of phase and loss in one arm of an interferometer involving probe states such as Holland-Burnett (HB) states and Greenberger-Horne-Zeilinger (gHZ) states [143].

There have been attempts to mitigate the fundamental incompatibility and reach the optimal limit using quantum criticality [180], quantum error correction [181], and increasing the variances of parameter generators [182]. With regard to optimizing resources, there has been an approach to approximate the efficiency of several incompatible measurements using a single measurement, and the resulting errors have been studied [183]. Furthermore, as a surprising fact, incompatibility has also been used as a resource to improve the accuracy of single parameter estimation schemes [184].

Chapter 3

Joint-estimation of phase and phase diffusion

In this chapter, we focus on one of the examples of noisy quantum interferometry introduced in Chapter 1, namely, the joint estimation of phase and phase diffusion. As emphasized earlier, phase diffusion is among the most deleterious types of noise for phase sensing. It is therefore necessary to study the joint-precision limits of this problem using probe states and measurements that are not only experimentally accessible but also sensitive to both phase and diffusion.

The material presented here is based on [185], and the exposition is organized as follows. We begin with a detailed motivation for the estimation of phase diffusion with the phase, including its physical origin, followed by the corresponding mathematical formalism, formulation, and the setup of our joint-estimation problem. Subsequently, we present and discuss our results, concluding with a brief summary. Throughout this analysis, we employ some of the tools from multiparameter estimation theory, as introduced in Chapter 2, to investigate the fundamental precision limits associated with this problem.

3.1 Motivation

The intrinsic quantum fluctuations of a light field gives rise to the fluctuation of the number of photons in it due to random spontaneous emission events. These events create photons with random phases leading to phase fluctuations of the field, which "diffuses" over the range: $[0, 2\pi]$. Assuming a single spontaneous emission event takes places in a time scale much shorter than the full evolution time of the field t and considering a spontaneous emission rate A, the time-dependent phase probability distribution reads: $P(\phi, t) = \frac{1}{\sqrt{2\pi\sigma(t)^2}} e^{-\phi^2/2\sigma(t)}$. $P(\phi, t)$ obeys the diffusion equation: $\partial P/\partial t = D(\partial^2 P/\partial \phi^2)$, where the standard deviation $\sigma(t) = \sqrt{At/2\langle n\rangle}$ is proportional to the shot noise limit, $\langle n\rangle$ is the average number of photons in the field, and $D = A/4\langle n\rangle$ is the diffusion coefficient. Thus, *phase diffusion* is inherently associated to the phase of a field. Besides its fundamental origin, phase fluctuations can also be a result of external disturbances in the field such as variations of certain properties such as the magnetization or the polarization of the medium in the path of the light. They can also originate from the micro-motions or deformations of the optical elements constituting an interferometer setup due to very small thermal fluctuations in the environment. Hence, minimizing these disturbances is essential to obtain a narrow linewidth and a coherent beam of light. As a result, the weaker the strength of the diffusion, the stronger is the imprint of phase on the probes, consequently, leading to a precise estimation of phase.

In general, phase diffusion is characterized by the diffusion coefficient D or simply the standard deviation of phase: $\sigma(t) \equiv \Delta$ for our purposes. Intrinsic phase diffusion is useful to obtain the natural linewidth of coherent fields such as single-mode lasers [1, 186, 187, 188, 189] and the power spectrum of a field as a function of the frequency [1]. It is also used in the development of efficient quantum random number generators based on quantum field fluctuations [190, 191, 192, 193]. External phase diffusion is not just limited to sensors that make use of light fields, but it is also prevalent in various other quantum sensors built on platforms such as trapped ions, spin qubits, superconducting circuits, Rydberg atoms, and even elementary particles to measure a variety of quantities such as electric and magnetic fields, temperature, and time. Also referred to as *dephasing*, phase diffusion depreciates the efficiency of all the aforementioned sensors [71, 72], and hence its precise estimation and careful tailoring of the sensors are indispensable. Remarkably, instead of a nuisance, it has also been used in decoherence microscopy, where it has been used to study the elusive properties of the probe itself [194]. It has also found applications in thermometry [195, 196] and optomechanics [197, 198]. As we have seen in Chapter 1, phase estimation is a crucial aspect in optical interferometry, and thus, its needless to mention that it must be studied by taking into account the phase diffusion [30, 31]. Another technique that "squeezes" phase diffusion to reduce noise in phase estimation has been demonstrated in [199].

Owing to the fact that the effects of diffusion may not be stationary, the estimation of diffusion along with phase offers a more nuanced estimation strategy. Furthermore, such a strategy may offer information not only about the underlying system but also about the way the system interacts with its environment. Therefore, in this chapter, we focus on the joint-estimation of phase and phase diffusion considering an important class of multiphoton probe states of fixed photon number and the double measurement based on our paper [185]. Prior to this work, Vidrighin et al. [34] investigated this problem with respect to the violation of a informational trade-off relation that holds for qubit probe states [200]. Another work also studied the precision limits of the same problem in the small and large diffusion regime [144]. The authors of these works have considered Holland-Burnett states, two-qubit states, and N00N states, employing measurement strategies such as double homodyne detection, general projective measurements, and collective measurements for information extraction. Notably, the latter is known to offer enhanced precision with respect to its saturation of the HCRB as seen in Section 2.1.4.3. From the point of view of estimation, phase diffusion is considered a nuisance parameter i.e., a parameter that appears in the model, but not of main interest. In practice, several nuisance may be present in the model, and estimating all of them can be resource expensive or even computationally challenging. Hence, assigning appropriate weights to these parameters that appear in the corresponding scalar bounds is seen as the optimal way to study the physics of relevant parameters such as phase.

3.2 Formalism

3.2.1 Two-dimensional probe states

3.2.1.1 Individual dephasing

Basic model: To understand the mathematical formalism of the model describing the encoding of phase and phase diffusion on a general probe state, we begin with the simple case of a local or *individual dephasing* of a qubit [19]. If we consider a qubit (system) S in the state: $|\psi\rangle_S = \alpha\,|0\rangle_S + \beta\,|1\rangle_S$ with $\rho_S = |\psi\rangle_S\,\langle\psi|_S$, dephasing is described by a physical process where the qubit and the environment E interacts in such a way that a scattering event occurs with a probability p.

As a result, the environment changes its state from $|0\rangle_E$ to $|1\rangle_E$ if S is in state $|0\rangle_S$ and to $|2\rangle_E$ if S is in state $|1\rangle_S$. This interaction rule on the qubit characterized by a map (isometry) $\mathcal{U} : \mathcal{H}_S \to \mathcal{H}_{SE}$ yields the composite state

$$|\Psi\rangle_{SE} = \alpha(\sqrt{1-p}\,|0\rangle_S\,|0\rangle_E + \sqrt{p}\,|0\rangle_S\,|1\rangle_E) + \beta(\sqrt{1-p}\,|1\rangle_S\,|0\rangle_E + \sqrt{p}\,|1\rangle_S\,|2\rangle_E) \tag{3.1}$$

Tracing out the environment, we obtain the output state of the qubit described by the following Kraus representation

$$\mathrm{Tr}_E(\rho_{SE}) = \rho_S^{(1)} = \Lambda(\rho_S) = K_1\rho_S K_1^\dagger + K_2\rho_S K_2^\dagger, \tag{3.2}$$

where $\Lambda(\cdot)$ is the individual dephasing channel, $K_1 = \sqrt{\frac{1+\eta}{2}}\mathbb{1}$ and $K_2 = \sqrt{\frac{1-\eta}{2}}\sigma_z$ are the Kraus operators, $\eta = \sqrt{1-p}$, σ_z is the Pauli z matrix.

After applying these Kraus operators, the output state reads

$$\rho_S^{(1)} = \begin{bmatrix} |\alpha|^2 & \alpha\beta^*\eta \\ \alpha^*\beta\eta & |\beta|^2 \end{bmatrix} \tag{3.3}$$

This results in the shrinking of the Bloch sphere to a prolate spheroid as shown in Fig. 3.1.

On applying the channel n times we get

$$\rho_S^{(n)} = \Lambda^n(\rho_S) = \begin{bmatrix} |\alpha|^2 & \alpha\beta^*\eta^n \\ \alpha^*\beta\eta^n & |\beta|^2 \end{bmatrix} \tag{3.4}$$

Substituting back $\eta = \sqrt{1-p}$ and if Γ is the scattering probability per unit time, for an infinitesimal time interval Δt, and considering a evolution over a time $t = n\Delta t$, we obtain

$$\rho_S^{(n)} = \begin{bmatrix} |\alpha|^2 & \alpha\beta^*(1-\frac{\Gamma t}{n})^{\frac{n}{2}} \\ \alpha^*\beta(1-\frac{\Gamma t}{n})^{\frac{n}{2}} & |\beta|^2 \end{bmatrix} \tag{3.5}$$

In the limit $n \to \infty$ this becomes

$$\rho_S^{(n)} = \begin{bmatrix} |\alpha|^2 & \alpha\beta^* e^{-\frac{\Gamma t}{2}} \\ \alpha^*\beta e^{-\frac{\Gamma t}{2}} & |\beta|^2 \end{bmatrix}, \tag{3.6}$$

from which, we can infer that for a *continuous dephasing* process, the off-diagonal elements exponentially decays for $t >> \Gamma^{-1}$.

Equivalently, if one considers a rotation of the qubit about the z-axis:
$R_z(\phi') = \mathcal{U}_{\phi'} = e^{-i\phi'\sigma_z/2}$ that gives rise to a phase ϕ', each scattering event with the environment leads to a random change in the phase, resulting in phase noise. After a time t, the resulting state, $\tilde{\rho}_{\phi,\Delta}$, averaged over all such phase fluctuations, reads

$$\tilde{\rho}_{\phi,\Delta} = \Lambda_{\phi,\Delta}(\rho_S) = \int_{-\infty}^{\infty} d\phi' p_{\phi,\Delta}(\phi')\mathcal{U}_{\phi'}\rho_S\mathcal{U}_{\phi'}^\dagger, \tag{3.7}$$

where $\Lambda_{\phi,\Delta}$ is the phase diffusion channel and $p_{\phi,\Delta}(\phi') = \frac{1}{\sqrt{2\pi\Delta^2}}e^{-\frac{(\phi'-\phi)^2}{2\Delta^2}}$ is the Gaussian probability distribution characterizing the phase noise with mean value ϕ and standard deviation Δ with Kraus operators $K(\phi') = \sqrt{p_{\phi,\Delta}(\phi')}\mathcal{U}_{\phi'}$, parametrized by ϕ'. $\tilde{\rho}_{\phi,\Delta}$ is analogous to $\rho_S^{(n)}$.

Further evaluation leads to

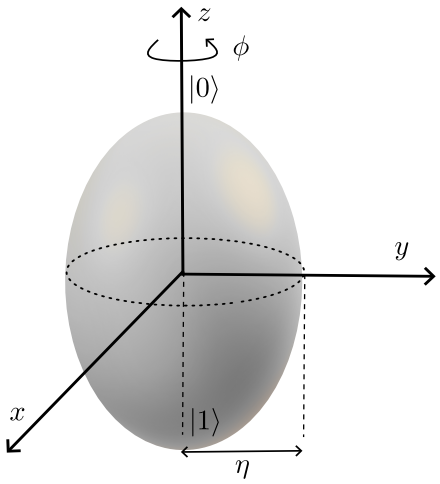

FIGURE 3.1: Effect of dephasing of a qubit leads to the shrinking of the Bloch sphere to a prolate spheroid aligned with the z-axis.

$$\tilde{\rho}_{\phi,\Delta} = \begin{bmatrix} |\alpha|^2 & \alpha\beta^* e^{-i\phi-\frac{\Delta^2}{2}} \\ \alpha^*\beta e^{i\phi-\frac{\Delta^2}{2}} & |\beta|^2 \end{bmatrix} \tag{3.8}$$

From the two physical pictures described above, we identify: $\Gamma t = \Delta$ which is the parameter quantifying phase diffusion which decoheres the qubit in the $\{|0\rangle, |1\rangle\}$ basis.

3.2.2 Higher-dimensional probe states

3.2.2.1 Collective dephasing

To translate the formalism of individual dephasing of qubits to multiphoton states, we make use of the Jordan-Schwinger (JS) map [201] (see Appendix A3 for more details). As a result, it is useful to think of photons constituting the multiphoton states as rather distinguishable particles with spins i.e., bosons and the operations in a Mach-Zehnder interferometer (MZI) written in terms of the bosonic operators are thus considered as rotations of these particles acting on abstract spin space.

Using the above correspondence, as illustrated in (Fig. 2), the particles are made distinguished spatially by a parallel scheme of N particles going through a phase-shift operation followed by dephasing. If the k-th particle (photon) undergoes a phase-shift operation $\mathcal{U}_\phi^{(k)} = e^{-i\phi\sigma_z^{(k)}/2}$ acting on the spin space of k-th photon, then the state with N photons undergoes a phase-shift $\mathcal{U}_\phi^{\otimes N} = \bigotimes_{k=1}^{N} e^{-i\phi\sigma_z^{(k)}/2} = e^{-i\phi\sum_{k=1}^{N}\sigma_z^{(k)}/2} = e^{-i\phi\hat{J}_z}$, where $\sum_{k=1}^{N}\frac{\sigma_z^{(k)}}{2} = \frac{\sigma_z^{(1)}}{2}\otimes_{k=2}^{N}\mathbb{1}^{(k)} + \cdots + \otimes_{k=1}^{N-1}\mathbb{1}^{(k)}\otimes\frac{\sigma_z^{(N)}}{2} = \hat{J}_z$ is an operator acting on the total spin space of N photons. Now, the N photons could experience dephasing either individually (Eq. 3.7) as we have seen in Section 3.2.1 or collectively, where each photon experiences the *same* phase fluctuation (see Figure), and therefore the multiphoton state constituting the N photons must be averaged over these fluctuations as follows

$$\rho_{\phi,\Delta} = \Lambda_\Delta(\rho) = \int_{-\infty}^{\infty} d\phi' p_{\phi,\Delta}(\phi')\mathcal{U}_{\phi'}\rho\mathcal{U}_{\phi'}^\dagger \tag{3.9}$$

This is known as *collective dephasing*. If we consider a two mode multiphoton state with a fixed photon number N as the input $\rho = |\psi\rangle\langle\psi|$ with

$$|\psi\rangle = \sum_{n=0}^{N} c_n |n, N-n\rangle , \tag{3.10}$$

writing the phase-shift operation $\mathcal{U}_{\phi'} = e^{-i\phi'\hat{J}_z} = e^{-i\frac{\phi'}{2}(\hat{a}^\dagger\hat{a}-\hat{b}^\dagger\hat{b})}$, and using $p_{\phi,\Delta}(\phi')$ Eq. 3.9 evaluates to

$$\rho_{\phi,\Delta} = \sum_{n,m=0}^{N} c_{n,m} e^{-i\phi(n-m)-\frac{\Delta^2}{2}(n-m)^2} |n, N-n\rangle\langle m, N-m| \tag{3.11}$$

As we can see, the effect of phase diffusion causes an exponential erasing of the off-diagonal elements of $\rho_{\phi,\Delta}$. For our problem, we consider a phase-shift operation acting on mode a of the MZI with mode b unaffected: $\mathcal{U}_{\phi'} = e^{-i\phi'\hat{a}^\dagger\hat{a}} = e^{-i\phi'\hat{J}_z}$. The last equality is due to the fact that we deal with states with a fixed photon number N, and as a result, the phase-shift operation induced by $\hat{J}_z$ is the same as the single-mode phase shift, which can be seen by writing: $e^{-i\phi'\hat{a}^\dagger\hat{a}} = e^{-i\phi'\hat{J}_z} e^{-i\frac{\phi'}{2}\hat{N}}$, where $e^{-i\frac{\phi'}{2}\hat{N}}$ is an irrelevant phase factor and $\hat{N} = \hat{a}^\dagger\hat{a} + \hat{b}^\dagger\hat{b}$ is the total photon number operator.

Physical interpretation: Combining the physical picture we provided for the individual dephasing channel as a scattering event between the system and particles of the environment and its extension to collective dephasing, we derive the following interpretation of phase diffusion of multiphoton states. In an MZI, the photons interact with the mirror changing its position: $\hat{x}_E = \frac{1}{\sqrt{2}}(\hat{a}_E^\dagger + \hat{a}_E)$ very slightly, and thus changing the effective path length and the relative phase of the photons. The individual dephasing picture tell us that this can be thought of as the mirror (a classical object) getting "scattered" by a photon with probability p, and changing its state from $|0\rangle_E$ i.e., ground state of a quantum harmonic oscillator to the states depending on the state of the photon (distinguishable particle) as dictated by the Eq. 3.1. The collective dephasing picture tell us that all the photons experience the same phase fluctuation. In the total space of system and environment, this interaction resulting from the coupling of $\hat{J}_z$ and $\hat{x}_E$ yields following output state

$$|\Psi_{\phi,\Delta}\rangle_{SE} = e^{-i\phi\hat{J}_z} e^{i\sqrt{2}\Delta\hat{J}_z\hat{x}_E} |\psi\rangle_S |0\rangle_E , \tag{3.12}$$

where $|\psi\rangle_S$ is initial state of the system given by Eq. 3.10. Making of use of the ground state wave function: ${}_E\langle x|0\rangle_E = \frac{1}{\pi^{1/4}} e^{-x^2/2}$, Eq. 3.11 is thus obtained as a result of tracing out the mirror degrees of freedom as follows

$$\mathrm{Tr}_E(|\Psi_{\phi,\Delta}\rangle\langle\Psi_{\phi,\Delta}|) = \int_{-\infty}^{\infty} dx\, {}_E\langle x|\Psi_{\phi,\Delta}\rangle\langle\Psi_{\phi,\Delta}|x\rangle_E = \rho_{\phi,\Delta} \tag{3.13}$$

3.3 Towards a comprehensive assessment of information

The performance of any metrological scheme is directly related to the amount of information one can obtain about the parameters. It involves two main components namely: (i) the measurement and (ii) the probe states, although, we keep in mind that the estimated parameters must also be uncorrelated. Until now, there exists numerical methods to obtain both the optimal measurements and the probe states for general problems. However, translating these into practically implementable set ups, in particular the optimal measurements is much harder or sometimes even impossible.

Subsequently, the actual estimation of the parameter requires post-processing of the measurement outcomes (see Section 2.1.2.5). Moreover, the numerical methods themselves become much tedious depending on the number of parameters and the dimensions of the probe state. Owing to these reasons, it is much easier to work with the fundamental bounds such as the CRB and the QCRB, as one can always think of them as the "asymptotic performance" of the optimal measurement and estimators that could be practically realized in the future. Therefore, in the context of assessing the information extraction, one could define figures of merit based on the CRB and the QCRB. Specifically, in our problem, we consider the joint-estimation of phase and phase diffusion, and define figures of merit in a two-fold, comprehensive manner quantifying: (i) the *information extraction* of the measurement and (ii) the *information content* of the probe states. As stated before, these measures should depend on the number of parameters and the dimensions of the probe states. In our case, as we will always deal with a two parameter estimation, we vary the latter i.e., we investigate the joint-precision limits of our problem for two dimensional probes (qubits) and a class of two-mode multiphoton states. Vidrighin et al. [34] formulated an informational trade-off relation holding for qubits and separable measurements, which will use as a benchmark to gauge the performance of our measurement on higher order multiphoton states.

3.4 Figures of merit

3.4.1 Information extraction

Given p parameters, the information extraction of a measurement M on a probe state $\rho_{\vec{\theta}}$ can be defined relative to the information extraction of the optimal measurement. This is captured by the following quantity involving the FIM and the QFIM

$$\Upsilon = \mathrm{tr}(F_C F_Q^{-1}) \tag{3.14}$$

For a two parameter estimation, in the absence of estimator correlations i.e., $F_{C(Q)\,i,j} = 0$, $i \neq j$, Υ simplifies to just a sum of the ratios of the FI and the QFI for each parameter

$$\Upsilon = \frac{F_{C\,1,1}}{F_{Q\,1,1}} + \frac{F_{C\,2,2}}{F_{Q\,2,2}} \tag{3.15}$$

3.4.1.1 Information trade-off relation for two-dimensional probes

The following information trade-off relation holds for two-dimensional probes and separable measurements which we refer to as the Single Qubit Bound (SQB).

$$\Upsilon \leq 1 \tag{3.16}$$

In the following, we show that the off-diagonal elements of the FIM and the QFIM vanishes and present the proof of Eq. 3.16

We consider a qubit in the Bloch sphere by letting $\alpha = \cos\theta/2$ and $\beta = \sin\theta/2$. Thus, Eq. 3.8 leads to

$$\tilde{\rho}_{\phi,\Delta} = \begin{bmatrix} \cos^2\frac{\theta}{2} & \cos\frac{\theta}{2}\sin\frac{\theta}{2}e^{-i\phi-\frac{\Delta^2}{2}} \\ \cos\frac{\theta}{2}\sin\frac{\theta}{2}e^{i\phi-\frac{\Delta^2}{2}} & \sin^2\frac{\theta}{2} \end{bmatrix} \tag{3.17}$$

A general 2D rank-1 POVM parametrized by θ_i, χ_i, and n_i for the i-th outcome acting on $\tilde{\rho}_{\phi,\Delta}$ is represented as

$$\Pi_i = n_i \begin{bmatrix} \cos^2\frac{\theta_i}{2} & \cos\frac{\theta_i}{2}\sin\frac{\theta_i}{2}e^{-i\chi_i} \\ \cos\frac{\theta_i}{2}\sin\frac{\theta_i}{2}e^{i\chi_i} & \sin^2\frac{\theta_i}{2} \end{bmatrix} \tag{3.18}$$

with $0 < n_i < 1$, $0 < \theta_i < \pi$, and $0 < \chi_i < 2\pi$. As for any valid POVM, $\Pi_i \geq 0$ and the completeness condition $\sum_i \Pi_i = \mathbb{1}$ reduces to the following set of equations

$$\sum_i n_i = 2 \tag{3.19a}$$

$$\sum_i n_i \cos\theta_i = 0 \tag{3.19b}$$

$$\sum_i n_i \sin\theta_i \sin\chi_i = 0 \tag{3.19c}$$

$$\sum_i n_i \sin\theta_i \cos\chi_i = 0 \tag{3.19d}$$

The corresponding probability distribution reads

$$p_{\phi,\Delta,\theta}(n_i,\theta_i,\chi_i) = \mathrm{Tr}(\tilde{\rho}_{\phi,\Delta}\Pi_i) = \frac{n_i}{2}\left(1 + \cos\theta\cos\theta_i + e^{-\frac{\Delta^2}{2}}\sin\theta\sin\theta_i\cos(\chi_i - \phi)\right) \tag{3.20}$$

The off-diagonal elements of the FIM are found to be

$$\begin{aligned} F_{C\,1,2} = F_{C\,2,1} &= \sum_i \frac{1}{\mathrm{Tr}(\tilde{\rho}_{\phi,\Delta}\Pi_i)}\left(\frac{\partial}{\partial\phi}\mathrm{Tr}(\tilde{\rho}_{\phi,\Delta}\Pi_i)\right)\left(\frac{\partial}{\partial\Delta}\mathrm{Tr}(\tilde{\rho}_{\phi,\Delta}\Pi_i)\right) \\ &= \sum_i \frac{n_i\Delta e^{-\Delta^2}\sin^2\theta\sin^2\theta_i\sin(2(\phi-\chi_i))}{4(1+\cos\theta\cos\theta_i + e^{-\frac{\Delta^2}{2}}\cos(\chi_i-\phi)\sin\theta\sin\theta_i)} \end{aligned} \tag{3.21}$$

Suppose for a POVM with k outcomes, one can have k equally spaced values each from the intervals: $n_i \in (0,1)$, $\theta_i \in (0,\pi)$, and $\chi_i \in (0,2\pi)$. For values of θ, θ_i and n_i in the respective intervals, the values of χ_i can be chosen symmetrically about ϕ i.e., for each projector with $\chi_i = \phi + \delta_i$, there is a corresponding projector with $\chi_i = \phi - \delta_i$. Furthermore, the presence of an odd function i.e., $\sin(2(\chi_i - \phi))$, in the numerator of the summand in Eq. 3.21 makes the contribution of such pairs of projectors to the summation zero. Therefore, for this POVM we get $F_{C\,1,2} = F_{C\,2,1} = 0$. For example, if $k = 50$, Eq. 3.21 evaluates over 50 equally spaced values each for $n_i \in (0,1)$, $\theta_i \in (0,\pi)$, and $\chi_i \in [\phi - \pi/15, \phi + \pi/15]$ to zero $\forall\ \theta \in [0,\pi]$ and $\Delta \in [0,2]$.

Further analytical calculations show that the off-diagonal elements of the QFIM vanish

$$F_{Q\,1,2} = F_{Q\,2,1} = \mathrm{Re}(\mathrm{Tr}(\tilde{\rho}_{\phi,\Delta}L_\phi L_\Delta)) = 0 \tag{3.22}$$

As a result of Eqs. 3.21 and 3.22, the FIM and the QFIM for this problem are diagonal and indeed, the information extraction is given by Eq. 3.15.

Now, the diagonal FIM elements are found to be

$$F_{C\,1,1} = \sum_i \frac{1}{\mathrm{Tr}(\tilde{\rho}_{\phi,\Delta}\Pi_i)}\left(\frac{\partial}{\partial\phi}\mathrm{Tr}(\tilde{\rho}_{\phi,\Delta}\Pi_i)\right)^2 = \sum_i \frac{n_i e^{-\Delta^2}\sin^2\theta\sin^2\theta_i\sin^2(\chi_i-\phi)}{2(1+\cos\theta\cos\theta_i+e^{-\frac{\Delta^2}{2}}\cos(\chi_i-\phi)\sin\theta\sin\theta_i)} \tag{3.23}$$

$$F_{C\,2,2} = \sum_i \frac{1}{\mathrm{Tr}(\tilde{\rho}_{\phi,\Delta}\Pi_i)}\left(\frac{\partial}{\partial\Delta}\mathrm{Tr}(\tilde{\rho}_{\phi,\Delta}\Pi_i)\right)^2 = \sum_i \frac{n_i\Delta^2 e^{-\Delta^2}\sin^2\theta\sin^2\theta_i\cos^2(\chi_i-\phi)}{2(1+\cos\theta\cos\theta_i+e^{-\frac{\Delta^2}{2}}\cos(\chi_i-\phi)\sin\theta\sin\theta_i)} \tag{3.24}$$

The diagonal QFIM elements are found to be

$$F_{Q\,1,1} = e^{-\Delta^2}\sin^2\theta \tag{3.25}$$

$$F_{Q\,2,2} = \frac{\Delta^2\sin^2\theta}{e^{\Delta^2}-1} \tag{3.26}$$

From Eq. 3.15, we obtain

$$\begin{aligned}\Upsilon = \sum_i \Bigg[&\frac{n_i\sin^2\theta_i\sin^2(\chi_i-\phi)}{2(1+\cos\theta\cos\theta_i+e^{-\frac{\Delta^2}{2}}\cos(\chi_i-\phi)\sin\theta\sin\theta_i)} \\ &+\frac{n_i(1-e^{-\Delta^2})\sin^2\theta_i\cos^2(\chi_i-\phi)}{2(1+\cos\theta\cos\theta_i+e^{-\frac{\Delta^2}{2}}\cos(\chi_i-\phi)\sin\theta\sin\theta_i)}\Bigg]\end{aligned} \tag{3.27}$$

$$= \sum_i \frac{n_i(\sin^2\theta_i\sin^2(\chi_i-\phi)+(1-e^{-\Delta^2})\sin^2\theta_i\cos^2(\chi_i-\phi))}{2(1+\cos\theta\cos\theta_i+e^{-\frac{\Delta^2}{2}}\cos(\chi_i-\phi)\sin\theta\sin\theta_i)} \tag{3.28}$$

$$= \sum_i \frac{n_i(\sin^2\theta_i\sin^2\theta-e^{-\Delta^2}\sin^2\theta_i\sin^2\theta\cos^2(\chi_i-\phi))}{2(1+\cos\theta\cos\theta_i+e^{-\frac{\Delta^2}{2}}\cos(\chi_i-\phi)\sin\theta\sin\theta_i)\sin^2\theta}, \tag{3.29}$$

where we have multiplied the numerator and the denominator by $\sin^2\theta$ and expanded out the numerator.

Using the identity: $(1+\cos\theta_i\cos\theta)^2-\sin^2\theta_i\sin^2\theta = (\cos\theta_i+\cos\theta)^2 \geq 0$, we get:

$$\sin^2\theta_i\sin^2\theta \leq (1+\cos\theta_i\cos\theta)^2 \tag{3.30}$$

Additionally, we note that since the L.H.S and the numerator of Eq. 3.29: $\sin^2\theta_i\sin^2\theta(1-e^{-\Delta^2}\cos^2(\chi_i-\phi))$ are both positive, the denominator must also be positive. Therefore, in Eq. 3.30, we subtract $e^{-\Delta^2}\sin^2\theta_i\sin^2\theta\cos^2(\chi_i-\phi))$ and divide by $\frac{2}{n_i}(1+\cos\theta\cos\theta_i+e^{-\frac{\Delta^2}{2}}\cos(\chi_i-\phi)\sin\theta\sin\theta_i)\sin^2\theta$ on both sides to arrive at

$$\begin{aligned}&\sum_i \frac{n_i(\sin^2\theta_i\sin^2\theta-e^{-\Delta^2}\sin^2\theta_i\sin^2\theta\cos^2(\chi_i-\phi))}{2(1+\cos\theta\cos\theta_i+e^{-\frac{\Delta^2}{2}}\cos(\chi_i-\phi)\sin\theta\sin\theta_i)\sin^2\theta} \\ &\leq \sum_i \frac{n_i[(1+\cos\theta_i\cos\theta)^2-e^{-\Delta^2}\sin^2\theta_i\sin^2\theta\cos^2(\chi_i-\phi)]}{2(1+\cos\theta\cos\theta_i+e^{-\frac{\Delta^2}{2}}\cos(\chi_i-\phi)\sin\theta\sin\theta_i)\sin^2\theta}\end{aligned} \tag{3.31}$$

This simplifies to

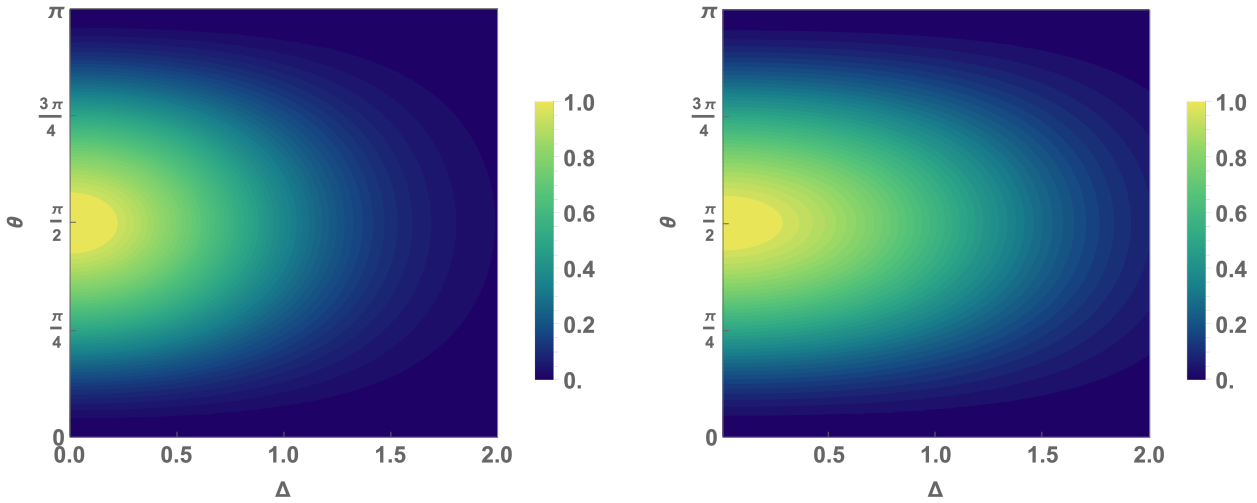

FIGURE 3.2: (a) Contour plot of $F_{Q\,1,1}$ versus Δ and θ and (b) Contour plot of $F_{Q\,2,2}$ versus Δ and θ.

$$\sum_i \frac{n_i(\sin^2\theta_i \sin^2\theta - e^{-\Delta^2}\sin^2\theta_i \sin^2\theta\cos^2(\chi_i-\phi))}{2(1+\cos\theta\cos\theta_i + e^{-\frac{\Delta^2}{2}}\cos(\chi_i-\phi)\sin\theta\sin\theta_i)\sin^2\theta} \leq \sum_i \frac{n_i}{2\sin^2\theta}[(1+\cos\theta_i\cos\theta) - e^{-\frac{\Delta^2}{2}}\sin\theta_i\sin\theta\cos(\chi_i-\phi)] \tag{3.32}$$

Making use of Eqs. 3.19c to evaluate the summation we get,

$$\Upsilon \leq \csc^2\theta \tag{3.33}$$

However, since always $\Upsilon \leq 2$ and $\csc^2\theta \in [1,\infty)$, we get: $\Upsilon \leq 2$, which is not a useful bound. A more informative bound can be obtained by comparing the information extraction of the POVM with the optimal state which corresponds to $\theta = \frac{\pi}{2}$ at which the QFI expressions (Eqs. 3.25 and 3.26) are maximized (see Figs. 3.2a and 3.2b).

The optimal state lies on the equator of the Bloch sphere (Fig. 3.3).

Therefore, Eq. 3.33 becomes

$$\Upsilon \leq 1 \tag{3.34}$$

This inequality is saturated when the measurement operators and the probe state both lie on the equator of the Bloch sphere i.e., when $\theta_i = \theta = \pi/2\ \forall\, i$, $\Upsilon = 1$.

3.4.2 Information availability

To capture the metrological resourcefulness of the probe state $\rho_{\phi,\Delta}$, we include another figure of merit based on the QCRB. Unlike the information extraction figure of merit, this is an absolute quantity for the joint information content of the probe state.

Why do we need this figure of merit? We note that high information extraction inferred through Υ does not necessarily mean that we gain more knowledge about the parameters. This is because of the relative character of Υ: one cannot distinguish states with low information content

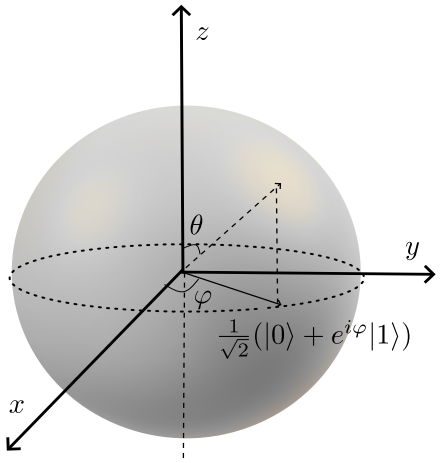

FIGURE 3.3: Equatorial states of a qubit in the Bloch sphere.

from higher ones, as both can point to high efficiencies. Therefore, alternatively one can also define: $\Upsilon = \mathrm{Tr}(F_C^{-1})$ as an absolute figure. However, since we are interested to see the violation of the the SQB for higher-dimensional probes, we work with $\Upsilon = \mathrm{Tr}(F_C F_Q^{-1})$ alongside Σ^2. Thanks to the available numerical methods [202] to obtain the optimal probe state for each parameter or for both parameters [177], a benchmark to the resourcefulness of the chosen probe state can still be made. However, the computation of the optimal states is beyond the scope of this thesis mainly due to the fact that we are interested in practically implementable probe states and a direct implementation of the optimal states (if computed) in experiments is not clear. The QCRB for our problem reads

$$\mathrm{tr}(W\mathrm{Cov}) \geq \mathrm{tr}(WF_Q^{-1}) \tag{3.35}$$

Assuming equal weights for ϕ and Δ, we have: $W = \mathbb{1}$. Thus,

$$\mathrm{Var}(\tilde{\phi}) + \mathrm{Var}(\tilde{\Delta}) \geq (F_{Q\,1,1})^{-1} + (F_{Q\,2,2})^{-1} \tag{3.36}$$

Note that when $F_{Q\,1,2} = F_{Q\,2,1} = 0$, $(F_Q^{-1})_{1,1} + (F_Q^{-1})_{2,2} = (F_{Q\,1,1})^{-1} + (F_{Q\,2,2})^{-1}$.

As a result, our figure of merit for information availability will be the sum of the inverse of the QFI for ϕ and Δ.

$$\Sigma^2 = (F_{Q\,1,1})^{-1} + (F_{Q\,2,2})^{-1} \tag{3.37}$$

3.5 Evaluation of information figures of merit for higher-dimensional probes

As one can see from the trade-off relation Eq. 3.16, the performance of the separable measurements on single qubit states are limited. Thus, as we have hinted earlier in Section 3.3, one may be interested to see the effects of increasing the dimension of the probe states on the figures of merit given that the number of parameters always remain fixed. More precisely, we are interested to see if the trade-off relation can be surpassed by such higher-order states. Besides, we also investigate their joint-information availability. These objectives will be explored in this section, which forms

the core result of our paper [185]. Additionally, one can also expect the bound to be violated for collective measurements (see Section 2.1.4.3).

3.5.1 Generalized Holland-Burnett states

We turn toward photonic states, in particular, two-mode multiphoton states with a fixed photon number N. A familiar state belonging to this class that yields Heisenberg-like scaling is *the Holland-Burnett (HB) state* [54] which is obtained by interfering Fock states of equal photon number on a balanced beamsplitter as follows (Fig. 3.4)

$$|\Psi^{\mathrm{HB}}(N/2,N/2)\rangle = \mathcal{U}_{\mathrm{BS}}\,|N/2,N/2\rangle = \sum_{n=0}^{N} \mathcal{C}_n(N)\,|n,N-n\rangle\,, \tag{3.38}$$

where $\mathcal{U}_{\mathrm{BS}}^{(1)} = \exp\left[-i\frac{\pi}{4}(a'^{\dagger}b' + b'^{\dagger}a')\right]$ is the balanced beamsplitter operation, i.e., with transmissivity $T = 1/2$ and a phase shift of $\pi/2$ between the transmitted and reflected beams, a' ($a'^{\dagger}$) as well as b' ($b'^{\dagger}$) are the annihilation (creation) operators corresponding to the input modes of the beamsplitter, $\mathcal{C}_n(N) = i^N\sqrt{2^{-N}\binom{N}{n}\binom{N}{\frac{N}{2}}}\;{}_2F_1\left(-N/2,-n;-N;2\right)$, and ${}_2F_1\left(a,b;c;z\right)$ is the hypergeometric function.

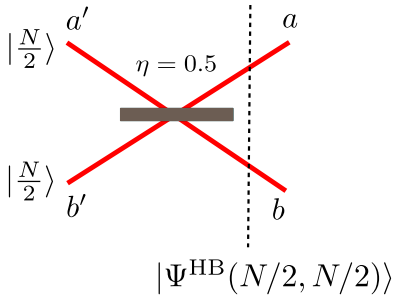

FIGURE 3.4: Creation of HB states by means of interfering $|N/2\rangle$ states on a 50:50 beamsplitter.

The HB states can be generalized to accommodate Fock states of unequal photon numbers i.e., $|k,N-k\rangle$ at the input to yield *the generalized Holland-Burnett (gHB) states* (Fig. 3.5). Therefore, we have

$$|\Psi^{\mathrm{gHB}}(k,N-k)\rangle = \mathcal{U}_{\mathrm{BS}}\,|k,N-k\rangle = \sum_{n=0}^{N} \mathcal{C}_n(N,k)\,|n,N-n\rangle\,, \tag{3.39}$$

where $\mathcal{C}_n(N,k) = (-1)^k\sqrt{2^{-N}\binom{N}{k}\binom{N}{n}}\;{}_2F_1\left(-k,-n;-N;2\right)$ are referred to as the Kravchuk coefficients [203]. Comparing with the general input states Eq. 3.10, $c_n = \mathcal{C}_n(N,k)$.

For example, the initial state $|1\rangle_a\,|1\rangle_b$ is a mode-separable state and the action of the beamsplitter creates the HB state: $\mathcal{U}_{\mathrm{BS}}^{(1)}\,|1\rangle_a\,|1\rangle_b = |\Psi^{\mathrm{HB}}(1,1)\rangle$ which is mode-entangled. This is because the beamsplitter is an entangling operation on the modes. However, the state $|1\rangle_a\,|1\rangle_b$ in the particle representation (see Appendix A2) reads: $\frac{1}{\sqrt{2}}(|a\rangle_1\,|b\rangle_2 + |b_1\rangle\,|a\rangle_2)$ which is particle-entangled. Moreover, as seen in Section 3.2.2.1, with respect to the Jordan map, the beamsplitter is a separable operation on the particles i.e., it locally rotates each photon around the x axis by $\Pi/2$

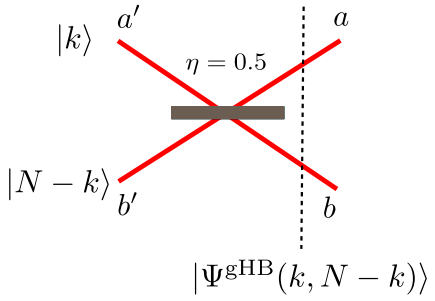

FIGURE 3.5: Creation of gHB states by means of interfering states $|k\rangle$ and $|N-k\rangle$ on a 50:50 beamsplitter.

and thus, does not change the initial particle entanglement. Therefore, in general, the HB state $|\Psi^{\mathrm{HB}}(N/2, N/2)\rangle$ contains *both* mode and particle entanglement. On the other hand, if we consider the state $|0\rangle_a |2\rangle_b$ which is also mode-separable, $\mathcal{U}_{\mathrm{BS}}^{(1)} |0\rangle_a |2\rangle_b = |\Psi^{\mathrm{gHB}}(0, 2)\rangle$ is mode-entangled. However, in the particle representation, $|0\rangle_a |2\rangle_b$ reads $|b\rangle_1 |b\rangle_2$ which is particle-separable since the action of the beamsplitter preserves the particle-separability of the state. Therefore, in general, it follows that gHB state $|\Psi^{\mathrm{gHB}}(0, N)\rangle$ is mode-entangled but particle-separable. As a consequence, strategies that include entanglement between the modes, particles or a combination of both can offer quantum enhancement in multiparameter quantum metrology [204].

Why non-Gaussian probes? Interferometers designed to be robust against noise—such as the one used in LIGO—typically rely on Gaussian states, in particular a combination of coherent and squeezed vacuum states [2, 205]. In our work, however, we investigate the robustness of two-mode Fock states. Low-photon-number Fock states are especially attractive because they are relatively easy to prepare (see Chapter 1). While the sensitivities and noise robustness of Gaussian states have often been compared with those of non-Gaussian states [206], more sophisticated Fock states, which benefit from both mode and particle entanglement, may offer superior robustness to noise than their Gaussian counterparts.

3.5.2 Phase diffused gHB states

As for any theoretical modeling of an experimental implementation, photonic losses must be accounted for, and hence, we model these losses with fictitious beamsplitter of transmissivity η_a and η_b corresponding to the respective output modes a and b of the beamsplitter. We note that the loss channel commutes with the phase-shift operation $\mathcal{U}_{\phi'} = e^{-i\phi'\hat{a}^\dagger\hat{a}}$. We will revisit this fact in more details along with the characterization of the photon-loss channel in Sections 4.2 and 4.2.1 of Chapter 4. The output gHB state reads

$$\begin{aligned}\rho_{\phi,\Delta}^{\mathrm{gHB\,(L)}}(k, N-k) &= \Lambda_\Delta(\rho_{\phi'}^{\mathrm{gHB\,(L)}}(k, N-k)) \\ &= \int_{-\infty}^{\infty} d\phi' p_{\phi,\Delta}(\phi') \mathcal{U}_{\phi'} \rho^{\mathrm{gHB\,(L)}}(k, N-k) \mathcal{U}_{\phi'}^\dagger,\end{aligned} \tag{3.40}$$

where $\rho^{\mathrm{gHB\,(L)}}$ is the loss-incorporated input gHB state given by

$$\rho^{\mathrm{gHB\,(L)}}(k, N-k) = \sum_{p=0}^{N} \sum_{q=0}^{N-p} \sum_{n,m=p}^{N-q} \mathcal{C}_{n,m,p,q}^{(\mathrm{L})}(N, k) \, |n-p, N-n-q\rangle \langle m-p, N-m-q| \,, \tag{3.41}$$

where $\mathcal{C}^{(\mathrm{L})}_{n,m,p,q}(N,k) = \mathcal{C}_n(N,k)\mathcal{C}_m(N,k)\sqrt{B^n_{p,q}B^m_{p,q}}$ and
$B^n_{pq} = \binom{n}{p}\binom{N-n}{q}\eta_a^{n-p}(1-\eta_a)^p\eta_b^{N-n-q}(1-\eta_b)^q$ quantifies the reduction in the probability amplitude if p and q photons are lost from modes a and b respectively.

Explicitly, $\rho^{\mathrm{gHB}}_{\phi,\Delta}(k,N-k)$ is given by

$$\rho^{\mathrm{gHB}\,(\mathrm{L})}_{\phi,\Delta}(k,N-k) = \sum_{p=0}^{N}\sum_{q=0}^{N-p}\sum_{n,m=p}^{N-q}\mathcal{C}^{(\mathrm{L})}_{n,m,p,q}(N,k)e^{-i\phi(n-m)-\frac{\Delta^2}{2}(n-m)^2} \times |n-p,N-n-q\rangle\langle m-p,N-m-q| \tag{3.42}$$

A schematic of this operation is shown in Fig. 3.8.

3.5.3 The double homodyne measurement

We assess the performance of the double homodyne measurement in terms of its information extraction. This is a Gaussian measurement i.e., it projects the probe state on to Gaussian state-like projectors. Although, it is standard to use such a measurement alongside Gaussian states, here we use to it on non-Gaussian states like the HB and the gHB states. In terms of practical deployment, it demonstrates higher efficiency in non-cryogenic conditions and has high noise rejection. In the following, we provide concise summary of this measurement based on the supplemental material of [34].

The measurement scheme involves two homodyne measurements of the output field quadratures $\hat{x}$ and $\hat{p}$. As a result, it is a continuous variable measurement complementary to the photon counting measurements which involves the measurement of discrete variables. The quadrature operator is parametrized by the phase φ as $\hat{x}(\varphi) = \frac{1}{2}(\hat{a}e^{-i\varphi} + \hat{a}^\dagger e^{i\varphi})$, and it is controlled by the phase φ_l of the local oscillator, a strong coherent state that interferes with one of the modes of the output state. The eigenstates of the quadrature operator can be written in the photon number basis as follows [207]

$$|x,\varphi\rangle = \pi^{-1/4}e^{-x^2/2}\sum_{n=0}^{\infty}\frac{e^{in\varphi}}{\sqrt{2^n n!}}\mathrm{H}_n(x)\,|n\rangle\,, \tag{3.43}$$

where $\mathrm{H}_n(x)$ are the Hermite polynomials. It is evident that the measurement of the output state involves projecting it onto coherent state-like projectors, thereby, constituting a Gaussian measurement. In reference to quantum metrology using quantum interferometers such as the Mach-Zehnder interferometers (MZI), the measurement will be assembled at the output of the MZI. Therefore, for the measurement of $\hat{x}$ ($\hat{x}(0)$) and $\hat{p}$ ($\hat{x}(\pi/2)$) operators with eigenvalues x and p respectively, we may write
$|\nu(x,p)\rangle = \mathcal{U}^{(\mathrm{o})}_{\mathrm{BS}}|x,p\rangle$, where $\mathcal{U}^{(\mathrm{o})}_{\mathrm{BS}}$ is the output balanced beamsplitter operation.

The corresponding POVM for the outcomes of quadrature measurements x and p reads $\Pi_{x,p} = |\nu(x,p)\rangle\langle\nu(x,p)|$. Defining the polar coordinates (r,χ), where $r = \sqrt{x^2+p^2}$ and $\chi = \tan^{-1}(p/x)$, and making use of Eq. 3.43, $|\nu(x,p)\rangle$ takes the following explicit form

$$|\nu^N_{pq}(r,\chi)\rangle = \sum_{n=p}^{N-q} g_{n,N-n}(r)e^{i(2n-N)\chi}\,|n-p,N-n-q\rangle \tag{3.44}$$

where $g_{n,N-n}(r) =$

$$\begin{cases} \sqrt{\dfrac{(n-p)!}{(N-n-q)!\pi}} e^{-r^2/2} r^{N-2n+p-q} (-1)^{N-2n+p-q} \mathrm{L}_{n-p}^{(N-2n+p-q)}(r^2) & \text{if } N-2n+p-q>0 \\ \sqrt{\dfrac{(N-n-q)!}{(n-p)!\pi}} e^{-r^2/2} r^{2n-N-p+q} \mathrm{L}_{N-n-q}^{(2n-N-p+q)}(r^2) & \text{if } N-2n+p-q<0 \\ \frac{e^{-r^2/2}}{\sqrt{\pi}} \mathrm{L}_{n-p}(r^2) & \text{if } N-2n+p-q=0 \end{cases}$$

with p and q lost photons included to reflect the lossy state on which the measurement is made, $\mathrm{L}_n^{(\alpha)}(r^2)$ are the generalized Laguerre polynomials, and $g_{n,N-n}(r)$ must satisfy $\int_0^\infty dr[g_{n,N-n}(r)]^2 r = 1/2\pi$.

The POVM $\Pi_{pq}^N(r,\chi) = |\nu_{pq}^N(r,\chi)\rangle \langle \nu_{pq}^N(r,\chi)|$ satisfies $\int_{\chi=0}^{2\pi} \int_{r=0}^{\infty} d\chi dr \Pi_{pq}^N(r,\chi) r = \mathbb{1}_{pq}$ i.e., integrating to identity matrix within the subspaces corresponding to the loss of p and q photons and $\Pi_{pq}^N(r,\chi) \geq 0$. The associated probability distribution with respect to the output state reads $p_{\phi,\Delta,\eta_a,\eta_b}(r,\chi) = \mathrm{Tr}(\rho_{\phi,\Delta}^{\mathrm{gHB\,(L)}} \Pi_{pq}^N(r,\chi))$

For the case of no photon losses i.e., $\eta_a = \eta_b = 1$, we work out the following closed-form expressions.

For the HB state: $\rho_{\phi,\Delta}^{\mathrm{HB}}(1,1)$:

$$p_{\phi,\Delta}(r,\chi) = \frac{e^{-r^2} r^4}{2\pi} (1 - e^{-2\Delta^2} \cos[2(\phi - 2\chi)]) \tag{3.45}$$

For the gHB state $\rho_{\phi,\Delta}^{\mathrm{gHB}}(0,2)$:

$$p_{\phi,\Delta}(r,\chi) = \frac{e^{-r^2} r^4}{4\pi} [1 + e^{-2\Delta^2} \cos[2(\phi - 2\chi)] - 4e^{-\frac{\Delta^2}{2}} \cos(\phi - 2\chi)(1 - r^{-2}) + 2(1 - r^{-2})^2] \tag{3.46}$$

For $N > 2$, the expressions become more cumbersome, and hence we focus on the simplest case $N = 2$. In following, we plot Eqs. 3.45 and 3.46 at different sets of values of ϕ, Δ, η_a, and η_b.

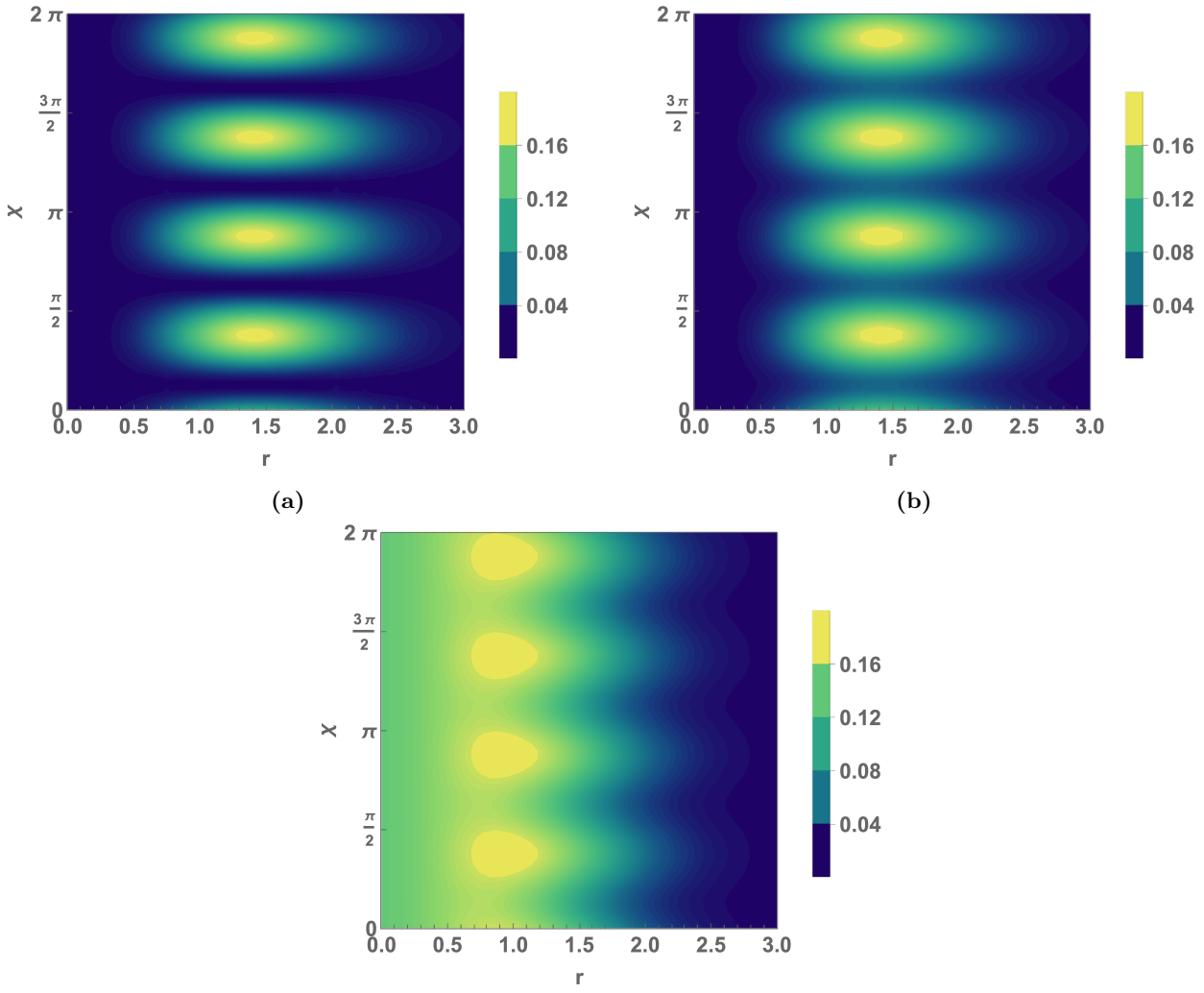

FIGURE 3.6: Contour plot of the double homodyne probability distribution for the HB state $\rho^{\mathrm{HB}}_{\phi,\Delta}(1,1)$ at three different degrees of noise: (a) $\phi = \pi/4$, $\Delta = 0.0001$, $\eta_a = 1$, and $\eta_b = 1$, (b) $\phi = \pi/4$, $\Delta = 0.5$, $\eta_a = 1$, and $\eta_b = 1$, and (c) $\phi = \pi/4$, $\Delta = 0.5$, $\eta_a = 0.5$, and $\eta_b = 0.5$

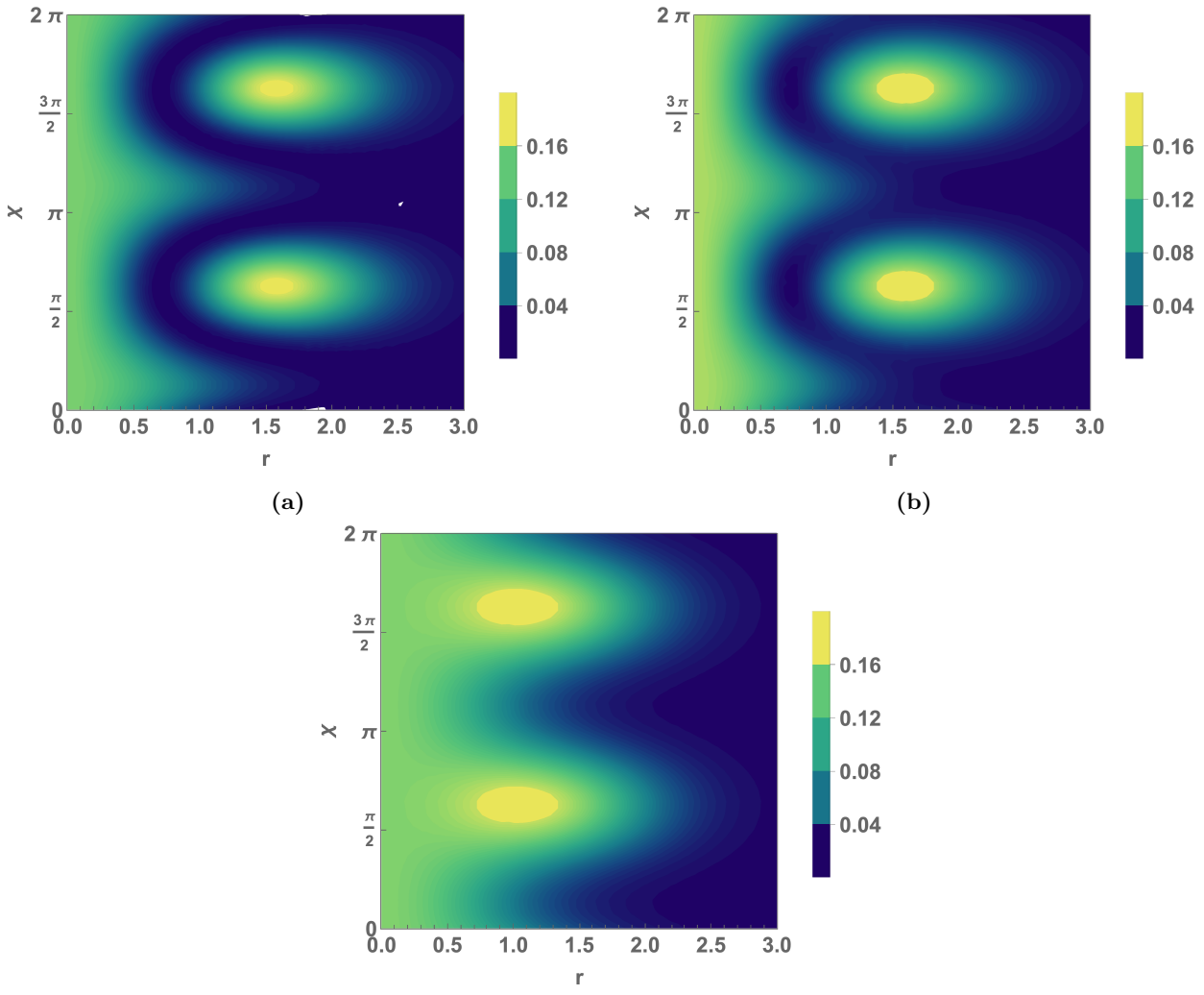

FIGURE 3.7: Contour plot of the double homodyne probability distribution for the gHB state $\rho^{\mathrm{gHB}}_{\phi,\Delta}(0,2)$ at three different degrees of noise: (a) $\phi = \pi/4$, $\Delta = 0.0001$, $\eta_a = 1$, and $\eta_b = 1$, (b) $\phi = \pi/4$, $\Delta = 0.5$, $\eta_a = 1$, and $\eta_b = 1$, and (c) $\phi = \pi/4$, $\Delta = 0.5$, $\eta_a = 0.5$, and $\eta_b = 0.5$

3.5.4 Metrological scheme

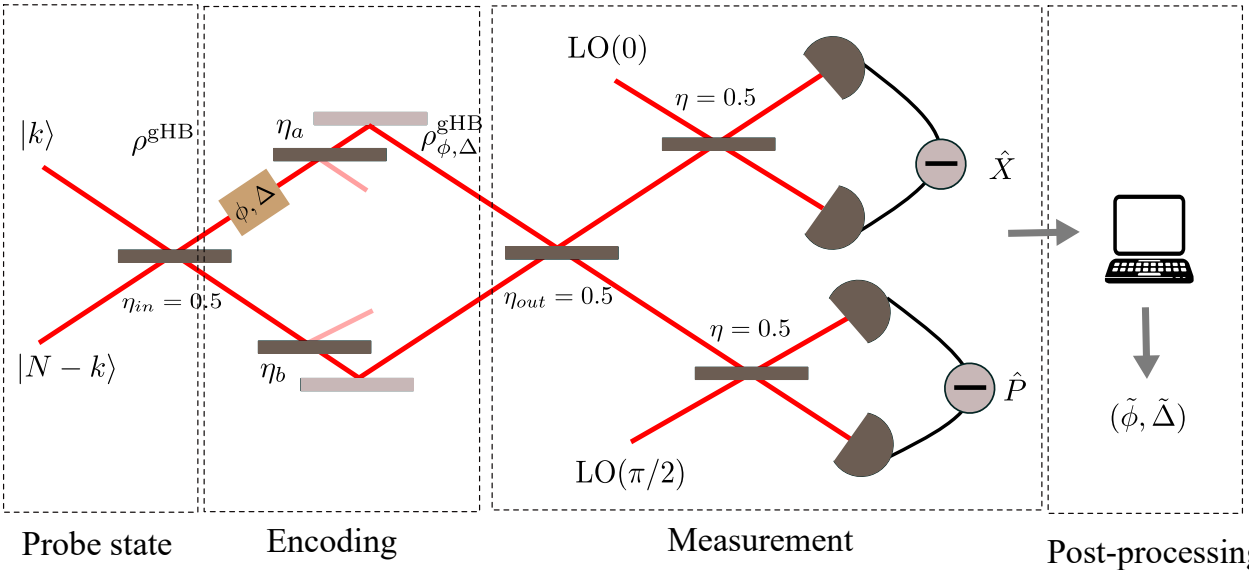

FIGURE 3.8: The theoretical scheme for the joint estimation of phase and phase diffusion involves a MZI followed by double homodyne detection. This setup provides the optimal strategy for the estimation of phase in the absence of phase diffusion with qubit probe states.

We are now ready to assemble the metrological scheme consisting of the gHB states and the double homodyne measurement in the MZI setup as seen in Fig. 3.8. We then tie it to tools from quantum estimation theory, more precisely, the figures of merits that we defined for a detailed analysis of the scheme's performance. As for any metrological scheme, we have the following four parts:

Input probe state: At the input of the interferometer, the gHB states are prepared as input probe states demonstrated in Section 1.4.2 of Chapter 1 and illustrated in using the input beamsplitter.

Encoding: For instance, a magnetic material or a dielectric of unknown magnetization or polarization respectively in the path of one of the interferometer arms, induces a relative phase-shift. As we have seen in Section 3.1, thermal fluctuations or radiation pressure could lead to the phase diffusive noise. Additionally, we assume known photon losses in both arms. These effects are collectively captured by Eq. 3.42

Measurement: The two modes of the encoded state are combined at the output beamsplitter to produce interference. The resulting state is then subjected to the double homodyne measurement by projecting the output state onto quadrature states.

Post-processing: From the double homodyne probability distribution, the computation of the log-likelihood function yields the MLE as described in 2.1.2.5.

3.5.5 FIM for the measurement

In the lossy case, the diagonal elements of the FIM read

$$F_{C\,1,1} = \int_{\chi=0}^{2\pi} \int_{r=0}^{\infty} \frac{(\partial_\phi p_{\phi,\Delta,\eta_a,\eta_b}(r,\chi))^2}{p_{\phi,\Delta,\eta_a,\eta_b}(r,\chi)} r dr d\chi, \tag{3.47}$$

$$F_{C\,2,2} = \int_{\chi=0}^{2\pi}\int_{r=0}^{\infty} \frac{(\partial_\Delta p_{\phi,\Delta,\eta_a,\eta_b}(r,\chi))^2}{p_{\phi,\Delta,\eta_a,\eta_b}(r,\chi)} r dr d\chi, \tag{3.48}$$

and the off-diagonal elements read

$$F_{C\,1(2),2(1)} = \int_{\chi=0}^{2\pi}\int_{r=0}^{\infty} \frac{(\partial_\phi p_{\phi,\Delta,\eta_a,\eta_b}(r,\chi)\partial_\Delta p_{\phi,\Delta,\eta_a,\eta_b}(r,\chi))}{p_{\phi,\Delta,\eta_a,\eta_b}(r,\chi)} r dr d\chi, \tag{3.49}$$

where $\partial_i = \frac{\partial}{\partial\alpha_i}$, $\vec{\alpha} = (\phi, \Delta, \eta_a, \eta_b)^\top$.

The double integrals are analytically hard to evaluate and only become more cumbersome with the inclusion of losses η_a, η_b and for higher dimensional states i.e., $N > 2$. Hence, for such states, we resort to a numerical computation making use of *Mathematica*'s `NIntegrate` function.

3.5.5.1 Phase independence of FI

Nevertheless, for the HB state: $\rho^{\mathrm{HB}}_{\phi,\Delta}(1,1)$, we make use of the probability distribution given by Eq. 3.45 and the diagonal elements are found to be

$$F_{C\,1,1} = \int_0^{2\pi} d\chi \frac{2e^{-2\Delta^2}\sin^2\left[2(\phi-2\chi)\right]}{\pi(e^{2\Delta^2}-\cos\left[2(\phi-2\chi)\right])} \tag{3.50}$$

$$F_{C\,2,2} = \int_0^{2\pi} d\chi \frac{8e^{-2\Delta^2}\Delta^2\cos^2\left[2(\phi-2\chi)\right]}{\pi(e^{2\Delta^2}-\cos\left[2(\phi-2\chi)\right])} \tag{3.51}$$

On substituting $\theta = \phi - 2\chi$, in Eqs. 3.50 and 3.51, we write

$$F_{C\,1,1} = \int_{-\phi}^{4\pi-\phi} d\theta \frac{e^{-2\Delta^2}\sin^2 2\theta}{\pi(e^{2\Delta^2}-\cos 2\theta)} \tag{3.52}$$

$$F_{C\,2,2} = \int_{-\phi}^{4\pi-\phi} d\theta \frac{8e^{-2\Delta^2}\Delta^2\cos^2 2\theta}{\pi(e^{2\Delta^2}-\cos 2\theta)} \tag{3.53}$$

Since the integrands are all periodic functions with a fundamental period of π, we can make use of the property for a function with period P: $\int_c^{P+c} dx f(x) = \int_0^P dx f(x)$ for any $c \in \mathbb{R}$, where $f(x+P) = f(x)$. Hence, for the period 4π,

$$F_{C\,1,1} = \int_0^{4\pi} d\theta \frac{e^{-2\Delta^2}\sin^2 2\theta}{\pi(e^{2\Delta^2}-\cos 2\theta)} \tag{3.54}$$

$$F_{C\,2,2} = \int_0^{4\pi} d\theta \frac{8e^{-2\Delta^2}\Delta^2\cos^2 2\theta}{\pi(e^{2\Delta^2}-\cos 2\theta)} \tag{3.55}$$

From Eqs. 3.54 and 3.55, it is clear that $F_{C\,1(2),1(2)}$ are independent of ϕ. In other words, the effect of ϕ is to shift the limits of the θ-integral by an amount $-\phi$ and due to the periodicity of the integrand in the range of integration, the area under the corresponding curves remains invariant under such shifts.

We have numerically verified that "phase-shift invariance" of the FI integral extends even to states with high photon numbers.

3.5.5.2 Off-diagonal elements:

Furthermore, for $N = 2$, the off-diagonal elements are

$$\begin{aligned} F_{C\,1,2} = F_{C\,2,1} &= \int_0^{2\pi} d\chi \frac{2e^{-2\Delta^2}\Delta \sin\left[4(\phi - 2\chi)\right]}{\pi(e^{2\Delta^2} - \cos\left[2(\phi - 2\chi)\right]} \\ &= \int_{-\phi}^{4\pi-\phi} d\theta \frac{2e^{-2\Delta^2}\Delta \sin 4\theta}{\pi(e^{2\Delta^2} - \cos 2\theta)} \\ &= \int_0^{4\pi} d\theta \frac{2e^{-2\Delta^2}\Delta \sin 4\theta}{\pi(e^{2\Delta^2} - \cos 2\theta)} \end{aligned} \tag{3.56}$$

The integrand has a fundamental period of $\pi/2$ and has local symmetry property over its period. One can also plot the corresponding integrands for even lossy states with $N > 2$, and graphically infer that the integral over $0 \leq \chi \leq 4\pi$ is zero in a straightforward manner. This implies that the symmetry properties of the integrand is trivially preserved for higher dimensional and lossy states.

3.5.6 QFIM for the probe state

Considering the vector: $\vec{\alpha} = (\phi, \Delta, \eta_a, \eta_b)^\top$ for compactness and writing $\rho_{\vec{\alpha}}^{\mathrm{gHB\,(L)}}$ in its eigenbasis $\rho_{\vec{\alpha}}^{\mathrm{gHB\,(L)}} = \sum_k \lambda_k(\vec{\alpha}) \left|e_k(\vec{\alpha})\right\rangle \left\langle e_k(\vec{\alpha})\right|$ and the SLDs:

$$L_\phi = \sum_{i,j} \frac{2\left\langle e_i(\vec{\alpha})\right| \partial_\phi \rho_{\vec{\alpha}} \left|e_j(\vec{\alpha})\right\rangle}{\lambda_i(\vec{\alpha}) + \lambda_j(\vec{\alpha})} \left|e_i(\vec{\alpha})\right\rangle \left\langle e_j(\vec{\alpha})\right| \tag{3.57}$$

$$L_\Delta = \sum_{i,j} \frac{2\left\langle e_i(\vec{\alpha})\right| \partial_\Delta \rho_{\vec{\alpha}} \left|e_j(\vec{\alpha})\right\rangle}{\lambda_i(\vec{\alpha}) + \lambda_j(\vec{\alpha})} \left|e_i(\vec{\alpha})\right\rangle \left\langle e_j(\vec{\alpha})\right| \tag{3.58}$$

the diagonal elements of the QFIM are given by

$$F_{Q\,1,1} = \mathrm{Tr}(\rho_{\vec{\alpha}}^{\mathrm{gHB\,(L)}} L_\phi^2) \tag{3.59}$$

$$F_{Q\,2,2} = \mathrm{Tr}(\rho_{\vec{\alpha}}^{\mathrm{gHB\,(L)}} L_\Delta^2) \tag{3.60}$$

In general, the diagonalization of $\rho_{\vec{\alpha}}^{\mathrm{gHB\,(L)}}$ to obtain the eigenvalues $\lambda_k(\vec{\alpha})$ and the eigenstates $\{|e_k(\vec{\alpha})\rangle\}$ is analytically not feasible.

Therefore, we use *Mathematica's* `Eigensystem` function to obtain a list of eigenvalues and eigenstates which is used to obtain the SLDs and then the QFIs.

3.5.6.1 Phase independence of QFI

The state in the Fock basis given by Eq. 3.42 under no losses, can be rewritten as

$$\rho_{\phi,\Delta}^{\mathrm{gHB}} = \sum_{n,m=0}^{N} \tilde{\mathcal{C}}_{n,m}(N,k,\Delta) \left|n, N-n\right\rangle_\phi \left\langle m, N-m\right|_\phi, \tag{3.61}$$

where we have absorbed the phase factor $e^{-i\phi(n-m)}$ into the orthonormal basis $\{|n, N-n\rangle\}$ to obtain a phase-dependent basis: $\{|n, N-n\rangle_\phi\}$ and

$\tilde{\mathcal{C}}_{n,m}(N,k,\Delta) = \mathcal{C}_n(N,k)\mathcal{C}_m(N,k)e^{-\frac{\Delta^2}{2}(n-m)^2}$. Also, note that we write $\rho^{\text{gHB}}_{\phi,\Delta}(k,N-k) \equiv \rho^{\text{gHB}}_{\phi,\Delta}$, omitting the explicit $(k,N-k)$ dependence henceforth.

In the phase-dependent basis, making use of Eq. 2.32 and the Hermiticity of the SLDs, we can write [144]

$$L_\phi = i \sum_{n,m=0}^{N} A_{n,m}(N,k,\Delta)\, |n,N-n\rangle_\phi \langle m,N-m|_\phi \tag{3.62}$$

$$L_\Delta = \sum_{n,m=0}^{N} B_{n,m}(N,k,\Delta)\, |n,N-n\rangle_\phi \langle m,N-m|_\phi\,, \tag{3.63}$$

where $A_{n,m}(N,k,\Delta) = -(n-m)\tilde{\mathcal{C}}_{n,m}(N,k,\Delta) \in \mathbb{R}$ and $B_{n,m}(N,k,\Delta) = -\Delta(n-m)^2\tilde{\mathcal{C}}_{n,m}(N,k,\Delta) \in \mathbb{R}$. Hence, $A_{n,m}(N,k,\Delta) = -A_{m,n}(N,k,\Delta)$ and $B_{n,m}(N,k,\Delta) = B_{m,n}(N,k,\Delta)$.

The QFIs are found to be

$$F_{Q\,1,1} = \text{Tr}(\text{Re}(\rho^{\text{gHB}}_{\phi,\Delta} L^2_\phi)) = -\sum_{n,n',m'} \tilde{\mathcal{C}}_{n,m'}(N,k,\Delta) A_{n,n'}(N,k,\Delta) A_{n',m'}(N,k,\Delta) \tag{3.64}$$

$$F_{Q\,2,2} = \text{Tr}(\text{Re}(\rho^{\text{gHB}}_{\phi,\Delta} L^2_\Delta)) = \sum_{n,n',m'} \tilde{\mathcal{C}}_{n,m'}(N,k,\Delta) B_{n,n'}(N,k,\Delta) B_{n',m'}(N,k,\Delta) \tag{3.65}$$

Thus, one can see that the QFIs are independent of ϕ and only depend on Δ. It is straightforward to generalize this analysis for the lossy state $\rho^{\text{gHB (L)}}_{\vec{\alpha}}$.

3.5.6.2 Off-diagonal elements

Due to the derivative of $\rho^{\text{gHB}}_{\phi,\Delta}$ with respect to the parameters, L_ϕ is purely imaginary, while L_Δ is purely real. Therefore, the off-diagonal elements vanish i.e.,

$$F_{Q\,1,2} = F_{Q\,2,1} = \text{Tr}(\text{Re}(\rho^{\text{gHB}}_{\phi,\Delta} L_\phi L_\Delta)) = 0 \tag{3.66}$$

3.5.6.3 Optimality of the double homodyne measurement for phase

Setting $\Delta = 0$ in Eq. 3.50, the double integral can be performed analytically, and we obtain

$$\begin{aligned} F_{C\,1,1} &= \int_{\chi=0}^{2\pi}\int_{r=0}^{\infty} dr d\chi \frac{2e^{-r^2-4\Delta^2} r^5 \sin^2\left[2(\phi-2\chi)\right]}{\pi(1-\cos\left[2(\phi-2\chi)\right])} \\ &= \int_{\chi=0}^{2\pi}\int_{r=0}^{\infty} dr d\chi \frac{4e^{-r^2} r^5}{\pi} \cos^2(\phi-2\chi) = 4 \end{aligned} \tag{3.67}$$

Using the formula for QFI for unitary models (Eq. 2.40), which is obtained as the variance of the generator of phase $\hat{a}^\dagger\hat{a}$, we obtain the QFI with the input state: $|\rho^{\text{gHB}}(1,1)\rangle$ (Eq. 3.39) as

$$
\begin{aligned}
F_{Q\,1,1} &= 4\mathrm{Var}(\hat{a}^\dagger\hat{a}) \\
&= 4\Big\{ \sum_{n,m=0}^{2} \mathcal{C}_m(2,k)\mathcal{C}_n(2,k)\,\langle m, 2-m|\,(\hat{a}^\dagger\hat{a})^2\,|n, 2-n\rangle \\
&- \Big[\sum_{n,m=0}^{2} \mathcal{C}_m(2,k)\mathcal{C}_n(2,k)\,\langle m, 2-m|\,\hat{a}^\dagger\hat{a}\,|n, 2-n\rangle \Big]^2 \Big\} \\
&= 4\Big\{ \sum_{n,m=0}^{2} \mathcal{C}_m(2,k)C_n(2,k)\,\langle m, 2-m|\,(\hat{a}^\dagger\hat{a} + (\hat{a}^\dagger)^2\hat{a}^2)\,|n, 2-n\rangle \\
&- \Big[\sum_{n,m=0}^{2} \mathcal{C}_m(2,k)C_n(2,k)\,\langle m, 2-m|\,\hat{a}^\dagger\hat{a}\,|n, 2-n\rangle \Big]^2 \Big\} \\
&= 4\Big\{ \underbrace{\sum_{n=0}^{2}(n+n(n-1))C_n(2,k)^2}_{2} - \Big[\underbrace{\sum_{n=0}^{2} nC_n(2,k)^2}_{1} \Big]^2 \Big\} \\
&= 4
\end{aligned}
\tag{3.68}
$$

where we have written $\hat{a}^\dagger\hat{a} = \hat{a}^\dagger\hat{a} + (\hat{a}^\dagger)^2\hat{a}^2$ making use of $[\hat{a}, \hat{a}^\dagger] = 1$ and $\hat{a}^\dagger\,|n\rangle = \sqrt{n+1}\,|n+1\rangle$, $\hat{a}\,|n\rangle = \sqrt{n}\,|n-1\rangle$.

From Eqs. 3.67 and 3.68, we have: $\frac{F_{C\,1,1}}{F_{Q\,1,1}} = 1$ implying that the double homodyne measurement is optimal for phase. In fact, this optimality for more general states has appeared in [34].

Additionally, an analytical expression in terms of N can be obtained for $F_{Q\,1,1}$ for a general gHB state is given by $N + 2k(N-k)$ [55]. From this expression, it is clear that the QFI is invariant under swapping the photons between the input two modes a' and b' i.e., $F_{Q\,1,1}(|\Psi^{\mathrm{gHB}}(k, N-k)\rangle) = F_{Q\,1,1}(|\Psi^{\mathrm{gHB}}(N-k, k)\rangle)$.

3.5.7 Application of the figures of merit

From the analysis of the previous section, we are ready to apply the figures of merit for our metrological scheme. In particular, the analysis of the off-diagonal elements, stipulates that the use of Υ (Eq. 3.37) and Σ^2 (Eq. 3.37) are justified.

3.5.7.1 Phase diffusion analysis

We begin with a comparative study on the information extraction of double homodyne measurement and the information availability considering the following input probe states: (i) the class of gHB states created by sending all N photons in one mode of the input beamsplitter: $|\Psi^{\mathrm{gHB}}(0, N)\rangle$ (ii) the HB states: $|\Psi^{\mathrm{HB}}(N/2, N/2)\rangle$, and (iii) the N00N states: $|\Psi^{\mathrm{N00N}}(N)\rangle = \frac{1}{\sqrt{2}}(|0, N\rangle + |N, 0\rangle)$. We note that, for a noiseless phase estimation, the $|\Psi^{\mathrm{gHB}}(0, N)\rangle$ state yields the shot-noise scaling (SNS), the HB state yields Heisenberg-like scaling [55], and the N00N state yields the Heisenberg scaling (HS) (see Section 1). As we mentioned earlier, the gHB states are particle-separable but mode-entangled but the HB and the N00N states are both particle and mode-entangled, and thus all of them have potential to offer quantum enhancement for the joint-estimation of phase and phase diffusion. At the same time, if we take into account the susceptibility of entanglement to noise, although the SNS can be surpassed, the HS is impossible to attain. This fact has been established using powerful mathematical tools to compute tight upper bounds to the QFI of output states in the

cases of photon losses, local dephasing, and phase diffusion [208, 209]. As a result, we never achieve HS for the estimation of Δ *per se*. Therefore, with the inclusion of photon losses and diffusion in our exposition, we expect to obtain reduced sensitivities but it is important to find out which states are least susceptible to noises. This will be at the crux of the following assessment where we incorporate regimes of noise to identify the most robust states. To this end, we assess the figures of merit with respect to the phase diffusion noise and consider equal known losses in both arms of the MZI: $\eta_a = \eta_b = \eta$.

For this problem, we find $[L_\phi, L_\Delta]$ and $\mathrm{Tr}(\rho^{\mathrm{gHB}}_{\phi,\Delta}[L_\phi, L_\Delta]) = 0$ (see Appendix A4), which implies that the QCRB coincides with the HCRB, and hence there exists a collective measurement such that $\Upsilon = 2$ (see Section 2.1.4.3). However, the deployment of collective measurements on asymptotically many copies of the probe state is experimentally changeling. Therefore, we evaluate the performance of the separable double homodyne measurement on our probe states keeping the qubit trade-off relation $\Upsilon \leq 1$ as the realistic benchmark.

Lastly, the advantage of the consideration of finite photon number states, as opposed to the indefinite photon number states, namely the squeezed states and the coherent states deployed in typical interferometers for quantum metrology, is the ease of engineering low photon number states. Therefore, we only consider such states and study their metrological yield.

Information extraction: The top row in Fig. 3.9 depicts the information extraction metric Υ as a function of the phase diffusion Δ for the lossless case in panel a), and for the case of 50% of losses in panel b). We have also marked the performance of equatorial qubit states at $\Upsilon = 1$ and the saturation value of the QCRB at $\Upsilon = 2$, which serve as benchmarks to asses the performance of our probe states. From panel a), we infer that the double homodyne measurement on the states: $|\Psi_{\mathrm{gHB}}(0, N)\rangle$ for $N = 4, 5, 6$, surpasses the SQB for all values of phase diffusive noise. For the chosen values of N, the value of Υ is noticeably higher than that of all qubit states. In fact, the higher the value of N, the closer to the saturation of the QCRB one can get (see Appendix A5), which illustrates the effect of using higher-dimensional probes on information extraction. The N00N states saturate the SQB since they can be reduced to two-dimensional subspaces with the computational basis: $\{|0, N\rangle, |N, 0\rangle\}$. Hence, for these states we can use Eq. 3.17 with $\phi \to N\phi$, $\Delta \to N\Delta$, and $\theta = \pi/2$. The curves obtained for the HB states fall below the N00N states in the grey area. Furthermore, the curves for gHB and HB states attain their asymptotic values for $\Delta > 1.2$.

Remarkably in panel b), we can find that even in the presence of 50% losses, the performance of the double homodyne measurement on $|\Psi_{\mathrm{gHB}}(0, N)\rangle$ states is still superior to that of HB and N00N states across all values of phase-diffusive noise. In contrast to panel a), the presence of losses significantly reduces the effectiveness of using the measurement on N00N states in comparison to HB states demonstrating the well-known susceptibility of the former to losses. Furthermore, among different partitions of N, the $|\Psi_{\mathrm{gHB}}(0, N)\rangle$ state yields the highest performance (see Appendix A6).

Information availability: The observations resulting from panels a) and b) are specific to the choice of double homodyne detection. However, it is also crucial to perform a measurement-independent analysis and identify the resourceful states by assessing their information content. In principle, the optimal measurements may be constructed from the SLDs of the respective parameters that fully exhaust the information content of the states. To this end, we utilize the quantity Σ^2 in the following.

The bottom row of Fig. 3.9 depicts Σ^2 for the lossless case – panel c), and for 50% of losses – panel d). From panel c), we conclude that Σ^2 for the $|\Psi_{\mathrm{gHB}}(0, N)\rangle$ states is lower than the corresponding bounds for the HB and the N00N states for diffusion values $\Delta > 0.6$. As a result, the $|\Psi_{\mathrm{gHB}}(0, N)\rangle$ states posses higher information about the parameters than the HB and the N00N states.

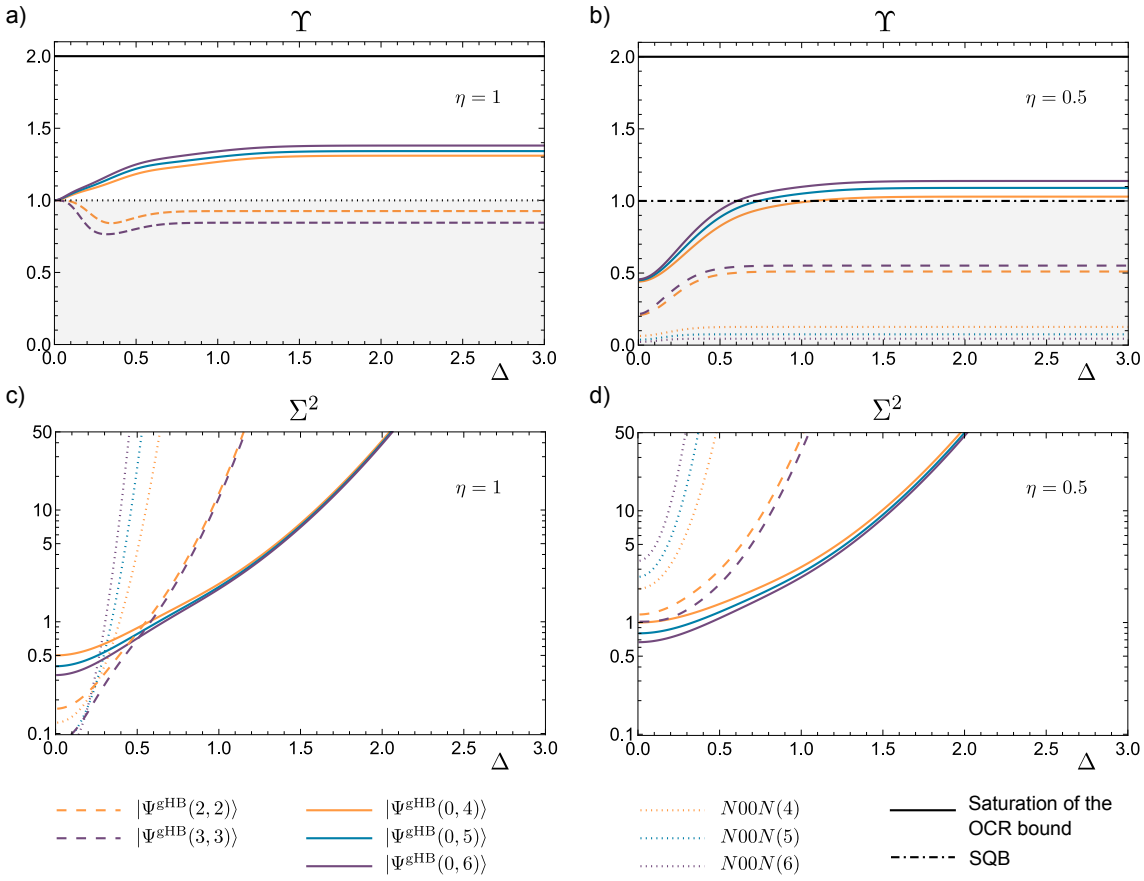

FIGURE 3.9: *Top row:* The trade-off quantity, considering the double homodyne measurement on gHB and N00N states, is plotted as a function of the phase diffusive parameter, Δ. The states with number of photons, $N = 4, 5, 6$, are shown. Panel a) represents the lossless case and panel b) corresponds to 50% photon losses. Note that the measurement extracts the highest amount of information about the parameters from the $|\Psi_{\mathrm{gHB}}(0, N)\rangle$ states across all values of Δ in both panels. *Bottom row:* The QCRB is plotted as a function of Δ for the same states considered in the top row, presented as a log plot. Panel c) illustrates the lossless case, while panel d) depicts the case with 50% photon losses. Note that, in panel c), the $|\Psi_{\mathrm{gHB}}(0, N)\rangle$ states possess the highest amount of information only for $\Delta > 0.6$. However, in panel d), they possess the highest amount of information for all values of Δ.

In panel d), with 50% photon losses, we observe that the $|\Psi_{\text{gHB}}(0,N)\rangle$ family of states retains higher information content than the HB and N00N states across all values of phase diffusive noise.

As a summary of our two-fold analysis, we infer that the joint estimation of phase and phase diffusion using the $|\Psi_{\text{gHB}}(0,N)\rangle$ family of states is robust to both phase diffusion and photon losses. This aligns with the performance of the double homodyne measurement in extracting information from these family of states for $\Delta > 0.6$.

3.5.7.2 Photon number analysis

We have seen from the phase diffusion analysis that the double homodyne measurement on the $|\Psi_{\text{gHB}}(0,N)\rangle$ achieves the highest performance in terms of both Υ and Σ^2. Nevertheless, this is a restricted set of probe states and thus, we expand this set to include states of the form: $|\Psi_{\text{gHB}}(k,N-k)\rangle$ for $k \neq 0$. More specifically, we explore the behavior of the family of gHB states created by partitioning k photons in one input of MZI and $N-k$ photons in the other. This would provide a comprehensive analysis of the precision limits of the joint estimation through the double homodyne measurement on various probe states within the gHB family. The results are presented in Fig. 3.10.

Information extraction: With this in mind, we compute Υ in the large diffusion region, i.e., for $\Delta > 1.2$, by arbitrarily setting $\Delta = 1.3$, where the values corresponding to all partitions of N attain saturation (see Appendix A6). In the top row of Fig. 3.10, we plot the trade-off quantity Υ with respect to the total input photons N for a fixed $k \in [0,6]$. We have analyzed the cases $\eta = 1$ in panel a) and $\eta = 0.5$ in panel b). As before, $\Upsilon = 1$ (SQB) and $\Upsilon = 2$ (maximal joint-sensitivity) are marked for references.

In panel a), we can immediately observe that the maximum violation of the SQB is demonstrated by the states with $k = 0$ among those with $k \in [0,6]$ for all values of N. While for other states, the violation of the SQB occurs at certain values of N. The occurrence of sharp points can be qualitatively understood as follows. We should notice first that our measurement strategy treats the two output modes of the MZI with equal weights: the measurement is essentially the same, up to a phase shift. Next, we refer to the curve highlighted in orange in Fig. 3.10 (a), corresponding to $k = 4$. For $N = 4$, all photons are delivered from one input. For a small phase $\phi \sim 0$, we would also obtain a similar output, with all photons emerging on the same arm. In these conditions, the measurement does extract information in an efficient way. Moreover, we note that the curve is plotted in the large diffusion region, yet the measurement still extracts information efficiently, showcasing once again the robustness of the probe state. As N is changed and more photons are added on the second input, we obtain the input photon configurations: $(4,1)$, $(4,2)$, and $(4,3)$ with a slight asymmetry between the modes. In such a case, our measurement, being fully symmetrical, does not second the quality of the probe, thus fails at resulting in optimized information. However, for $N = 8$, the state becomes a conventional HB state that shows complete symmetry between the two arms, and the measurement becomes efficient again [54]. Additionally, starting from $N = 9$ onwards, we retrieve the asymmetry as previously observed, but its impact becomes lower at higher values of N, where most of the energy is increasingly concentrated in the second mode. Under these conditions, Υ starts growing again and asymptotically approaches the curve for $k = 0$.

From panel b), we can infer that even in the presence of 50% photon losses, all the features similar to those observed in the lossless case are preserved. The only exception is that the double homodyne measurement on N00N states no longer saturates the SQB and performs much worse compared to the $|\Psi_{\text{gHB}}(k,N-k)\rangle$ family of states.

Information availability: We next investigate the metrological resourcefulness of our probe states

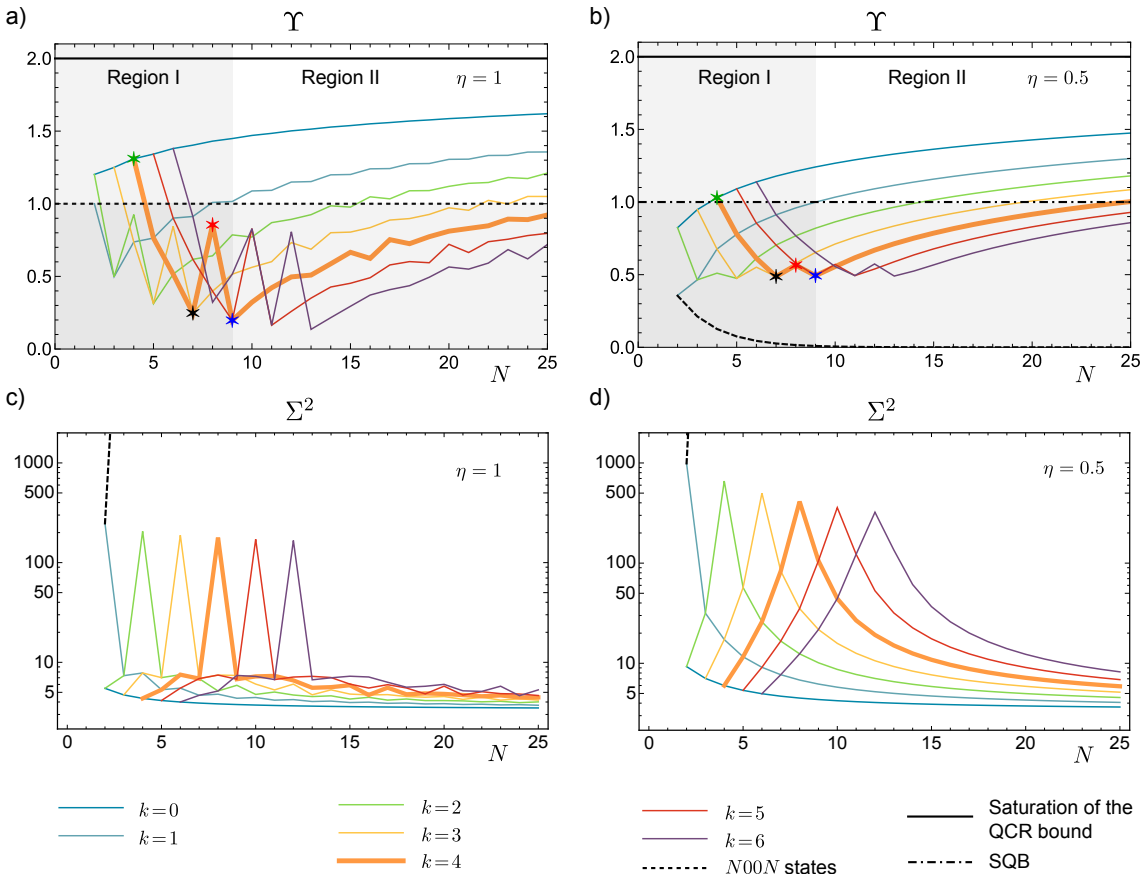

FIGURE 3.10: *Top row:* The trade-off quantity, considering the double homodyne measurement on the family of gHB states $|\Psi_{\mathrm{gHB}}(k, N-k)\rangle$; $k \in [0, 6]$, and N00N states, is plotted as a function of the number of photons, N. In the saturation region (i.e., $\Delta > 1.2$ in Fig. 3.9), the value $\Delta = 1.3$ is chosen. Panel a) represents the lossless case and panel b) corresponds to 50% photon losses. Note that the measurement extracts the highest amount of information from the family of gHB states with $k = 0$ across all values of N in both the panels. The plots for each value of k can be divided into two regions of distinct characteristics. For instance, for $k = 4$ (highlighted in orange), region I is characterized by the existence of sharp points corresponding to the states: $|\Psi_{\mathrm{gHB}}(4, 0)\rangle$ (green star), $|\Psi_{\mathrm{gHB}}(4, 3)\rangle$ (black star), $|\Psi_{\mathrm{gHB}}(4, 4)\rangle$ (red star), and $|\Psi_{\mathrm{gHB}}(4, 5)\rangle$ (blue star). However, region II is marked by steadily increasing curves with occasional numerical noise fluctuations. Note that this same behavior is also exhibited for other values of k. *Bottom row:* The QCRB is plotted as a function of N for the same states and the value of Δ considered in the top row, presented as a log plot. Note that the family of gHB states with $k = 0$ possess the highest amount of information for all values of N in both the panels.

and N00N states. In the bottom row of Fig. 3.10, we plot Σ^2 as a function of N, again by setting $\Delta = 1.3$ in panel c) ($\eta = 1$) and in panel d) ($\eta = 0.5$).

From panel c), we can infer that the value of Σ^2 for the $|\Psi_{\rm gHB}(k, N-k)\rangle$ states is lower than the corresponding bound for the N00N states across all values of N. Consequently, the information content of the $|\Psi_{\rm gHB}(k, N-k)\rangle$ states is higher than that of the N00N states. In particular, the maximum information content is possessed by the states with $k = 0$ among those with $k \in [0, 6]$ for all values of N. These curves show sharp features, similar to those in Fig. 3.10 (a). In order to illustrate their origin, we first reiterate that Σ^2 depends on the absolute values of the achievable uncertainties, and not on their value relative to the CRB as for Υ. Therefore, saturating the relative precision may not result in a reduced uncertainty when comparing different situations. For instance, refer to the curve for $k = 4$ (in orange): there is a peak in correspondence of $N = 8$, i.e., of the production of HB states. Given that the curves are plotted in the large diffusion region ($\Delta = 1.3$), the HB state offers lower joint-sensitivity than the neighboring gHB states at $N = 7$ and $N = 9$. If we consider $\eta = 1$, a closer inspection of the QFIs for ϕ and Δ reveals that $F_{Q\,1,1}$ at $N = 7$ and $N = 9$ is roughly 32 times larger than at $N = 8$. Similarly, $F_{Q\,2,2}$ at these values of N is about 11 times larger than at $N = 8$ (see Appendix A6). As a result, the total error at $N = 8$ exhibits a sudden jump. This feature further highlights the importance of Σ^2 i.e., although the information extraction from HB states is higher at the prescribed values of Δ and η, the information content itself is much lower. Therefore, the occurrence of peaks in the top and bottom rows, indicate two different aspects of information. Starting from $N = 9$ onward, we retrieve an asymmetric input photon configuration, and the information content or sensitivities of the states asymptotically approach those of $k = 0$. In panel d), for the case of 50% losses, we observe similar features as in panel c) further emphasizing the robustness of $|\Psi_{\rm gHB}(k, N-k)\rangle$ states to both phase diffusive noise and photon losses in comparison to the N00N states.

In summary, Fig. 3.10 underscores the impressive resilience of a broad class of gHB states, namely, the $|\Psi_{\rm gHB}(k, N-k)\rangle$ states for the joint estimation of phase and phase diffusion under highly noisy conditions. The corresponding observations made coincide with the performance of the double homodyne measurement in extracting information from these states with the exceptional case at $N = 2k$.

3.5.8 Phase and phase diffusion sensitivities of the probe states

In Fig. 3.11, we have plotted the individual QFIs for states with a specific photon number ($N = 4$) for a better picture of the characteristics inferred from Figs. 3.9 and 3.10. For ϕ and $\Delta \sim 0$, at $\eta = 1$ and $\Delta = 0$, the gHB state: $|\Psi^{\rm gHB}(0, 4)\rangle$ is at the SNS, the N00N state is at the HS, and the HB state is at the Heisenberg-like scaling. For $\Delta > 0.7$, regardless of the value of η, the mode and the particle entanglement of the HB and the N00N states becomes prone to noises and the sensitivity deteriorates below the SNS. However, in this regime, the $|\Psi^{\rm gHB}(0, 4)\rangle$ state maintains a higher sensitivity than the other two states for all the following values of Δ. These features are preserved even for higher photon numbers as seen in the previous section.

In Fig. 3.12, considering $N = 4$, we plot the individual QFIs for the partition $k = 1$ corresponding to the gHB state: $|\Psi^{\rm gHB}(1, 3)\rangle$ along with the HB and the N00N state. As indicated by the plot in the bottom row of Fig. 3.10, the state with $k = 1$, outperforms both the HB and the N00N states especially in the large diffusion region i.e., $\Delta > 1.2$. Therefore, although we know that the particle separable state with $k = 0$ shows the best performance, it is followed by the state with $k = 1$, which is both particle and mode-entangled. This is because in the particle representation:
$|1, 3\rangle \rightarrow \frac{1}{\sqrt{4}}(|a\rangle_1 |b\rangle_2 |b\rangle_3 |b\rangle_4 + |b\rangle_1 |a\rangle_2 |b\rangle_3 |b\rangle_4 + |b\rangle_1 |b\rangle_2 |a\rangle_3 |b\rangle_4 + |b\rangle_1 |b\rangle_2 |b\rangle_3 |a\rangle_4)$ (see Appendix A2).

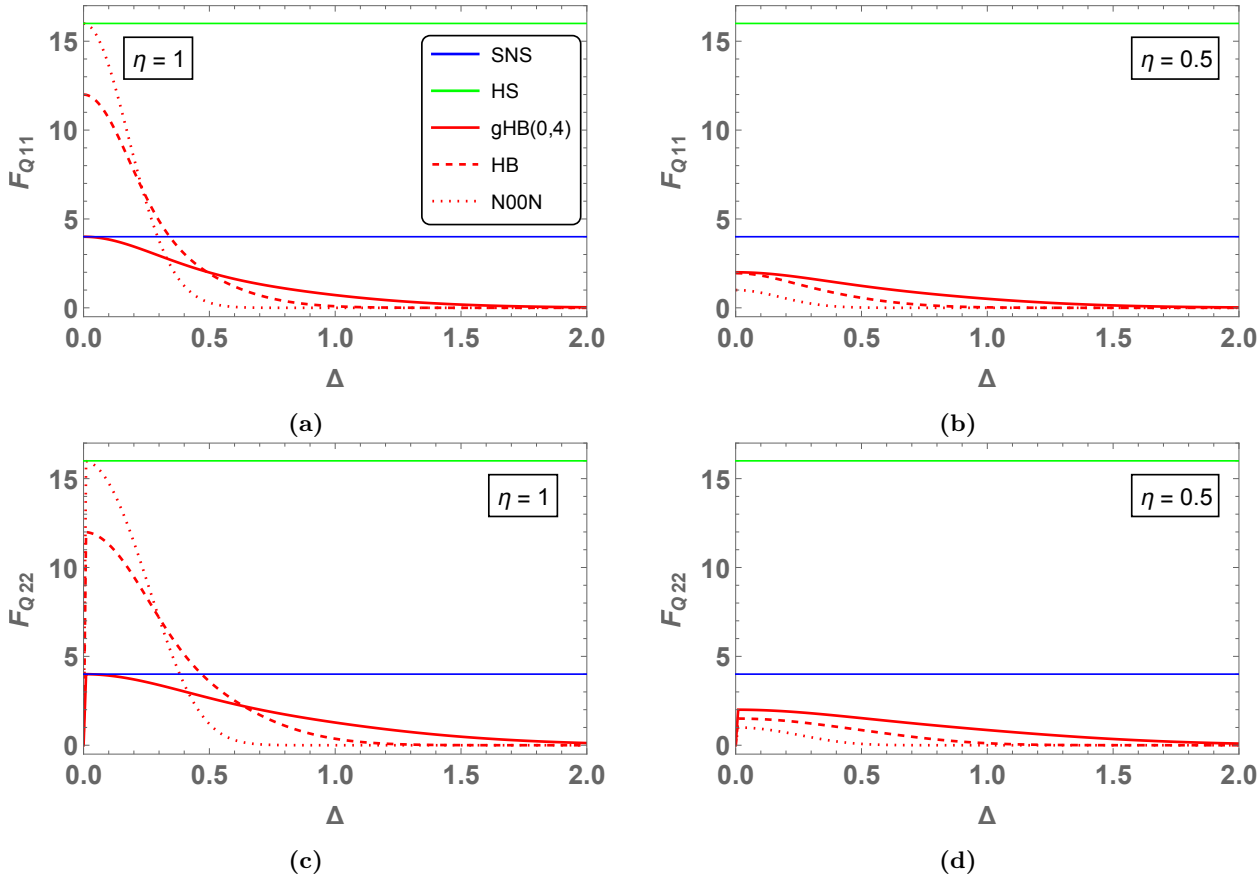

FIGURE 3.11: Plot of QFIs for phase and phase diffusion, $F_{Q\,1,1}$ and $F_{Q\,2,2}$, as a function of phase diffusion Δ with $N = 4$ for $\eta = 1$ (panels (a) and (c)) and $\eta_a = 0.5$ (panels (b) and (d)). The gHB state: $|\Psi^{\mathrm{gHB}}(0,4)\rangle$ (solid line), the HB state: $|\Psi^{\mathrm{HB}}(2,2)\rangle$ (dashed line), and the N00N(4) state (dotted line) are considered. Note that in all panels, for $\Delta > 0.7$, both the HB and the N00N states fall below SNS, while the gHB state displays higher sensitivity for all values of Δ.

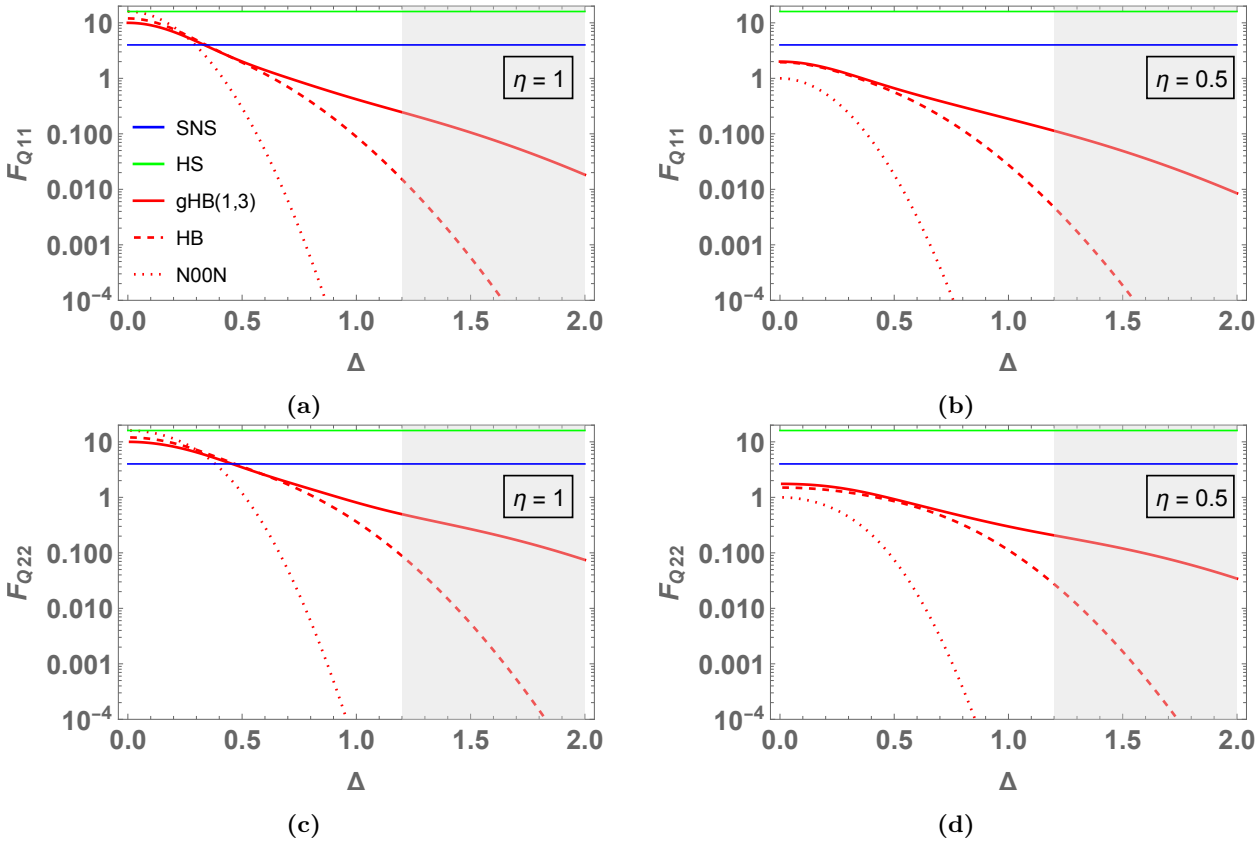

FIGURE 3.12: Plot of QFIs for phase and phase diffusion, $F_{Q\,1,1}$ and $F_{Q\,2,2}$, as a function of phase diffusion Δ with $N = 4$ for $\eta = 1$ (panels (a) and (c)) and $\eta_a = 0.5$ (panels (b) and (d)). The gHB state with the partition: $|\Psi^{\mathrm{gHB}}(1,3)\rangle$ (solid line), the HB $|\Psi^{\mathrm{HB}}(2,2)\rangle$ (dashed line), and the N00N(4) state (dotted line) are considered. The QFI values are plotted with a logarithmic scale on the y-axis to reflect the characteristics in the large diffusion region i.e., $\Delta > 1.2$ (grey shaded area), while the axis labels correspond to the actual QFI values. Note that the considered gHB state performs better than both the HB and the N00N here.

The performance of the state decreases with increasing values of k, as illustrated in Fig. 3.10. Hence, for all gHB states ($k \neq N/2$), we conjecture that an interplay of particle and mode entanglement offers a quantum enhancement that is robust against both phase diffusion and photon losses in comparison to the HB and the N00N states.

3.5.9 Discussion

For the sake of completeness, in reference to Fig. 3.9, we draw the following parallels to the results obtained in [34]. One of the features that characterize the trade-off curves in the top row of Fig. 3.9 is the existence of the saturation region for $\Delta > 1.2$. This implies that the double homodyne measurement cannot extract more information from a given probe state after a certain cut-off value of phase diffusion denoted as Δ_{cutoff}. Hence, its value is different for different gHB and HB states (see Appendix A6). Incidentally, in [34], the existence of the saturation region was not reported, as their trade-off curves were plotted only up to $\Delta = 1$. Our findings support two observations from [34] when one considers only the states with $N=6$ in the top row of Fig. 3.9. Firstly, in the lossless case, the double homodyne measurement performs better with N00N states than with HB states. Secondly, in the presence of 50% losses, the measurement performs better with HB states than with N00N states. Additional violations of the SQB have been reported in [34] with the employment of collective measurements on two-qubit states and general projective measurements on the HB state. However, devising an experimental setup for these cases poses a substantial challenge. In contrast, our observed violations, achieved through double homodyne measurements on gHB states, act as a suitable platform for an experimental implementation.

Considering the gHB state $|\Psi_{\text{gHB}}(0,6)\rangle$, in the lossless case, we achieve a sensitivity gain of 44.97% compared to the N00N state. In the presence of 50% losses, we achieve a sensitivity gain of 106.53% compared to the HB state. Hence, the sensitivity obtained through the double homodyne measurement on the gHB state has more than doubled compared to the same with the HB state in the lossy case.

In the top row of Figs. 3.9 and 3.10, the reference line $\Upsilon = 2$ corresponds to the information extraction by collective measurements. This sets the benchmark to assess the information extraction of the double homodyne measurement on various probe states. Analogously, in the bottom row of Figs. 3.9 and 3.10, we need a reference line to evaluate the information content of the probe states. In principle, this line is obtained by calculating the QCR bound for the optimal probe state, which contains the maximum information available for extraction about both parameters. Nevertheless, we have not included it because, in general, determining the optimal probe state in a multiparameter setting is still an open problem. Furthermore, the non-existence of a single probe state that allows for optimal sensitivity for all parameters is referred to as probe incompatibility, which has been studied in [175]. Therefore, as the value of N increases, our probe states contain more information, approaching that of the optimal state.

Examining the top row of Fig. 3.10, we observe that among the states with $k \in [0,6]$, those with $k = 0$ require the fewest photons to surpass the SQB, specifically when $N=2$. Therefore, double homodyne measurement on the $|\Psi_{\text{gHB}}(0,N)\rangle$ states are best suited for extracting higher amounts of information with a low number of photons, in a resource-efficient manner. However, as we increase k, the number of photons required to surpass the SQB also increases highlighting the resource inefficiency of these states.

3.6 Summary

In this chapter we introduced a two-fold, comprehensive figure of merit to capture the information extraction of a measurement and the information availability of probe states. Although these can be regarded as general figures of merit valid for p parameters and any measurement and probe states, we have focused on the performance of the double homodyne measurement and gHB states, which are tailor-made for the experimental realization of joint estimation of phase and phase diffusion in quantum interferometry. In particular, the following two aspects were essential to our findings: (a) the information extraction measure was defined relative to the QFI of each parameter with an aim to assess the violation of an information trade-off relation holding for qubits using higher-dimensional multiphoton states and (b) since an inference of high information extraction does not necessarily imply high information content, we identified the regions of information availability to which the regions of high information extraction correspond. These aspects were numerically investigated for a wide variety of gHB states with varying partitions, demonstrating the power of mode and particle entanglement in quantum enhancement of multiparameter precision.

Chapter 4

Measurement compatibility in optical interferometry

In Chapter 3, we investigated the joint estimation limits for the phase and diffusion for a specific set of probes and a Gaussian measurement. However, the underlying aspect that dictates these joint estimation limits is the non-commutativity or the extent of compatibility of optimal observables for the estimation of each parameter. This introduces trade-offs in the uncertainty of jointly estimating two parameters due to the lack of a common optimal observable and it is further affected by our choice of measurement. Therefore, in this chapter, we investigate multiparameter problems from the general perspective of compatibility that leads to estimation trade-offs as opposed to the resourcefulness of probes and measurement performance. To this end, we mainly focus on the estimation of phase and loss in an interferometer and supplement the results with the estimation of phase and phase diffusion. As seen in Section 2.3, metrological compatibility is essential for an optimal information extraction of uncorrelated parameters at the levels of measurement and probe state. Besides fundamental and probe compatibility, *measurement compatibility* represents the additional incompatibility that is brought with a chosen measurement scheme.

This chapter presents the work of [210], which investigates measurement compatibility in quantum interferometry using practical strategies based on double homodyne detection and photon counting on gHB states. The chapter is organized as follows. We begin by motivating the concept of measurement compatibility, with particular emphasis on the role of separable measurements in multiparameter estimation. We then introduce the main examples used to study compatibility and outline their key properties. Next, we discuss the motivation for jointly estimating phase and loss and describe the corresponding photon-loss channel. We then introduce the relevant figures of merit and present our results for the joint estimation of phase and loss as well as phase and diffusion. Finally, we conclude with a discussion and summary of the main findings.

4.1 Motivation

4.1.1 What is measurement compatibility?

Given a probe state $\rho_{\vec{\theta}}$, the non-commutativity of the optimal measurements for each parameter θ_i gives rise to fundamental incompatibility. In its presence, optimal information extraction for all parameters $\vec{\theta}$ cannot be achieved unless (i) the optimal measurements are weakly compatible or (ii) one uses a dedicated optimal measurement scheme for each parameter.

However, for certain problems, there exists *strong* fundamental incompatibility, i.e., $\mathrm{Tr}(\rho_{\vec{\theta}}[L_\phi, L_\eta]) \neq 0$. In this case, option (ii) becomes the only viable strategy. A further issue here is that using individual optimal measurements for p parameters requires p times the resources compared to the weakly compatible scenario. The practical difficulty in constructing the optimal measurement for a given parameter presents yet another challenge, mainly because there is no general recipe for designing optimal measurement schemes tailored to a specific estimation problem.

Nevertheless, the HCRB remains a tight bound in this regime and is, in principle, attainable via collective measurements. Unfortunately, collective measurements are also difficult to implement experimentally. For these practical reasons, it becomes essential to investigate the limits of the multiparameter setting using measurement strategies based on standard quantum-optical detection techniques, namely homodyne detection and photon counting, and to benchmark their performance against the HCRB.

Given the reduced advantage offered by separable measurements over collective ones, the measurement compatibility of any chosen measurement captures this residual incompatibility, excluding the fundamental incompatibility.

Towards the investigation of measurement compatibility, and extending beyond problems in optical interferometry, relatively little work has been done to the best of our knowledge. To name a few, the authors of [22] defined a figure of merit known as the *Regret* of FI for a given measurement M: $\mathrm{R}(M) = F_C(M) - F_Q$, which captures the sub-optimality of M in extracting information about all parameters. Francesco et al. [143] numerically studied the gap between the CRB and the HCRB considering an optimal measurement constructed from the SLD for phase using a class of two-mode multiphoton states with a fixed photon number.

4.1.2 Separable measurements in multiparameter estimation

The performance of separable measurements in the multiparameter setting is fundamentally limited by the *Collective Quantum Enhancement* (CQE) [166] i.e., the advantage offered by collective measurements or more simply the gap between the NHCRB and the HCRB and the fundamental compatibility (which we refer to as FC for now) i.e., the gap between the HCRB and the QCRB. By choosing practical separable measurements such as the double homodyne [34, 211] and the photon counting measurements, we study the gap between the CRB and the HCRB, namely the measurement compatibility, as our main figure of merit. A more realistic figure of merit is defined with respect to the optimal separable measurement characterized by the gap between the CRB and the NHCRB. All of this can be summarized in the following diagram (Fig. 4.1), where the use of a separable measurement can be identified on a scale for joint-parameter uncertainty (see Section 2.1.5.3 for more details).

4.1.3 The examples

We choose two paradigmatic examples:

Joint-estimation of phase and loss FC $\neq 1$ and CQE $= 1$	Joint-estimation of phase and diffusion FC $= 1$ and CQE $\neq 1$

Note that the value of 1 indicates no gap. These examples perfectly fit our investigation since the joint-estimation of phase and loss in one arm has a strong fundamental incompatibility i.e.,

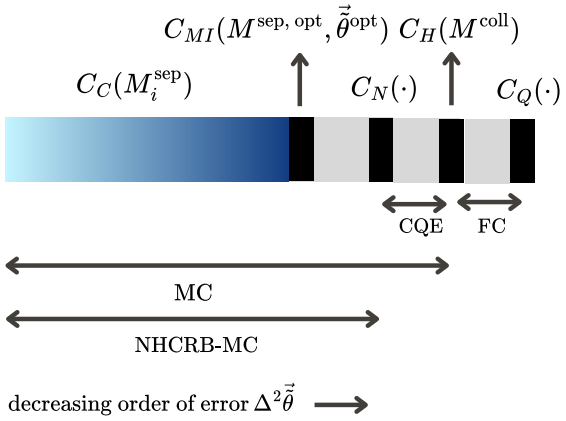

FIGURE 4.1: A scale representing the hierarchy of bounds on the joint-uncertainty $\Delta^2\vec{\theta}$. C_C, C_N, C_Q denote the CRB, NHCRB, and the QCRB respectively. The entries in brackets denote the character of measurement that attains the respective bounds i.e., M_i^{sep} - given separable measurement, $M^{\text{sep, opt}}, \vec{\theta}^{\text{opt}}$ - optimal separable measurement and optimal estimator and M^{coll} - collective measurement. The entry $(\cdot)$ are associated to bounds that are not tight in general. The abbreviations MC and NHCRB-MC stand for measurement compatibility and NHCRB-based measurement compatibility respectively.

$\text{Tr}(\rho_{\phi,\eta_a}[L_\phi, L_{\eta_a}]) \neq 0$ or FC $\neq 1$ [142]. On the other hand, the joint-estimation of phase and phase diffusion has weak fundamental compatibility i.e., $\text{Tr}(\rho_{\phi,\Delta}[L_\phi, L_{\eta_a}]) = 0$ or FC $= 1$ [34].

Lastly, for the sake of completeness, we also mention the example of joint-estimation of phase and equal loss in both arms. This is an exceptional case under the umbrella of joint-estimation of phase and loss, where the fundamental incompatibility actually vanishes. We refer the interested reader to [177], where the authors have investigated fundamental and probe compatibilities for this case considering optimal probe states. We also validate their results in Section 4.6.5.

In Fig. 4.2, we depict the two types of measurements that will be considered to assess the measurement compatibility in our estimation problems.

4.1.4 Fundamental compatibility in our examples

In general, the presence of strong fundamental incompatibility between phase and loss can be intuitively understood as follows. As we know from Eq. 2.40, the QFI for phase is given by the variance of its generator (photon number) as $F_\phi = 4\text{Var}(\hat{n})$. Since we consider phase-shift in mode a, we have: $\hat{n} = \hat{a}^\dagger\hat{a}$. Hence, the phase uncertainty is given by: $\text{Var}(\phi) \geq \frac{1}{\text{Var}(\hat{n})}$. As a result, states with the highest photon-number variance yield the lowest phase uncertainty. In fact, this happens for the N00N state [27, 49, 212]. In contrast, the optimal state for the estimation of loss is the Fock state with a fixed photon number N [213]. This is because loss can be thought of as the decay rate of the field energy due to the system's interaction with the environment. As a result, the system starts with a zero energy uncertainty state (since Fock states are eigenstates of the field Hamiltonian) and ends up in a finite energy uncertainty state (lossy mixed state) which directly corresponds to losses. These aspects manifest itself into probe incompatibility and fundamental incompatibility of

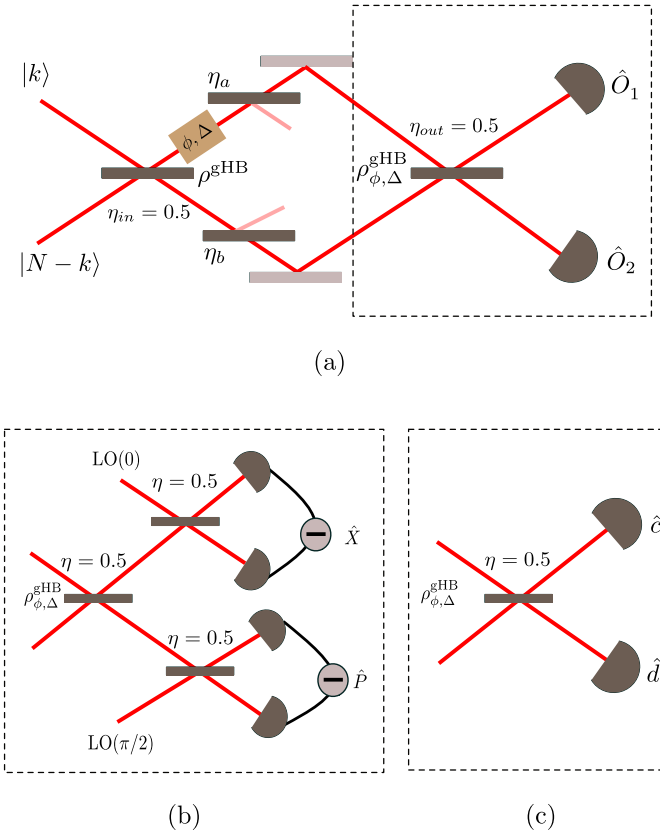

FIGURE 4.2: (a) Overall scheme for the joint estimation of phase and photon loss, and joint estimation of phase and phase diffusion. Two unknown parameters are estimated simultaneously: (i) phase ϕ and photon loss in the phase-shifted arm of a MZI, η_a, and (ii) phase ϕ and phase diffusion Δ. The measurement part consists of separate analyses of the measurement compatibility for (b) double homodyne and (c) photon-counting measurements.

the problem. Probe incompatibility can be overcome in the settings of one mode or single mode probe states with increasing the number of photons or introducing entanglement in the two mode scenario. However, it is has been found that the fundamental aspect of the problem is indeed the fundamental incompatibility which cannot be overcome except in the scenario of estimation of equal loss in both arms of the MZI [177]. Furthermore, if there are no losses in mode b, a closed-form expression for the commutation condition has appeared in [142], which relates it to the QFI of the phase: $\text{Tr}(\rho_{\phi,\eta_a}[L_\phi, L_{\eta_a}]) = \frac{iF_{Q\,1,1}}{2\eta_a}$. This fact implies that, for values of loss where the probe state ρ_{ϕ,η_a} exhibits weaker sensitivity to phase, the fundamental incompatibility is reduced and it can only be fully overcome at the expense of acquiring no information about phase.

The presence of weak fundamental compatibility between phase and diffusion can be attributed to the example depicted in Fig. 3.11(c) for $N = 4$. In the small diffusion regime ($\Delta < 0.2$, $\eta = 1$), for the estimation of diffusion, the N00N states are optimal i.e., yields performance close to the HS. In the large diffusion regime ($\Delta > 0.2$, $\eta = 1$), the gHB state: $|\Psi^{\text{gHB}}(0, N)\rangle$ performs close to the optimal states for diffusion. This picture is consistent with the estimation of phase where the same states exhibit maximal sensitivity in each regime as shown in Fig. 3.11(a). This numerical result holds for even states with $N > 4$ (see Appendix A5). Due to this, one may expect the generators of phase and phase diffusion to be weakly compatible.

4.1.5 Collective quantum enhancement in our examples

The problem of joint estimation of phase and loss has no CQE or CQE = 1, implying that the use of collective measurements offer no advantage over separable ones, whereas the joint estimation of phase and diffusion provides CQE or CQE $\neq$ 1, signifying the effectiveness of collective measurements. This difference may be intuitively understood from the following argument. Firstly, we note that since the phase and loss estimators are uncorrelated, we can immediately infer that using only the quantumness of the probe, one can enhance the phase resolution up to the HL and the quantumness of the measurement has no effect. For loss estimation, one simply needs to count the photons at the output of the MZI regardless of the amount of entanglement between the photons or how widely distributed the photon numbers are. In this sense, the quantum effects neither at the probe nor at the measurement level should influence the loss estimation. On the other hand, the phase diffusion can be associated with estimating randomly varying phases over a period of time. Therefore, the estimation of diffusion is even more resource-demanding than that of phase estimation. As a result, the presence of entanglement at the measurement should further enhance the precision and beat the performance of uncorrelated measurements.

4.1.6 Why estimate phase and loss concurrently?

Having already highlighted the importance of the simultaneous estimation of phase and phase diffusion, it is important to note that photon loss is unavoidable in any realistic interferometer—whether during state preparation, parameter encoding, or detection. The losses are typically modeled using beamsplitters with transmissivity η. Since photon loss is a major limitation, the performance of quantum-enhanced optical interferometry protocols must always be evaluated in its presence [206, 57, 67]. The first comprehensive theoretical analysis of phase estimation in the presence of loss was presented in [26, 56], where the optimal states were calculated numerically. On the other hand, the estimation of loss with non-Gaussian [213] and Gaussian states [214] have also been studied. Nevertheless, a more robust estimation strategy calls for the simultaneous estimation of both phase and photon losses. While the joint sensitivity of this problem has been analyzed [143, 142], the question of compatibility in such models has received much less attention until most recently in [177].

4.2 The photon-loss channel

Considering the gHB state as the input and losses in both modes of an MZI, the photon-loss channel can be characterized using the following Kraus representation [26]

$$\rho^{\mathrm{gHB}}_{\eta_a,\eta_b} = \Lambda_{\eta_a,\eta_b}(\rho^{\mathrm{gHB}}) = \sum_{p=0}^{N}\sum_{q=0}^{N-p} K_{b,q,\eta_b} K_{a,p,\eta_a} \rho^{\mathrm{gHB}} K^{\dagger}_{a,p,\eta_a} K^{\dagger}_{b,q,\eta_b} \tag{4.1}$$

If p and q photons are lost from the modes a and b, respectively, then $K_{a,p,\eta_a} = \sqrt{\frac{(1-\eta_a)^p}{p!}}\sqrt{\eta_a^{\hat{a}^\dagger \hat{a}}}\hat{a}^p$, $K_{b,q,\eta_b} = \sqrt{\frac{(1-\eta_b)^q}{q!}}\sqrt{\eta_b^{\hat{b}^\dagger \hat{b}}}\hat{b}^q$ are the Kraus operators that make up the photon-loss channel.

4.2.1 Commutativity of phase-shift and photon loss operations

Next, we note that the phase-shift operation and the photon-loss channel commute. This can be seen as follows. Considering the phase-shift operation in mode a as before: $\mathcal{U}_{\phi'} = e^{-i\phi' \hat{a}^\dagger \hat{a}}$, we

expand the operator $e^{i\phi'\hat{a}^\dagger\hat{a}}\hat{a}^p e^{-i\phi'\hat{a}^\dagger\hat{a}}$ as follows

$$e^{i\phi'\hat{a}^\dagger\hat{a}}\hat{a}^p e^{-i\phi'\hat{a}^\dagger\hat{a}} = \hat{a}^p + [i\phi'\hat{a}^\dagger\hat{a}, \hat{a}^p] + \frac{1}{2!}[i\phi'\hat{a}^\dagger\hat{a}, [i\phi'\hat{a}^\dagger\hat{a}, \hat{a}^p]] + \frac{1}{3!}[i\phi'\hat{a}^\dagger\hat{a}, [i\phi'\hat{a}^\dagger\hat{a}, [i\phi'\hat{a}^\dagger\hat{a}, \hat{a}^p]]] \dots \tag{4.2}$$

where we have used the Baker-Campbell-Hausdorff formula:
$e^X Y e^{-X} = Y + [X, Y] + \frac{1}{2!}[X, [X, Y]] + \frac{1}{3!}[X, [X, [X, Y]]] \dots$ with $X = i\phi\hat{a}^\dagger\hat{a}$ and $Y = \hat{a}^k$.

Noticing $[\hat{a}^\dagger\hat{a}, \hat{a}] = -\hat{a}$, $[\hat{a}^\dagger\hat{a}, \hat{a}^2] = -2\hat{a}^2$, $[\hat{a}^\dagger\hat{a}, \hat{a}^3] = -3\hat{a}^3$, and so on, we obtain the general formula: $[\hat{a}^\dagger\hat{a}, \hat{a}^p] = -p\hat{a}^p$. Making use of this in Eq. 4.2, we have

$$e^{i\phi'\hat{a}^\dagger\hat{a}}\hat{a}^p e^{-i\phi'\hat{a}^\dagger\hat{a}} = \hat{a}^p - i\phi' p\hat{a}^p - \frac{\phi'^2 p^2}{2!}\hat{a}^p + \frac{i\phi'^3 p^3}{3!}\hat{a}^p \dots = \hat{a}^p e^{-ip\phi'} \tag{4.3}$$

Operating $e^{-i\phi'\hat{a}^\dagger\hat{a}}$ from the left on both sides we get the identity

$$\hat{a}^p e^{-i\phi'\hat{a}^\dagger\hat{a}} = e^{-i\phi'\hat{a}^\dagger\hat{a}}\hat{a}^p e^{-ip\phi'} \tag{4.4}$$

Applying the phase-shift operation *after* the photon-loss channel ρ^{gHB}, and making use of Eq. 4.1, we write explicitly

$$\begin{aligned}\mathcal{U}_{\phi'}\Lambda_{\eta_a,\eta_b}(\rho^{\text{gHB}})\mathcal{U}_{\phi'}^\dagger &= \rho^{\text{gHB}}_{\phi',\eta_a,\eta_b} \\ &= \sum_{p=0}^{N}\sum_{q=0}^{N-p}\Bigg[\left(\sqrt{\frac{(1-\eta_b)^q}{q!}}\sqrt{\eta_b^{\hat{b}^\dagger\hat{b}}}\hat{b}^q\right)\left(\sqrt{\frac{(1-\eta_a)^p}{p!}}e^{-i\phi'\hat{a}^\dagger\hat{a}}\sqrt{\eta_a^{\hat{a}^\dagger\hat{a}}}\hat{a}^p\right)\rho^{\text{gHB}} \\ &\quad\cdot\left(\sqrt{\frac{(1-\eta_a)^p}{p!}}(\hat{a}^\dagger)^p\sqrt{\eta_a^{\hat{a}^\dagger\hat{a}}}e^{i\phi'\hat{a}^\dagger\hat{a}}\right)\left(\sqrt{\frac{(1-\eta_b)^q}{q!}}(\hat{b}^\dagger)^q\sqrt{\eta_b^{\hat{b}^\dagger\hat{b}}}\right)\Bigg]\end{aligned} \tag{4.5}$$

Using $[e^{-i\phi'\hat{a}^\dagger\hat{a}}, \sqrt{\eta_a^{\hat{a}^\dagger\hat{a}}}] = [\sqrt{\eta_a^{\hat{a}^\dagger\hat{a}}}, e^{i\phi'\hat{a}^\dagger\hat{a}}] = 0$,

$$\begin{aligned}&= \sum_{p=0}^{N}\sum_{q=0}^{N-p}\Bigg[\left(\sqrt{\frac{(1-\eta_b)^q}{q!}}\sqrt{\eta_b^{\hat{b}^\dagger\hat{b}}}\hat{b}^q\right)\left(\sqrt{\frac{(1-\eta_a)^p}{p!}}\sqrt{\eta_a^{\hat{a}^\dagger\hat{a}}}e^{-i\phi'\hat{a}^\dagger\hat{a}}\hat{a}^p\right)\rho^{\text{gHB}} \\ &\quad\cdot\left(\sqrt{\frac{(1-\eta_a)^p}{p!}}(\hat{a}^\dagger)^p e^{i\phi'\hat{a}^\dagger\hat{a}}\sqrt{\eta_a^{\hat{a}^\dagger\hat{a}}}\right)\left(\sqrt{\frac{(1-\eta_b)^q}{q!}}\sqrt{\eta_b^{\hat{b}^\dagger\hat{b}}}(\hat{b}^\dagger)^q\right)\Bigg]\end{aligned} \tag{4.6}$$

Multiplying $e^{ip\phi'}$ on both sides of Eq. 4.4 and its complex conjugate, we get:
$\hat{a}^p e^{-i\phi'\hat{a}^\dagger\hat{a}}e^{ip\phi'} = e^{-i\phi'\hat{a}^\dagger\hat{a}}\hat{a}^p$ and $e^{-ip\phi'}e^{i\phi'\hat{a}^\dagger\hat{a}}(\hat{a}^\dagger)^p = (\hat{a}^\dagger)^p e^{i\phi'\hat{a}^\dagger\hat{a}}$, which we use in the above equation to obtain

$$\begin{aligned}&= \sum_{p=0}^{N}\sum_{q=0}^{N-p}\Bigg[\underbrace{\left(\sqrt{\frac{(1-\eta_b)^q}{q!}}\sqrt{\eta_b^{\hat{b}^\dagger\hat{b}}}\hat{b}^q\right)}_{K_{b,q,\eta_b}}\underbrace{\left(\sqrt{\frac{(1-\eta_a)^p}{p!}}\sqrt{\eta_a^{\hat{a}^\dagger\hat{a}}}\hat{a}^p\right)}_{K_{a,p,\eta_a}}e^{-i\phi'\hat{a}^\dagger\hat{a}}\rho^{\text{gHB}}e^{i\phi'\hat{a}^\dagger\hat{a}} \\ &\quad\cdot\underbrace{\left(\sqrt{\frac{(1-\eta_a)^p}{p!}}(\hat{a}^\dagger)^p\sqrt{\eta_a^{\hat{a}^\dagger\hat{a}}}\right)}_{K^\dagger_{a,p,\eta_a}}\underbrace{\left(\sqrt{\frac{(1-\eta_b)^q}{q!}}\sqrt{\eta_b^{\hat{b}^\dagger\hat{b}}}(\hat{b}^\dagger)^q\right)}_{K^\dagger_{b,q,\eta_b}}\Bigg],\end{aligned} \tag{4.7}$$

where the $e^{ip\phi'}$ factor cancels out with its complex conjugate. Thus,

$$\rho^{\mathrm{gHB}}_{\phi',\eta_a,\eta_b} = \mathcal{U}_{\phi'}\Lambda_{\eta_a,\eta_b}(\rho^{\mathrm{gHB}})\mathcal{U}^\dagger_{\phi'} = \Lambda_{\eta_a,\eta_b}(\mathcal{U}_{\phi'}\rho^{\mathrm{gHB}}\mathcal{U}^\dagger_{\phi'}), \tag{4.8}$$

which is same as applying the phase-shift operation *before* the photon-loss channel. Applying the phase-diffusion channel given by Eq. 3.40, we obtain

$$\begin{aligned}\rho^{\mathrm{gHB}}_{\phi,\eta_a,\eta_b,\Delta} &= \Lambda_\Delta(\Lambda_{\eta_a,\eta_b}(\mathcal{U}_{\phi'}\rho^{\mathrm{gHB}}\mathcal{U}^\dagger_{\phi'})) \\ &= \int_{-\infty}^{\infty} p_{\phi,\Delta}(\phi')\Big(\sum_{p=0}^{N}\sum_{q=0}^{N-p} K_{b,q,\eta_b}K_{a,p,\eta_a}\mathcal{U}_{\phi'}\rho^{\mathrm{gHB}}\mathcal{U}^\dagger_{\phi'}K^\dagger_{a,p,\eta_a}K^\dagger_{b,q,\eta_b}\Big)d\phi',\end{aligned} \tag{4.9}$$

Equivalent to Eq. 3.42, the above equation takes the following explicit form

$$\rho^{\mathrm{gHB}}_{\phi,\eta_a,\eta_b,\Delta} = \sum_{p=0}^{N}\sum_{q=0}^{N-p}\sum_{n,m=p}^{N-q}\mathcal{A}_{n,m,p,q}(N,k,\eta_a,\eta_b,\phi,\Delta)\,|n-p,N-n-q\rangle\langle m-p,N-m-q|\,, \tag{4.10}$$

where $\mathcal{A}_{n,m,p,q}(N,k,\eta_a,\eta_b,\phi,\Delta) = \mathcal{C}_{n,m,p,q}(N,k,\eta_a,\eta_b)e^{-i\phi(n-m)-\frac{\Delta^2}{2}(n-m)^2}$ and $\mathcal{C}_{n,m,p,q}(N,k,\eta_a,\eta_b) \equiv \mathcal{C}^{(\mathrm{L})}_{n,m,p,q}(N,k)$ as given by Eq. 3.41.

4.3 Figures of merit

Following the ultimate limits to the precision described in detail in Section 2.1, we now introduce the measures of compatibility relevant to our analysis. Since we are interested in studying these measures not only as functions of the parameter values but also in relation to the parameter weights, we make the dependence on the weight matrix W explicit.

4.3.1 Fundamental compatibility figure of merit

A measure of fundamental incompatibility that has a geometric character by Belliardo and Giovannetti [171]. In this work, considering up to three qubits, this measure has been applied to the example of estimation of rotations of the qubits about the y and z axis subject to local depolarizing noise showcasing its operational meaning. In its essence, for the gHB probe state $\rho^{\mathrm{gHB}}_{\vec{\alpha}}$, where $\vec{\alpha} = (\phi,\eta_a,\eta_b,\Delta)^\top$, it is given by the ratio of the HCRB to the QCRB as

$$r_{BG}(\rho^{\mathrm{gHB}}_{\vec{\alpha}},W,\vec{\alpha}) = \frac{C_H(\rho^{\mathrm{gHB}}_{\vec{\alpha}},W)}{C_Q(\rho^{\mathrm{gHB}}_{\vec{\alpha}},W)} \tag{4.11}$$

This represents the *intrinsic* compatibility of the estimation problem as the HCRB captures the fundamental incompatibility of the problem. Since $C_H \geq C_Q$ and $C_H \leq 2C_Q$, we have: $r_{BG} \in [1,2]$.

4.3.2 Main figure of merit

As we described earlier, in the presence of strong fundamental incompatibility, the choice of a *separable* measurement M gives rise to some residual incompatibility which can be quantified by the ratio of the CRB to the HCRB

$$r_H^C(M, \rho_{\vec{\alpha}}^{\mathrm{gHB}}, W, \vec{\alpha}) = \frac{C_C(M, \rho_{\vec{\alpha}}^{\mathrm{gHB}}, W)}{C_H(\rho_{\vec{\alpha}}^{\mathrm{gHB}}, W)}, \tag{4.12}$$

leading to our central figure of merit. We note that $r_H^C \in [1, \infty)$ with $r_H^C = 1$ indicating full measurement compatibility and $r_H^C >> 1$ implies low compatibility.

For ν separable identical copies of the probe state $\rho_{\vec{\alpha}}^{\mathrm{gHB}\otimes\nu}$, the additivity property of C_C, C_Q, and C_H renders r_{BG} and r_H^C independent of ν i.e.,

$$\frac{C_{H(C)}(\rho_{\vec{\alpha}}^{\mathrm{gHB}\otimes\nu})}{C_{Q(H)}(\rho_{\vec{\alpha}}^{\mathrm{gHB}\otimes\nu})} = \frac{C_{H(C)}(\rho_{\vec{\alpha}}^{\mathrm{gHB}})}{C_{Q(H)}(\rho_{\vec{\alpha}}^{\mathrm{gHB}})}. \tag{4.13}$$

4.3.3 NHCRB-based measurement compatibility

r_H^C is a stronger figure of merit since it captures the performance of a separable measurement with respect to the HCRB which, in general, is attained by only collective measurements. However, owing to the practical infeasibility of deploying these measurements, a weaker figure of merit with a practical viewpoint can be defined with respect to the NHCRB attained by the optimal separable measurement. Given this consideration, we define

$$r_N^C(M, \rho_{\vec{\alpha}}^{\mathrm{gHB}}, W, \vec{\alpha}) = \frac{C_C(M, \rho_{\vec{\alpha}}^{\mathrm{gHB}}, W)}{C_N(\rho_{\vec{\alpha}}^{\mathrm{gHB}}, W)} \tag{4.14}$$

Similar to r_H^C, $r_N^C \in [1, \infty]$. The subadditivity of the NHCRB (Eq. 2.79) implies

$$\frac{C_C(\rho_{\vec{\alpha}}^{\mathrm{gHB}\otimes\nu})}{C_N(\rho_{\vec{\alpha}}^{\mathrm{gHB}\otimes\nu})} \geq \frac{C_C(\rho_{\vec{\alpha}}^{\mathrm{gHB}})}{C_N(\rho_{\vec{\alpha}}^{\mathrm{gHB}})} \tag{4.15}$$

When the measurement is optimal, $C_C = C_N$, and thus r_H^C becomes

As we have already seen in Section 2.1.5.1, and as introduced earlier, the CQE—the advantage offered by collective measurements over separable ones—is quantified by

$$r_H^N(\rho_{\vec{\alpha}}^{\mathrm{gHB}}, W, \vec{\alpha}) = \frac{C_N(\rho_{\vec{\alpha}}^{\mathrm{gHB}}, W)}{C_H(\rho_{\vec{\alpha}}^{\mathrm{gHB}}, W)} \tag{4.16}$$

Since the maximal quantum enhancement due to collective measurements is given by the number of parameters p, we have $r_H^N \in [1, p]$, where $r_H^N = 1$ corresponds to a scenario in which collective measurements offer no advantage over separable ones.

For the ν-copy state $\rho^{\mathrm{gHB}\otimes\nu}$,

$$\frac{C_N(\rho_{\vec{\alpha}}^{\mathrm{gHB}\otimes\nu})}{C_H(\rho_{\vec{\alpha}}^{\mathrm{gHB}\otimes\nu})} = \frac{\nu C_N(\rho_{\vec{\alpha}}^{\mathrm{gHB}\otimes\nu})}{C_H(\rho_{\vec{\alpha}}^{\mathrm{gHB}})}, \tag{4.17}$$

where we used the additivity of the HCRB: $\nu C_H(\rho^{\mathrm{gHB}\otimes\nu}) = C_H(\rho^{\mathrm{gHB}})$.

Since we know $\lim_{\nu\to\infty} \nu C_N(\rho_{\vec{\alpha}}^{\mathrm{gHB}\otimes\nu}) = C_H$, taking $\lim_{\nu\to\infty}$ on both sides of Eq. 4.17,

$$\lim_{\nu\to\infty}\frac{C_N(\rho_{\vec{\alpha}}^{\mathrm{gHB}\otimes\nu})}{C_H(\rho_{\vec{\alpha}}^{\mathrm{gHB}\otimes\nu})}=\lim_{\nu\to\infty}\frac{\nu C_N(\rho_{\vec{\alpha}}^{\mathrm{gHB}\otimes\nu})}{C_H(\rho_{\vec{\alpha}}^{\mathrm{gHB}})}=1. \tag{4.18}$$

Therefore, for a large number of copies of the probe state, the NHCRB should converge to the HCRB.

We consider the weight matrix $W(y)=\begin{bmatrix}2y & 0\\ 0 & 2(1-y)\end{bmatrix}$, $y\in[0,1]$. From this choice, we can identify the identity matrix at $y=0.5$ corresponding to an unbiased penalization with the extremal cases at $y=0$ and $y=1$ yielding rank-1 matrices that correspond to the penalization of the error in only one of the two parameters. Additionally, this allows us to obtain bounds on linear combinations of estimation errors of individual parameters. Therefore, the behaviour of the measurement and the fundamental compatibility will be assessed with respect to the extent of prioritizing and penalizing the error on one parameter over the other.

4.3.4 Evaluation of the measures

The evaluation of measurement compatibility r_H^C is not analytically feasible in general. This is because, a general closed-form solution to C_H is not known except in the case of the so-called D-invariant models which finds a clear operational meaning in unitary models (Section 2.1.3.3), where each parameter is associated to its generator [151]. In this case, as we have mentioned in Section 2.73, $C_H\leq\overline{C}_H$, where $\overline{C}_H$ is the HCRB for the D-invariant model. Since our problem does not belong to this class, we solve a convex optimization problem formulated as an SDP which is then solved numerically (see Chapter 5 for more details). As we have stated earlier, the evaluation of C_C is considering the double homodyne POVM and lossy state is analytically not feasible. The bounds C_N and C_Q required for the evaluation of the r_N^C and r_{BG} respectively are computed numerically using the `QuanEstimation` package.

4.4 Joint-estimation of phase and loss in one arm

We consider the metrological scheme in Fig. 4.2 and begin our analysis by treating the estimation of phase and loss in the arm of the MZI where phase-shift occurs by considering separately the cases of no loss and known loss in the other arm separately. This is because allowing unknown losses in the reference arm alters the behavior of compatibility, differing from the case where the losses are known, both in terms of the weights and the amount of losses. We investigate the measurement compatibilities of the double homodyne and photon counting measurement both with respect to the HCRB and the NHCRB.

4.4.1 Parameter weights analysis

4.4.1.1 No loss on the reference arm

Our first application concerns the joint estimation of phase and loss in one arm of the interferometer [142]. The corresponding output probe state $\rho_{\phi,\eta_a}^{\mathrm{gHB}}$ is obtained from Eq. 4.10 by setting $\eta_b=1$ (no loss on the reference arm), $\Delta=0$ (no dephasing). Crucially, this output has a direct sum structure $\rho_{\phi,\eta_a}^{\mathrm{gHB}}=\bigoplus_{p=0}^{N}p_p\left|\xi_{\phi,\eta_a}(p)\right\rangle\left\langle\xi_{\phi,\eta_a}(p)\right|$, where each term $|\xi_{\phi,\eta_a}(p)\rangle=$

$\frac{1}{\sqrt{p_p}}\sum_{n=p}^{N}\mathcal{C}_n(N,k)e^{-in\phi}\sqrt{B_p^n}\,|n-p,N-n\rangle$ is a pure state belonging to the subspace corresponding to the loss of p photons, with a normalization factor or the associated probability, p_p [26, 142]. These states are also orthogonal i.e., $\langle\xi_{\phi,\eta_a}(p),\xi_{\phi,\eta_a}(p')\rangle=\delta_{pp'}$. Although we have computed the QCRB numerically here, the linearity of QFI on direct sums: $F_Q(\bigoplus_{p=0}^{N}p_p\,|\xi_{\phi,\eta_a}(p)\rangle\langle\xi_{\phi,\eta_a}(p)|)=\sum_{p=0}^{N}p_pF_Q(|\xi_{\phi,\eta_a}(p)\rangle\langle\xi_{\phi,\eta_a}(p)|)$ [20, 215] allows us, in principle, to calculate the QCRB analytically.

Double homodyne measurement: Fig. 4.3 depicts the measurement compatibility r_H^C and, for comparison, the fundamental compatibility measure r_{BG} as a function of the weight y for our choice of double homodyne measurement on different probe states. The bounds depend on the value of the estimated parameter η_a, but are independent of ϕ (following the symmetry argument for ϕ presented in Section 3.5.5.1). Specifically, in panel (a), we consider HB states for $N=2,4,6,8$, in panel (b), we consider the gHB states: $|\Psi_{\text{gHB}}(0,N)\rangle$ for $N=2,3,4,5,6,7,8$. We compute the CRB, QCRB, and HCRB at $\eta_a=0.5$ so that the compatibilities are studied in scenario of moderate loss. We remark that for this lossy model there is no advantage in the adoption of collective measurements, or, in different words, the parameter $r_H^N=C_N/C_H$ is 1 for all states and weights we consider (see Figs. 4.13 and 4.15). This is connected to the fact that the two parameters, phase and loss, are strongly incompatible: $\text{Tr}(\rho_{\phi,\eta_a}^{gHB}[L_\phi,L_{\eta_a}])\neq 0$ [152]. Notice that the extreme points $y=0$ and $y=1$ correspond to a single-parameter estimation, thus the notion of compatibility does not apply.

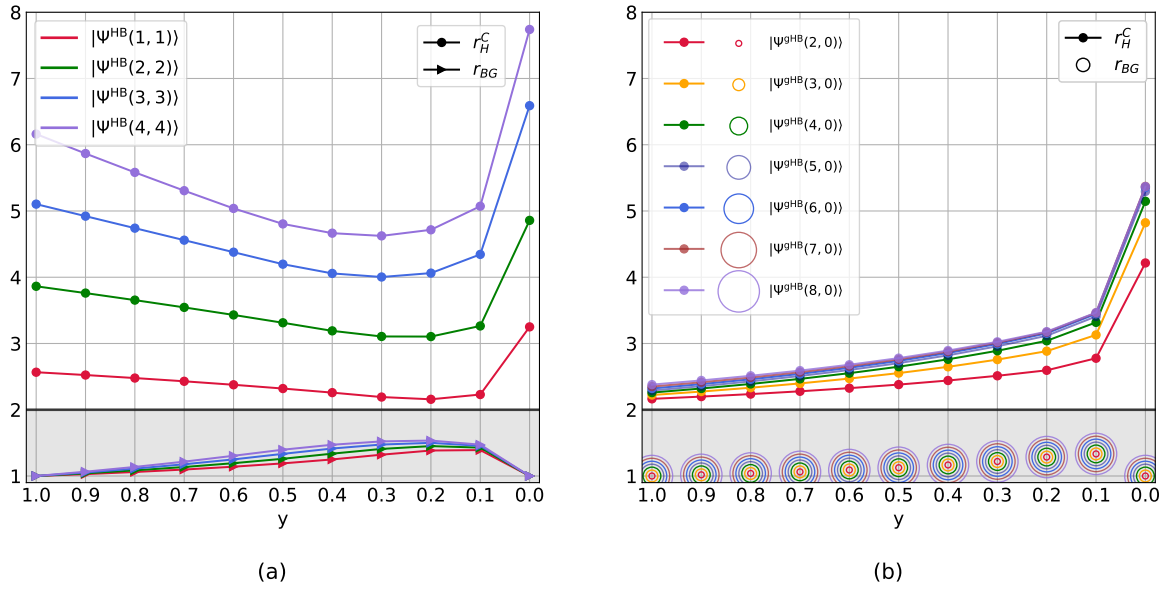

FIGURE 4.3: Plot of measurement compatibility measure r_H^C and fundamental compatibility measure r_{BG} versus the weights y for the joint-estimation of phase and losses in one arm of the MZI. HB states with $N=2,4,6,8$ (panel (a)) and gHB states with $N=2,3,4,5,6,7,8$ (panel (b)), and double homodyne measurement are considered. In panel (b) the plotting of r_{BG} employs concentric circles of varying colors to represent the near-perfect overlap of compatibilities for different values of N, as indicated by their common center. Note that in the following plots, such overlapping points are depicted in this manner. The curves are plotted at $\eta_a=0.5$ and $\Delta=0$. For HB states, the measurement compatibility decreases significantly as N increases, while the fundamental compatibility decreases only slightly as N increases.

In panel 4.3(a), for all values of N, r_H^C shows a similar behaviour, with a minimum value achieved

around $y = 0.2$, corresponding to the maximal compatibility allowed by our choice of measurement. As N increases, the overall magnitude of r_H^C also increases, signaling that double homodyne becomes more inefficient at extracting information. We can thus investigate whether this is at least partly mirrored in the behaviour of the fundamental compatibility r_{BG}. This reaches the value 1 at the extremes, as expected for single-parameter problems, and exhibits a maximum around $y = 0.2$, only weakly depending on N. On the other hand, fundamental incompatibility too increases with the number of photons, as r_H^C does, although on a different scale.

In panel 4.3(b), there occurs an increase of r_H^C as a function of N, but this dependency is much less pronounced. In contrast to panel (a), the best compatibility conditions for r_H^C occur in proximity of pure phase estimation, close to $y = 0.9$, corresponding to maximal measurement compatibility. Interestingly, we find that, at the level of individual photon number, the behavior of r_H^C mirrors that of r_{BG}. The latter also follows the behavior observed in panel (a). However, at the collective level, in contrast to measurement compatibility, the fundamental compatibility remains constant with the number of photons.

Photon counting: Fig. 4.4 reports the same analysis now carried out for photon counting performed at the two outputs of the MZI. Panel 4.4(a) shows HB states with $N = 2, 4, 6, 8$ and panel 4.4(b) shows gHB states with $N = 2, 3, 4, 5, 6, 7, 8$. For HB states, we find that for $N = 2$, $r_H^C \approx 1$ up to $y = 0.2$, thus showing good compatibility.

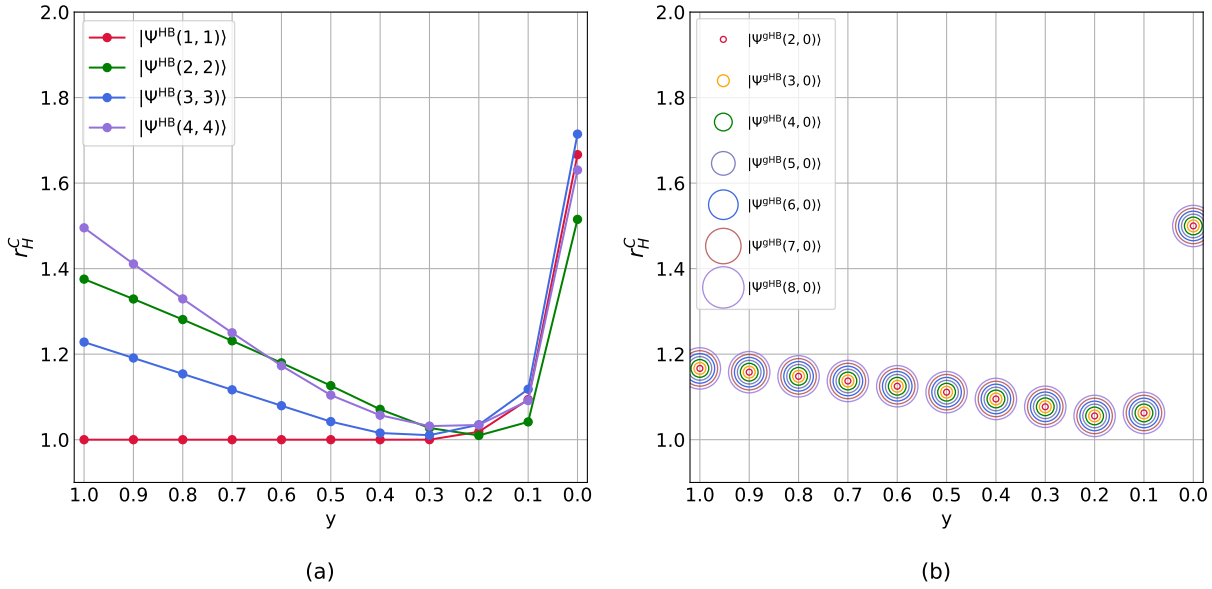

FIGURE 4.4: Plot of measurement compatibility measure r_H^C versus the weights y for photon counting for the joint-estimation of phase and loss in one arm of the MZI. HB states with $N = 2, 4, 6, 8$ (panel(a)) and gHB states with $N = 2, 3, 4, 5, 6, 7, 8$ (panel(b)) are considered. Note that the measurement compatibility remains relatively high compared to that of the double homodyne measurement, with the highest compatibility observed at $N = 2$. The other known parameters are taken at the same values as those used in the assessment of the double homodyne measurement.

On the other hand, for the remaining values of N we considered, the trend becomes non-monotonic, with a minimum value of r_H^C achieved near $y = 0.3$. For gHB states, instead, the behaviour is independent on the photon number N, with a minimum found in the same region as in the previous case. For all those cases, the compatibility remains satisfactory when $y \in [0.9, 0.1]$, as it stays below 1.5. This observation is in line with previous studies that have highlighted a

better metrological performance of photon counting, a non-Gaussian measurement, on non-Gaussian probes [211].

4.4.1.2 Known loss on the reference arm

We now extend our study to the joint estimation of phase and loss in one arm of the interferometer, while assuming a known amount of loss in the other arm. The corresponding output probe state $\tilde{\rho}^{\text{gHB}}_{\phi,\eta_a}$ is obtained from Eq. 4.10 by setting $\eta_b = 0.5$ (50% loss on the reference arm) and $\Delta = 0$. The output can be expressed as $\tilde{\rho}^{\text{gHB}}_{\phi,\eta_a} = \sum_{p=0}^{N}\sum_{q=0}^{N-p} p_{p,q}\,|\xi_{\phi,\eta_a}(p,q)\rangle\langle\xi_{\phi,\eta_a}(p,q)|$, where each term $|\xi_{\phi,\eta_a}(p,q)\rangle = \frac{1}{\sqrt{p_{p,q}}}\sum_{n=p}^{N-q}\mathcal{C}_n(N,k)e^{-in\phi}\sqrt{B^n_{p,q}}\,|n-p,N-n-q\rangle$ is a pure state conditioned on the number of lost photons, p and q, in each arm [26]. Unlike, $\rho^{\text{gHB}}_{\phi,\eta_a}$, $\tilde{\rho}^{\text{gHB}}_{\phi,\eta_a}$ does not have a direct sum structure since the states corresponding to the same total number of lost photons $r = p+q$ do not satisfy orthogonality. However, we note that, due to the convexity of QFI [20, 215], one can still obtain an analytical upper bound to the QFI (for more details see [26]). We remark that in this case too the computation of the QFI and that of the QCRB could be performed analytically. However, the measurement compatibility requires the HCRB, and determining its analytical expression is challenging for reasons mentioned in Section 4.3.4.

Double homodyne measurement: In Fig. 4.5, we plot r^C_H and r_{BG} as a function of y for the double measurement on different probe states. Specifically, in panel (a), we consider HB states for $N = 2,4,6,8$, in panel (b), we consider the gHB states: $|\Psi_{\text{gHB}}(0,N)\rangle$ for $N = 2,3,4,5,6,7$, and compute the CRB, QCRB, and HCRB at $\eta_a = 0.5$.

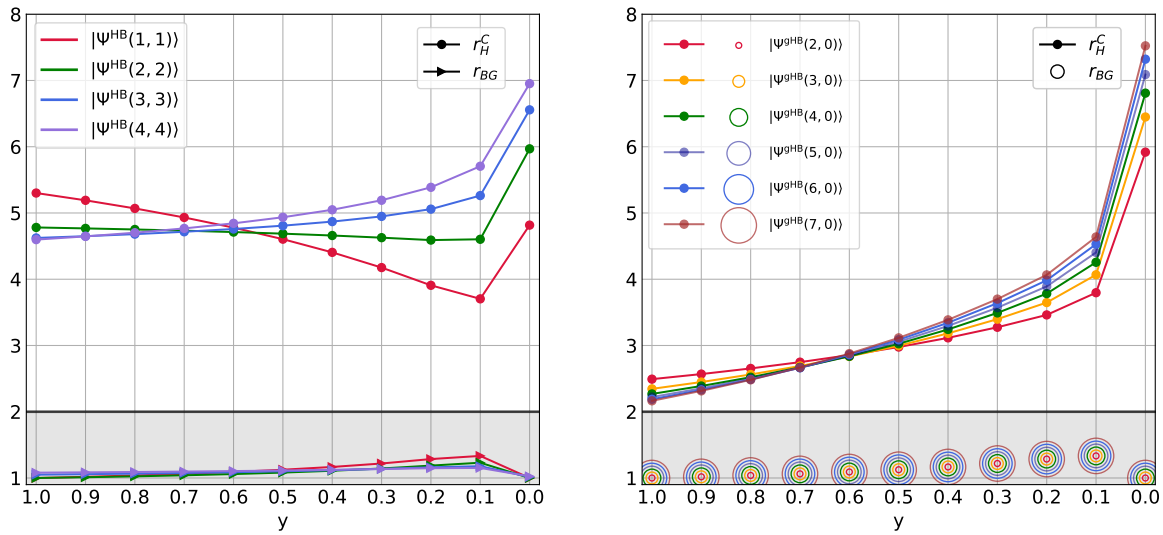

FIGURE 4.5: Plot of measurement compatibility measure r^C_H and fundamental compatibility measure r_{BG} versus the weights y for the joint-estimation of phase and losses in one arm of the MZI with a known amount of loss on the reference arm. HB states with $N = 2,4,6,8$ (panel (a)) and gHB states with $N = 2,3,4,5,6,7$ (panel (b)), and double homodyne measurement are considered. The curves are plotted at $\eta_a = 0.5$, $\eta_b = 0.5$, and $\Delta = 0$. Note that for HB and gHB states, the measurement compatibility exhibits an intersection at $y = 0.6$, causing its behavior with respect to N to change on either side of this point. In contrast, the fundamental compatibility increases slightly as N increases.

In panel 4.5(a), we observe different orderings in compatibility for phase and loss depending

on the photon number N. When phase has more weight, $y \simeq 1$, increasing the photon number appears advantageous for r_H^C: one can attribute this to more distinct fringes in the probabilities of the two-homodyne outcomes. On the other hand, when loss has more weight, $y \simeq 0$, lower N results in better compatibility. As a consequence, the curves show an intersection around $y = 0.6$. The inspection of the fundamental incompatibility via r_{BG} reveals that this feature is specific to our choice of measurement, with higher N allowing for better compatibility, at a difference with respect to the previous case (panel Fig. 4.3(a)). In panel 4.5(b), the same trends are found for the double homodyne measurement, with an intersection occurring around $y = 0.6$. Both the individual and the collective behaviours of r_{BG} remain the same as in Fig. 4.3(b).

Varying loss in reference arm: An investigation for generic loss reveals that the crossing point depends on the level of loss. Looking at the extreme cases, it is found that, for high losses on the reference arm ($\eta_b = 0.1$), r_H^C decreases as N increases regardless y, whereas for low losses ($\eta_b = 1$), it increases with N for all values of y (see Appendix A7).

Photon counting: In Fig. 4.6, we investigate the measurement compatibility for photon counting for this setting. In particular, panel 4.6(a) corresponds to HB states with $N = 2, 4, 6, 8$ and panel 4.6(b) corresponds to gHB states with $N = 2, 3, 4, 5, 6, 7$. In panel 4.6(a), we find that collectively, r_H^C exhibits the same features with respect to N. For a given N, the minimum value is achieved at $y = 0.9$ i.e., when the errors on loss bear little importance. However, with the increase in the number of photons, r_H^C also increases. In panel 4.6(b), r_H^C remains constant and close to 1 for all values of N, except in proximity of $y = 1$.

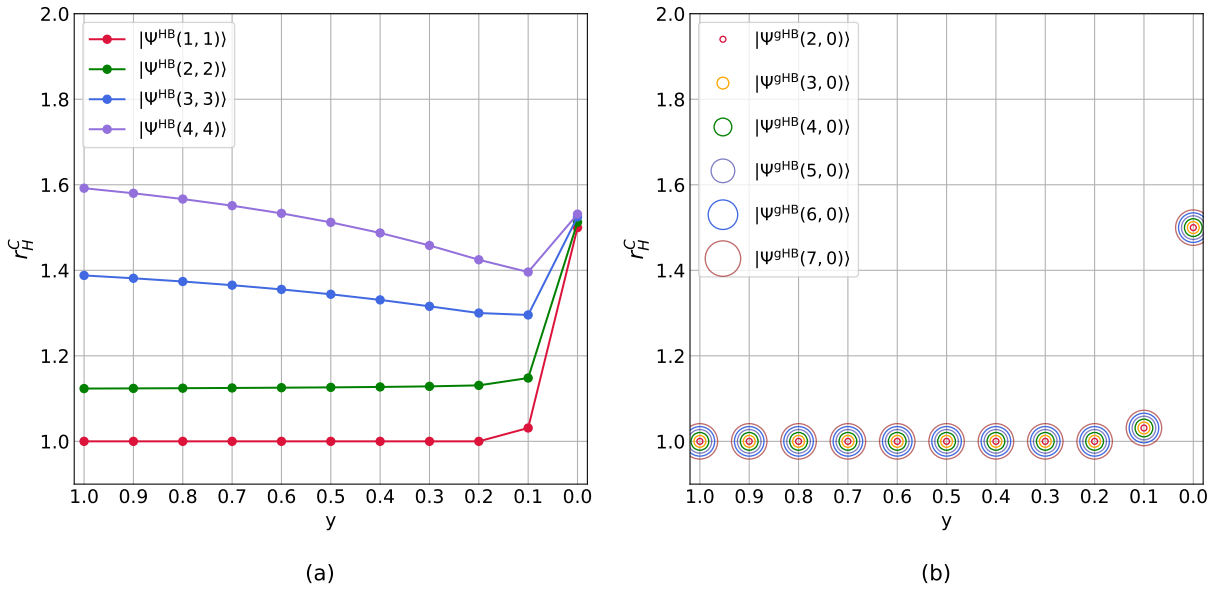

FIGURE 4.6: Plot of measurement compatibility measure r_H^C versus the weights y for photon counting for the joint-estimation of phase and losses in one arm of the MZI with a known amount of loss on the reference arm. HB states with $N = 2, 4, 6, 8$ (panel(a)) and gHB states with $N = 2, 3, 4, 5, 6, 7$ (panel(b)) are considered. Notably, the measurement compatibility remains high in this case as well, exceeding that of the double homodyne measurement, with optimal compatibility occurring at $N = 2$. However, the compatibility strongly decreases as N increases. The other known parameters are taken at the same values as those used in the assessment of the double homodyne measurement.

4.4.2 Loss analysis

An analysis at different levels of losses η_a and η_b is reported in Fig. 4.7 for the double homodyne measurement, illustrating its performance in terms of compatibility of different states for equal weights for the two parameters, $y = 0.5$. For moderate loss, measurement compatibility (panel 4.7(a)) only shows a weak dependence on η_a and η_b, while a decrease in transmission entails a decrease of the compatibility as N grows. Inspection of the fundamental compatibility r_{BG} (panel 4.7(b)) shows that, in the central region, compatibility is not assured for intermediate loss: this makes it relatively easier to approach the Holevo limit with a realistic measurement. A similar analysis for photon counting with respect to different values of losses is illustrated in Fig. 4.8. One can infer that, overall, this choice of the measurement offers better compatibility than homodyne, as its value remains below 1.8. Photon counting seems more effective in achieving the limit of HCRB in this multiparameter example.

Note that we have considered the HB states in Fig. 4.8 since r_H^C for the gHB state: $|\Psi^{\mathrm{gHB}}(N,0)\rangle$ with $N = 2$ and $N = 4$ coincide with each other similar to Figs. 4.4(b) and 4.6(b). Nevertheless, we have observed higher compatibility even for these states.

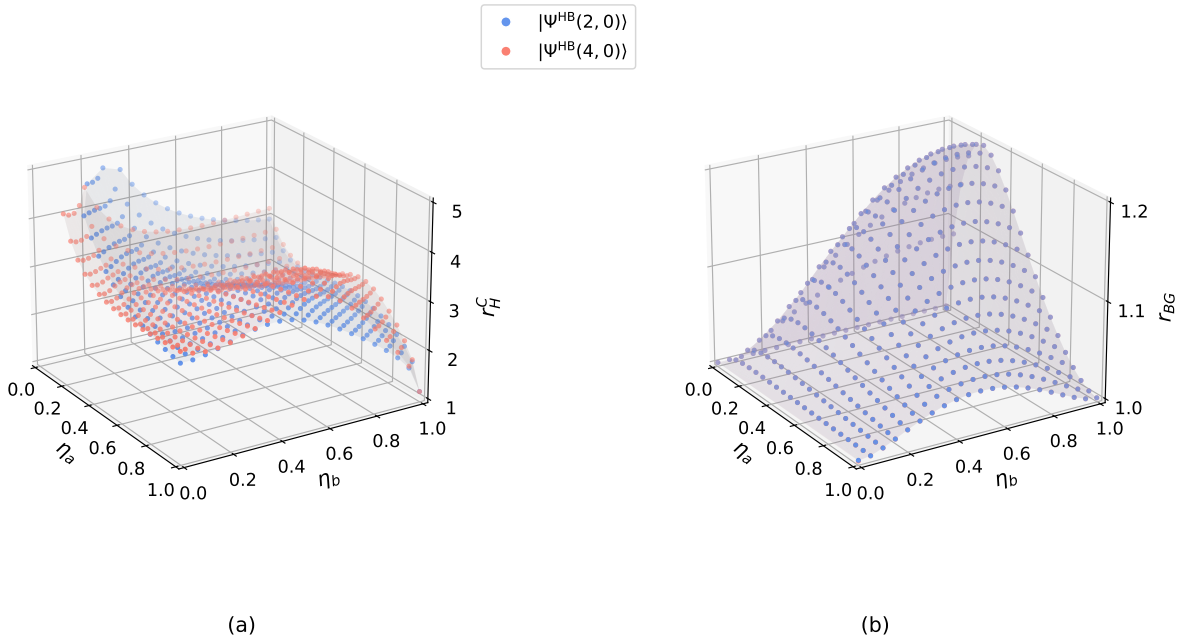

FIGURE 4.7: *Joint-estimation of phase and loss:* Three-dimensional plots of double homodyne measurement compatibility r_H^C (panel (a)) and fundamental compatibility r_{BG} (panel (b)) seen as a function of the losses, η_a and η_b, in each arm with equal parameter weights i.e., at $y = 0.5$. The probe state considered here is the gHB state $|\Psi_{\mathrm{gHB}}(N,0)\rangle$ with $N = 2$ (blue dots) and $N = 4$ (red dots) which create smooth surfaces. Note that the points closer to low values of losses exhibit high measurement and fundamental compatibilities. Also, note that the fundamental compatibility does not vary with respect to the chosen values of N for almost all pairs of values of losses resulting in overlapping points.

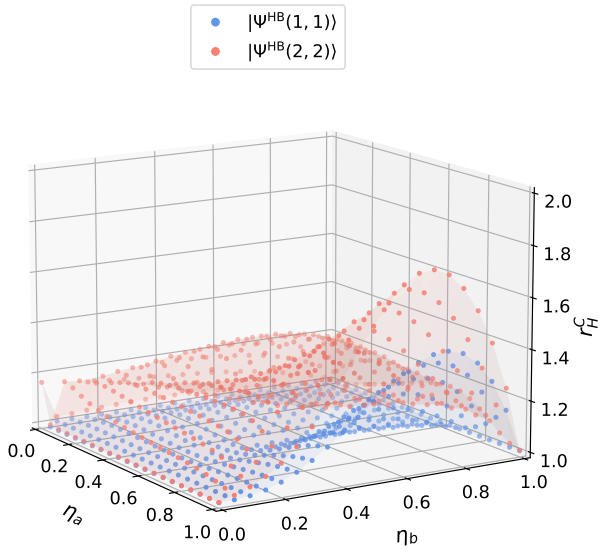

FIGURE 4.8: *Joint-estimation of phase and loss for photon counting:* Three-dimensional plots of measurement compatibility r_H^C versus losses at equal weights. The probe state considered here are the HB states: $|\Psi_{\text{gHB}}(1,1)\rangle$ and (blue dots) and $|\Psi_{\text{gHB}}(2,2)\rangle$ (red dots) which create smooth surfaces. Note that for the combinations of η_a and η_b plotted here, the compatibility remains relatively high.

4.5 Joint-estimation of phase and phase diffusion

In last example, we consider the joint estimation of phase and phase diffusion while assuming known amount of losses in both arms. For simplicity, the output probe state $\rho_{\phi,\Delta}^{\text{gHB}}$ is obtained from Eq. 4.10 by setting equal amount of losses in both arms, $\eta_a = \eta_b = \eta$, yielding
$\rho_{\phi,\Delta}^{\text{gHB}} =$
$\sum_{p=0}^{N}\sum_{q=0}^{N-p}\sum_{n,m=p}^{N-q}\mathcal{A}_{n,m,p,q}(N,k,\eta_{a0},\phi,\Delta)\,|n-p,N-n-q\rangle\,\langle m-p,N-m-q|$.

Double homodyne measurement: In Fig. 4.9, panel (a) represents the plots of r_H^C and r_{BG} versus y for HB states with $N = 2,4,6,8$ and panel (b) represents the same plots for gHB states with $N = 2,3,4,5,6,7$. We set $\Delta = 0.1$ and $\eta_{a0} = 0.999$ (99.9% transmission loss in both arms).

Firstly, we report a recognizable behavior of r_{BG}: since phase and phase diffusion correspond to observables that are weakly compatible i.e.,
$\text{Tr}(\rho_{\phi,\Delta}^{\text{gHB}}[L_\phi, L_\Delta]) = 0$ [185, 34, 144], the system reaches maximal fundamental compatibility i.e., $r_{BG} = 1$ for all values of y in both panels. As for the behavior of r_H^C, in panel 4.9 (a), we find an inversion of the ordering as for the case of loss in Fig. 4.5, but this time with the opposite trends. The curves intersect around $y = 0.9$ due to which, for $y \leq 0.9$, the overall magnitude of r_H^C increases as N increases, whereas for $y > 0.9$, the magnitude decreases as N increases. In panel 4.9(b), most features observed in panel 4.9(a) remain the same, except that the dependence of r_H^C on N at $y = 1$ is much less pronounced.

Photon counting: For the photon counting measurement, we find that the FIM is singular for HB

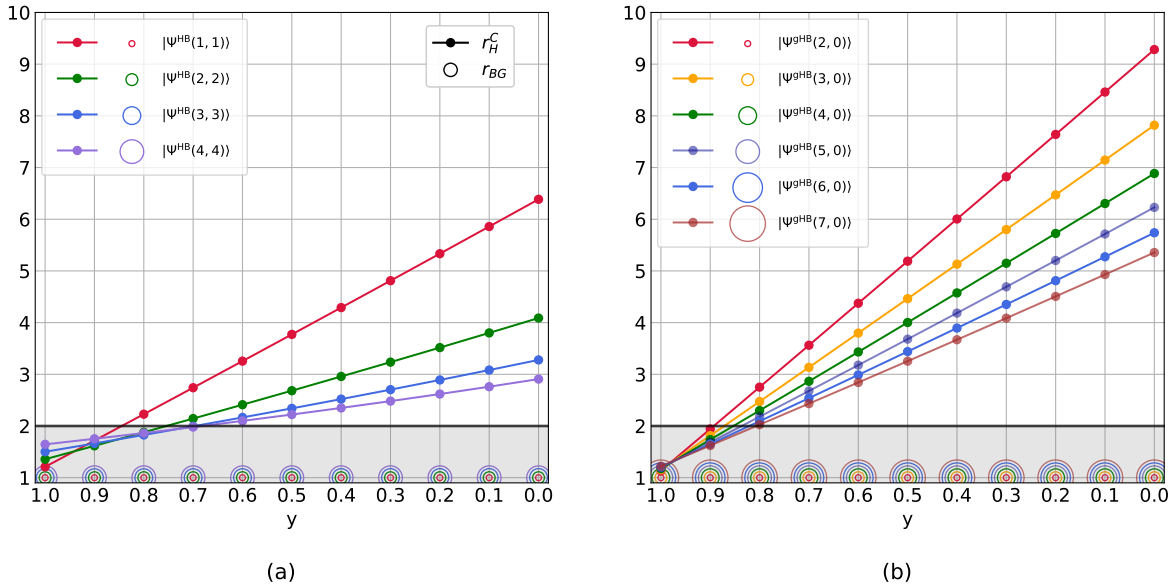

FIGURE 4.9: Plot of measurement compatibility measure r_H^C and fundamental compatibility measure r_{BG} versus the weights y for the joint-estimation of phase and phase diffusion in the MZI with equal losses in both arms. HB states with $N = 2, 4, 6, 8$ (panel (a)) and gHB states with $N = 2, 3, 4, 5, 6, 7$ (panel (b)), and double homodyne measurement are considered. The curves are plotted at $\eta = 0.999$ and $\Delta = 0.1$.

states, while for gHB states it reaches large values in general, and singularity may occur. We could attribute this to the fact that intensity measurement at the outputs of the MZI cannot distinguish a decrease in contrast due to the shift of the fringes (associated to ϕ) or to an overall reduction of visibility (associated to Δ). An auxiliary phase shift may be introduced in order to resolve such an ambiguity [140].

4.5.1 Double homodyne versus optimal separable measurement

The weak compatibility in this multiparameter example determines that an advantage may exist in the use of collective measurements, as captured by the HCRB. It is thus meaningful to focus on optimal separable strategies, identified by the NHCRB, thus using the associated compatibility r_H^N. We find that our example is characterized by the presence of a gap: $1 \leq r_H^N \leq 2$ (see Figs. 4.14 and 4.16). Notice that, since we deal with a two-parameter estimation ($p = 2$), the measure cannot exceed 2 as mentioned in Section 4.3.3. As a result, the quantity r_N^C, the NHCRB-based measurement compatibility, earns its relevance here and is plotted in Fig. 4.10 against the parameter weights, for the same set of probe states and parameter values of η and Δ as in Fig. 4.9. We desume that r_N^C paints a more optimistic picture of our measurements, with higher compatibility values i.e., $r_N^C \leq 2$ achieved when $0.5 \leq y \leq 1$ in panel 4.10 (a), and $r_N^C \leq 2.2$ when $0.7 \leq y \leq 1$ in panel 4.10(b), for all values of N considered.

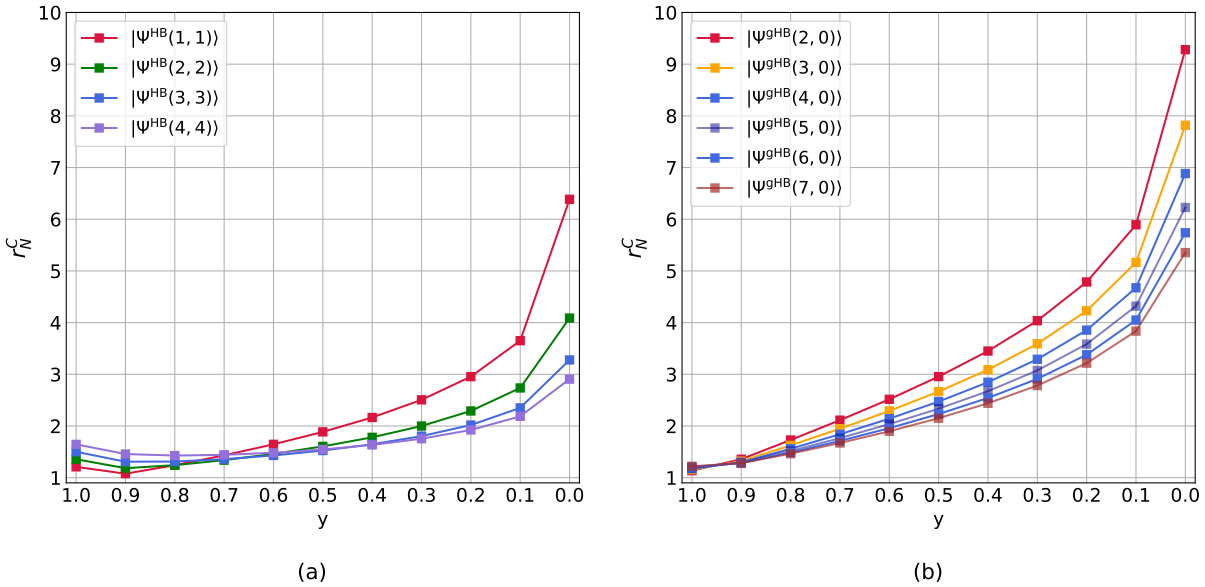

FIGURE 4.10: Plot of NHCRB-based measurement compatibility r_N^C versus the weights y for the joint-estimation of phase and phase diffusion in the MZI with equal losses in both arms. HB states with $N = 2, 4, 6, 8$ (panel (a)) and gHB states with $N = 2, 3, 4, 5, 6, 7$ (panel (b)), and double homodyne measurement are considered. The curves are plotted at $\eta = 0.999$ and $\Delta = 0.1$.

4.6 Discussion

4.6.1 Effectiveness of double homodyne measurement

In view of practical considerations, we note the following about the double homodyne measurement in terms of it compatibility. A closer inspection of the performance of the double homodyne measurement under varying losses in each mode, η_a and η_b, with equal parameter weights (see Fig. 4.7(a)), reveals important insights into the practical relevance of our results. For the state $|\Psi_{\text{gHB}}(2,0)\rangle$, we find that the measurement compatibility, r_H^C, remains below 2.2 for a number of coordinates (η_a, η_b) within the ranges: $0.8 \leq \eta_a \leq 1$ and $0.8 \leq \eta_b \leq 1$. For the state $|\Psi_{\text{gHB}}(4,0)\rangle$, the region corresponding to the same upper bound of r_H^C occurs within the ranges: $0.9 \leq \eta_a \leq 1$ and $0.9 \leq \eta_b \leq 1$. Although, these regions may appear rather far from the ideal limit, they still offer relatively high compatibility in practice. We base this on the fact that the double homodyne measurement is viewed as an outstanding solution in metrology for its high efficiency and high noise rejection. For the case of phase diffusion, instead, in comparison with Fig. 4.9, the results in Fig. 4.10 shed a more optimistic light when the measurement is benchmarked against the best-performing separable measurement characterized by the NHCRB. The relevance of r_H^C becomes even more clear when considered alongside the fundamental compatibility, r_{BG}. Owing to the fact that the value of r_{BG} remains consistently below 1.05 not only in the ranges: $0.8 \leq \eta_a \leq 1$ and $0.8 \leq \eta_b \leq 1$ but also in the high loss regions (Fig. 4.7(b)), the double homodyne measurement is closer to optimal information extraction.

4.6.2 Sensitivities for phase and loss

In Fig. 4.11, we present a closer investigation of the individual QFIs for phase and loss for the HB and the gHB state: $|\Psi^{\mathrm{gHB}}(0,N)\rangle$ for $N = 2, 4, 6$, and 8. Specifically, the top row represents the case of $\eta_b = 1$ (no loss in the reference arm) and the bottom row represents the case of $\eta_b = 0.5$ (50% loss in the reference arm). In these cases, we can infer that for a given value of N, the QFI for loss is always greater than that of phase. Alternatively, for $\eta_b = 1$, closed-form expressions for the QFI considering a general definite photon number input state $|\psi_{\mathrm{in}}\rangle = \sum_{n=0}^{N} c_n |n, N-n\rangle$ have been derived in [142].

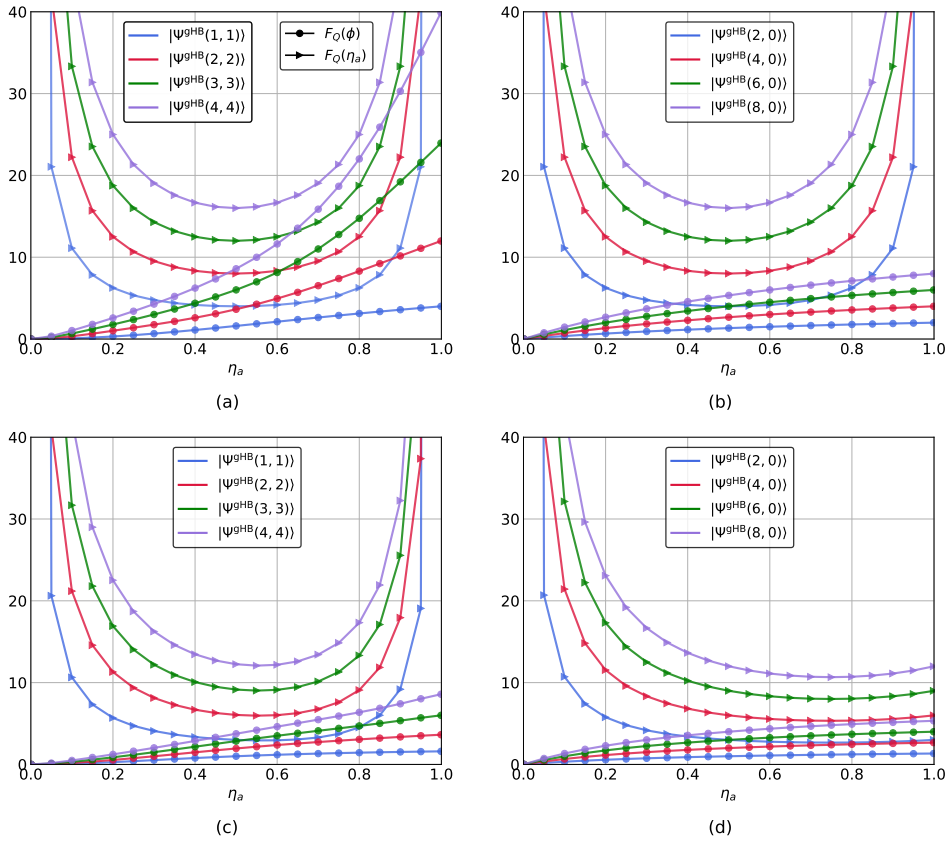

FIGURE 4.11: *Top row:* QFIs for phase and loss for the joint-estimation of phase with no loss on the reference arm for the HB and the gHB state: $|\Psi^{\mathrm{gHB}}(0,N)\rangle$ with $N = 2, 4, 6$, and 8. *Bottom row:* Considering 50% loss on the reference arm the same set of states.

However, at the measurement level, this condition is not necessarily met by the FI matrix of the double homodyne measurement. Considering $\eta_b = 1$, if one were to consider the optimal states for phase and loss, the corresponding QFIs read: $F_{Q\,\phi} = \frac{4\eta_a N}{1-\eta_a}$ [216, 27, 208, 217] and $F_{Q\,\eta_a} = \frac{N}{\eta_a(1-\eta_a)}$ [213, 214, 218]. Plotting these as a function of η_a for a given N indicates a crossing of the curves exactly at $\eta_a = 0.5$ (see Fig. 4.12). This feature implies that in the regime of high loss i.e., $\eta < 0.5$, it is harder to estimate phase than loss, whereas in the regime of low loss i.e., $\eta > 0.5$, it is harder to estimate loss than phase.

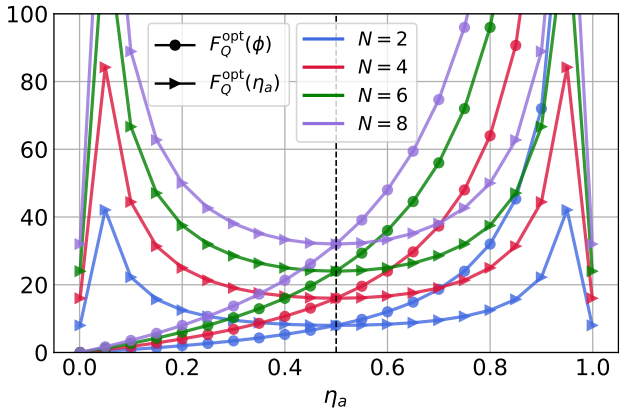

FIGURE 4.12: QFIs for phase and loss considering the respective optimal states with $N = 2, 4, 6$, and 8.

4.6.3 What happens under minimal losses?

We have inspected the behavior of measurement and fundamental compatibility under lossy scenarios. To further elucidate the connection between compatibility and losses in the system, we consider an ideal scenario of minimal losses i.e., $\eta_a = \eta_b = 0.999$, $\Delta = 0$ in Eq. 4.10 while estimating phase and loss in one arm jointly. Considering HB and gHB states with $N = 2, 4, 6$, numerical results show that $r_{BG} \approx 1$ for all values of y, indicating maximal fundamental compatibility. As for the measurement compatibility, we find that the $r_H^C \approx 1$ at $y = 1$ reaching maximal measurement compatibility due to the optimality of the double homodyne measurement in estimating phase [34]. Moreover, r_H^C remains below 1.5 for $y \geq 0.5$ for all the probe states considered (see Appendix A8), hence the double homodyne measurement closely attains the HCRB even with individual copies. This can be understood by considering that r_H^C may be approximated as

$$r_H^C \approx \frac{2y(F_{C\,\phi})^{-1} + 2(1-y)(F_{C\,\eta})^{-1}}{2y(F_{Q\,\phi})^{-1} + 2(1-y)(F_{Q\,\eta})^{-1}} \tag{4.19}$$

since $C_H \approx C_Q$ and $F_{C,Q\,i,j} = 0$ for $i \neq j$. For low loss, the conditions $F_{C\,\eta} \gg F_{C\,\phi}$ and $F_{Q\,\eta} \gg F_{Q\,\phi}$ are satisfied, implying that their contribution to the measurement compatibility is small around $y = 1$. As a result, the dominant contribution comes from $F_{C\,\phi}$ and $F_{Q\,\phi}$, and the ensuing optimality of the measurement keeps the ratio r_H^C fairly constant and closer to 1. This behavior can also be seen in Fig. 4.7, in the low-loss regime with $y = 0.5$.

4.6.4 Separable versus collective measurements

The collective measurements required to attain the HCRB are experimentally challenging to implement. Therefore, with the view of practical feasibility, one must turn towards finite-copy separable measurements, although this comes at a cost of reduced precision. Firstly, we mention that in the case of pure state models, the HCRB is attainable with optimal measurements already at a single-copy level [161]. Secondly, for more general models, the NHCRB is attainable with separable measurement on finite number of identical copies of the probe state in many cases. These include the estimation of qubit rotations in the presence of phase damping using a two qubit probe and more interestingly, the joint-estimation of phase and loss in one arm [165]. However, it must be noted that the NHCRB is not always tight—for instance, in the model described in Example *A*

of [167]. In this case, although $C_N = C_Q$, the presence of fundamental incompatibility renders the NHCRB unattainable with any separable measurement. A tight, ultimate precision bound for separable measurements was formulated by Hayashi [168], and more recently, a strict gap between this tight bound and the NHCRB was demonstrated using conic programming [169], further cautioning that there exist cases where the NHCRB is not attainable.

For the joint-estimation of phase and loss in one arm, a single-copy optimal measurement obtained from the SLD for phase with random single-photon input states of the form: $|\psi\rangle = c_0 |0,1\rangle + c_1 |1,0\rangle$ has been demonstrated to fully attain the HCRB for $\eta_a \geq 0.5$ [143]. Furthermore in [143], it has been numerically demonstrated that there exists certain values of N and η_a at which this measurement attains the HCRB. This inference is in agreement with our numerical result $r_H^N = 1$. We can conjecture that this is due to the fact that the output probe, in this case, is expressed as a direct sum of pure states corresponding to the number of lost photons and there exists a separable measurement with a direct-sum structure achieving the HCRB [161]. However, in the case of phase diffusion, the loss of direct sum structure may signal the impossibility to attain the HCRB at a single-copy level. Furthermore, it has been shown that if the HCRB cannot be attained at a single-copy level, it can never be attained with any finite number of copies, which makes the single-copy attainability a fundamental one [219]. Of course, collective measurements on infinitely many copies are known to saturate the HCRB, but they are resource inefficient. Nevertheless as mentioned earlier, with finite resources and separable measurements, one can still attain the NHCRB.

In the following sections, we will investigate the CQE for the joint-estimation of phase and loss in one arm and for the joint-estimation of phase and phase diffusion.

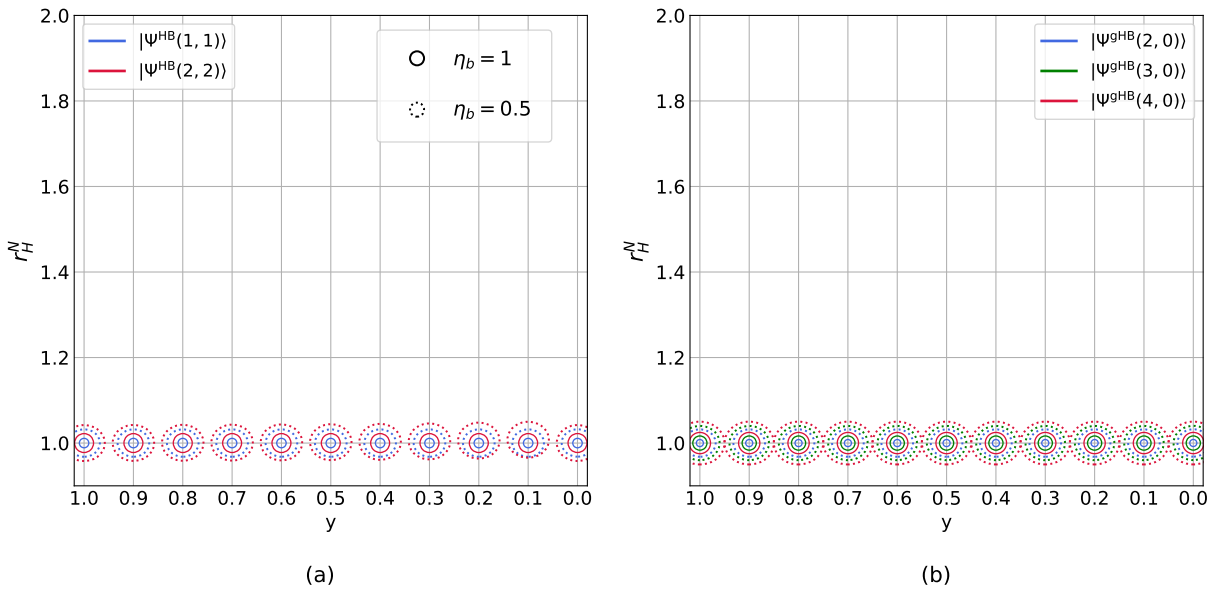

FIGURE 4.13: Plot of r_H^N versus weights at $\eta_b = 0.5$, $\Delta = 0.001$ for (a) the HB state with $N = 2, 4$ and (b) the gHB state: $|\Psi^{\text{gHB}}(N,0)\rangle$ with $N = 2, 3, 4$. Note that for all values of weights, collective measurements offer no advantage over separable ones.

4.6.4.1 Parameter weights analysis

Phase and loss: We study the behavior of the ratio r_H^N quantifying the CQE with respect to the parameter weights. In Fig. 4.13, the points are plotted for $\eta_b = 1$ and $\eta_b = 0.5$ in a combined manner. For both the cases of lossless and lossy reference beams and the HB and the gHB states considered, we notice that $r_H^N \sim 1$ for all values of y. This indicates that regardless of the resourcefulness of the states and the extent of losses in the reference beam here, the extent of penalization on either parameters has no bearing on the advantage offered by collective measurements.

Phase and diffusion: The behavior of r_H^N with respect to the parameter weights for the same set of probe states reveals a fundamentally different attribute of the CQE for this estimation problem. In Fig. 4.14, we plot the measure for $\eta_a = \eta_b = 0.999$ and $\Delta = 0.1$. We notice that, for all values of y, there is a gap between the NHCRB and the HCRB implying that the collective measurements offer some advantage. In particular, as the number of photons increases, the CQE decreases due to the following: (i) intuitively, the presence of more photons makes the state more prone to decoherence, and accordingly the quantumness of the measurement decreases, reducing its advantage over separable ones, and (ii) mathematically, we know from Section 2.1.5.2 that $\lim_{N\to\infty} NC_N(\rho_{\vec{\theta}}^{\otimes N}) = C_H$. Even though we deal with a single copy of the probe, one may, by analogy using the Jordan map, regard individual photons as spatially distinguishable particles, in which case the NHCRB asymptotically tends to the HCRB as the number of particles increases.

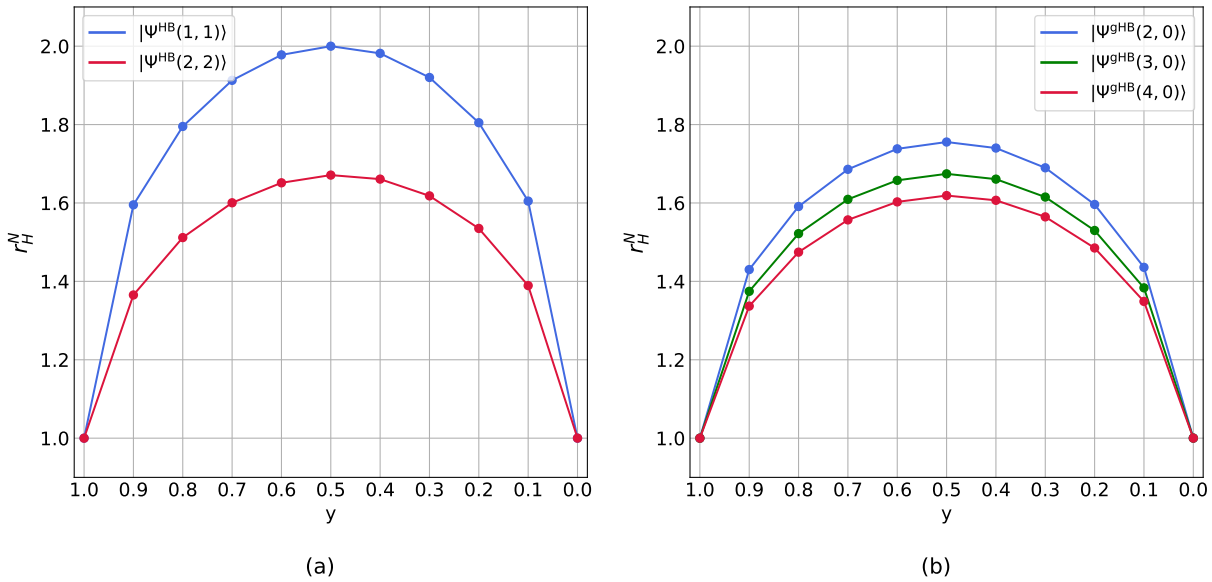

FIGURE 4.14: Plot of r_H^N versus weights at $\eta_a = \eta_b = 0.999$, $\Delta = 0.1$ for (a) the HB state with $N = 2, 4$ and (b) the gHB state: $|\Psi^{\text{gHB}}(N, 0)\rangle$ with $N = 2, 3, 4$. Note that for equal weights i.e., $y = 0.5$, the gap between the NHCRB and the HCRB is the maximum for a given state indicating a maximal CQE at this point.

4.6.4.2 Loss and phase diffusion analysis

Having examined the behavior of r_H^N with respect to the weights, we now study how this measure varies with different parameter values.

Phase and loss: In Fig. 4.15, we plot r_H^N as a three-dimensional plot versus the losses in each arm

η_a and η_b at equal weights $y = 0.5$. As expected, for the gHB state: $|\Psi_{\text{gHB}}(N, 0)\rangle$ with $N = 2, 4$, the collective measurements offer no advantage over separable for all pairs of losses considered. We have checked that the HB state with the same photon numbers also exhibit the same behavior.

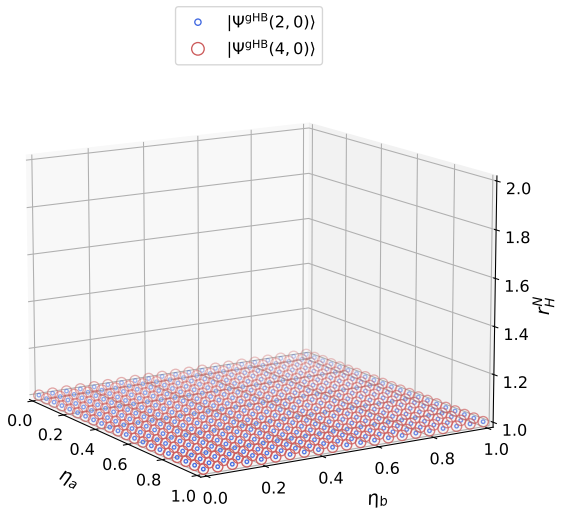

FIGURE 4.15: Three-dimensional plot of r_H^N versus losses at equal weights. The probe state considered here is the gHB state: $|\Psi_{\text{gHB}}(N, 0)\rangle$ with $N = 2, 4$. The points are plotted as concentric circles with varying diameters. Since they share a common center, this indicates that the points overlap. Note that for all pairs of losses considered, collective measurements offer no advantage over separable ones for the joint-estimation of phase and loss in one arm.

Phase and diffusion: In Fig. 4.16, we plot r_H^N versus the diffusion parameter Δ for the HB state and the gHB state: $|\Psi_{\text{gHB}}(N, 0)\rangle$ with $N = 2, 4$. For the HB state ($N = 2$), in the small diffusion region i.e., $0 \leq \Delta \leq 0.5$, the CQE remains close to its maximal value 2. For $\Delta > 0.5$, the CQE drops indicating that the quantum enhancement drops when the diffusion becomes large. In contrast, the curves for HB state ($N = 4$) and the gHB states begin at maximal CQE and quickly drops attaining saturation for large diffusion, although the former exhibits a non-montonic behavior. With respect to photon numbers, for each set of probe states, the CQE, unsurprisingly, decreases as N increases.

The observations made from Figs. 4.13, 4.14, 4.15, and 4.16 are in agreement with our expectation that loss of photons is a classical process, and therefore should be unaffected by the use of collective measurements. In contrast, diffusion or phase fluctuation benefits from entanglement in the measurement.

4.6.5 Fundamental compatibility for the estimation of equal losses on both arms

In this section, we supplement our findings for the joint-estimation of phase and loss in one arm with the scenario of joint-estimation of phase and equal loss $\eta_a = \eta_b = \eta$ in both arms. This is a special case where the fundamental incompatibility vanishes implying that the optimal measurements for phase and loss are compatible. In the context of the HB and the gHB states $|\Psi_{\text{gHB}}(N, 0)\rangle$, Fig. 4.17

indicates that $r_{BG} = 1$ for all values of losses and parameter weights. These results are consistent with earlier findings for two-mode Fock states [24], Gaussian states [220], and more recently in [177].

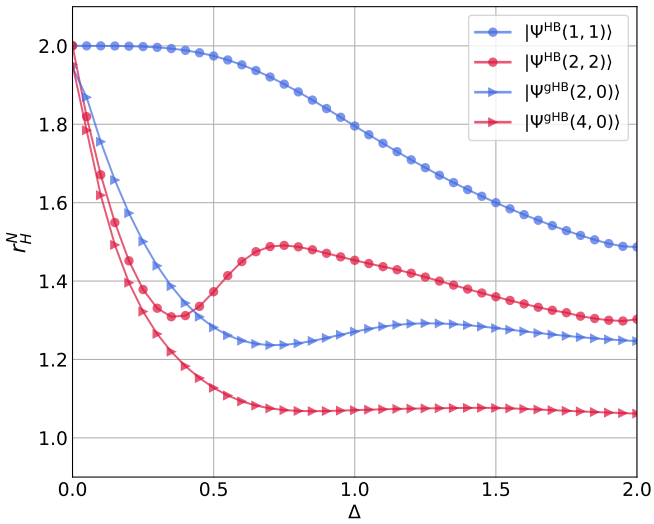

FIGURE 4.16: Plot of r_H^N versus phase diffusion at equal weights. The probe states considered here are the HB state and the gHB state: $|\Psi_{\text{gHB}}(N,0)\rangle$ with $N = 2, 4$. Note that For low diffusion, the value starts close to the maximal CQE, $r_H^N = 2$, and decreases as diffusion increases, indicating that the enhancement gradually diminishes.

In fact, in [24], the scenario of estimating equal losses together with phase was considered as an example in which the three aspects of metrological compatibility—probe compatibility, fundamental compatibility, and uncorrelated estimators—are satisfied. This occurs because the optimal measurement for loss is simply a photon counting measurement that counts the total number of lost photons $r = p+q$ in each arm yielding a binomial distribution: $p_\eta(r) = \text{Tr}(\rho_{\phi,\eta}\Pi_r) = \binom{N}{r}\eta^{N-r}(1-\eta)^r$, from which η is estimated. Furthermore, $F_{C\,\eta} = \sum_{r=0}^{N} \frac{1}{p_\eta(r)}\left(\frac{\partial p_\eta(r)}{\partial \eta}\right)^2 = \frac{N}{\eta(1-\eta)} = F_{Q\,\eta}^{\text{opt}}$, which is the expression for the QFI for the optimal probe state for loss [213]. This is also seconded by the optimal measurement for phase, the double homodyne, which also involves photon counters, and therefore there is no fundamental incompatibility. In fact, from the SLDs for phase and loss, it is shown that there exists strong compatibility i.e., $[L_\phi, L_\eta] = 0$ meaning that separable measurements can actually saturate the QCRB yielding optimal performance [24]. We also numerically demonstrate this by computing r_H^N for this case (see Appendix A9) Additionally, we note that regardless of the state $\rho_{\phi,\eta}$, the optimal measurement is always the one that counts the total number of lost photons. Hence, a state with the highest photon-number variance—optimal for phase estimation—also performs equally well for optimal loss estimation, indicating that there is no probe incompatibility in this case either.

4.7 Summary

In this chapter, we asked the question: *how far are we from the performance of collective measurements and optimal information extraction when considering practical separable measurements?* This is limited by the CQE and fundamental compatibility. We addressed this in the following manner.

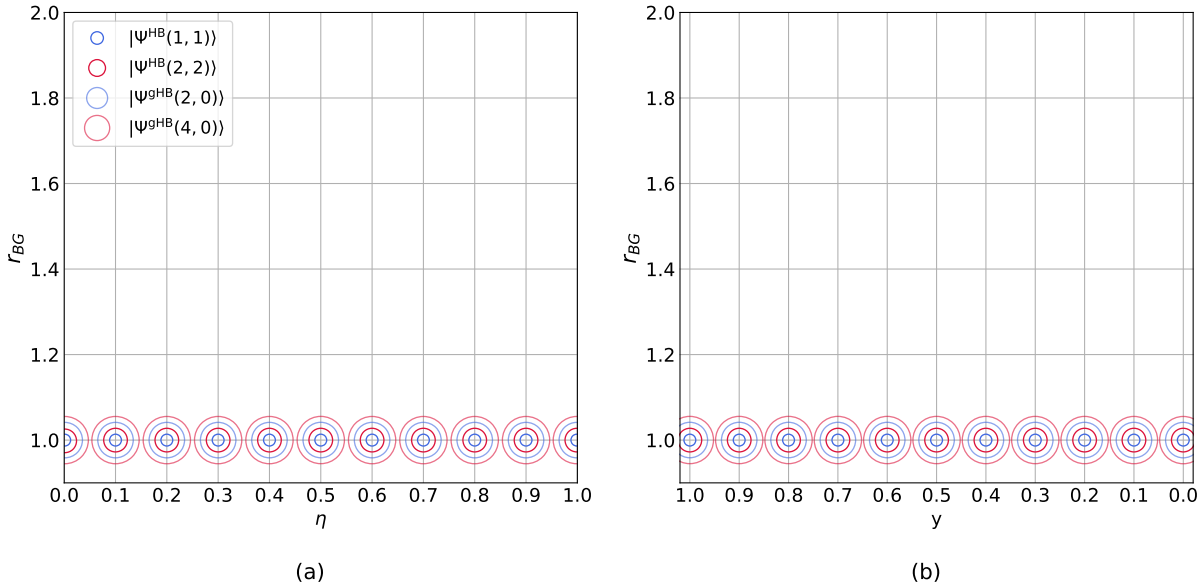

FIGURE 4.17: Plot of r_{BG} versus (a) loss at equal weights in and (b) weights at $\eta = 0.5$. The probe states considered here are the HB state and the gHB state: $|\Psi_{\text{gHB}}(N,0)\rangle$ with $N = 2$ and $N = 4$. Note that the fundamental incompatibility vanishes for this case both with respect to loss, weights, and the values of N considered.

We began by investigating the compatibility offered by double homodyne and photon counting, the standard benchmarks for practical photonics-based quantum sensing protocols. By defining a measure known as the measurement compatibility with respect to the HCRB, we quantitatively studied the behavior for the joint-estimation of phase and loss in one arm with a lossless and lossy reference beams. We used non-Gaussian probe states, in particular the gHB states, and thus the evaluation of the HCRB must take a numerical route, since the model does not belong to the D-invariant class of models. Our results demonstrate that photon counting yields better performance compared to double homodyne for all cases considered, which can be attributed to the use of a non-Gaussian measurement compatible with a non-Gaussian probe [211]. Owing to the high practical efficiency of the double homodyne measurement, we have specified the regions of high compatibility, although this requires maintaining the loss in each arm above 80%, which occurs for a gHB state with $N = 2$. Given the ease of preparing low dimensional probe states, we have also identified relatively high compatibility for these states for both measurements.

A more realistic benchmark for separable measurements is set by the NHCRB, which, although not tight in a few cases, can be attained by a separable measurement for this estimation problem [165, 143]. In view of this, we have defined an alternative measurement compatibility measure based on the NHCRB. However, this measure is only relevant in our second example, the joint estimation of phase and phase diffusion, where a 'fully quantum' metrological scheme—including collective measurements—offers an advantage due to the non-classical nature of the phase-diffusion process, as opposed to the classical process of photon loss where no quantum advantage exists. Furthermore, for the same example, we note that both the HCRB- and NHCRB-based measurement compatibility apply only to double homodyne, since the FIM for photon counting becomes singular. This arises because photon counting cannot uniquely identify all values of phase and diffusion, leading to linearly dependent rows or columns of the FIM.

Estimated parameters	Attainability of bounds	Fundamental compatibility condition
Phase and loss in one arm: $\{\phi, \eta_a\}$ ($\eta_b = 1$ and $\eta_b = 0.5$)	$C_{MI} = C_N = C_H > C_Q$	$[L_\phi, L_\eta] \neq 0$ [142]
Phase and phase diffusion: $\{\phi, \Delta\}$	$C_{MI} = C_N > C_H = C_Q$	$\mathrm{Tr}(\rho_{\phi,\Delta}[L_\phi, L_\Delta]) = 0$ [185, 34]
Phase and equal loss in both arms: $\{\phi, \eta\}$	$C_{MI} = C_N = C_H = C_Q$	$[L_\phi, L_\eta] = 0$ [24]

Table 4.1: A table summarizing the attainability of bounds and the fundamental compatibility condition for the joint estimation problems we have dealt with.

In Table 4.1, we summarize the attainability of the relevant bounds for the estimation problems considered through the equivalence of the MIB, C_{MI}, to the other bounds. This is because the MIB corresponds to a situation where both the optimal separable measurement and the optimal estimator have been found (see Section 2.1.5.3). We have also listed the conditions for fundamental compatibility in each case.

We conclude by highlighting three key takeaways from the table: (i) a separable measurement can attain the HCRB for the joint estimation of phase and loss in one arm, (ii) only collective measurements can achieve optimal performance for the joint estimation of phase and diffusion, and (iii) a separable measurement can attain optimal performance for the joint estimation of phase and equal loss.

Chapter 5

Numerical methods

In this chapter, we present the program developed for the numerical computation of the HCRB for higher-order gHB states, which was used to obtain the corresponding results in Chapter 4. In particular, we introduce several improvements to the existing `HCRB` function from the `QuanEstimation` toolbox, enabling a more efficient and optimized evaluation of the bound. The resulting implementation has been extensively tested and produces accurate results for gHB states with high photon numbers. The full code is publicly available at [221].

We begin by describing the reformulation steps required to numerically solve the convex optimization problem for computing the HCRB. Following this reformulation, the problem is cast as a semidefinite program (SDP), implemented in the `CVXPY` modelling framework, and solved using the `MOSEK` solver. In doing so, we demonstrate a step-by-step Python implementation and highlight improvements made through methods for error handling and the optimization of specific parts of the program.

5.1 SDP formulation

5.1.1 Reformulation of $Z(\vec{X})$ matrix

We introduce the basis $\{\lambda_i\}$, where λ_i are Hermitian matrices orthonormal with respect to the Hilbert-Schmidt norm i.e., $\mathrm{Tr}(\lambda_i\lambda_j) = \delta_{i,j}$. The basis is constructed from the SU(n) generators with the inclusion of the identity matrix. For example, for a two-dimensional state, we have the Pauli matrices and the identity matrix and for the three-dimensional state, we have the Gell-Mann matrices and the identity matrix.

In reference to Eq. 2.67, the elements of the complex matrix $Z(\vec{X})$ read: $[Z(\vec{X})]_{i,j} = \mathrm{Tr}(\rho_{\vec{\theta}} X_i X_j)$, where $\rho_{\vec{\theta}}$ is a general d-dimensional state. Writing, X_i, X_j, and $\rho_{\vec{\theta}}$ in the introduced basis, we have

$$X_i = \sum_{k=1}^{d^2} c_{i,k}\lambda_k = \vec{x}_i \tag{5.1a}$$

$$X_j = \sum_{l=1}^{d^2} c_{j,l}\lambda_l = \vec{x}_j \tag{5.1b}$$

$$\rho_{\vec{\theta}} = \sum_{m=1}^{d^2} (s_{\vec{\theta}})_m \lambda_m = \vec{s}_{\vec{\theta}} \tag{5.1c}$$

Hence,

$$[Z(\vec{X})]_{i,j} = \mathrm{Tr}(\rho_{\vec{\theta}} X_i X_j) = \mathrm{Tr}\left[\left(\sum_{m=1}^{d^2} (s_{\vec{\theta}})_m \lambda_m\right)\left(\sum_{k=1}^{d^2} c_{i,k}\lambda_k\right)\left(\sum_{l=1}^{d^2} c_{j,l}\lambda_l\right)\right] \tag{5.2}$$

The above equation can be rewritten as

$$[Z(\vec{X})]_{i,j} = \sum_{k,l=1}^{d^2} c_{i,k} c_{j,l} [S_{\vec{\theta}}]_{k,l}, \tag{5.3}$$

where $[S_{\vec{\theta}}]_{k,l} = \sum_{m=1}^{d^2} \mathrm{Tr}(\lambda_k\lambda_l\lambda_m)(s_{\vec{\theta}})_m$ are identified as the elements of a matrix $S_{\vec{\theta}}$.
More compactly, one can write

$$[Z(\vec{X})]_{i,j} = \underbrace{\begin{bmatrix} c_{i,1} & \dots & c_{i,d^2} \end{bmatrix}}_{\vec{x}_i^\top} \underbrace{\begin{bmatrix} (S_{\vec{\theta}})_{1,1} & \dots & (S_{\vec{\theta}})_{1,d^2} \\ \vdots & \ddots & \vdots \\ (S_{\vec{\theta}})_{d^2,1} & \dots & (S_{\vec{\theta}})_{d^2,d^2} \end{bmatrix}}_{S_{\vec{\theta}}} \underbrace{\begin{bmatrix} c_{j,1} \\ \vdots \\ c_{j,d^2} \end{bmatrix}}_{\vec{x_j}} \tag{5.4}$$

The equivalence between Eqs. 5.3 and 5.4 can be easily checked for arbitrary values of d^2. As a result,

$$[Z(\vec{X})]_{i,j} = \vec{x}_i^\top S_{\vec{\theta}} \vec{x_j} \tag{5.5}$$

For an estimation of p parameters, we introduce a matrix $\mathbb{X} \in \mathbb{R}^{d^2 \times p}$

$$\mathbb{X} = \begin{bmatrix} c_{1,1} & \dots & c_{p,1} \\ \vdots & \ddots & \vdots \\ c_{1,d^2} & \dots & c_{p,d^2} \end{bmatrix}, \tag{5.6}$$

where the p-th column of $\mathbb{X}$ corresponds to the vector $\vec{x_p}$.
In terms of this matrix, we have

$$Z(\vec{X}) = \mathbb{X}^\top S_{\vec{\theta}} \mathbb{X} \tag{5.7}$$

5.1.2 Reformulation of constraints

5.1.2.1 Positive semi-definiteness

One can decompose $S_{\vec{\theta}}$ via the LDL (Cholesky) decomposition as $S_{\vec{\theta}} = LDL^\dagger = L\sqrt{D}\sqrt{D}L^\dagger$. Letting $R = (L\sqrt{D})^\dagger$, we can write $S_{\vec{\theta}} = R_{\vec{\theta}}^\dagger R_{\vec{\theta}}$. Using this, the first constraint in the minimization (Eq. 2.61) reads

$$\mathrm{Cov} \geq \mathbb{X}^\top R_{\vec{\theta}}^\dagger R_{\vec{\theta}} \mathbb{X} \tag{5.8}$$

Eq. 5.8 represents the constraint for positive semi-definiteness in terms of the optimization variables $\vec{X}$ and Cov. If we consider the block matrix

$$M = \begin{bmatrix} \text{Cov} & \mathbb{X}^\top R_{\vec{\theta}}^\dagger \\ R_{\vec{\theta}} \mathbb{X} & \mathbb{1}_{d^2} \end{bmatrix}, \tag{5.9}$$

the Schur complement of the identity block $\mathbb{1}_{d^2}$ of M given by:
$M/\mathbb{1}_{d^2} = \text{Cov} - \mathbb{X}^\top R_{\vec{\theta}}^\dagger R_{\vec{\theta}} \mathbb{X}$ is positive semi-definite due to Eq. 5.8. As a result, thanks to the Haynsworth inertia additivity formula, M is also positive semi-definite. Therefore,

$$M = \begin{bmatrix} \text{Cov} & \mathbb{X}^\top R_{\vec{\theta}}^\dagger \\ R_{\vec{\theta}} \mathbb{X} & \mathbb{1}_{d^2} \end{bmatrix} \geq 0 \tag{5.10}$$

5.1.2.2 Local unbiasedness

The local unbiasedness condition from Eq. 2.50 can be rewritten as

$$\text{Tr}\left(\frac{\partial \rho_{\vec{\theta}}}{\partial \theta_j} X_i\right) = \sum_{m,k=1}^{d^2} \frac{\partial (s_{\vec{\theta}})_m}{\partial \theta_j} c_{i,k} \,\text{Tr}(\lambda_m \lambda_k) = \sum_{m,k=1}^{d^2} \frac{\partial (s_{\vec{\theta}})_m}{\partial \theta_j} c_{i,k} \delta_{m,k} = \delta_{i,j} \tag{5.11}$$

Since the matrices $\{\lambda_i\}$ are orthonormal, the Hilbert-Schmidt inner product $\text{Tr}(\lambda_m \lambda_k) = \delta_{m,k}$. Hence,

$$\text{Tr}\left(\frac{\partial \rho_{\vec{\theta}}}{\partial \theta_j} X_i\right) = \sum_{m=1}^{d^2} \frac{\partial (s_{\vec{\theta}})_m}{\partial \theta_j} c_{i,m} = \delta_{i,j} \tag{5.12}$$

For estimation of p parameters, we can write the condition Eq. 5.12 more compactly as

$$= \underbrace{\begin{bmatrix} c_{1,1} & \cdots & c_{1,d^2} \\ \vdots & \ddots & \vdots \\ c_{p,1} & \cdots & c_{p,d^2} \end{bmatrix}}_{\mathbb{X}^\top} \underbrace{\begin{bmatrix} \frac{\partial (s_{\vec{\theta}})_1}{\partial \theta_1} & \cdots & \frac{\partial (s_{\vec{\theta}})_1}{\partial \theta_p} \\ \vdots & \ddots & \vdots \\ \frac{\partial (s_{\vec{\theta}})_{d^2}}{\partial \theta_1} & \cdots & \frac{\partial (s_{\vec{\theta}})_{d^2}}{\partial \theta_p} \end{bmatrix}}_{\frac{\partial \vec{s}_{\vec{\theta}}}{\partial \vec{\theta}}} = \mathbb{1}_p, \tag{5.13}$$

where $\frac{\partial \vec{s}_{\vec{\theta}}}{\partial \vec{\theta}}$ is a matrix of size $d^2 \times p$, whose p-th column corresponds to the derivative of the state $\vec{s}_{\vec{\theta}}$ with respect to the parameter θ_p i.e., the vector $\frac{\partial \vec{s}_{\vec{\theta}}}{\partial \theta_p}$.

Analogous to Eq. 2.52b, the local unbiasedness condition becomes

$$\text{Tr}(\nabla \rho_{\vec{\theta}} \vec{X}^\top) = \mathbb{X}^\top \frac{\partial \vec{s}_{\vec{\theta}}}{\partial \vec{\theta}} = \mathbb{1}_p \tag{5.14}$$

Making use of Eqs. 5.10 and 5.14, the convex optimization problem (Eq. 2.67) is cast into the following SDP problem.

$$\begin{aligned} \min_{\mathrm{Cov},\mathbb{X}} \quad & \mathrm{tr}(W\mathrm{Cov}) \\ \text{subject to} \quad & \begin{bmatrix} \mathrm{Cov} & \mathbb{X}^\top R_{\vec{\theta}}^\dagger \\ R_{\vec{\theta}}\mathbb{X} & \mathbb{1}_{d^2} \end{bmatrix} \geq 0 \\ & \mathbb{X}^\top \frac{\partial \vec{s}_{\vec{\theta}}}{\partial \vec{\theta}} = \mathbb{1}_p \end{aligned} \tag{5.15}$$

5.2 Implementation in Python

In this section, we translate the SDP formulation described above into a Python program. We present the main components of our numerical code and highlight the optimizations and improvements (in boxes) implemented to achieve efficient computation for gHB states, in comparison with the program associated with the `HCRB` function in the `QuanEstimation` package. For the full version of the code, including the construction of gHB states and regularization, one may refer to [221].

1. **Inputs:** The `hcrb` function takes three user-provided inputs: (i) `state`, a $d \times d$ matrix representing the output probe state; (ii) `derstate`, a list of length `par` containing all derivatives of `state`; and (iii) `W`, the weight matrix parametrized by y, as defined in Chapter 4.

```
import numpy as np
def hcrb(state,derstate,W):
    d=len(state)
    num=d*d
    par=len(derstate)
```

Error handling: Since `state` is not always full rank, we regularize it by adding a small fraction of a suitable state to avoid numerical instabilities. This regularization is carried out as: $(1-\epsilon)\rho_{\vec{\theta}} + \epsilon\sigma$, where σ is a full-rank state such as the thermal state $\sigma = \frac{\langle n\rangle^n}{(1+\langle n\rangle)^{n+1}} |n\rangle\langle n|$ [221].

2. **Basis:** According to Eq. 5.1, `b1` is a list consisting of $d \times d$ matrices of length d^2. These are the basis matrices which are Hermitian and orthogonal with respect to the Hilbert-Schmidt inner product. `b1` is constructed using the following algorithm.

```
    list2=[]
    list3=[]
    list4=[]
    list5=[]
    list6=[]
    for i in range(0,d):
        for j in range(i+1,d):
# create first list of sparse matrices with entries according to list indices
            m1=np.zeros((d,d),dtype=np.complex128)
            m1[i,j]=1j
            m1[j,i]=1j
```

```
            list2.append(m1/np.sqrt(2))
# create second list of sparse matrices with entries according to list indices
            m2=np.zeros((d,d),dtype=np.complex128)
            m2[i,j]=-1
            m2[j,i]=1
            list3.append(m2/np.sqrt(2))
# create a list of vectors
    for i in range(0,d-1):
        m3=np.zeros(d,dtype=np.complex128)
        m3[i]=1j
        m3[i+1]=-1j
        list4.append(m3)
# orgothonalize the vectors
        org=np.linalg.qr(np.array(list4).T)[0]
        l1=org[:,i]
        list5.append(l1)
# transform each vector to a diagonal matrix
        l2=np.diag(list5[i])
        list6.append(l2)
    b1=[np.identity(d)/np.sqrt(d)]+[mat*(-1j) for mat in (list2+list3+list6)]
```

Optimization: The basis generated by the `suN_generator` function in the `HCRB` function is replaced with the output of `b1`, resulting in a significant speedup.

3. **The derivative matrix:** In view of Eq. 5.13, `dersmatrix` is the matrix $\frac{\partial \vec{s}_{\vec{\theta}}}{\partial \vec{\theta}}$ containing the derivatives of the state with respect to the parameters. This is constructed as follows.

```
    vecdrho=[]
    for i in range(0,par):
        for j in range(0,num):
            vecdrho1=np.real(np.trace(np.dot(derstate[i],b1[j])))
            vecdrho.append(vecdrho1)
    length = len(vecdrho)
    dersmatrix=np.array([vecdrho[i*length // par: (i+1)*length // par] for i in
        range(par)]).T
```

Optimization: In contrast to the `HCRB` function, the use of `dersmatrix` avoids the iterations over the number of parameters in the local unbiasedness constraint that appears later in the code reducing the complexity by p^2.

4. **Construction of $S_{\vec{\theta}}$ and $R_{\vec{\theta}}$ matrices:**

The matrix $[S_{\vec{\theta}}]_{k,l} = \sum_{m=1}^{d^2} \mathrm{Tr}(\lambda_k \lambda_l \lambda_m)\,(s_{\vec{\theta}})_m$ in Eq. 5.3 is constructed using following two-step algorithm:

(a) Part corresponding to λ_k: Convert the list `b1` into a matrix `c1` of size $d^2 \times d^2$, where each row of `c1` consists of the flattened entries of the corresponding element of `b1`.

(b) Part corresponding to $\sum_{m=1}^{d^2} \lambda_l \lambda_m s_{\vec{\theta}}$: For each j from 1 to d^2, compute the matrices `(b1[j] @ state).T` and store them in a list `l2`. Convert `l2` into a matrix `c2` of size $d^2 \times d^2$ in the same way as in step 1, so that each row of `c2` contains the flattened entries of the corresponding element of `l2`.

Finally, $S_{\vec{\theta}}$ is simply obtained as the matrix product: `np.matmul(c1, np.transpose(c2))`.

```
c1=np.array(b1).flatten().reshape(num,num)
l2=[]
for j in range(num):
    l3=(b1[j] @ state).T.copy()
    l2.append(l3)
c2=np.array(l2).flatten().reshape(num,num)
S1=np.matmul(c1,np.transpose(c2))
```

Optimization: In contrast to the conventional element-wise construction of S which requires iterations over d^2 for each row and column, the approach described above reduces the complexity by d^2.

As mentioned earlier beside Eq. 5.8, the matrix $R_{\vec{\theta}}$ is obtained from the LDL decomposition of $S_{\vec{\theta}}$ as follows.

```
import scipy as sc
    lu, d, perm = sc.linalg.ldl(S1, lower=0)
    R=np.conjugate(np.dot(lu,np.sqrt(d))).T
```

In the following steps, the SDP given by Eq. 5.15 is implemented.

5. **Optimization variables:**

   We solve the SDP by making use of the `CVXPY` modeling framework. `X` ($\mathbb{X}$ matrix) and `V` (the covariance matrix) are the optimization variables within this framework.

```
import cvxpy as cp
    V = cp.Variable((par, par))
    X = cp.Variable((num, par))
```

6. **Constraints:**

   The constraints are translate into:

```
    constraints = [cp.bmat([[V, X.T @ R.conj().T], [R @ X, np.identity(num)]]) >> 0]
    constraints += [X.T @ dersmatrix == np.identity(par)]
```

7. **Solution:**

   The SDP is solved via:

```
import mosek
    prob = cp.Problem(cp.Minimize(cp.trace(W @ V)), constraints)
    prob.solve(solver=cp.MOSEK,verbose=True)
```

```
    return prob.value
```

which ends the program.

> *Optimization:* The use of the `MOSEK` solver [222] further improves the speed of the program.

Chapter 6

Conclusions and outlook

To recap, the central aim of this thesis has been to help bridge the gap between the theoretical precision limits developed in multiparameter quantum metrology and their experimental implementation, ensuring a smooth translation from theory to experiment. Towards this goal, we assessed the performance of our main metrological scheme in the setting of quantum interferometry. This scheme used a class of definite photon number states (gHB states) as probe states and with the aim of practical realizability, we deployed separable measurements such as homodyne and photon counters along with the considerations of decoherence present in the MZI. We considered two of the most important decoherence models namely that of phase diffusion and photon losses. Since in most cases, the noise is not characterized apriori, we estimated it along with the phase, a typical parameter of interest in any interferometer. Naturally, this lead us to take the multiparameter approach where the use of practical separable measurements always introduced a trade-off in information extraction among different parameters. This has been the subject of chapter 3, wherein, for the estimation of phase and diffusion, we have investigated the performance of the double homodyne measurement on gHB states in reference to general separable measurements on two-dimensional states. This was captured by the violation of an informational trade-off relation that is respected by two-dimensional probes. For completeness, we also investigated the information content of the probes themselves in addition to information extractability that is specific to the choice of measurement. The results demonstrated that the probe states generated by sending all N photons in one arm of the MZI exhibited the best robustness against noise followed by states obtained from other partitions of N photons in two arms.

Independently, there exists the issue of fundamental incompatibility in any multiparameter problem that lead to estimation trade-offs in the first place. This has been the main subject of interest in chapter 4. We described the issue of measurement incompatibility, and to this end, the estimation of phase and loss provided a paradigmatic example to investigate how far-off are practical separable measurements from the HCRB, a tight fundamental bound that takes into account the fundamental incompatibility. The measurement compatibility, rather, has been investigated for both homodyne and photon counting measurements and for a more realistic performance benchmark we chose the NHCRB, the bound attained by the optimal separable measurement. For completeness, we have also performed the same analysis for the case of phase diffusion. Our results demonstrated that photon counting exhibits higher measurement compatibility than homodyne detection—linked to the use of a non-Gaussian measurement on a non-Gaussian state—for the cases of (i) no loss in the reference arm (not affected by the phase shift) and (ii) a known amount of loss in the reference arm. Lastly, we emphasize that our restriction to the use of separable measurements stems from the impracticality of collective measurements that is known to attain the HCRB.

Despite the promising results obtained for the problems we considered, there is still room to make results that point towards even more realistic experimental scenarios. As a result, there remains the following open questions which could act as future directions to our work. One must note that our results uses tools from local estimation theory which assumes significant prior knowledge on the parameters. In situations, where one operates under lack of prior knowledge, one needs to employ tools from the global (Bayesian) estimation theory which asymptotically (for large repetitions of the experiment) coincides with the local approach. Furthermore, it is important to note that the estimations we considered are *static* in nature i.e., we estimate the value of parameters after some evolution time of the state. Recently, real-time sensing, where the inference happens dynamically as the state evolves in time has been gaining quite some interest with some works already done in this domain [33, 139, 223]. Therefore, the application of a global estimation theory and real-time sensing to our problems may steer our results even more closer to practical setups.

We point out that while our work essentially investigated the performance of metrological schemes by pairing non-Gaussian (gHB states) probes with Gaussian and non-Gaussian (photon counting) measurements. It might be of interest to see the metrological performance of the other combinations: Gaussian probes with Gaussian and non-Gaussian measurements in such noisy interferometric setups. In particular, the existence of a general Gaussian measurement [224] that could potentially saturate the NHCRB in these settings might be of interest.

Lastly, since the gap between the NHCRB and the HCRB is upper bounded by the number of parameters and can be reduced by increasing the number of copies of the probe [165, 166, 170], the impact of estimation of more than two parameters and more than one copy of the probe on measurement compatibility could further extend our results.

Appendix

A1 Bayesian estimators

In this section, we provide some background on the Bayesian framework. It is intended as an extension of the efficient estimators in Section 2.1.2.5 and supports the description of Bayesian inference in Section 1.4.5.2. A stricter framework is given by the Bayesian approach, where the prior knowledge of the parameter is already built into the framework. Here, the unknown parameter is stochastic in nature and follows the prior distribution $p(\theta_i)$.

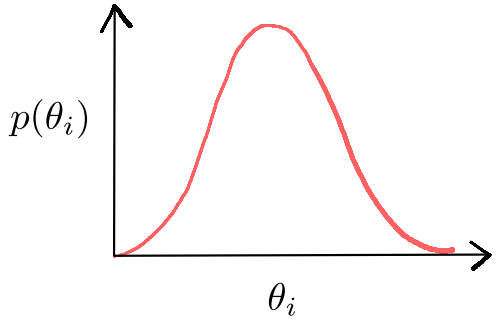

FIGURE 1: Prior probability distribution.

Since all parameter values $\theta_i \in [a_1, \ldots, a_n]$ are accounted for through the prior, the Bayesian estimator is by definition a global estimator unlike the efficient estimators of the Frequentist approach which holds for the exponential family of distributions and the MLE. The prior knowledge becomes relevant only with a finite data sample i.e., for a finite number of repetitions of the experiment. As we have know already from Eq. 1.25 in Section. 1.4.5.2 that the optimal unbiased estimator, in this context, the OBE, is given by the mean of the posterior distribution $p(\theta_i|x)$. Thus, the optimal Bayesian cost i.e., the variance of the OBE averaged over the prior is given by the variance of the posterior distribution averaged over $p(x)$ as follows

$$\overline{\mathrm{Var}}(\tilde{\theta}_i^{\mathrm{OBE}}) = \int d\theta_i p(\theta_i) \mathrm{Var}(\tilde{\theta}_i^{\mathrm{OBE}}) = \int d\theta_i p(\theta_i) \int dx p(x|\theta_i)(\tilde{\theta}_i^{\mathrm{OBE}} - \theta_i)^2 \tag{1}$$

$$= \int dx p(x) \int d\theta_i p(\theta_i|x)(\langle\theta_i\rangle|_{p(\theta_i|x)} - \theta_i)^2 \tag{2}$$

The average over $p(x)$ in the last inequality is due to the Bayes theorem $p(x|\theta_i)p(\theta_i) = p(\theta_i|x)p(x)$.

A2 Particle representation of multiphoton states

In this section, we provide a short background on the particle representation to understand how quantum enhancement may arise from particle and mode entanglement across different partitions of gHB states (Section 3.5.1). Consider the following mode representation of a multiphoton state in N modes

$$|\mathcal{N}\rangle = |n_1\rangle_{m_1} \otimes \cdots \otimes |n_N\rangle_{m_N}\,, \tag{3}$$

where n_k photons are present in the mode m_k and the state has N photons in total across all modes i.e., $\sum_{k=1}^{N} n_k = N$.

Since photons are intrinsically indistinguishable particles, one needs to take a symmetric combination over all possible ways photons occupy the modes, and as a result the particle representation of $|\mathcal{N}\rangle$ reads

$$|\mathcal{N}\rangle \xrightarrow{\text{particle rep.}} \sqrt{\frac{n_1!\ldots n_N!}{N!}} \sum_{\Pi} |\Pi(\{\underbrace{m_1,\ldots m_1}_{n_1},\ldots \underbrace{m_N,\ldots,m_N}_{n_N}\})\rangle\,, \tag{4}$$

where $\Pi(\{1,\ldots N\})$ denotes the permutation of the elements of a list: $\{1,\ldots,N\}$.

For example, the multiphoton state in two modes a and b: $|2\rangle_a |2\rangle_b$ is a mode-separable state takes the following form in the particle representation

$$\begin{aligned} |2\rangle_a |2\rangle_b &= \frac{1}{\sqrt{6}} \sum_{\Pi} |\Pi(\{a,a,b,b\})\rangle \\ &= \frac{1}{\sqrt{6}}(|a\rangle_1 |a\rangle_2 |b\rangle_3 |b\rangle_4 + |a\rangle_1 |b\rangle_2 |a\rangle_3 |b\rangle_4 + |a\rangle_1 |b\rangle_2 |b\rangle_3 |a\rangle_4 \\ &\qquad + |b\rangle_1 |a\rangle_2 |a\rangle_3 |b\rangle_4 + |b\rangle_1 |a\rangle_2 |b\rangle_3 |a\rangle_4 + |b\rangle_1 |b\rangle_2 |a\rangle_3 |a\rangle_4), \end{aligned} \tag{5}$$

which is clearly entangled in particles.

A3 The Jordan–Schwinger map

To supplement the discussion in Section 3.2.2.1, we describe the Jordan–Schwinger correspondence. Crucially, this allows us to interpret how decoherence, such as photon losses and collective dephasing (phase diffusion) act at the level of individual photons by treating them as distinguishable particles as we will see below.

The components of the total angular momentum operator $\hat{J}$: $\{\hat{J}_x, \hat{J}_y, \hat{J}_z\}$ are mapped to bosonic (creation and annihilation) operators $\{\hat{a}^\dagger, \hat{b}^\dagger, \hat{a}, \hat{b}\}$ which simplifies the computation of output state of a MZI given an input state and the phase precision scaling (as seen in Section 1.3.1) [3]. We define the components of the total angular momentum operator

$$\hat{J}_x = \frac{1}{2}(\hat{a}^\dagger \hat{b} + \hat{b}^\dagger \hat{a}) \tag{6a}$$

$$\hat{J}_y = \frac{i}{2}(\hat{b}^\dagger \hat{a} - \hat{a}^\dagger \hat{b}) \tag{6b}$$

$$\hat{J}_z = \frac{1}{2}(\hat{a}^\dagger \hat{a} - \hat{b}^\dagger \hat{b}) \tag{6c}$$

Suppose if there exists certain degrees of freedom, such as time bins, so that N photons are prepared in N respective time bins, then one can introduce the notion of N distinguishable photons in N modes. Hence, in the mode representation we have the state

$$|\mathcal{N}^{(d)}\rangle = |1\rangle_{m_1} \otimes \cdots \otimes |1\rangle_{m_N}\,, \tag{7}$$

where we have used $|\mathcal{N}^{(d)}\rangle$ for a multiphoton state of distinguishable photons. The state in the particle representation reads

$$|\mathcal{N}^{(d)}\rangle \xrightarrow{\text{particle rep.}} |m_1\rangle_1 \otimes \ldots |m_N\rangle_N\,, \tag{8}$$

where it is clear that the k-th photon occupies the m_k mode.

In the theory of angular momentum, the operators $\hat{J}_{\mathrm{i}}\,;\mathrm{i} \in (x,y,z)$ are the generators of rotations $R_{\mathrm{i}}(\theta)$ around the i-th axis by an angle θ such that $R_{\mathrm{i}}(\theta) = e^{-i\theta\hat{J}_{\mathrm{i}}}$. Therefore, using Eq. 6, one can see that the 50:50 beamsplitter operation (with a $-\pi/2$ phase difference between the transmitted and the reflected beams) is a rotation around the x axis by $\pi/2$: $\mathcal{U}_{BS} = R_x(\pi/2) = e^{-i\frac{\pi}{2}\hat{J}_x}$ and the phase shift operation is a rotation around the z axis by ϕ: $\mathcal{U}_\phi = R_z(\phi) = e^{-i\phi\hat{J}_z}$, where $\phi = \phi_b - \phi_a$ as seen in Section 1.2.1.

In relation to Eq. 1.5, the full MZI operation is realized as a sequence of rotations around x axis by $\pi/2$, z axis by ϕ, and x axis by $-\pi/2$ (corresponding to a 50:50 beamsplitter with a $\pi/2$ phase difference between the transmitted and the reflected beams). Thus, the relation between the input and the output operators read

$$\begin{bmatrix}\hat{J}'_x\\ \hat{J}'_y\\ \hat{J}'_z\end{bmatrix} = \underbrace{\begin{bmatrix}1 & 0 & 0\\ 0 & 0 & 1\\ 0 & -1 & 0\end{bmatrix}}_{R_x(-\pi/2)\equiv\text{BS}\,2} \underbrace{\begin{bmatrix}\cos\phi & -\sin\phi & 0\\ \sin\phi & \cos\phi & 0\\ 0 & 0 & 1\end{bmatrix}}_{R_z(\phi)\equiv\text{phase shift}} \underbrace{\begin{bmatrix}1 & 0 & 0\\ 0 & 0 & -1\\ 0 & 1 & 0\end{bmatrix}}_{R_x(\pi/2)\equiv\text{BS}\,1} \begin{bmatrix}\hat{J}_x\\ \hat{J}_y\\ \hat{J}_z\end{bmatrix} \tag{9}$$

$$\begin{bmatrix}\hat{J}'_x\\ \hat{J}'_y\\ \hat{J}'_z\end{bmatrix} = \underbrace{\begin{bmatrix}\cos\phi & 0 & \sin\phi\\ 0 & 1 & 0\\ -\sin\phi & 0 & \cos\phi\end{bmatrix}}_{R_y(\phi)} \begin{bmatrix}\hat{J}_x\\ \hat{J}_y\\ \hat{J}_z\end{bmatrix}, \tag{10}$$

where the MZI operation is simply a rotation around the y axis by ϕ.

Relevance to phase sensing scaling: Since $\hat{J}_z$ is relevant for calculating the phase precision scalings (Section 1.3.1), from Eq. 10, we have

$$\langle\hat{J}'_z\rangle\big|_{|\psi_{out}\rangle} = -\sin\phi\langle\hat{J}_x\rangle\big|_{|\psi_{in}\rangle} + \cos\phi\langle\hat{J}_z\rangle\big|_{|\psi_{in}\rangle}, \tag{11}$$

which is then used to compute $\Delta\phi = \Delta\hat{J}'_z/|d_\phi\langle\hat{J}'_z\rangle|$ via the EPF (Eq. 1.8).

The decoherence picture: Thanks to this mapping, each individual photon (distinguishable particle) may be treated as a individual spins undergoing a local rotation $R^k_{\mathrm{i}}(\theta)$ acting on the k-th photon. Thus, the effective rotations on the total spin space can be written as $R^{\otimes N}_{\mathrm{x}}(-\pi/2) = \bigotimes_{k=1}^{N} R^k_x(-\pi/2) = \mathcal{U}_{\mathrm{BS}} = e^{i\frac{\pi}{2}\hat{J}_x} = \exp\left(i\frac{\pi}{4}(\hat{a}^\dagger\hat{b} + \hat{b}^\dagger\hat{a})\right)$ and $R^{\otimes N}_{\mathrm{z}}(\phi) = \bigotimes_{k=1}^{N} R^k_z(\phi) = \mathcal{U}_\phi = e^{-i\phi\hat{J}_z} = \exp\left(-i\frac{\phi}{2}(\hat{a}^\dagger\hat{a} - \hat{b}^\dagger\hat{b})\right)$. The MZI scheme along with the decoherence effects we considered in chapters 3 and 4 is summarized in Fig. 2, which indicates that

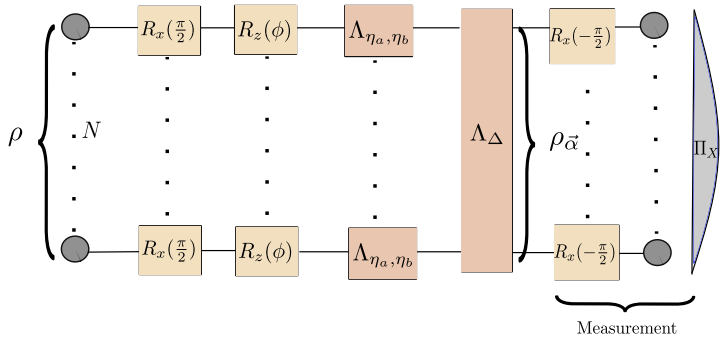

FIGURE 2: The photons in a general two mode multiphoton state $|\psi\rangle = \sum_{n=0}^{N} c_n |n, N-n\rangle$ are treated as N distinguishable particles with spin, each labeled by their distinguishing degree of freedom. Each particle undergoes a sequence of rotations constituting the first beamsplitter, the phase shift, and the second beamsplitter operations. Note that the in the encoded state $\rho_{\vec{\alpha}}$, $\vec{\alpha} = (\eta_a, \eta_b, \Delta)^\top$. Under the influence of noise, photon loss acts locally, whereas phase diffusion has a global effect.

the photon loss channel Λ_{η_a,η_b} acts individually on each photon (see Fig. 3.1), whereas the phase diffusion Λ_Δ acts collectively on all photons.

A4 Commutation condition for the joint-estimation of phase and phase diffusion

Here, we numerically demonstrate that the problem of joint-estimation of phase and phase diffusion exhibits weak compatibility.

From Eqs. 3.62 and 3.63, we write

$$L_\phi = i \sum_{n',m'=0}^{N} A_{n',m'}(N,k,\Delta) \, |n', N-n'\rangle_\phi \langle m', N-m'|_\phi \tag{12}$$

$$L_\Delta = \sum_{n'',m''=0}^{N} B_{n'',m''}(N,k,\Delta) \, |n'', N-n''\rangle_\phi \langle m'', N-m''|_\phi \tag{13}$$

Hence,

$$\begin{aligned} \rho^{\mathrm{gHB}}_{\phi,\Delta} L_\phi L_\Delta = i \sum_{n,n',n'',m''=0}^{N} & C_{n,n'}(N,k,\Delta) A_{n',n''}(N,k,\Delta) \\ & \times B_{n'',m''}(N,k,\Delta) \, |n, N-n\rangle_\phi \langle m'', N-m''|_\phi \, , \end{aligned} \tag{14}$$

$$\begin{aligned} \rho^{\mathrm{gHB}}_{\phi,\Delta} L_\Delta L_\phi = i \sum_{n,n',n'',m'=0}^{N} & C_{n,n''}(N,k,\Delta) A_{n',m'}(N,k,\Delta) \\ & \times B_{n'',n'}(N,k,\Delta) \, |n, N-n\rangle_\phi \langle m', N-m'|_\phi \, , \end{aligned} \tag{15}$$

Then the commutation condition can be evaluated as

$$\mathrm{Tr}(\rho_{\phi,\Delta}[L_\phi, L_\Delta]) = i \sum_{n,n',n''=0}^{N} C_{n,n''}(N,k,\Delta) A_{n',n}(N,k,\Delta) B_{n'',n'}(N,k,\Delta), \tag{16}$$

Eq. 16 is a summation involving a product of six hypergeometric functions, and hence it is difficult to obtain a closed-form solution for it. Therefore, in Fig. 3, we plot Eq. 16 for HB states and gHB states $|\Psi^{\mathrm{gHB}}(N,0)\rangle$ with $N = 2, 4, 6$. We can infer that the commutation condition vanishes for all the states considered which supports the weak compatibility of present for the joint-estimation of phase and phase diffusion.

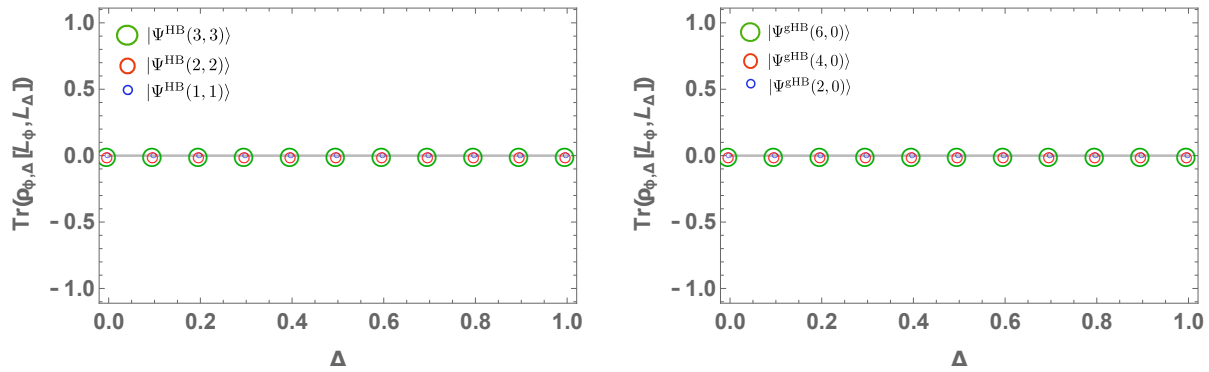

FIGURE 3: Demonstration of the existence of weak compatibility for the joint-estimation of phase and phase diffusion for specific cases of HB and gHB states.

A5 Information extraction versus Δ for $|\Psi_{\mathrm{gHB}}(0,N)\rangle$

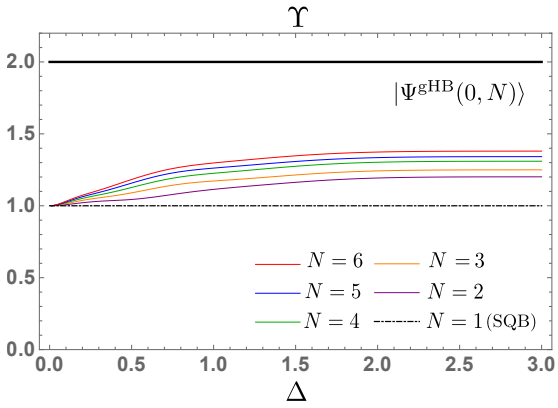

FIGURE 4: The trade-off quantity is plotted as function of Δ for the family of gHB states, $|\Psi_{\mathrm{gHB}}(0,N)\rangle$; $N \in [1,6]$. The SQB and the saturation value of the QCR bound are taken as references. Note that the higher the value of N, the greater the violation of the SQB.

In this section, for $\delta = N$, we analyze the behaviour of the trade-off quantity for various values of N with respect to the phase diffusion parameter. The lossless case is considered in Fig. 4 and we can find that greater violations of the SQB occur at higher values of N. Although states with $N > 6$ are of theoretical interest from the perspective of sensitivity gain, they are highly susceptible to experimental imperfections. It is important to note that violations occur even for states with $N < 4$.

A6 Features of information figure of merits for $|\Psi_{\text{gHB}}(k, N-k)\rangle$

A6.1 Information extraction

Following the discussion in Section 3.5.9, in this section we demonstrate the behavior of information extraction for different partitions of a gHB state with a given N.

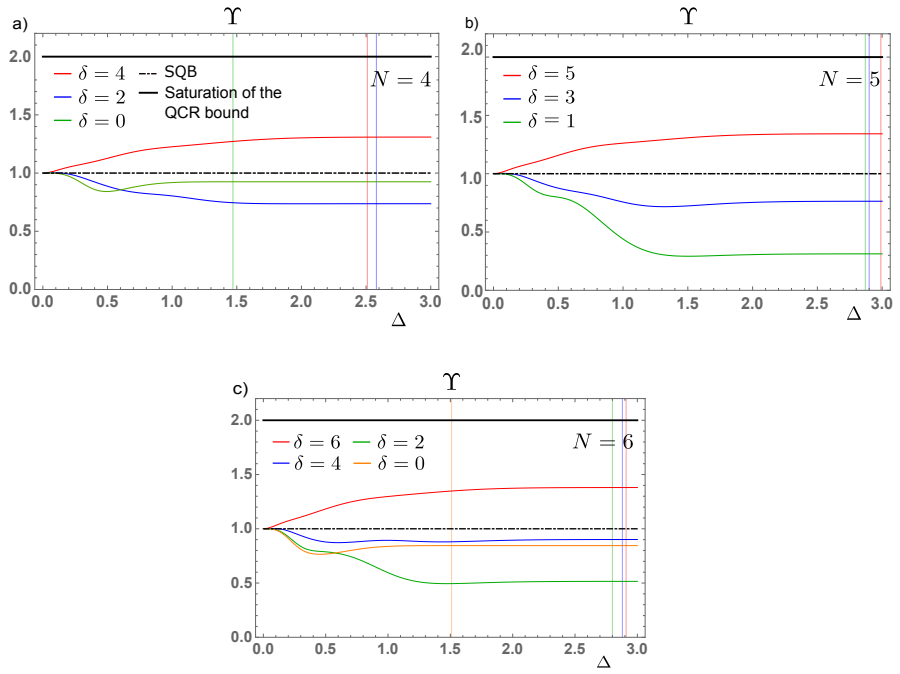

FIGURE 5: The trade-off quantity is plotted as a function of Δ for different partitions of gHB states with a given value N. In each panel, for a given value of δ, a vertical grid line represents the corresponding cutoff value, Δ_{cutoff}. Note that the maximum violation of the SQB is demonstrated by states with $\delta = N$.

For a fixed value of N, we analyze the behaviour of the trade-off quantity for various partitions of N with respect to the phase diffusion parameter. The partitions are denoted as $\delta = h_2 - h_1$, where $h_1 = n$ and $h_2 = N - n$. Again, the lossless case is considered in Fig. 5, and we can clearly observe that the maximum violation of the SQB is demonstrated by the gHB states with $\delta = N$, i.e., the state $|\Psi_{\text{gHB}}(0, N)\rangle$, among all other partitions. Particularly, $\delta = 0$ corresponds to the HB state. Also, we find that the saturation region for the trade-off quantity exists for all values of δ. However, as stated earlier in Section 3.5.9, the cut-off value, Δ_{cutoff}, after which the saturation occurs is different for each state. A suitable value of Δ must be chosen in this region such that all the gHB states regardless of the values of N and δ attain saturation. This is the basis for choosing $\Delta = 1.3$ in Fig. 3.10.

A6.2 Information availability

To supplement the discussion of Section 3.5.7.2, in this section, we take a closer look at the region where peaks appear in Fig. 3.10, in particular for the partition $k = 4$ at $N = 7, 8, 9$. In Fig. 6, we have plotted the diagonal elements of the QFIM for the states considered at both $\eta = 1$ and $\eta = 0.5$. From the top and bottom rows, one can infer that the sensitivity offered by the HB state $|\Psi^{\text{HB}}(4, 4)\rangle$ $(N = 8)$ is lower than that of the neighboring gHB states: $|\Psi^{\text{gHB}}(3, 4)\rangle$ $(N = 7)$ and

$|\Psi^{\mathrm{gHB}}(5,4)\rangle$ ($N=9$) (refer to Fig. 3.10).

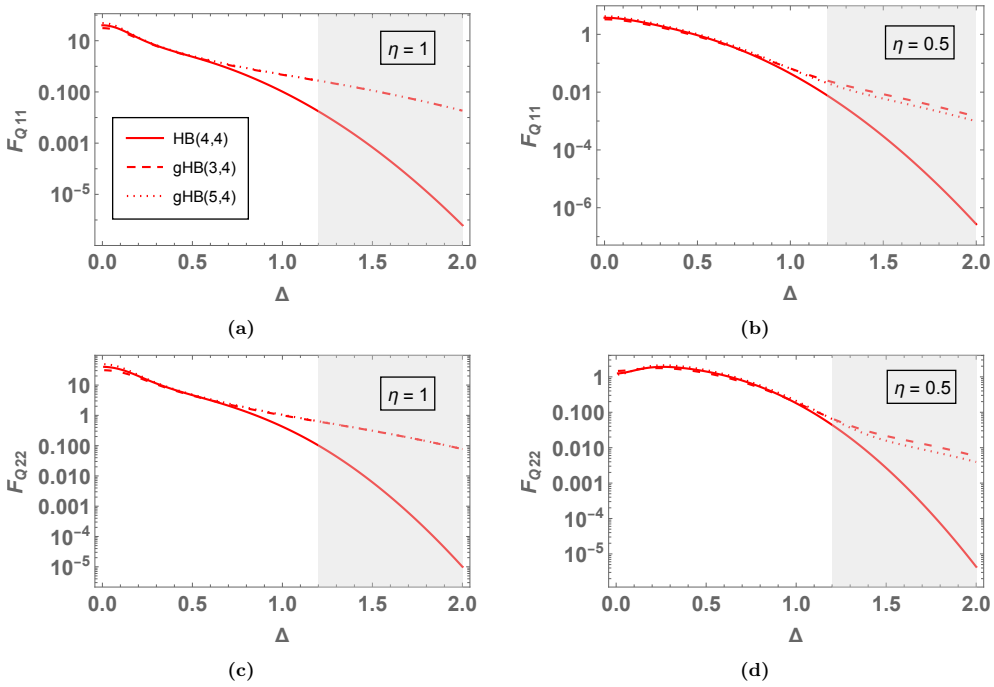

FIGURE 6: Plot of QFIs for phase and phase diffusion, $F_{Q\,1,1}$ and $F_{Q\,2,2}$, as a function of phase diffusion Δ with $k=4$ and $N=\{7,8,9\}$ for $\eta=1$ (panels (a) and (c)) and $\eta_a=0.5$ (panels (b) and (d)). The HB state: $|\Psi^{\mathrm{HB}}(4,4)\rangle$ (solid line), the gHB state $|\Psi^{\mathrm{HB}}(3,4)\rangle$ (dashed line), and the gHB state: $|\Psi^{\mathrm{HB}}(5,4)\rangle$ (dotted line) are considered. Note that, in all panels, for the large diffusion region $\Delta > 1.2$ (grey shaded area), the HB state offers much lower sensitivity than the gHB states.

A7 Measurement compatibility with respect to the weights under varying loss on the reference arm

In this section, we demonstrate the behavior of measurement compatibility with respect to the weights for the double homodyne measurement as one varies the loss on the reference arm η_b by keeping η_a at a fixed value. In Fig. 7, we have obtained the plots for gHB states with $N=2,3,4$ and HB states with $N=2,4$. In the regime of high losses on the reference arm i.e., $\eta_b=0.1$, the overall value of r_H^C decreases as N increases. However, with $\eta_b=0.5$, there is a crossing at $y=0.6$. When the loss in the reference arm is low, the overall value of r_H^C increases as N increases. We infer that these features are an artifact of the measurement since they remain qualitatively the same for the class of probe states considered here.

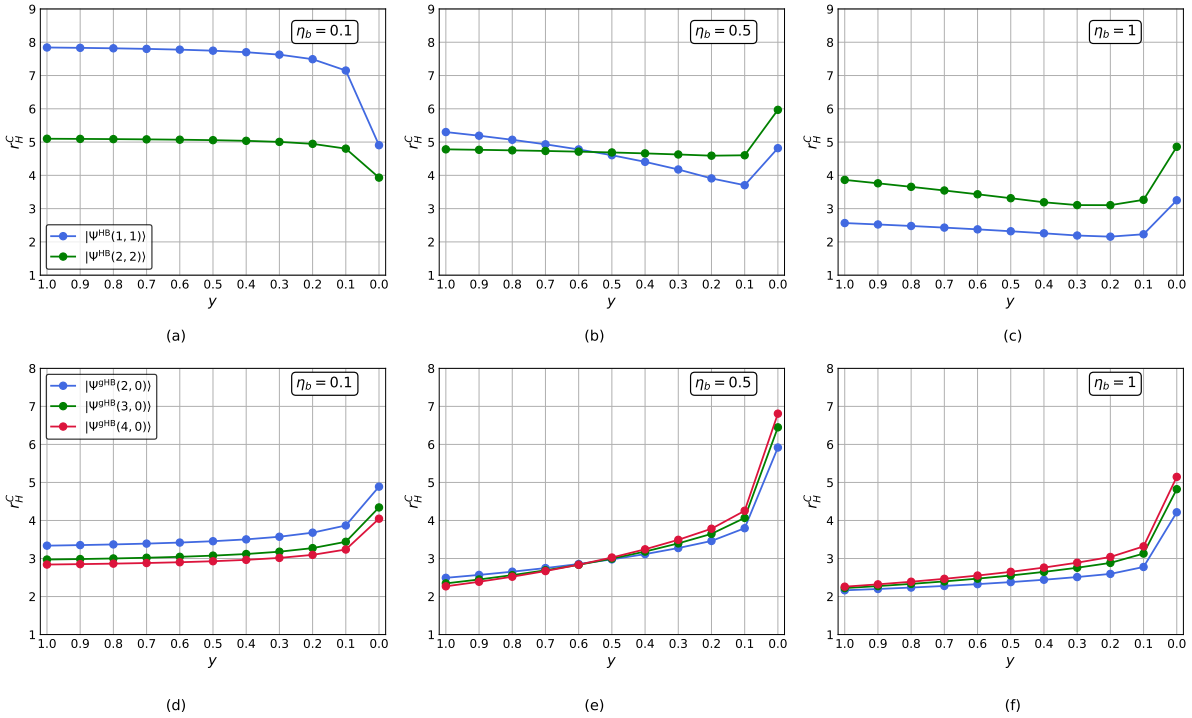

FIGURE 7: *Top row:* Plot of measurement compatibility measure r_H^C versus the weights y for the joint-estimation of phase and loss considering HB states with $N = 2, 4$ at different values of loss on reference arm, namely, $\eta_b = 0.1$, $\eta_b = 0.5$, and $\eta_b = 1$. *Bottom row:* The same plots for gHB states with $N = 2, 3, 4$. The double homodyne measurement is considered and the curves in all the panels are plotted at $\eta_a = 0.5$ and $\Delta = 0$.

A8 Compatibility with respect to the weights under minimal losses

In this section, in Fig. 8, we depict the behavior of both measurement and fundamental compatibilities with respect to the weights under minimal losses in both arms i.e., $\eta_a = \eta_b = 0.999$ for gHB and HB states with $N = 2, 4, 6$. Considering r_H^C for $y = 1$ (phase estimation), due to the manifestation of the optimality of the double homodyne measurement, we get $r_H^C = 1$. However, the value of r_H^C remains below 1.5 until $y = 0.5$ which indicates that, in the multiparameter setting, even though the optimality for a joint estimation is non-achievable, the measurement compatibility performs very well. On the other hand, we find that the value of $r_{BG} \approx 1$ for all values of y.

Therefore, since the double homodyne measurement is optimal for phase estimation, one finds higher compatibility when weights are chosen closer to phase estimation.

As weights are chosen closer to loss estimation, the sub-optimality or the incompatibility of the measurement in estimating loss becomes more pronounced leading to higher values of r_H^C (refer to Eq.). At the same time, as we are estimating extremely low values of losses, the joint-estimation of phase and loss effectively becomes a single-parameter phase estimation problem for which $C_H \approx C_Q$. However, the incompatibility term in C_H becomes more pronounced when one estimates higher values of losses. Thus, in the case of very low losses, the interplay of C_C, C_H, and C_Q, combined with the parameter weights, gives rise to a region where the HCRB is closely attainable with the double homodyne measurement on individual copies of the probe.

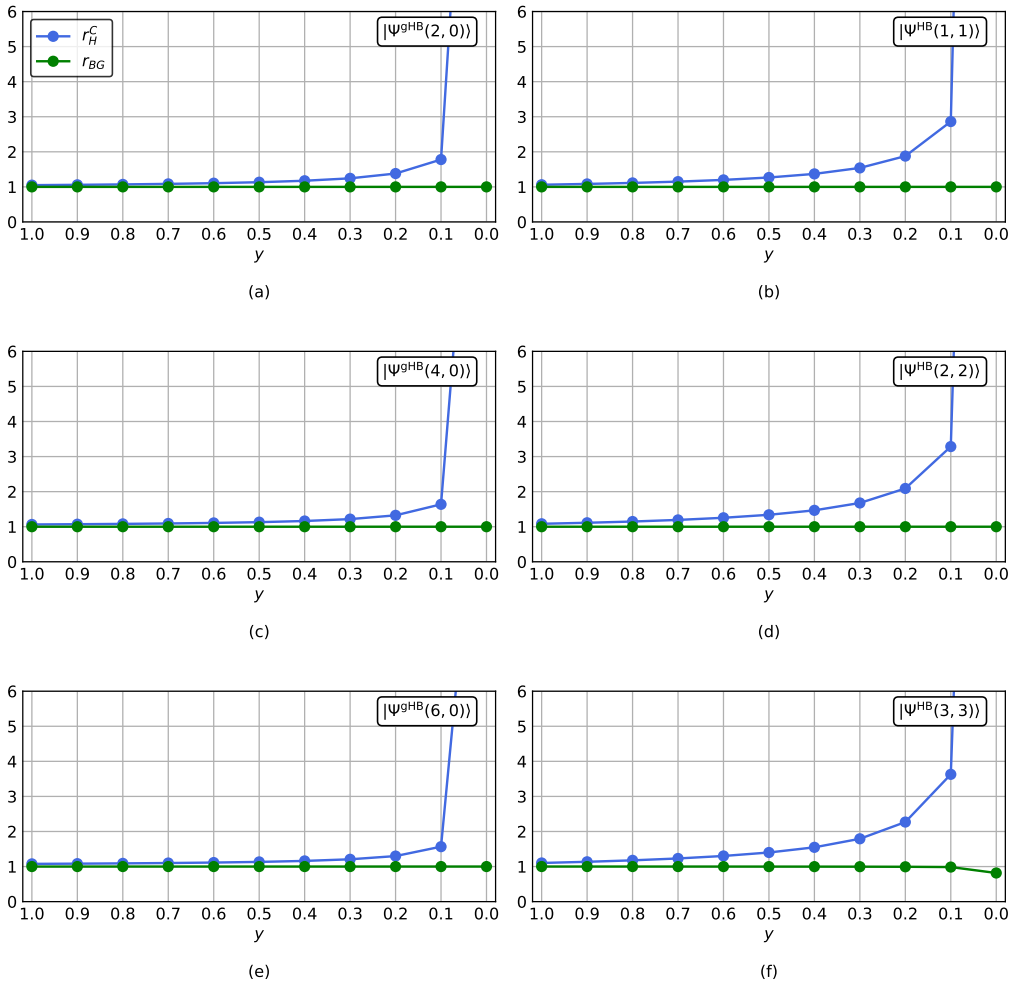

FIGURE 8: Plot of measurement compatibility r_H^C and fundamental compatibility r_{BG} versus the weights y for the joint-estimation of phase and loss with $\eta_a = \eta_b = 0.999$ and $\Delta = 0$ (minimal losses). gHB and HB states with $N = 2, 4, 6$ and double homodyne measurement are considered here. Note that for $y \geq 0.5$, r_H^C remains below 1.5 implying that the HCRB is closely attained by the double homodyne measurement.

A9 Collective quantum enhancement for the estimation of equal losses on both arms

We recall from Section 4.6.4 that collective measurements offer no advantage over separable ones for the cases of the estimation of phase and loss in the phase-shifted arm with (i) no loss and (ii) known amount of loss in the reference arm. In this section, we demonstrate that this is the case even for the joint estimation of phase and equal losses on both arms. This is highlighted in Fig. 9 for the HB and the gHB state $|\Psi^{\mathrm{gHB}}(N,0\rangle$ with $N=2,4$.

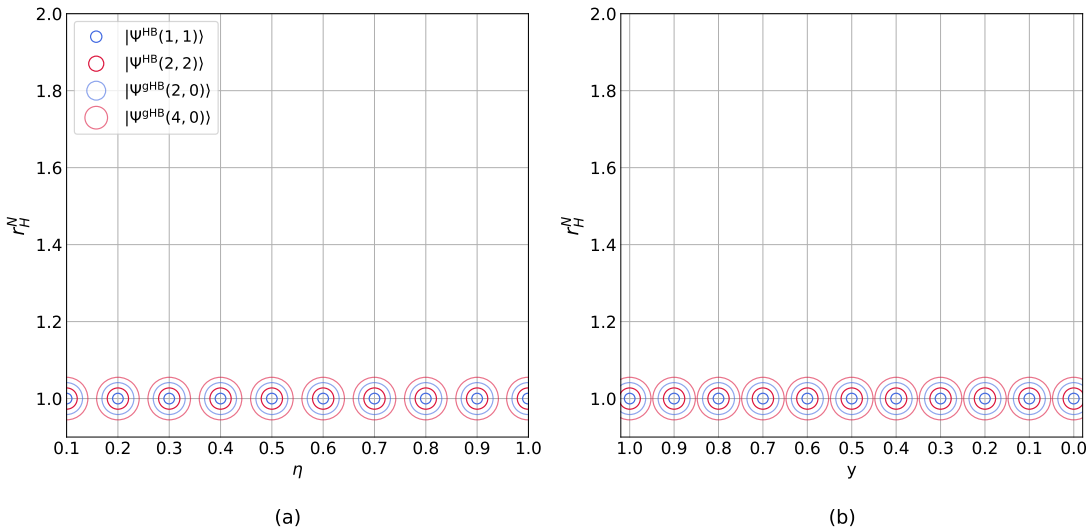

FIGURE 9: Plot of r_H^N versus (a) loss at equal weights in and (b) weights at $\eta = 0.5$. The probe states considered here are the HB state and the gHB state: $|\Psi_{\mathrm{gHB}}(N,0)\rangle$ with $N=2$ and $N=4$. The CQE vanishes for this case both with respect to loss, weights, and the values of N considered consistent with the case of estimation of loss in one arm. The point $\eta = 0$ is excluded due to numerical instabilities.

Bibliography

[1] Scully, M. O., and M. S. Zubairy (1997), *Quantum optics* (Cambridge university press).

[2] Caves, C. M. (1981), "*Quantum-mechanical noise in an interferometer*," Physical Review D **23** (8), 1693.

[3] Yurke, B., S. L. McCall, and J. R. Klauder (1986), "*Su (2) and su (1, 1) interferometers*," Physical Review A **33** (6), 4033.

[4] Giovannetti, V., S. Lloyd, and L. Maccone (2011), "*Advances in quantum metrology*," Nature photonics **5** (4), 222.

[5] Pezze, L., A. Smerzi, M. K. Oberthaler, R. Schmied, and P. Treutlein (2018), "*Quantum metrology with nonclassical states of atomic ensembles*," Reviews of Modern Physics **90** (3), 035005.

[6] Giovannetti, V., S. Lloyd, and L. Maccone (2004), "*Quantum-enhanced measurements: beating the standard quantum limit*," Science **306** (5700), 1330.

[7] Giovannetti, V., S. Lloyd, and L. Maccone (2006), "*Quantum metrology*," Physical review letters **96** (1), 010401.

[8] Tóth, G., and I. Apellaniz (2014), "*Quantum metrology from a quantum information science perspective*," Journal of Physics A: Mathematical and Theoretical **47** (42), 424006.

[9] Demkowicz-Dobrzański, R., M. Jarzyna, and J. Kołodyński (2015), "*Quantum limits in optical interferometry*," Progress in Optics **60**, 345.

[10] Barbieri, M. (2022), "*Optical quantum metrology*," PRX Quantum **3** (1), 010202.

[11] Rademacher, M., J. Millen, and Y. L. Li (2020), "*Quantum sensing with nanoparticles for gravimetry: when bigger is better*," Advanced Optical Technologies **9** (5), 227.

[12] Rodenburg, B., L. Neukirch, A. Vamivakas, and M. Bhattacharya (2016), "*Quantum model of cooling and force sensing with an optically trapped nanoparticle*," Optica **3** (3), 318.

[13] Tikhonenkov, I., M. G. Moore, and A. Vardi (2010), "*Optimal gaussian squeezed states for atom interferometry in the presence of phase diffusion*," Physical Review A—Atomic, Molecular, and Optical Physics **82** (4), 043624.

[14] Liu, Y., G. Jin, and L. You (2010), "*Quantum-limited metrology in the presence of collisional dephasing*," Physical Review A—Atomic, Molecular, and Optical Physics **82** (4), 045601.

[15] Qvarfort, S., A. Serafini, P. F. Barker, and S. Bose (2018), "*Gravimetry through non-linear optomechanics*," Nature communications **9** (1), 3690.

[16] Ruppert, L., A. Rakhubovsky, and R. Filip (2022), "*High-precision multiparameter estimation of mechanical force by quantum optomechanics*," Scientific Reports **12** (1), 16022.

[17] Aasi, J., J. Abadie, B. Abbott, R. Abbott, T. Abbott, M. Abernathy, C. Adams, T. Adams, P. Addesso, R. Adhikari, *et al.* (2013), "*Enhanced sensitivity of the ligo gravitational wave detector by using squeezed states of light*," Nature Photonics **7** (8), 613.

[18] Casella, G., and R. Berger (2024), *Statistical inference* (CRC press).

[19] Preskill, J. (1998), "*Lecture notes for physics 229: Quantum information and computation*," California institute of technology **16** (1), 1.

[20] Helstrom, C. W. (1969), "*Quantum detection and estimation theory*," Journal of Statistical Physics **1**, 231.

[21] Holevo, A. S. (2011), *Probabilistic and statistical aspects of quantum theory*, Vol. 1 (Springer Science & Business Media).

[22] Lu, X.-M., and X. Wang (2021), "*Incorporating heisenberg's uncertainty principle into quantum multiparameter estimation*," Physical Review Letters **126** (12), 120503.

[23] Kull, I., P. A. Guérin, and F. Verstraete (2020), "*Uncertainty and trade-offs in quantum multiparameter estimation*," Journal of Physics A: Mathematical and Theoretical **53** (24), 244001.

[24] Ragy, S., M. Jarzyna, and R. Demkowicz-Dobrzański (2016), "*Compatibility in multiparameter quantum metrology*," Physical Review A **94** (5), 052108.

[25] Banaszek, K., R. Demkowicz-Dobrzański, and I. A. Walmsley (2009), "*Quantum states made to measure*," Nature Photonics **3** (12), 673.

[26] Demkowicz-Dobrzanski, R., U. Dorner, B. Smith, J. Lundeen, W. Wasilewski, K. Banaszek, and I. Walmsley (2009), "*Quantum phase estimation with lossy interferometers*," Physical Review A—Atomic, Molecular, and Optical Physics **80** (1), 013825.

[27] Escher, B., R. L. de Matos Filho, and L. Davidovich (2011), "*General framework for estimating the ultimate precision limit in noisy quantum-enhanced metrology*," Nature Physics **7** (5), 406.

[28] Suzuki, J., Y. Yang, and M. Hayashi (2020), "*Quantum state estimation with nuisance parameters*," Journal of Physics A: Mathematical and Theoretical **53** (45), 453001.

[29] Lehmann, E. L., and G. Casella (2006), *Theory of point estimation* (Springer Science & Business Media).

[30] Genoni, M. G., S. Olivares, and M. G. Paris (2011), "*Optical phase estimation in the presence of phase diffusion*," Physical review letters **106** (15), 153603.

[31] Genoni, M. G., S. Olivares, D. Brivio, S. Cialdi, D. Cipriani, A. Santamato, S. Vezzoli, and M. G. Paris (2012), "*Optical interferometry in the presence of large phase diffusion*," Physical Review A **85** (4), 043817.

[32] Guo, L.-S., B.-M. Xu, J. Zou, and B. Shao (2016), "*Magnetic field sensing subject to correlated noise with a ring spin chain*," Scientific Reports **6** (1), 33254.

[33] Amorós-Binefa, J., and J. Kołodyński (2025), "*Noisy atomic magnetometry with kalman filtering and measurement-based feedback*," PRX Quantum **6** (3), 030331.

[34] Vidrighin, M. D., G. Donati, M. G. Genoni, X.-M. Jin, W. S. Kolthammer, M. Kim, A. Datta, M. Barbieri, and I. A. Walmsley (2014), "*Joint estimation of phase and phase diffusion for quantum metrology*," Nature communications **5** (1), 3532.

[35] Kok, P., and B. W. Lovett (2010), *Introduction to optical quantum information processing* (Cambridge university press).

[36] Flamini, F., N. Spagnolo, and F. Sciarrino (2018), "*Photonic quantum information processing: a review*," Reports on Progress in Physics **82** (1), 016001.

[37] Aharonovich, I., D. Englund, and M. Toth (2016), "*Solid-state single-photon emitters*," Nature photonics **10** (10), 631.

[38] Allen, L., M. W. Beijersbergen, R. Spreeuw, and J. Woerdman (1992), "*Orbital angular momentum of light and the transformation of laguerre-gaussian laser modes*," Physical review A **45** (11), 8185.

[39] Padgett, M., J. Courtial, and L. Allen (2004), "*Light's orbital angular momentum*," Physics today **57** (5), 35.

[40] Marcikic, I., H. De Riedmatten, W. Tittel, H. Zbinden, and N. Gisin (2003), "*Long-distance teleportation of qubits at telecommunication wavelengths*," Nature **421** (6922), 509.

[41] Schreiber, A., A. Gábris, P. P. Rohde, K. Laiho, M. Štefaňák, V. Potoček, C. Hamilton, I. Jex, and C. Silberhorn (2012), "*A 2d quantum walk simulation of two-particle dynamics*," Science **336** (6077), 55.

[42] Lorz, L., E. Meyer-Scott, T. Nitsche, V. Potoček, A. Gábris, S. Barkhofen, I. Jex, and C. Silberhorn (2019), "*Photonic quantum walks with four-dimensional coins*," Physical Review Research **1** (3), 033036.

[43] Zhong, T., H. Zhou, R. D. Horansky, C. Lee, V. B. Verma, A. E. Lita, A. Restelli, J. C. Bienfang, R. P. Mirin, T. Gerrits, *et al.* (2015), "*Photon-efficient quantum key distribution using time–energy entanglement with high-dimensional encoding*," New Journal of Physics **17** (2), 022002.

[44] Nunn, J., L. Wright, C. Söller, L. Zhang, I. Walmsley, and B. Smith (2013), "*Large-alphabet time-frequency entangled quantum key distribution by means of time-to-frequency conversion*," Optics express **21** (13), 15959.

[45] Gianani, I., M. Sbroscia, and M. Barbieri (2020), "*Measuring the time–frequency properties of photon pairs: A short review*," AVS Quantum Science **2** (1).

[46] Adesso, G., S. Ragy, and A. R. Lee (2014), "*Continuous variable quantum information: Gaussian states and beyond*," Open Systems & Information Dynamics **21** (01n02), 1440001.

[47] Ma, J., X. Wang, C.-P. Sun, and F. Nori (2011), "*Quantum spin squeezing*," Physics Reports **509** (2-3), 89.

[48] Braunstein, S. L., and P. Van Loock (2005), "*Quantum information with continuous variables*," Reviews of modern physics **77** (2), 513.

[49] Lee, H., P. Kok, and J. P. Dowling (2002), "*A quantum rosetta stone for interferometry*," Journal of Modern Optics **49** (14-15), 2325.

[50] Olivares, S., and M. Paris (2007), "*Optimized interferometry with gaussian states*," Optics and Spectroscopy **103** (2), 231.

[51] Dowling, J. P. (2008), "*Quantum optical metrology–the lowdown on high-n00n states*," Contemporary physics **49** (2), 125.

[52] Rarity, J., P. Tapster, E. Jakeman, T. Larchuk, R. Campos, M. Teich, and B. Saleh (1990), "*Two-photon interference in a mach-zehnder interferometer*," Physical review letters **65** (11), 1348.

[53] Bollinger, J. J., W. M. Itano, D. J. Wineland, and D. J. Heinzen (1996), "*Optimal frequency measurements with maximally correlated states*," Physical Review A **54** (6), R4649.

[54] Holland, M. J., and K. Burnett (1993), "*Interferometric detection of optical phase shifts at the heisenberg limit*," Physical review letters **71** (9), 1355.

[55] Thekkadath, G., M. Mycroft, B. Bell, C. Wade, A. Eckstein, D. Phillips, R. Patel, A. Buraczewski, A. Lita, T. Gerrits, *et al.* (2020), "*Quantum-enhanced interferometry with large heralded photon-number states*," NPJ quantum information **6** (1), 89.

[56] Dorner, U., R. Demkowicz-Dobrzanski, B. J. Smith, J. S. Lundeen, W. Wasilewski, K. Banaszek, and I. A. Walmsley (2009), "*Optimal quantum phase estimation*," Physical review letters **102** (4), 040403.

[57] Kacprowicz, M., R. Demkowicz-Dobrzański, W. Wasilewski, K. Banaszek, and I. Walmsley (2010), "*Experimental quantum-enhanced estimation of a lossy phase shift*," Nature Photonics **4** (6), 357.

[58] Huelga, S. F., C. Macchiavello, T. Pellizzari, A. K. Ekert, M. B. Plenio, and J. I. Cirac (1997), "*Improvement of frequency standards with quantum entanglement*," Physical Review Letters **79** (20), 3865.

[59] Rubin, M. A., and S. Kaushik (2007), "*Loss-induced limits to phase measurement precision with maximally entangled states*," Physical Review A—Atomic, Molecular, and Optical Physics **75** (5), 053805.

[60] Gilbert, G., M. Hamrick, and Y. S. Weinstein (2008), "*Use of maximally entangled n-photon states for practical quantum interferometry*," Journal of the Optical Society of America B **25** (8), 1336.

[61] Higgins, B. L., D. W. Berry, S. D. Bartlett, H. M. Wiseman, and G. J. Pryde (2007), "*Entanglement-free heisenberg-limited phase estimation*," Nature **450** (7168), 393.

[62] Higgins, B. L., D. W. Berry, S. D. Bartlett, M. W. Mitchell, H. M. Wiseman, and G. J. Pryde (2009), "*Demonstrating heisenberg-limited unambiguous phase estimation without adaptive measurements*," New Journal of Physics **11** (7), 073023.

[63] Demkowicz-Dobrzański, R. (2010), "*Multi-pass classical vs. quantum strategies in lossy phase estimation*," Laser physics **20** (5), 1197.

[64] De Martini, F. (1998), "*Amplification of quantum entanglement*," Physical review letters **81** (14), 2842.

[65] De Martini, F. (1998), "*Quantum superposition of parametrically amplified multiphoton pure states*," Physics Letters A **250** (1-3), 15.

[66] Vitelli, C., N. Spagnolo, L. Toffoli, F. Sciarrino, and F. De Martini (2010), "*Enhanced resolution of lossy interferometry by coherent amplification of single photons*," Physical review letters **105** (11), 113602.

[67] Spagnolo, N., C. Vitelli, V. G. Lucivero, V. Giovannetti, L. Maccone, and F. Sciarrino (2012), "*Phase estimation via quantum interferometry for noisy detectors*," Physical Review Letters **108** (23), 233602.

[68] Cable, H., and G. A. Durkin (2010), "*Parameter estimation with entangled photons produced by parametric down-conversion*," Physical review letters **105** (1), 013603.

[69] Matthews, J. C., X.-Q. Zhou, H. Cable, P. J. Shadbolt, D. J. Saunders, G. A. Durkin, G. J. Pryde, and J. L. O'brien (2016), "*Towards practical quantum metrology with photon counting*," npj Quantum Information **2** (1), 1.

[70] Bai, K., Z. Peng, H.-G. Luo, and J.-H. An (2019), "*Retrieving ideal precision in noisy quantum optical metrology*," Physical review letters **123** (4), 040402.

[71] Degen, C. L., F. Reinhard, and P. Cappellaro (2017), "*Quantum sensing*," Reviews of modern physics **89** (3), 035002.

[72] Brivio, D., S. Cialdi, S. Vezzoli, B. T. Gebrehiwot, M. G. Genoni, S. Olivares, and M. G. Paris (2010), "*Experimental estimation of one-parameter qubit gates in the presence of phase diffusion*," Physical Review A—Atomic, Molecular, and Optical Physics **81** (1), 012305.

[73] Wang, K., X. Wang, X. Zhan, Z. Bian, J. Li, B. C. Sanders, and P. Xue (2018), "*Entanglement-enhanced quantum metrology in a noisy environment*," Physical Review A **97** (4), 042112.

[74] Albarelli, F., M. A. Rossi, D. Tamascelli, and M. G. Genoni (2018), "*Restoring heisenberg scaling in noisy quantum metrology by monitoring the environment*," Quantum **2**, 110.

[75] Nichols, R., T. R. Bromley, L. A. Correa, and G. Adesso (2016), "*Practical quantum metrology in noisy environments*," Physical Review A **94** (4), 042101.

[76] Gao, Y., P. M. Anisimov, C. F. Wildfeuer, J. Luine, H. Lee, and J. P. Dowling (2010), "*Super-resolution at the shot-noise limit with coherent states and photon-number-resolving detectors*," Journal of the Optical Society of America B **27** (6), A170.

[77] Jiang, K., H. Lee, C. C. Gerry, and J. P. Dowling (2013), "*Super-resolving quantum radar: Coherent-state sources with homodyne detection suffice to beat the diffraction limit*," Journal of Applied Physics **114** (19).

[78] Louisell, W., A. Yariv, and A. Siegman (1961), "*Quantum fluctuations and noise in parametric processes. i.*" Physical Review **124** (6), 1646.

[79] Couteau, C. (2018), "*Spontaneous parametric down-conversion*," Contemporary Physics **59** (3), 291.

[80] Mitchell, M. W., J. S. Lundeen, and A. M. Steinberg (2004), "*Super-resolving phase measurements with a multiphoton entangled state*," Nature **429** (6988), 161.

[81] Jennewein, T., C. Simon, G. Weihs, H. Weinfurter, and A. Zeilinger (2000), "*Quantum cryptography with entangled photons*," Physical review letters **84** (20), 4729.

[82] Franson, J. D. (1989), "*Bell inequality for position and time*," Physical review letters **62** (19), 2205.

[83] Bouwmeester, D., J.-W. Pan, K. Mattle, M. Eibl, H. Weinfurter, and A. Zeilinger (1997), "*Experimental quantum teleportation*," Nature **390** (6660), 575.

[84] Bouwmeester, D., J.-W. Pan, M. Daniell, H. Weinfurter, and A. Zeilinger (1999), "*Observation of three-photon greenberger-horne-zeilinger entanglement*," Physical Review Letters **82** (7), 1345.

[85] Kwiat, P. G., K. Mattle, H. Weinfurter, A. Zeilinger, A. V. Sergienko, and Y. Shih (1995), "*New high-intensity source of polarization-entangled photon pairs*," Physical Review Letters **75** (24), 4337.

[86] Vidal, F., and A. Tadjeddine (2005), "*Sum-frequency generation spectroscopy of interfaces*," Reports on Progress in Physics **68** (5), 1095.

[87] Gerry, C. C., and P. L. Knight (2023), *Introductory quantum optics* (Cambridge university press).

[88] Ono, T., R. Okamoto, and S. Takeuchi (2013), "*An entanglement-enhanced microscope*," Nature communications **4** (1), 2426.

[89] Hofmann, H. F., and T. Ono (2007), "*High-photon-number path entanglement in the interference of spontaneously down-converted photon pairs with coherent laser light*," Physical Review A—Atomic, Molecular, and Optical Physics **76** (3), 031806.

[90] Pezzé, L., and A. Smerzi (2008), "*Mach-zehnder interferometry at the heisenberg limit with coherent and squeezed-vacuum light*," Physical review letters **100** (7), 073601.

[91] Seshadreesan, K. P., P. M. Anisimov, H. Lee, and J. P. Dowling (2011), "*Parity detection achieves the heisenberg limit in interferometry with coherent mixed with squeezed vacuum light*," New Journal of Physics **13** (8), 083026.

[92] d'Ariano, G., C. Macchiavello, and M. G. Paris (1995), "*Optimized phase detection*," Physics Letters A **198** (4), 286.

[93] Hong, C.-K., Z.-Y. Ou, and L. Mandel (1987), "*Measurement of subpicosecond time intervals between two photons by interference*," Physical review letters **59** (18), 2044.

[94] Durkin, G. A., and J. P. Dowling (2007), "*Local and global distinguishability in quantum interferometry*," Physical review letters **99** (7), 070801.

[95] Killoran, N., M. Cramer, and M. B. Plenio (2014), "*Extracting entanglement from identical particles*," Physical review letters **112** (15), 150501.

[96] Castellini, A., R. Lo Franco, L. Lami, A. Winter, G. Adesso, and G. Compagno (2019), "*Indistinguishability-enabled coherence for quantum metrology*," Physical Review A **100** (1), 012308.

[97] Polino, E., M. Valeri, N. Spagnolo, and F. Sciarrino (2020), "*Photonic quantum metrology*," AVS Quantum Science **2** (2).

[98] Hadfield, R. H., J. Leach, F. Fleming, D. J. Paul, C. H. Tan, J. S. Ng, R. K. Henderson, and G. S. Buller (2023), "*Single-photon detection for long-range imaging and sensing*," Optica **10** (9), 1124.

[99] McKay, K. (1954), "*Avalanche breakdown in silicon*," Physical Review **94** (4), 877.

[100] Eisaman, M. D., J. Fan, A. Migdall, and S. V. Polyakov (2011), "*Invited review article: Single-photon sources and detectors*," Review of scientific instruments **82** (7).

[101] Nevet, A., A. Hayat, and M. Orenstein (2011), "*Ultrafast three-photon counting in a photomultiplier tube*," Optics letters **36** (5), 725.

[102] Fitch, M., B. Jacobs, T. Pittman, and J. Franson (2003), "*Photon-number resolution using time-multiplexed single-photon detectors*," Physical Review A **68** (4), 043814.

[103] Hadfield, R. H. (2009), "*Single-photon detectors for optical quantum information applications*," Nature photonics **3** (12), 696.

[104] You, L. (2020), "*Superconducting nanowire single-photon detectors for quantum information*," Nanophotonics **9** (9), 2673.

[105] Na, N., Y.-C. Lu, Y.-H. Liu, P.-W. Chen, Y.-C. Lai, Y.-R. Lin, C.-C. Lin, T. Shia, C.-H. Cheng, and S.-L. Chen (2024), "*Room temperature operation of germanium–silicon single-photon avalanche diode*," Nature **627** (8003), 295.

[106] Kalashnikov, D. A., S. H. Tan, M. V. Chekhova, and L. A. Krivitsky (2011), "*Accessing photon bunching with a photon number resolving multi-pixel detector*," Optics Express **19** (10), 9352.

[107] Robinson, D. L., and B. D. Metscher (1987), "*Single-photon detection with avalanche photodiodes*," in *Conference on Lasers and Electro-Optics* (Optica Publishing Group) Chap. NA, p. WI47.

[108] Yanikgonul, S., V. Leong, J. R. Ong, T. Hu, S. Y. Siew, C. E. Png, and L. Krivitsky (2021), "*Integrated avalanche photodetectors for visible light*," Nature communications **12** (1), 1834.

[109] Gramuglia, F., M.-L. Wu, C. Bruschini, M.-J. Lee, and E. Charbon (2021), "*A low-noise cmos spad pixel with 12.1 ps sptr and 3 ns dead time*," IEEE Journal of Selected Topics in Quantum Electronics **28** (2: Optical Detectors), 1.

[110] Mičuda, M., O. Haderka, and M. Ježek (2008), "*High-efficiency photon-number-resolving multichannel detector*," Physical Review A—Atomic, Molecular, and Optical Physics **78** (2), 025804.

[111] Jiang, L. A., E. A. Dauler, and J. T. Chang (2007), "*Photon-number-resolving detector with 10 bits of resolution*," Physical Review A—Atomic, Molecular, and Optical Physics **75** (6), 062325.

[112] Limongi, L., F. Martini, T. H. Dao, A. Gaggero, H. Hasnaoui, I. Lopez-Gonzalez, F. Chiarello, F. De Matteis, A. Quaranta, A. Salamon, *et al.* (2025), "*Linearly multiplexed photon number resolving single-photon detectors array*," Optics Communications **575**, 131244.

[113] Kahl, O., S. Ferrari, V. Kovalyuk, A. Vetter, G. Lewes-Malandrakis, C. Nebel, A. Korneev, G. Goltsman, and W. Pernice (2017), "*Spectrally multiplexed single-photon detection with hybrid superconducting nanophotonic circuits*," Optica **4** (5), 557.

[114] Resta, G. V., L. Stasi, M. Perrenoud, S. El-Khoury, T. Brydges, R. Thew, H. Zbinden, and F. Bussières (2023), "*Gigahertz detection rates and dynamic photon-number resolution with superconducting nanowire arrays*," Nano Letters **23** (13), 6018.

[115] Fukuda, D., G. Fujii, T. Numata, A. Yoshizawa, H. Tsuchida, H. Fujino, H. Ishii, T. Itatani, S. Inoue, and T. Zama (2009), "*Photon number resolving detection with high speed and high quantum efficiency*," Metrologia **46** (4), S288.

[116] Fukuda, D., G. Fujii, T. Numata, K. Amemiya, A. Yoshizawa, H. Tsuchida, H. Fujino, H. Ishii, T. Itatani, S. Inoue, *et al.* (2011), "*Titanium-based transition-edge photon number resolving detector with 98% detection efficiency with index-matched small-gap fiber coupling*," Optics express **19** (2), 870.

[117] Höpker, J. P., T. Gerrits, A. Lita, S. Krapick, H. Herrmann, R. Ricken, V. Quiring, R. Mirin, S. W. Nam, C. Silberhorn, *et al.* (2019), "*Integrated transition edge sensors on titanium in-diffused lithium niobate waveguides*," APL Photonics **4** (5).

[118] Lamas-Linares, A., B. Calkins, N. A. Tomlin, T. Gerrits, A. E. Lita, J. Beyer, R. P. Mirin, and S. W. Nam (2012), "*Nanosecond-scale timing jitter in transition edge sensors at telecom and visible wavelengths*," arXiv preprint arXiv:1209.5721 .

[119] Raj, V., A. Azem, M. Patterson, D. K. Namburi, J. F. Young, and R. H. Hadfield (2025), "*Waveguide integrated superconducting nanowire single-photon detectors for integrated photonics*," Journal of Physics D: Applied Physics **58** (24), 243001.

[120] Fleming, F., W. McCutcheon, E. E. Wollman, A. D. Beyer, V. Anant, B. Korzh, J. P. Allmaras, L. Narváez, S. Leedumrongwatthanakun, G. S. Buller, *et al.* (2025), "*High-efficiency, high-count-rate 2d superconducting nanowire single-photon detector array*," Optics Express **33** (13), 27602.

[121] Korzh, B., Q.-Y. Zhao, J. P. Allmaras, S. Frasca, T. M. Autry, E. A. Bersin, A. D. Beyer, R. M. Briggs, B. Bumble, M. Colangelo, *et al.* (2020), "*Demonstration of sub-3 ps temporal resolution with a superconducting nanowire single-photon detector*," Nature Photonics **14** (4), 250.

[122] Craiciu, I., B. Korzh, A. D. Beyer, A. Mueller, J. P. Allmaras, L. Narváez, M. Spiropulu, B. Bumble, T. Lehner, E. E. Wollman, *et al.* (2023), "*High-speed detection of 1550 nm single photons with superconducting nanowire detectors*," Optica **10** (2), 183.

[123] Reddy, D. V., R. R. Nerem, S. W. Nam, R. P. Mirin, and V. B. Verma (2020), "*Superconducting nanowire single-photon detectors with 98% system detection efficiency at 1550 nm*," Optica **7** (12), 1649.

[124] Allevi, A., M. Bina, S. Olivares, and M. Bondani (2017), "*Homodyne-like detection scheme based on photon-number-resolving detectors*," International Journal of Quantum Information **15** (08), 1740016.

[125] Hamamatsu Photonics, (2024), "*S13773 and s15193 si pin photodiode datasheet*," Accessed: 2025-10-11.

[126] Raffaelli, F., G. Ferranti, D. H. Mahler, P. Sibson, J. E. Kennard, A. Santamato, G. Sinclair, D. Bonneau, M. G. Thompson, and J. C. Matthews (2018), "*A homodyne detector integrated onto a photonic chip for measuring quantum states and generating random numbers*," Quantum Science and Technology **3** (2), 025003.

[127] Cooper, M., C. Söller, and B. J. Smith (2013), "*High-stability time-domain balanced homodyne detector for ultrafast optical pulse applications*," Journal of Modern Optics **60** (8), 611.

[128] Grosshans, F., and P. Grangier (2001), "*Effective quantum efficiency in the pulsed homodyne detection of a n-photon state*," The European Physical Journal D-Atomic, Molecular, Optical and Plasma Physics **14** (1), 119.

[129] Heim, B., D. Elser, T. Bartley, M. Sabuncu, C. Wittmann, D. Sych, C. Marquardt, and G. Leuchs (2010), "*Atmospheric channel characteristics for quantum communication with continuous polarization variables*," Applied Physics B **98** (4), 635.

[130] Jouguet, P., S. Kunz-Jacques, A. Leverrier, P. Grangier, and E. Diamanti (2013), "*Experimental demonstration of long-distance continuous-variable quantum key distribution*," Nature photonics **7** (5), 378.

[131] Lvovsky, A. I., and M. G. Raymer (2009), "*Continuous-variable optical quantum-state tomography*," Reviews of modern physics **81** (1), 299.

[132] Smithey, D. T., M. Beck, M. G. Raymer, and A. Faridani (1993), "*Measurement of the wigner distribution and the density matrix of a light mode using optical homodyne tomography: Application to squeezed states and the vacuum*," Physical review letters **70** (9), 1244.

[133] Lobino, M., D. Korystov, C. Kupchak, E. Figueroa, B. C. Sanders, and A. Lvovsky (2008), "*Complete characterization of quantum-optical processes*," Science **322** (5901), 563.

[134] Bruynsteen, C., M. Vanhoecke, J. Bauwelinck, and X. Yin (2021), "*Integrated balanced homodyne photonic–electronic detector for beyond 20 ghz shot-noise-limited measurements*," Optica **8** (9), 1146.

[135] Ng, S. Q., G. Zhang, C. Lim, and C. Wang (2024), "*A chip-integrated homodyne detection system with enhanced bandwidth performance for quantum applications*," Quantum Science and Technology **9** (4), 045010.

[136] Jia, Y., X. Wang, X. Hu, X. Hua, Y. Zhang, X. Guo, S. Zhang, X. Xiao, S. Yu, J. Zou, *et al.* (2023), "*Silicon photonics-integrated time-domain balanced homodyne detector for quantum tomography and quantum key distribution*," New Journal of Physics **25** (10), 103030.

[137] D'ariano, G. M., M. G. Paris, and M. F. Sacchi (2000), "*Parameter estimation in quantum optics*," Physical Review A **62** (2), 023815.

[138] Olivares, S., and M. G. Paris (2009), "*Bayesian estimation in homodyne interferometry*," Journal of Physics B: Atomic, Molecular and Optical Physics **42** (5), 055506.

[139] Clark, L. A., and J. Kołodyński (2025), "*Efficient inference of quantum system parameters by approximate bayesian computation*," Physical Review Applied **23** (4), 044040.

[140] Roccia, E., V. Cimini, M. Sbroscia, I. Gianani, L. Ruggiero, L. Mancino, M. G. Genoni, M. A. Ricci, and M. Barbieri (2018), "*Multiparameter approach to quantum phase estimation with limited visibility*," Optica **5** (10), 1171.

[141] Belliardo, F., V. Cimini, E. Polino, F. Hoch, B. Piccirillo, N. Spagnolo, V. Giovannetti, and F. Sciarrino (2024), "*Optimizing quantum-enhanced bayesian multiparameter estimation of phase and noise in practical sensors*," Physical Review Research **6** (2), 023201.

[142] Crowley, P. J., A. Datta, M. Barbieri, and I. A. Walmsley (2014), "*Tradeoff in simultaneous quantum-limited phase and loss estimation in interferometry*," Physical Review A **89** (2), 023845.

[143] Albarelli, F., J. F. Friel, and A. Datta (2019), "*Evaluating the Holevo Cramér-Rao bound for multiparameter quantum metrology*," Physical review letters **123** (20), 200503.

[144] Szczykulska, M., T. Baumgratz, and A. Datta (2017), "*Reaching for the quantum limits in the simultaneous estimation of phase and phase diffusion*," Quantum Science and Technology **2** (4), 044004.

[145] Kay, S. M. (1993), *Fundamentals of statistical signal processing: estimation theory* (Prentice-Hall, Inc.).

[146] Tsang, M. (2012), "*Ziv-zakai error bounds for quantum parameter estimation*," Physical review letters **108** (23), 230401.

[147] Van der Vaart, A. W. (2000), *Asymptotic statistics*, Vol. 3 (Cambridge university press).

[148] Durham, G. B., and A. R. Gallant (2002), "*Numerical techniques for maximum likelihood estimation of continuous-time diffusion processes*," Journal of Business & Economic Statistics **20** (3), 297.

[149] Pedersen, A. R. (1995), "*Consistency and asymptotic normality of an approximate maximum likelihood estimator for discretely observed diffusion processes*," Bernoulli , 257.

[150] Nagaoka, H. (2005), "*A new approach to Cramér-Rao bounds for quantum state estimation*," in *Asymptotic theory of quantum statistical inference: Selected Papers* (World Scientific) pp. 100–112.

[151] Demkowicz-Dobrzański, R., W. Górecki, and M. Guţă (2020), "*Multi-parameter estimation beyond quantum fisher information*," Journal of Physics A: Mathematical and Theoretical **53** (36), 363001.

[152] Albarelli, F., M. Barbieri, M. G. Genoni, and I. Gianani (2020), "*A perspective on multi-parameter quantum metrology: From theoretical tools to applications in quantum imaging*," Physics Letters A **384** (12), 126311.

[153] Tsang, M., F. Albarelli, and A. Datta (2020), "*Quantum semiparametric estimation*," Physical Review X **10** (3), 031023.

[154] Albarelli, F., M. Tsang, and A. Datta (2019), "*Upper bounds on the Holevo Cram\'er-Rao bound for multiparameter quantum parametric and semiparametric estimation*," arXiv preprint arXiv:1911.11036 .

[155] Carollo, A., B. Spagnolo, A. A. Dubkov, and D. Valenti (2019), "*On quantumness in multi-parameter quantum estimation*," Journal of Statistical Mechanics: Theory and Experiment **2019** (9), 094010.

[156] Guţă, M., and J. Kahn (2006), "*Local asymptotic normality for qubit states*," Physical Review A—Atomic, Molecular, and Optical Physics **73** (5), 052108.

[157] Kahn, J., and M. Guţă (2009), "*Local asymptotic normality for finite dimensional quantum systems*," Communications in Mathematical Physics **289** (2), 597.

[158] Massar, S., and S. Popescu (1995), "*Optimal extraction of information from finite quantum ensembles*," Physical review letters **74** (8), 1259.

[159] Yamagata, K., A. Fujiwara, and R. D. Gill (2013), "*Quantum local asymptotic normality based on a new quantum likelihood ratio*," Annals of Statistics **41** (4), 2197.

[160] Yang, Y., G. Chiribella, and M. Hayashi (2019), "*Attaining the ultimate precision limit in quantum state estimation*," Communications in Mathematical Physics **368**, 223.

[161] Matsumoto, K. (2002), "*A new approach to the Cramér-Rao-type bound of the pure-state model*," Journal of Physics A: Mathematical and General **35** (13), 3111.

[162] Vaneph, C., T. Tufarelli, and M. G. Genoni (2013), "*Quantum estimation of a two-phase spin rotation*," Quantum Measurements and Quantum Metrology **1** (1), 12.

[163] Suzuki, J. (2016), "*Explicit formula for the holevo bound for two-parameter qubit-state estimation problem*," Journal of Mathematical Physics **57** (4).

[164] Hayashi, M. (2005), *Asymptotic theory of quantum statistical inference: selected papers* (World Scientific).

[165] Conlon, L. O., J. Suzuki, P. K. Lam, and S. M. Assad (2021), "*Efficient computation of the Nagaoka–Hayashi bound for multiparameter estimation with separable measurements*," npj Quantum Information **7** (1), 110.

[166] Das, A., L. O. Conlon, J. Suzuki, S. K. Yung, P. K. Lam, and S. M. Assad (2025), "*Holevo Cramér-Rao bound: How close can we get without entangling measurements?*" Quantum **9**, 1867.

[167] Conlon, L. O., J. Suzuki, P. K. Lam, and S. M. Assad (2025), "*Role of the extended Hilbert space in the attainability of the quantum Cramér–Rao bound for multiparameter estimation*," Physics Letters A **542**, 130445.

[168] Hayashi, M. (1997), "*A linear programming approach to attainable Cramér-Rao type bounds*," in *Quantum Communication, Computing, and Measurement* (Springer) pp. 99–108.

[169] Hayashi, M., and Y. Ouyang (2023), "*Tight Cramér-Rao type bounds for multiparameter quantum metrology through conic programming*," Quantum **7**, 1094.

[170] Conlon, L. O., J. Suzuki, P. K. Lam, and S. M. Assad (2022), "*The gap persistence theorem for quantum multiparameter estimation*," arXiv preprint arXiv:2208.07386 .

[171] Belliardo, F., and V. Giovannetti (2021), "*Incompatibility in quantum parameter estimation*," New Journal of Physics **23** (6), 063055.

[172] Horodecki, P., Ł. Rudnicki, and K. Życzkowski (2022), "*Five open problems in quantum information theory*," PRX Quantum **3** (1), 010101.

[173] Guo, W., W. Zhong, X.-X. Jing, L.-B. Fu, and X. Wang (2016), "*Berry curvature as a lower bound for multiparameter estimation*," Physical Review A **93** (4), 042115.

[174] Ozawa, M. (2004), "*Uncertainty relations for joint measurements of noncommuting observables*," Physics Letters A **320** (5-6), 367.

[175] Albarelli, F., and R. Demkowicz-Dobrzański (2022), "*Probe incompatibility in multiparameter noisy quantum metrology*," Physical Review X **12** (1), 011039.

[176] Hayashi, M., and Y. Ouyang (2024), "*Finding the optimal probe state for multiparameter quantum metrology using conic programming*," npj Quantum Information **10** (1), 111.

[177] Ohno Bezerra, M. E., F. Albarelli, and R. Demkowicz-Dobrzański (2025), "*Simultaneous optical phase and loss estimation revisited: measurement and probe incompatibility*," Journal of Physics A: Mathematical and Theoretical .

[178] Candeloro, A., Z. Pazhotan, and M. G. Paris (2024), "*Dimension matters: precision and incompatibility in multi-parameter quantum estimation models*," arXiv preprint arXiv:2403.07106 .

[179] Candeloro, A., M. G. Paris, and M. G. Genoni (2021), "*On the properties of the asymptotic incompatibility measure in multiparameter quantum estimation*," Journal of Physics A: Mathematical and Theoretical **54** (48), 485301.

[180] Di Fresco, G., B. Spagnolo, D. Valenti, and A. Carollo (2022), "*Multiparameter quantum critical metrology*," SciPost Physics **13** (4), 077.

[181] Górecki, W., S. Zhou, L. Jiang, and R. Demkowicz-Dobrzański (2020), "*Optimal probes and error-correction schemes in multi-parameter quantum metrology*," Quantum **4**, 288.

[182] Xia, B., J. Huang, H. Li, H. Wang, and G. Zeng (2023), "*Toward incompatible quantum limits on multiparameter estimation*," Nature Communications **14** (1), 1021.

[183] Chen, H., L. Wang, and H. Yuan (2024), "*Simultaneous measurement of multiple incompatible observables and tradeoff in multiparameter quantum estimation*," npj Quantum Information **10** (1), 98.

[184] Jae, J., J. Lee, K.-G. Lee, M. Kim, and J. Lee (2023), "*Metrological power of incompatible measurements*," arXiv preprint arXiv:2311.11785 .

[185] Jayakumar, J., M. E. Mycroft, M. Barbieri, and M. Stobińska (2024), "*Quantum-enhanced joint estimation of phase and phase diffusion*," New Journal of Physics **26** (7), 073016.

[186] Schawlow, A. L., and C. H. Townes (1958), "*Infrared and optical masers*," Physical review **112** (6), 1940.

[187] Lax, M. (1967), "*Classical noise. v. noise in self-sustained oscillators*," Physical Review **160** (2), 290.

[188] Henry, C. (2003), "*Theory of the linewidth of semiconductor lasers*," IEEE Journal of Quantum Electronics **18** (2), 259.

[189] Sargent III, M., M. Scully, and W. Lamb Jr (1970), "*Buildup of laser oscillations from quantum noise*," Applied Optics **9** (11), 2423.

[190] Jofre, M., M. Curty, F. Steinlechner, G. Anzolin, J. Torres, M. Mitchell, and V. Pruneri (2011), "*True random numbers from amplified quantum vacuum*," Optics express **19** (21), 20665.

[191] Xu, F., B. Qi, X. Ma, H. Xu, H. Zheng, and H.-K. Lo (2012), "*Ultrafast quantum random number generation based on quantum phase fluctuations*," Optics express **20** (11), 12366.

[192] Abellan, C., W. Amaya, M. Jofre, M. Curty, A. Acín, J. Capmany, V. Pruneri, and M. W. Mitchell (2014), "*Ultra-fast quantum randomness generation by accelerated phase diffusion in a pulsed laser diode*," Optics express **22** (2), 1645.

[193] Septriani, B., O. de Vries, and M. Gräfe (2019), "*New insights in phase diffusion process in a gain-switched semiconductor laser for quantum random number generation (qrng)*," in *Quantum Information and Measurement* (Optica Publishing Group) Chap. 1, pp. F5A–44.

[194] Cole, J. H., and L. C. Hollenberg (2009), "*Scanning quantum decoherence microscopy*," Nanotechnology **20** (49), 495401.

[195] Xie, D., C. Xu, and A. M. Wang (2017), "*Optimal quantum thermometry by dephasing*," Quantum information processing **16** (6), 155.

[196] Stace, T. M. (2010), "*Quantum limits of thermometry*," Physical Review A—Atomic, Molecular, and Optical Physics **82** (1), 011611.

[197] Brawley, G., M. Vanner, P. E. Larsen, S. Schmid, A. Boisen, and W. Bowen (2016), "*Nonlinear optomechanical measurement of mechanical motion*," Nature communications **7** (1), 10988.

[198] Aspelmeyer, M., T. J. Kippenberg, and F. Marquardt (2014), "*Cavity optomechanics*," Reviews of Modern Physics **86** (4), 1391.

[199] Cialdi, S., E. Suerra, S. Olivares, S. Capra, and M. G. Paris (2020), "*Squeezing phase diffusion*," Physical Review Letters **124** (16), 163601.

[200] Altorio, M., M. G. Genoni, M. D. Vidrighin, F. Somma, and M. Barbieri (2015), "*Weak measurements and the joint estimation of phase and phase diffusion*," Physical Review A **92** (3), 032114.

[201] Schwinger, J., L. Biedenharn, and H. Van Dam (1965), "*Quantum theory of angular momentum*," .

[202] Macieszczak, K. (2013), "*Quantum fisher information: Variational principle and simple iterative algorithm for its efficient computation*," arXiv preprint arXiv:1312.1356 .

[203] Mycroft, M. E., T. McDermott, A. Buraczewski, and M. Stobińska (2023), "*Proposal for the distribution of multiphoton entanglement with optimal rate-distance scaling*," Physical Review A **107** (1), 012607.

[204] Gessner, M., L. Pezzè, and A. Smerzi (2018), "*Sensitivity bounds for multiparameter quantum metrology*," Physical review letters **121** (13), 130503.

[205] The LIGO Scientific Collaboration (LSC), (2011), "*A gravitational wave observatory operating beyond the quantum shot-noise limit*," Nature Physics **7** (12), 962.

[206] Demkowicz-Dobrzański, R., K. Banaszek, and R. Schnabel (2013), "*Fundamental quantum interferometry bound for the squeezed-light-enhanced gravitational wave detector geo 600*," Physical Review A—Atomic, Molecular, and Optical Physics **88** (4), 041802.

[207] Welsch, D.-G., W. Vogel, and T. Opatrnỳ (1999), "*Ii homodyne detection and quantum-state reconstruction*," in *Progress in Optics*, Vol. 39 (Elsevier) pp. 63–211.

[208] Demkowicz-Dobrzański, R., J. Kołodyński, and M. Guţă (2012), "*The elusive heisenberg limit in quantum-enhanced metrology*," Nature communications **3** (1), 1063.

[209] Escher, B., L. Davidovich, N. Zagury, and R. de Matos Filho (2012), "*Quantum metrological limits via a variational approach*," Physical review letters **109** (19), 190404.

[210] Jayakumar, J., M. Barbieri, and M. Stobińska (2025), "*Measurement compatibility in multiparameter quantum interferometry*," Physical Review A **112** (4), 042604.

[211] Zhong, W., L. Zhou, and Y.-B. Sheng (2021), "*Double-port measurements for robust quantum optical metrology*," Phys. Rev. A **103**, 042611.

[212] Dowling, J. P. (1998), "*Correlated input-port, matter-wave interferometer: Quantum-noise limits to the atom-laser gyroscope*," Physical Review A **57** (6), 4736.

[213] Adesso, G., F. Dell'Anno, S. De Siena, F. Illuminati, and L. Souza (2009), "*Optimal estimation of losses at the ultimate quantum limit with non-gaussian states*," Physical Review A—Atomic, Molecular, and Optical Physics **79** (4), 040305.

[214] Monras, A., and M. G. Paris (2007), "*Optimal quantum estimation of loss in bosonic channels*," Physical review letters **98** (16), 160401.

[215] Fujiwara, A. (2001), "*Quantum channel identification problem*," Physical Review A **63** (4), 042304.

[216] Knysh, S., V. N. Smelyanskiy, and G. A. Durkin (2011), "*Scaling laws for precision in quantum interferometry and the bifurcation landscape of the optimal state*," Physical Review A—Atomic, Molecular, and Optical Physics **83** (2), 021804.

[217] Kołodyński, J., and R. Demkowicz-Dobrzański (2010), "*Phase estimation without a priori phase knowledge in the presence of loss*," Physical Review A—Atomic, Molecular, and Optical Physics **82** (5), 053804.

[218] Nair, R. (2018), "*Quantum-limited loss sensing: Multiparameter estimation and bures distance between loss channels*," Physical Review Letters **121** (23), 230801.

[219] Conlon, L., J. Suzuki, P. Lam, and S. Assad (2022), "*The gap persistence theorem for quantum multiparameter estimation (2022)*," arXiv preprint arXiv:2208.07386 .

[220] Nichols, R., P. Liuzzo-Scorpo, P. A. Knott, and G. Adesso (2018), "*Multiparameter gaussian quantum metrology*," Physical Review A **98** (1), 012114.

[221] Jayakumar, J. (2025), "*HCRB for gHB states*," .

[222] MOSEK ApS, (2024), "*MOSEK Fusion API for Python 10.2.5*," .

[223] Amorós-Binefa, J., and J. Kołodyński (2021), "*Noisy atomic magnetometry in real time*," New Journal of Physics **23** (12), 123030.

[224] Oh, C., C. Lee, C. Rockstuhl, H. Jeong, J. Kim, H. Nha, and S.-Y. Lee (2019), "*Optimal gaussian measurements for phase estimation in single-mode gaussian metrology*," npj Quantum Information **5** (1), 10.